



THE HONG KONG  
POLYTECHNIC UNIVERSITY

香港理工大學

Pao Yue-kong Library

包玉剛圖書館

---

## Copyright Undertaking

This thesis is protected by copyright, with all rights reserved.

**By reading and using the thesis, the reader understands and agrees to the following terms:**

1. The reader will abide by the rules and legal ordinances governing copyright regarding the use of the thesis.
2. The reader will use the thesis for the purpose of research or private study only and not for distribution or further reproduction or any other purpose.
3. The reader agrees to indemnify and hold the University harmless from and against any loss, damage, cost, liability or expenses arising from copyright infringement or unauthorized usage.

### IMPORTANT

If you have reasons to believe that any materials in this thesis are deemed not suitable to be distributed in this form, or a copyright owner having difficulty with the material being included in our database, please contact [lbsys@polyu.edu.hk](mailto:lbsys@polyu.edu.hk) providing details. The Library will look into your claim and consider taking remedial action upon receipt of the written requests.

**PHOTOTHERMAL GAS  
SPECTROSCOPY WITH HOLLOW-CORE  
PHOTONIC BANDGAP FIBRE:  
FROM FUNDAMENTAL MECHANISM  
TO DISTRIBUTED SENSING  
APPLICATION**

**LIN YUECHUAN**

**Ph.D**

**The Hong Kong Polytechnic University**

**2018**

The Hong Kong Polytechnic University

Department of Electrical Engineering

**Photothermal Gas Spectroscopy with  
Hollow-core Photonic Bandgap Fibre:  
From Fundamental Mechanism to  
Distributed Sensing Application**

**LIN YUECHUAN**

A thesis submitted in partial fulfillment of the requirements for  
the degree of *Doctor of Philosophy*

August 2017

---

## **CERTIFICATE OF ORIGINALITY**

I hereby declare that this thesis is my own work and that, to the best of my knowledge and belief, it reproduces no material previously published or written, nor material that has been accepted for the award of any other degree or diploma, except where due acknowledgement has been made in the text.

\_\_\_\_\_ (Signed)

LIN Yuechuan (Name of Student)

LIN YUECHUAN

2018

*To my beloved family*

## Abstract

Photothermal interferometry (PTI) is a powerful spectroscopic technique for trace gas analysis with characteristics of ultra-sensitivity, unique selectivity and non-intrusiveness. It usually adapts a pump-probe configuration: the absorption of periodically modulated pump beam in gas molecules causes localized heating, resulting in changes in temperature, pressure and density, and hence modulating the refractive index of the probe beam, that propagates in the same gas sample and accumulates phase modulation. The photothermal phase modulation of the probe beam is detected via an optical interferometer with high precision.

PTI has been well developed in free-space optics arrangements but its performance is limited by the beam divergence, beam spot size, bulky system size and complexity in optical alignment. It usually requires high pump power to achieve ultra-sensitivity. The hollow-core photonic bandgap fibres (HC-PBFs) can confine both the light and gas molecules within the central hollow core over a long length with low loss and provide a higher light intensity with a given optical power. Since the PTI signal is directly proportional to gas absorption length and pump light intensity, PTI in HC-PBFs can achieve much better photothermal (PT) efficiency while makes it possible for the development of all-fibre optical gas sensors with ultra-sensitivity, high selectivity and compact size. It is also capable of developing remote, multiplex points and distributed sensing. Our group has demonstrated a first PTI in HC-PBFs and obtained a limit of detection (LOD) as good as  $2.3 \times 10^{-9} \text{ cm}^{-1}$ , which is comparable with that in free-space optics arrangements but uses only

tens of mW pump power. It enhances the detection sensitivity by nearly 3 orders of magnitude and achieves unprecedented dynamic range of nearly six orders of magnitude, compared with the previously reported gas sensors using HC-PBFs.

However, the mechanism and dynamics of PT phase modulation in HC-PBFs are still not well understood, even though they are essential for the further development of PTI gas sensors. On the other hand, the system used in the preliminary work on PTI with HC-PBFs is still far behind the requirement for practical in-situ gas sensing applications. The objectives of this dissertation are to investigate the fundamental mechanism and dynamics of PT phase modulation, to optimize the performance of PTI sensors and to exploit the possibility of distributed gas sensing application with HC-PBFs.

To investigate the mechanism and dynamics of PT phase modulation in HC-PBFs, we developed a theoretical model and designed a PTI sensor using a pulsed pump source. We proposed a numerical model solved by finite element method to analyze the thermal conduction process in HC-PBFs. Several parameters that affect the efficiency of PT phase modulation in HC-PBFs, i.e. the thermal conduction time, pulse durations of pump beam and the size of hollow-core, are studied. It has been found that the PT efficiency will increase as increasing the pump pulse duration until it reaches  $\sim 1.2 \mu s$ . For pump pulse duration  $> 1.2 \mu s$ , further increasing the pump pulse duration would not enhance the PT efficiency any further. Meanwhile, for pulsed pump source with pulse duration  $> 1.2 \mu s$ , the normalized photothermal phase modulation coefficient is found to be  $\sim 1.5 \text{ rad} \cdot \text{cm} \cdot \text{mW}^{-1} \cdot \text{m}^{-1}$ , normalized to  $1 \text{ cm}^{-1}$  gas absorption coefficient, 1 mW peak pump power and 1 m effective absorption length. The characteristic time constants of leading/trailing parts of PTI output pulse signals are determined by the thermal conduction time of buffered gas in HC-PBFs and non-radiative relaxation time of absorptive gas molecules. The numerical simulation provides an effective way to comprehend and explain the PT phase modulation in HC-PBFs and forms a fundamental reference to optimize the

design of PTI sensors. The results of our numerical model agree well with the experimental results. The LOD down to ppb (parts-per-billion in volume ratio) level of  $C_2H_2$  gas detection using pulsed pump source can be expected.

Towards the real industrial applications of PTI, we studied optimized performance of all-fibre PTI HC-PBFs sensors. The frequency dependence of PT phase modulation in HC-PBFs using a continuous-wave (CW) intensity-modulated pump beam was investigated by use of a fibre-optic Mach-Zehnder interferometer (MZI). We found that there is no significant difference of PT phase modulation efficiency for pump modulation frequency  $f_p < 330kHz$ . However, for  $f_p$  from  $440kHz$  to  $2MHz$ , the PT phase modulation efficiency rolls off quickly. The experimental results agree well with that of our numerical simulation and the normalized PT phase modulation coefficient for a CW sinusoidally intensity-modulated pump source is  $\sim 0.76 rad \cdot cm \cdot mW^{-1} \cdot m^{-1}$ . Such a frequency-dependent PT response can benefit to further optimize the performance of photothermal gas spectroscopy system. The PTI sensors with Mach-Zehnder interferometer (MZI) requires active stabilization with an electric servo-loop control and also requires a nearly perfect length match between the sensing and reference arms to reduce the laser phase noise, which is complex and inconvenient for the applications in harsh environment, remote and multiplexed sensing. We developed a modified all-fibre Sagnac interferometer with passively stabilization based on a  $3 \times 3$  loop coupler. The minimum detectable phase of Sagnac interferometer is measured as  $4 \times 10^{-7} rad / \sqrt{Hz}$ . With PT Sagnac interferometer, we achieved LOD of  $7.8 \times 10^{-8} cm^{-1}$  (or 67 ppb for  $C_2H_2$  detection, 1-s integration time) with a 1.1-m-long HC-PBFs and 45.6 mW peak pump power working at optimized pump modulation frequency. The PT Sagnac interferometry demonstrated a satisfactory long-term stability with maximum signal fluctuations of 1% for over 4.5 hrs under laboratory environment. The PTI with a modified Sagnac interferometer is capable of developing remote and multiplex points sensors.

We studied distributed gas sensing with fibre-optic PTI. With CW intensity-modulated pump source, we derived a general formula to estimate the magnitude of PT phase modulation distributed over a long length HC-PBFs in the presence of absorptive gas molecules. We demonstrated a quasi-distributed photothermal gas spectroscopy with 2 sections of sensing HC-PBFs (each with 28 m length) using a dual-pulse heterodyne multiplexed phase demodulation system. The quasi-distributed gas sensor provides a LOD down to 10 ppb ( $1.2 \times 10^{-8} \text{ cm}^{-1}$ ) for  $C_2H_2$  detection with 55 mW peak pump power. Theoretically, it is possible to multiplex  $\sim 20$  HC-PBF sensors. By incorporating phase-sensitive optical time domain reflectometry ( $\phi - OTDR$ ) with dual-pulse heterodyne phase detection, we demonstrated a distributed photothermal gas sensor with a 200-m-long HC-PBFs by use of backscattering signals from the surface scattering of HC-PBFs, which results from random fluctuations of the hollow-core dimensions along fibre. Without signal averaging, we achieved LOD down to 5 ppm ( $5.8 \times 10^{-6} \text{ cm}^{-1}$ ) for  $C_2H_2$  detection with 62.5 mW peak pump power. The distributed sensing length as long as a few kilometers of HC-PBFs could be expected with high sensitivity. This work is the first demonstration of distributed gas sensor using PTI in HC-PBFs and is of full potential for developing an all-fibre and non-destructive distributed gas sensor using a single long-length HC-PBFs with high sensitivity.

# List of publications

## *Journal papers*

1. **Y.C. Lin**, W. Jin, F. Yang, J. Ma, C. Wang, H.L. Ho and Y. Liu, 'Pulsed photothermal interferometry for spectroscopic gas detection with hollow-core optical fibre', *Scientific Reports*, **6**, pp. 39410, 2016.
2. **Y.C. Lin**, W. Jin, F. Yang, Y.Z. Tan and H.L. Ho, 'Performance optimization of hollow-core fibre photothermal gas sensors', *Optics Letters*, **42**(22), 2017.
3. **Y.C. Lin**, F. Liu, X.G. He, W. Jin, M. Zhang, F. Yang, H.L. Ho, Y.Z. Tan and L.J. Gu, 'Distributed gas sensing with optical fibre photothermal interferometry', *Optics Express*, **25**(25), 2017.
4. Y. Qi, F. Yang, **Y.C. Lin**, W. Jin and H.L. Ho, 'Nano-waveguide enhanced photothermal interferometry spectroscopy', *Journal of Lightwave Technology*, **35**(24), pp. 5267 - 5275, 2017
5. Y.Z. Tan, W. Jin, F. Yang, Y. Qi, C.Z. Zhang, **Y.C. Lin** and H.L. Ho, 'Hollow-core fiber-based high finesse resonating cavity for high sensitivity gas detection', *Journal of Lightwave Technology*, **35**(14), pp. 2887-2893, 2017.
6. F. Yang, W. Jin, **Y.C. Lin**, C. Wang, H.L. Ho and Y.Z. Tan, 'Hollow-core microstructured optical fiber gas sensors', *Journal of Lightwave Technology*, **35**(16), pp. 0733-8724, 2016.

7. F. Yang, Y.Z. Tan, W. Jin, **Y.C. Lin**, Y. Qi and H.L. Ho, 'Hollow-core fiber Fabry–Perot photothermal gas sensor', *Optics Letters*, **41**(13), pp. 3025-3028, 2016.

*Conference papers*

1. **Y.C. Lin**, W. Jin, F. Yang, and H.L. Ho, 'Pulsed photothermal interferometry for high sensitivity gas detection with hollow-core photonic bandgap fibre', In *Optical Fiber Sensors Conference (OFS), 2017 25th*, pp. 1-4. IEEE, 2017.
2. **Y.C. Lin**, W. Jin, F. Yang, and C. Wang, 'Highly sensitive and stable all-fiber photothermal spectroscopic gas sensor', In *CLEO: Science and Innovations*, pp. STu4H-3. Optical Society of America, 2016.
3. **Y.C. Lin**, W. Jin, F. Yang, and Y. Liu, 'Dynamics of photothermal phase modulation in a gas-filled hollow-core photonic bandgap fiber', In *Asia-Pacific Optical Sensors Conference*, pp. W3A-2. Optical Society of America, 2016.
4. **Y.C. Lin**, W. Jin, J. Ma, C. Wang, F. Yang, and H.L. Ho, 'Stabl operation of all-optical fibre photoacoustic sensors', *Workshop on Specialty Optical Fibers and Their Applications*, pp. WT4A.34, Optical Society of America, 2015.

## **Acknowledgements**

I would like to express my most profound appreciation to my chief supervisor, Prof. Wei Jin, for his generous support and continuous guidance throughout my PhD study. My commence stage of the 4 years was arduous and confused. Fortunately, thanks to the kind help from Prof. Jin with his patience and wisdom of enlightenment to pull me through. His wealth of research experience, broad research perspective and knowledge help and inspire me a lot. I enjoyed the time meeting with him, presenting my research, discussing and solving the problems with him. His prudent attitude towards the science and personality of integrity will be remarkably beneficial for my future career.

It is incredibly gorgeous to work with my outstanding lab-mates. I am grateful to Dr. Fan Yang, Dr. Jun Ma, Dr. Chao Wang, Dr. Yingchun Cao and Dr. Wa Jin for helping me start my research when I initially joint the lab. I also enjoyed our gatherings and sweating on the sports field that make my life much more unforgettable and enjoyable. Especially, I owe many thanks to Dr. Hoi Lut Ho for his persistent contributions to our lab, meticulously managing the experimental facility in order and always cordially willingness to help me. Thanks to his effort, the experience on conducting experiments in our lab is thoroughly enjoyed and concentrated. I also want to express my thanks to Dr. Yanzhen Tan and Dr. Congzhe Zhang for their helpful discussions and aids in my experiments.

I have to address my deep gratefulness to my beloved family. Without your understanding and support in times of trouble and frustration, I would not be able

to finish my PhD degree. In particular, I want to show many thanks to my elder brother, Mr. Hechuan Lin. It is a great honor and fortune to have your support and encouragement.

I also want to thanks for the worthy help from Prof. Min Zhang (Peking University), Prof. Yang Liu (Hong Kong Polytechnic University) and Prof. Tao Zhu (Chongqing University). I would like to acknowledge the supports from all my dear friends, especially thanks to Dr. Kun Chen (University of California, Berkeley) and Dr. Xinbai Li (Peking University) for their precious friendship. I must also thanks to Dr. Fei Liu, Dr. Xiangge He and Dr. Lijuan Gu from Peking University and Dr. Qian He from Chongqing University for their help during my carrying out the distributed sensing experiments.

# Table of contents

<b>List of figures</b>	<b>XIII</b>
<b>List of tables</b>	<b>XXV</b>
<b>Nomenclature</b>	<b>XXVII</b>
<b>1 Introduction</b>	<b>1</b>
1.1 Literature review . . . . .	1
1.1.1 Gas sensors . . . . .	1
1.1.2 Fibre-optic gas sensors . . . . .	3
1.1.3 Hollow-core photonic bandgap fibre sensors . . . . .	7
1.2 Research motivations . . . . .	12
1.2.1 Principles of PT phase modulation and optimized performance of PTI with HC-PBFs . . . . .	12
1.2.2 Distributed PT gas spectroscopy with HC-PBFs . . . . .	13
1.3 Thesis outline . . . . .	15
<b>2 Background knowledge</b>	<b>17</b>
2.1 Background of ro-vibration spectra . . . . .	17
2.1.1 Light-matter interaction . . . . .	17
2.1.2 Diatomic molecular spectra . . . . .	19
2.1.3 Parameters of gas spectroscopy . . . . .	27

---

2.1.4	Ro-vibration spectra of acetylene . . . . .	32
2.2	Wavelength modulation spectroscopy . . . . .	34
2.2.1	Principles of WMS . . . . .	37
2.2.2	Optimized parameters for WMS . . . . .	40
2.3	Summary . . . . .	43
<b>3</b>	<b>Photothermal gas spectroscopy</b>	<b>45</b>
3.1	Photothermal spectroscopy . . . . .	45
3.1.1	Photothermal effect . . . . .	45
3.1.2	Detection of photothermal effect . . . . .	46
3.2	Photothermal interferometry . . . . .	49
3.2.1	Fibre-optic interferometry . . . . .	51
3.2.2	PTI with open-path gas cells . . . . .	68
3.3	PTI with HC-PBFs . . . . .	77
3.3.1	HC-PBFs as ideal gas cell for photothermal spectroscopy . .	77
3.3.2	Advantages of PTI in HC-PBFs . . . . .	80
3.4	Summary . . . . .	85
<b>4</b>	<b>Mechanism and dynamics of PT phase modulation in HC-PBFs</b>	<b>87</b>
4.1	Mathematical modeling . . . . .	88
4.1.1	Theoretical model . . . . .	88
4.1.2	Computed results . . . . .	95
4.2	Experiments with pulsed pump beam . . . . .	100
4.2.1	Experimental set-up . . . . .	100
4.2.2	Comparison between the measured results and computed results . . . . .	104
4.2.3	Trace gas detection with pulsed PT spectroscopy . . . . .	105
4.3	Discussion about the results . . . . .	108
4.4	Maximum allowable laser power . . . . .	109

---

4.5	Summary . . . . .	111
<b>5</b>	<b>Performance optimization of PT gas spectroscopy</b>	<b>113</b>
5.1	Frequency dependence of PT phase modulation in HC-PBFs . . . . .	114
5.2	Optimized PT Sagnac interferometry with HC-PBFs . . . . .	118
5.2.1	Experimental set-up . . . . .	118
5.2.2	Experiments results . . . . .	121
5.3	Discussion on noise properties of PT Sagnac interferometer . . . . .	124
5.3.1	Theoretical analysis . . . . .	124
5.3.2	Comparison between experimental and theoretical results . . . . .	130
5.4	Models of PT phase modulation in open-path gas cells . . . . .	131
5.5	Summary . . . . .	135
<b>6</b>	<b>Distributed gas sensing with optical fibre photothermal interferometry</b>	<b>137</b>
6.1	Basic principles . . . . .	137
6.1.1	Distributed PT phase modulation along a HC-PBFs . . . . .	137
6.1.2	Detection of PT phase modulation . . . . .	140
6.2	Experimental set-up . . . . .	142
6.3	Signal processing . . . . .	144
6.4	Quasi-distributed sensing experiment . . . . .	149
6.5	Distributed sensing experiment . . . . .	153
6.6	Discussion . . . . .	158
6.7	Summary . . . . .	161
<b>7</b>	<b>Conclusions and future work</b>	<b>163</b>
7.1	Conclusions . . . . .	163
7.2	Future work . . . . .	165
	<b>References</b>	<b>167</b>



# List of figures

1.1	Schematic drawing fibre-optic sensors based on direct gas absorption. PD: photo-detector; SMF: single-mode fibre; $I_0$ : input laser intensity; $I_t$ : transmitted laser intensity. . . . .	3
1.2	Schematic drawing air-silica cross-section of a index-guiding PCF and computed fundamental mode field by use of finite-element method (FEM). Magnitude of electric field has been normalized to the central maximum. To guarantee that only fundamental mode is guided in triangular PCFs (so-called 'endless single mode fibre', i.e. single mode guiding at any wavelength [38]), the air filling fraction should meet the criteria $d/\lambda < 0.4$ . . . . .	6
1.3	Schematic drawing of HC-PBF. The inset shows the optical microscopy image of cross-section of commercial available HC-PBF, i.e. HC-1550-02, [45, 46] . . . . .	8
2.1	Illustration of light-matter interaction process. $h = 6.63 \times 10^{-34} J \cdot s$ is the Planck's constant [83]; $\nu_0$ : input laser frequency; $\nu_s$ : Stokes frequency shift. . . . .	18
2.2	Illustration of different energy levels. $E''$ and $E'$ indicate the lower and higher electronic energy levels, respectively [83]. . . . .	19
2.3	Diatomic molecule with rigid rotor approximation [83]. . . . .	20

2.4	Simple harmonic oscillator model of a linear diatomic molecule. $r_{min}$ indicates the minimum compression distance between the two charges [83]. . . . .	22
2.5	Potential energy for SHO and AHO model with vibration states; $U$ : potential energy for vibrational states [83]. . . . .	24
2.6	Illustration of ro-vibration transitions and its corresponding spectra [83]. . . . .	25
2.7	Illustration of fundamental vibration modes of acetylene [85]. . . . .	26
2.8	Illustration of lineshape function. $\gamma_i$ is the half-width-half-maximum (HWHM) of a lineshape, $i$ indicates the different lineshape function in the following discussion. . . . .	28
2.9	Absorption lines of $\nu_1 + \nu_3$ band of $C_2H_2$ in the wavelength range of 1510-1545 nm . . . . .	33
2.10	(a) absorption spectrum with line profile in the vicinity of P(9) absorption line; (b) the Lorentzian line-fit for P(9) absorption line. The lower part is the fit residuals. . . . .	34
2.11	Illustration of WMS methods. PD: photo-detector; DAQ: data-acquisition card; PC: personal computer. . . . .	37
2.12	Schematic drawing for illustrating the principles of WMS. . . . .	38
2.13	The first four orders of harmonics with different modulation depth. . . . .	40
2.14	The definition of maximum and amplitude of first and second harmonics. . . . .	41
2.15	The optimized $m$ for the 1st- and 2n-order harmonics. . . . .	42
3.1	Illustration of process involved in the photothermal spectroscopy. The upper corner shows the non-radiative relaxation process. The modulated continuous wave or a pulsed wave is usually adapted as the pump source. CW: continuous-wave. . . . .	46

---

3.2	Illustration of photothermal lens generation. The left side represents its equivalent diverging lens. PD: photo-detector. . . . .	47
3.3	Illustration of photothermal deflection spectroscopy: (a) transverse geometry; (b) collinear geometry. . . . .	49
3.4	Illustration of PT interferometry using a Mach-Zehnder interferometer. The thicknesses of the line could somehow indicate the relative strength of electric field. PZT: piezo-electric transducer. . . . .	50
3.5	Illustration of Mach-Zehnder interferometer. . . . .	52
3.6	The first kind Bessel function against the modulation depth $m$ . The number on the line indicates the value of $m$ where the first maximum of Bessel function could be achieved. . . . .	55
3.7	The illustration of interferometric output amplitude as a function of phase signal. . . . .	57
3.8	Illustration of active homodyne stabilization of MZI. The number on the coupler indicates the power coupling coefficients. FB: feedback. . . . .	58
3.9	Illustration of $3 \times 3$ Sagnac interferometer. . . . .	62
3.10	Illustration about the influence of size of gas cell as function of $r/w$ . The simulation assumes that the radius of pump beam is fixed at $w = 0.5mm$ and different ratio of $b/w$ . The vertical value indicates the relative temperature rise. The pump beam is a CW unmodulated laser. . . . .	76
3.11	Illustration about the pulse durations dependence of PT effect with short pulses. The beam radius is $0.5mm$ with $t_c \sim 0.03s$ . . . . .	77
3.12	Illustration about the CW modulation frequency dependence of PT effect. The beam radius is $0.5mm$ with $1/t_c \sim 320Hz$ . . . . .	78

- 3.13 Mode field profile in the form of power distribution of (a) fundamental mode  $LP_{01}$  and (b) lowest high order modes  $LP_{11}$  mode with both axial direction along the fibre geometry in unit of  $\mu m$ ; (c) the normalized power distribution of both mode fields (red line is of  $LP_{01}$  and blue line is of  $LP_{11}$ ), indicated by the dashed lines in (a)(b). 83
- 4.1 Geometric of modeling the PT phase modulation in (a) HC-PBFs and (b) free-space optics. The red-filled part in the core center is the gas-filled place. The thick boundary indicates the silica glass. (c) image of cross-section of commercial available hollow-core fibre HC-1550-02 from NKT. . . . . 89
- 4.2 Detail of the computed models. (a) The gas sample is enclosed within the central air core by a  $\sim 70nm$  thick fused silica solid boundary. The intensity profiles of both pump and probe beam are assumed identical as Gaussian beams and have the same beam radius. (b) the temporal form of heat source as a function of time and thermal relaxation time. In this illustration, the pulse duration is  $t_0 = 2\mu s$  and the thermal relaxation time is  $\tau = 74ns$  for  $C_2H_2$  under s.t.p condition. . . . . 91
- 4.3 The results of numerical modeling. The HC-PBFs has a core radius of  $5.5\mu m$  and a beam radius of  $4.03\mu m$ . The pulse duration is  $2\mu s$  for (a) and (b). It has been assumed that the peak pump power is 25 mW and length of HC-PBFs is 0.62 m filled with 100 ppm  $C_2H_2$  in  $N_2$ . (a) temporal changes of  $\Delta T(r,t)$ ; (b) two-dimension of temperature changes at the time of  $1.5\mu s$  after launching the pump beam. (c) The PT phase modulation against time with different pulse durations; (d) the peak magnitude of PT phase modulation with different pulse duration. . . . . 96

- 
- 4.4 Simulation results with curve fitting demonstrate both the (a) leading and (b) trailing part, showing the dynamics of PT phase modulation. (c) the influence of  $\tau$  on the characteristic time constant; (d) The peak magnitude of PT phase modulation with a fixed pulse energy of 5 nJ for different pump pulse durations. All other parameters of simulation are identical to that of Fig. 4.3. . . . . . 97
- 4.5 Pump-probe configuration of experimental set-up with a modified Sagnac interferometer. The length of HC-PBFs is 0.62 m. The pump source is an external-cavity diode laser (ECDL) with nominal central wavelength of 1530.371 nm. Filter 3: filters out the undesired ASE noise output from EDFA; Filter 1, 2: filters out the residual pump beam and allow the pass of probe beam; BS: broadband source (probe, at 1553.33 nm); PC: polarization controller; BD: balanced detector; AOM: acoustic-optic modulator for intensity modulation of pump beam. . . . . 102
- 4.6 Simulated output Sagnac interferometer with the pulse durations of  $2\ \mu\text{s}$  and  $15\ \mu\text{s}$ . The phase modulation is simulated as the PT-induced pulsed phase modulation. . . . . 103
- 4.7 Experimental measuring the interferometric outputs with pulse duration of  $2\ \mu\text{s}$  and  $40\ \mu\text{s}$ . . . . . 103
- 4.8 Waveform output from interferometer.(a) output for the same peak pump power but different pulse durations;(b) the peak magnitude of measured PT phase modulation for different pump pulse duration. The peak pump power is 20.2 mW. The gas sample is 0.62-m-long HC-PBFs filled with 7500 ppm  $C_2H_2$  gas. . . . . 103

- 
- 4.9 Comparison between the numerical modeling results and the experimental results for the PT phase modulation with pump pulse duration of (a) 325 ns and (b)  $2\mu s$ . Curve fitting results of (c) leading and (d) trailing part of experimentally measured PT phase modulation signal with pulse duration of  $2\mu s$ . . . . . 106
- 4.10 Sensitive trace gas detection with pulsed pump beam PT spectroscopic technique. (a) Boxcar averager output with average times of 10 and 10k; (b) the linear performance of SNR against  $\sqrt{N}$ ; (c) Output from BD against the peak pump power with the same pulse duration of  $3\mu s$ ; (d) the spectral line measurement, compared with the Lorentzian curve fit. . . . . 107
- 5.1 Experimental set-up for the measuring the frequency-dependence of PT phase modulation in a gas-filled HC-PBFs. HPF, LPF: high- and low-pass filter; PD1 and PD2:photo-detector. . . . . 115
- 5.2 (a) Frequency dependent of PT phase modulation in HC-PBFs. The light-green solid line is the simulation results while the red dot is the measured results. The inset (i) and (ii) are the simulated results in time-domain for modulation frequency of 600 kHz and 3.7 MHz, respectively. (b) Simulation results of optimum frequencies for some HC-PBFs. HC-PBFs-MIR means an HC-PBFs with a large core size for mid-infrared guidance, while the others are HC-PBFs available in NKT Photonics. . . . . 117

- 5.3 The experimental set-up of PT gas spectroscopy. Filter 1, 2: band-pass filters centered at the probe wavelength to filter out the residual pump; Filter 3: bandpass filter centered at the pump wavelength to filter out the undesired ASE noise; Filter 4: bandpass filter to select a narrow band light from the SLD, which is subsequently amplified and used as the probe beam. BD:balanced photo-detector; DAQ: data-acquisition card;PC:polarization controller; DP: fibre-optic depolarizer. Inset: cross-section of HC-1550-02. . . . . 119
- 5.4 (a) Schematic drawing of gas cell;(b) ESA output of PZT phase modulator iwth amplitude of 5 mrad. . . . . 120
- 5.5 (a) Second harmonic lock-in amplifier output waveform when pump wavelength is scanned across the P(9) line 1530.37 nm with different pump power. The  $C_2H_2$  gas concentration is  $\sim 100$  ppm, pressured into  $\sim 1.1$ -m-long HC-PBFs (HC-1550-02, NKT Photonics).(b) Second harmonic output signal amplitudes and  $1\sigma$  noises as function of peak pump power levels. The noises were measured with the wavelength of pump beam fixed but tuned away from the absorption line. The  $1\sigma$  value was calculated from a recording over  $\sim 2$  min. . . 122
- 5.6 (a) Allan deviation measurement results. The red solid line is the curve fit result with  $y = A/\sqrt{t} + B$ . (b) Results of stability test over several hours. The gas concentration is 1000 ppm. The wavelength of the pump beam is periodically scanned across the absorption line, and the maximum value of R-output of lock-in amplifier is recorded and plotted against the time. The measurement was conducted under the normal laboratory condition and environment. . . . . 124
- 5.7 Simulated results of thermo-dynamic phase noise in optical fibres with Sagnac loop length of 2 km. . . . . 127

5.8	Simulated results of Rayleigh backscattering phase noise in optical fibres with Sagnac loop length of 2 km and spectral bandwidth of 1.2 nm of probe beam. . . . .	130
5.9	Noise properties of Sagnac interferometer with simulated results and experimental measured results. . . . .	131
5.10	Parameters for the calculation of frequency-dependence of PT phase modulation in the free-space optics with beam radius of $w = 0.5mm$ . . . . .	133
6.1	Schematic drawing of a HC-PBFs with a pump and a probe beam propagating within it. Inset: scanning electron microscope (SEM) cross-sectional image of a commercial HC-PBFs (NKT HC-1550-02) [168]. . . . .	138
6.2	(a) PT phase modulation due to pump absorption over a section $[z, z + dz]$ of HC-PBFs. The backscattered probe beams shown as dashed blue lines are used to detect the distributed phase modulation, forming the basis for distributed gas sensing. (b) PT phase modulation over a length ( $L_t$ ) of sensing HC-PBFs sandwiched between the two SMFs. The back-reflected probe beams at the HC-PBFs/SMF joints are used to detect the phase modulation, which forms the basis for quasi-distributed gas sensing. The line thickness of backscattered/reflected signal indicates the relative signal strength. . . . .	139
6.3	Schematic of the experimental set-up. The sensing could be either distributed (Case 1) or quasi-distributed sensing manner (Case 2). The green dashed arrows indicate the pump directions. AOM: acoustic-optic modulator; SMF: single-mode fibre; EDFA: erbium-doped amplifier; PD: photo-detector; PC: polarization controller; DFB: distributed feedback laser. WDM: wavelength-division multiplexer. OC: optical fibre coupler. . . . .	143

- 
- 6.4 Illustration of pulse sequence at different locations in the system and sampling at the system output, for quasi-distributed sensing system. (a) trigger pulses for AOM; (b) dual pulses launched in to the sensing block with a temporal offset; (c) pulse waveform reflected from the sensing block; (d) data sampling at the PD output. The left-bottom corner indicates the coordinate directions. . . . . 146
- 6.5 Illustration of digital lock-in detection and subsequent processing to obtain the PT phase modulation signals [185]. . . . . 146
- 6.6 Illustration of signal processing in distributed sensing system. . . . 148
- 6.7 Schematic of procedure to obtain time-dependent phase modulation signals in distributed sensing system. . . . . 148
- 6.8 A typical measured output from the PD for a quasi-distributed sensing system with two HC-PBFs sensors. . . . . 150
- 6.9 The recovered frequency spectrums of the recovered PT phase modulation for (a) HC-PBFs 1 with 7.8 mW pump power and  $\sim 2700$  ppm  $C_2H_2$  in  $N_2$ , (b) HC-PBFs 2 with 55 mW pump power and  $\sim 44$  ppm  $C_2H_2$  in  $N_2$ . The dB re rad is define as  $20\log_{10}(x\text{rad}/1\text{rad})$ . The measured magnitude of PT phase modulation is 0.05 rad (-26 dB re rad) for HC-PBFs 1 and 0.13 rad (-17.7 dB re rad) for HC-PBFs 2; (c) The spectrum of the recovered phase modulation for HC-PBFs 2 when the pump was tuned to the center of the absorption line, away from the absorption line, and turned off. (d) The time domain waveforms of the recovered PT phase modulation for the two sensors. 151

6.10 Measured interfering backscattering traces with pump power was turned off. There are three sections labelled as P1, P2 and P3, corresponding to the spatial locations respectively at 131 m, 251 m and 335 m with the lengths of 131 m SMF, 120 m HC-PBFs and 84 m HC-PBFs. The upper diagram is the illustration of fibre alignment of sensing block. At P1, the mechanical splicing between an angle-cleaved SMF and HC-PBFs is used. A  $\sim 116$  m long HC-PBFs is then mechanical spliced to a  $\sim 3.4$  m short HC-PBFs (P2), which consists two  $\sim 1.7$  m gas-filled HC-PBFs. Another  $\sim 80$  m long HC-PBFs was mechanically spliced at P2, whose end was connected by a  $\sim 4.2$  m gas-filled HC-PBFs at P3. . . . . 153

6.11 The phase distribution along the sensing fibre. The upper diagram shows the fibre alignment and segments of sensing fibre. The position P1, P2 and P3 corresponds to the spatial location of 131 m, 251 m and 335 m, respectively. The displayed spatial locations range from 60 m to 338 m. . . . . 155

6.12 The phase distributed along the sensing fibre with: (a) pump wavelength tuned away from the absorption line; (b) pump beam turned off. The figures share the same color legend as that in Fig.6.11. . . . 155

6.13 The three dimension demonstration of gas presence at the spatial location P2. . . . . 157

- 6.14 The PT phase modulation signals in time and frequency domain (a) (c) for spatial location at P2 and (b) (d) for spatial location at P3. The signals have been filtered by a digital band-pass filter with central frequency of 500 Hz and bandwidth of 200 Hz. In (c), the signal level is 0.35 rad and the noise floor is 0.012 rad and 0.013 rad when the pump is tuned away from gas absorption and switched off, respectively. In (d), the signal level is 0.19 rad and noise floors are 0.02 rad and 0.01 rad, respectively. The all plots share the same legend shown in (a) as on: aligned to the center of absorption line, away: away from absorption and off: switched off. . . . . 158



# List of tables

- 1.1 Detection limits of absorption-based optical fibre gas sensors . . . . . 10
- 4.1 Maximum phase changes for different sizes of cores . . . . . 100
- 5.1 Parameters for calculation of thermo-dynamic phase noise . . . . . 126
- 5.2 Parameters for calculation of Rayleigh backscattering phase noise . 129



# Nomenclature

$\kappa$  lattice constant

$\alpha, \alpha(\nu)$  gas absorption coefficient related to concentration  $C$

$\alpha_0, \alpha_0(\nu)$  gas spectral absorption coefficient for a relative 100% concentration at specific wavenumber  $\nu$

$\alpha_c$  power loss coefficients

$\alpha_f$  power attenuation constant of optical fibre

$\alpha_T$  linear thermal expansion coefficient

$\bar{\Psi}$  electrical field transverse profile of light beam

$\beta$  propagation constant of light wave in optical waveguide

$\Delta\phi$  phase shift or difference between to electric waves

$\Delta E$  energy difference between the two energy states of molecule

$\Delta L$  absolute length changes of optical fibre

$\Delta S_{\Delta P}$  spectral density function

$\Delta\nu$  the wavenumber difference between two energy states during transitions

$\Delta$  normalized laser frequency deviation from the gas absorption line center

---

$\Delta\beta$	modulation depth expressed in the form of propagation constant
$\eta$	photo-detector responsivity (i.e., quantum efficiency for electron generated by a single photon)
$\Gamma$	degree of coherence between the two interfering waves
$\gamma$	half-width half-maximum of lineshape function
$\hbar$	reduced Planck's constant
$\mathfrak{S}$	finesses of an optical cavity
$\kappa$	thermal conductivity
$\Lambda$	mean free path of gas molecules
$\lambda$	wavelength of light
$\mu$	dipole moment
$\mu_m$	reduced mass of diatomic molecule
$\mu_{\text{Euler}}$	Euler's constant
$\Omega$	angular frequency of light
$\omega$	modulation frequency of optical phase
$\omega_m, \omega_p$	modulation frequency of signal; $p$ indicates the modulation frequency of pump beam
$\Omega_{rot,vib}$	rotational/vibrational angular velocity of diatomic molecule
$\phi$	optical phase
$\Phi_n$	detection phase in lock-in amplifier

- $\phi_{\Delta} = 2\phi_{\Delta'}$  phase asymmetric factor between the two output ports of directional coupler
- $\phi_{\epsilon}$  phase shift of desired signal and picked-up noise
- $\Psi$  phase shift between frequency modulation and intensity modulation
- $\rho$  density
- $\sigma(\nu)$  absorption cross section per molecule
- $\tau$  thermal relaxation time
- $\tau_c$  coherence time of light source
- $\tau_d$  time delay between the two interfering waves
- $\tau_{\text{int}}$  integration time of feedback servo-loop
- $\tau_{\text{trans}}$  lifetime of a transition
- $\Theta$  wave function
- $\Upsilon$  moment of inertia
- $\epsilon$  strain applied on optical fibre
- $\zeta$  polarization-related factor for optical interference
- $\xi$  elasto-optical coefficient
- $\Xi_{\text{pump}}, \Xi_{\text{probe}}$  area-normalized light intensity function
- $\zeta$  a modified factor in the anharmonic oscillator model
- $A$  gas absorbance
- $A_{21,12}, B_{12,21}$  Einstein's A and B coefficient

---

$B$	detection bandwidth
$B_J$	rotational constant
$C$	gas concentration
$c$	light speed in vacuum
$C_p$	specific heat at constant pressure
$d$	diameter
$D_T$	thermal diffusivity
$D_v$	centrifugal distortion constant
$D_{eq}$	bond-dissociation energy
$dn/dT, \partial n/\partial T$	thermo-optic coefficient
$E$	electrical field
$e$	elementary charge
$E', E''$	higher/lower energy state
$E_0$	pulse energy
$e_0, e(t)$	error signals
$F(J)$	rotation energy for quantum number $J$
$f_\infty, f(t)$	focal length at infinity or as a function of time
$F_v, B_v$	vibration-states related rotational energy/constant
$g$	acceleration of gravity
$G(\nu)$	vibrational energy for a specific wavenumber

---

$g(\nu)$	normalized lineshape function
$g_0$	gain factor of feedback loop
$g_{1,2}$	statistical weights (or degeneracy factor) of energy state 1, 2
$h$	Planck's constant
$I$	light intensity
$i_\nu$	with subscripts, output current amplitude
$J$	quantum number for total angular momentum
$J_0, J_1, J_n$	zero/first/nth order of Bessel function
$k$	spatial angular frequency (wavenumber) of the wave
$k_B$	Boltzmann constant
$K_p, K_i, K_d$	proportional, integral and derivative gain factor for PID control
$k_s$	spring constant
$Kn$	Knudsen number
$L$	physical length
$M$	molecular weight
$m$	modulation index (depth) or magnitude of phase shift
$m_1, m_2$	mass of atom/molecule
$N$	number of gas molecules
$n_0$	refractive index of material
$N_L$	Loschmidt number

$N_{\text{num}}$	total number of degrees of freedom for ro-vibration transition
$N_{\text{tot}}$	total molecular number density
$P$	optical power
$p$	pressure
$p_{12}$	strain-optic coefficient
$Q(r, t)$	pump beam in both cross-sectional profile as a function of time
$q_H$	heat source due to photothermal effect
$R$	responsivity of photo-detector
$r_1, r_2$	distance between the two atoms/molecules
$r_e$	equilibrium separation distance between two atoms in diatomic molecule
$R_T$	load resistance
$R_v$	volts to radians constant transform factor
$S$	Rayleigh backscattering coefficient
$S(t)$	time-varying function of pulse waveform for heat source
$S_0$	line strength or spectral line intensity
$T$	temperature
$t$	time index
$T(v, J)$	total energy of ro-vibration transition
$t_0$	pulse width
$t_c$	characteristic thermal conduction time constant

$t_d$  time delay between the two interfering waves

$T_{\text{abs}}$  ambient temperature

$t_{c1}, t_{c2}$  time constant for PT phase modulation in HC-PBF

$U$  potential field

$V$  visibility of interferometric output signal

$\nu, \nu_0, \nu_s$  optical frequency of light wave

$V_0$  with subscripts, voltage signals

$\nu_{\text{convect}}$  thermal convection velocity

$w$  beam radius

$x, y, z, r$  coordinates indices

$x_\nu$  normalized laser frequency

$x_{\text{vib}}$  a coefficient related to second order oscillating in anharmonic oscillator model



# Chapter 1

## Introduction

### 1.1 Literature review

#### 1.1.1 Gas sensors

Detection of trace gas with high sensitivity, unique selectivity and fast analysis is of significant importance in diverse aspects, including environmental assessment and monitoring, medical diagnosis, industrial process supervision, as well as the national defense security application [1–7]. In the medical diagnosis, the monitoring of characteristic exhale gas components resulting from some featured disease can benefit the early diagnosis and help the treatment of patients [8, 9]. In industrial applications, such as on oil wells or pipe lines, the detection of gas leakage in the first timing can avoid the occurrence of disaster and reduce the loss [10].

There are a variety of techniques applied to trace gas detection. Mass spectrometry has proved to be a highly sensitive methods to detect the gas molecules. In mass spectrometry, the molecules are firstly ionized and charged by external applied electric field when pass through the designed path. Different molecules with different mass reach the electron multipliers at different time and thus the molecules could be selectively detected. However, the mass spectrometry have been limited

by the possible overlap of certain molecules. For detection of large molecules, the mass spectrometry could be a better choice over laser spectroscopy due to the broad absorption band of molecules.

Another popular method is gas chromatography where the gas molecules pass through a pre-defined column (a type of small tube) and reach the detectors at different time, depending on the molecular properties and their interaction with the specific column filling. Due to its principle, only sequential measurement could be performed and also the detection time could be as long as several minutes. Chemiluminescence is a process of photon emissions (luminescence) when the excited gas molecules relax to the ground state, although accompanying with heat generation. The chemiluminescence depends on the chemical reaction between the gas of interest and the surface of polymeric dyes. Even though it offers fast detection, the chemiluminescence is only limited to a few gas molecules detection (ozone and nitrogen dioxide) and the calibration is required (thus it is not an absolute quantity measuring). In most cases, the chemical reaction processes are irreversible and the regular replacements of polymeric dyes are required. Fluorescence spectroscopy is one of the most applied gas detection approaches, which detects the emitted fluorescence signal (photons) when the excited gas molecules relax to ground state. The fluorescence spectroscopy offers the similar advantages as laser spectroscopy but limited by the very weak fluorescence generation. It is feasible to apply the fluorescence spectroscopy in infrared spectra since in UV spectra the absorption band are very broad that may deteriorate the selectivity. However, the fluorescence in infrared region is very inefficient due to the existence of competitive non-radiative relaxation. Also, the fluorescence photons could be only collected in some specific and small angles, even though they are emitted in all directions.

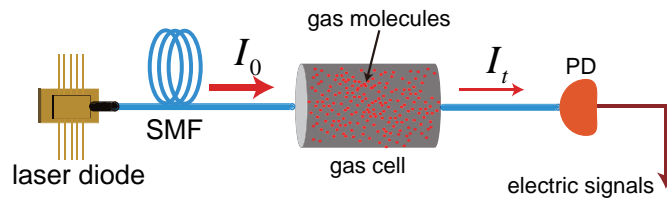


Fig. 1.1 Schematic drawing fibre-optic sensors based on direct gas absorption. PD: photo-detector; SMF: single-mode fibre;  $I_0$ : input laser intensity;  $I_t$ : transmitted laser intensity.

### 1.1.2 Fibre-optic gas sensors

Compared with all the measurements above, laser absorption spectroscopy (LAS) offers overwhelming advantages in trace gas detection by use of high performance laser source. Since its advent in as early as 1960s, lasers, which has the prominent characteristics of capability of emitting highly coherent radiation with highly stable optical power and frequency operation, has been developed to its fullest advantages in trace gas analysis [11, 12]. By probing the 'finger-print' transition between the molecular or atomic energy levels, LAS offers a non-intrusive and capable of remote sensing for quantitatively detection of trace gases while satisfying the stringent requirement of high sensitivity and distinct selectivity [13, 14]. On the other hand, in virtue of the rapid development of laser and optical fibre technology, the fibre-optic sensors evolve from its earliest demonstration around mid-1970s at an unparalleled speed [15–20]. Fibre-optic sensors, by the use of optical fibre as sensing element as well as light transmission cables, have distinctive and overwhelming advantages in the aspects of compactness, flexibility, high reliability, low cost, immunity to electromagnetic interference (EMI) and capability of remote and distributed sensing [20]. There are plentiful of techniques have been proposed to fully explore the fibre-optic gas sensors, including absorption, surface plasmon resonance, fluorescence, spontaneous or stimulated scattering [13, 17, 18]. Even though they demonstrate their own sensing strength and advantages, we mainly focus on the laser-absorption based fibre-optic gas sensors.

In fact, the optical method has been widely used to analyzing the chemical species before the advent of optical fibres [21]. The most of techniques are based on the measurement of light spectral attenuation due to the involvement of 'finger-print' transition between the energy levels of trace gas. Many of the vibration or rotation-vibration transition occur at the traditional transmission window of silica fibre, in a range of  $0.8 - 1.8\mu m$ . The principles of LAS follows Beer-Lambert law as [17]:

$$I_t(\nu) = I_0(\nu) \exp(-\alpha_0(\nu)CL) \quad (1.1)$$

where  $I_0$  is the input light intensity,  $I_t$  is the transmitted light intensity,  $\alpha_0(\nu)(cm^{-1})$  is the spectral absorption coefficient of target gas molecular for a relative 100% gas concentration at a specific wavelength,  $\nu(cm^{-1})$  is the wavenumber of light beam,  $C$  is a dimensionless gas concentration in a volume ratio and  $L(in\ cm)$  is the light-gas interaction length. A typical open-path gas cell laser spectroscopy can be illustrated in Fig. 1.1. Usually it adapts a pair of fibre pigtailed graded-index (GRIN) lenses, with one end to collimate the light out of the single mode fibre (SMF) and the other one to collect the transmitted light into the SMF. The light-gas interaction occurs at the intermediate space between the paired GRIN lenses within the gas cell. The minimum detectable gas concentration of 75 ppm acetylene ( $C_2H_2$ ) has been achieved with effective gas absorption length of  $\sim 25\ mm$  [22]. The etalon effect resulting from the reflections of fibre/lens joints and the surface of GRIN lens have been identified as the main interference noise [23, 24]. By the use of wavelength modulation method, the etalon induced undesired interfered noise can be greatly reduced [23].

Eq. 1.1 indicates that longer absorption length and/or stronger gas absorption strength can result in a better absorption signal. However, the typical working distance of commercial available GRIN lens has been limited to  $< 50\ mm$  which mainly constrained by the divergences of light beam propagating in free space. Even

though by the use of cascaded GRIN lenses could increase the effective absorption length [25, 26], it may add the complexity and cumbersomeness in the construction of sensors. The other effective choice to increase the effective gas absorption length is using multi-pass optical cavity as gas cell, such as Herriott cell or White cells. But the cavity-approaches are usually bulky, expensive and difficult in optical alignment and stabilization, making them unsuitable for in-situ applications [27].

One of the most attractive characteristics for fibre-optic sensors is that optical fibres could not only serve as light transmission cables but also sensing elements, making it extraordinary in constructing an all-fibre gas sensing system [20]. Evanescent-wave spectroscopy, by measuring the spectral attenuation induced by gas absorption of evanescent field of optical fibre, has been widely explored by the use of side-polished fibres [28], tapered micro/nano fibres [29, 30], D-shaped fibres [31] and also index-guide photonic crystal fibres (PCFs) [32, 33]. The efforts mainly focus on increasing the fractional power of guided optical modes located in the evanescent field, which can interact with the surrounding gas molecules. Side-polished fibres and D-shaped fibre have small fractions of electromagnetic (EM) field interactive with the external environment and thus difficult to achieve high sensitivity. For D-shaped fibre with up to 0.2% fractional power in evanescent field, the gas detection sensitivity is usually as better as  $1 \times 10^{-4} \text{ cm}^{-1}$  compared with the same absorption length open-path optical gas sensors [31]. Sub-micron diameter tapered fibre could locate larger than 20% power percentage in evanescent field (in theoretical calculation for standard SMF, there are 26.6%, 48% and 93.5% for fibre diameters of  $1 \mu\text{m}$ ,  $0.8 \mu\text{m}$  and  $0.5 \mu\text{m}$ , respectively) and even though smaller diameter could achieve much larger evanescent-wave power, they suffer from difficult fabrications [34, 35].

Index-guiding PCFs, schematic drawing of cross-section shown in Fig. 1.2, are waveguides with a pattern of air holes distributing periodically over the cross-section and running along the entire length of fibre. The index-guiding PCFs provide the

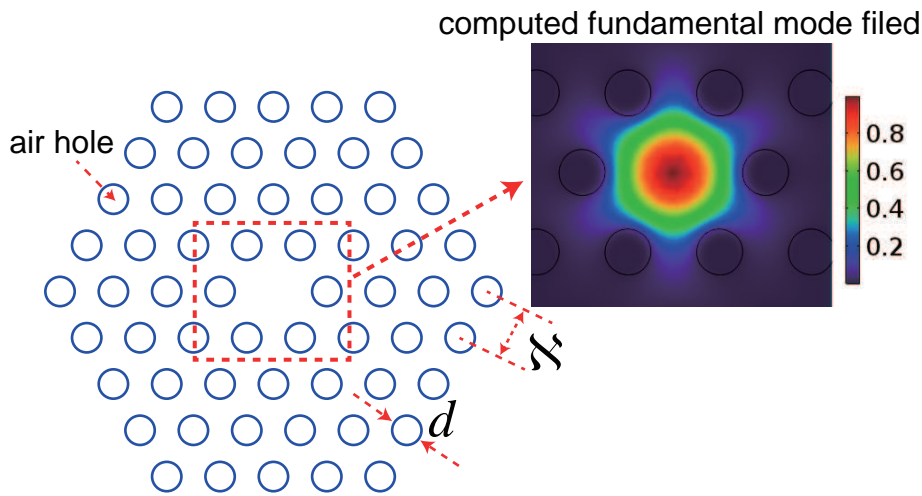


Fig. 1.2 Schematic drawing air-silica cross-section of an index-guiding PCF and computed fundamental mode field by use of finite-element method (FEM). Magnitude of electric field has been normalized to the central maximum. To guarantee that only fundamental mode is guided in triangular PCFs (so-called 'endless single mode fibre', i.e. single mode guiding at any wavelength [38]), the air filling fraction should meet the criteria  $d/\Lambda < 0.4$ .

possibility of control and guide light by a modified total internal reflection (TIA), which are similar to the guidance mechanism of SMFs. By optimizing the fibre parameters, such as lattice pitches  $\Lambda$  and air-hole diameters  $d$ , a large overlap (few tens of percent fractional power in evanescent field) between the evanescent field and gas sample located in the air holes could be achieved [36]. The other attractive characteristics of PCFs are their potential for achieving fibres with higher nonlinearity, tunable dispersion, high birefringence and/or endless-single mode transmission [37, 38].

The first experimental demonstration of gas sensing with index-guiding PCF has been conducted by Hoo et al [39] with expected sensitivity down to parts-per-million (ppm in volume ratio) for the detection of  $C_2H_2$ . However, one of the most challenging work is the response time of index-guiding PCF gas cell. Both the theoretical and experimental results show that for  $\sim 1$ -m-long PCF with two ends open to the air, it would take about 1 min to entirely fill the PCF by gas self-diffusion

process. Using longer PCF would enable a longer effective gas absorption length, but the response time of PCFs would also increase significantly.

### 1.1.3 Hollow-core photonic bandgap fibre sensors

Due to the possible morphological management of air-holes pattern, the PCFs (may also called as micro-structured fibres or holey fibres) offer a great flexibility in controlling the refractive index (RI) contrast between the core and cladding, and thus managing the optical properties of waveguides, which is inaccessible with conventional silica fibres [38, 40, 41]. However, even though it has been demonstrated a long light-gas interaction length, the index-guiding PCFs can only provide limited overlap between the transmitted light and target gas molecules, which is far from an ideal gas with 100% light-gas overlap over a long distance with low loss.

The idea of using a photonic crystal bandgap by introducing a central air defect came into sight. To form a photonic bandgap (PBG), the photonic structure should have a lattice constant on the order of wavelength with a large index contrast in a proper geometry configuration of constituting materials [42]. With a large core size ( $> 0.47$  lattice constant) of air-holes in cladding, it has been demonstrated the possibility of guiding light in air core [43]. It is until 1999 that the first photonic bandgap guiding fibres, i.e. hollow-core photonic bandgap fibres (HC-PBFs), were produced by Philip Russell when the large air-filling fraction in cladding was achievable [44]. HC-PBFs, as shown in Fig. 1.3, trap light within the central air-core surrounded by a periodic wavelength-scale lattice (formed by air-holes micro-channels, typically a few hundred nm of thickness) running along its length. The light guiding mechanism in HC-PBFs is based on the photonic bandgap, rather than the TIA in index-guiding PCFs [44].

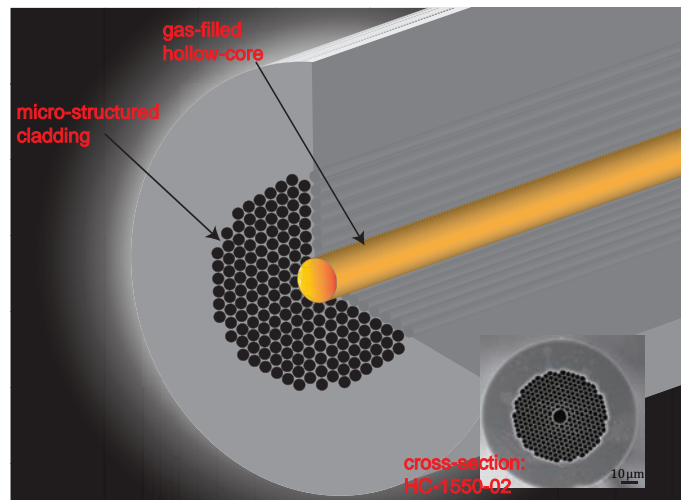


Fig. 1.3 Schematic drawing of HC-PBF. The inset shows the optical microscopy image of cross-section of commercial available HC-PBF, i.e. HC-1550-02, [45, 46]

One of the most appealing features of HC-PBFs is their promising application in ultra-low loss fibres. The ultimate loss of  $\sim 0.15 \text{ dB/km}$  of conventional silica fibres results from the Rayleigh backscattering and material absorption and it has little prospect of improvement. However, the loss of HC-PBF could be reduced down to a level significantly lower than that of conventional fiber since the most of light propagates in the air where the Rayleigh scattering and material absorption are very low. The fibre loss of  $13 \text{ dB/km}$  in  $1550 \text{ nm}$  [47] has been reported respectively. The attenuations resulting from the modal coupling and roughness scattering at the air-glass interface have been confirmed both theoretically [48] and experimentally [49]. By the use of a larger core design which may reduce the overlap between the guided core mode and silica, a minimum loss of  $1.72 \text{ dB/km}$  at  $1565 \text{ nm}$  has been achieved with a 19-cell core design (removing 19-capillaries in the center of fibre cross-section)[49]. The surface roughness may ultimately limits the attenuation of HC-PBF and it is plausible to expect a loss of  $0.2 \text{ dB/km}$  in  $1620 \text{ nm}$  or  $0.13 \text{ dB/km}$  in  $1900 \text{ nm}$  [50]. On the other hand, due to the large contrast ( $\sim 10^{-2}$ ) between the effective RI of core and cladding which enables very tightly confinement of light within the hollow-core, the bending loss of HC-PBF could be very low even with a

bending diameter of 1 cm [51]. The low bending loss of HC-PBF makes it suitable for construction of much compact system.

The possibility of using a HC-PBF as a efficient gas cell was proposed by Cregan in 1999, as early as the advent of HC-PBF [44]. The use of HC-PBF as a gas cell has been reported as early as in 2005[52] and its advantages are quite straightforward. The HC-PBF could offer a excellent light-matter interaction efficiency since it confines both light and gas-material within the central hollow-core in a nearly single-transverse mode over a long distance with only reliable loss [43]. Furthermore, it is fully potential for an all-fibre practical, compact and easy-to-use device and system design. Furthermore, the transmission window (extending over  $\sim 200nm$ ) of a typical HC-PBF could be design to operate in the vicinity of 1550 nm telecom-band, where strong absorption of a variety of gas molecules  $C_2H_2, CO_2, NH_4, CO, H_2S, CH_4$  lies [53–55], which makes the HC-PBF gas cell possible to be integrated into a system with conventional single-mode fibre components.

The investigation of gas diffusion process within the HC-PBF was first demonstrated by Hoo in 2004 [56]. Afterwards, the feasibility of HC-PBF gas sensors with high sensitivity was achieved by Ritari [57]. After a while, plentiful works have been reported to make the full exploration of HC-PBF gas sensors and the Table 1 presents the current works done for fibre-optic gas sensor. Nwaboh et.al demonstrated a HC-PBF gas sensor by the use of 5.27-m-long HC-PBF fibre and a noise equivalent concentration (NEC) of 311 ppm or absorption (NEA) of  $2.6 \times 10^{-3} cm^{-1}$  of  $CO_2$  sensing was achieved at  $2 \mu m$  wavelength region [58]. A. Cubillas et al presented a NEC of  $\sim 10 ppm$  or NEA of  $3.7 \times 10^{-6} cm^{-1}$  of methane ( $CH_4$ ) sensing with 5.1-m-long HC-PBF at  $1.6 \mu m$  absorption line [59–61].

However, the coherent mode mixings or interferences between the supported modes within HC-PBF have been found to be detrimental to the ultimate sensitivity of HC-PBF-based gas sensors when using direct laser absorption spectroscopy [69, 74]. The use of longer HC-PBF still cannot achieve desirable sensitivity (the use of 27-

Table 1.1 Detection limits of absorption-based optical fibre gas sensors

Gas species	Wavelength ( $\mu\text{m}$ )	Gas cell	Technique	NEC <sup>a</sup> (ppm)	NEA <sup>b</sup> ( $\text{cm}^{-1}$ )	References
Methane	1.650	30 cm fibre pigtail cell	DAS <sup>c</sup>	7600	$3.3 \times 10^{-3}$	[62]
Acetylene	1.53	10 cm open-path	DAS	3	$3.5 \times 10^{-6}$	[63]
Methane	1.666	0.5 m D-fibre	Evanescent wave	1000	$3.7 \times 10^{-4}$	[64]
Methane	1.65	7 cm HC-PBF	DAS	647	$2.8 \times 10^{-4}$	[65]
Methane	1.666	13.7 cm HC-PBF	WMS <sup>d</sup>	158	$1.8 \times 10^{-5}$	[66]
Methane	1.645	5.1 m HC-PBF	DAS	10	$1.6 \times 10^{-6}$	[59]
Carbon dioxide	2.005	5.27 m HC-PBF	DAS	311	$2.6 \times 10^{-3}$	[58]
Acetylene	1.530	27 m HC-PBF	DAS	50	$5.8 \times 10^{-5}$	[67]
Ethane	3.35	5.69 m HC-PBF	DAS	0.9	$4.6 \times 10^{-5}$	[68]
Acetylene	1.53	13 m HC-PBF	WMS	1	$1.2 \times 10^{-6}$	[69]
Acetylene	1.53	10 m HC-PBF	PTI (MZI)	0.002	$2.3 \times 10^{-9}$	[70]
Acetylene	1.53	0.3 m HC-PBF	PTI (in-fibre MZI)	1	$1.2 \times 10^{-6}$	[71]
Acetylene	1.53	2 cm HC-PBF	PTI (FPI)	0.44	$5 \times 10^{-7}$	[70]
Acetylene	1.53	0.62 m HC-PBF	PTI (pulsed Sagnac)	3.3	$4 \times 10^{-6}$	Author <sup>e</sup> [72]
Acetylene	1.53	1.1-m HC-PBF	PTI (CW Sagnac)	0.067	$7.7 \times 10^{-8}$	Author [73]

<sup>a</sup>NEC: noise equivalent concentration.

<sup>b</sup>NEA: noise equivalent absorption.

<sup>c</sup>DAS: direct absorption spectroscopy.

<sup>d</sup>WMS: wavelength modulation spectroscopy.

<sup>e</sup>Author: work done by the author and will be presented in this thesis.

m-long HC-PBF could only achieve a NEC of 50 ppm or NEA of  $5.9 \times 10^{-5} \text{ cm}^{-1}$  of acetylene  $\text{C}_2\text{H}_2$  at 1530.37 nm in [67]) and longer fibre would dramatically compromise the response time of HC-PBF gas cell [53]. By modifying the splicing between HC-PBF and SMF, F. Yang contributed a lot of works on the analyzing and reducing mode interference and achieved a sensitivity of 1 ppm or  $1.2 \times 10^{-6} \text{ cm}^{-1}$  of  $\text{C}_2\text{H}_2$  with 13-m-long HC-PBF. The mode interference (MI) noises cannot be completely eliminated since the current commercial available HC-PBFs support a number of modes and the interferences between the modes could result in the intensity fluctuation of transmitted light beam [69]. Even though the efforts have been made to search for a single-mode guided HC-PBF [75, 76], the truly single-mode HC-PBF is still not available.

The photothermal (PT) gas spectroscopy by the use of HC-PBF breaks the MI-noise-limited sensitivity of previous HC-PBF gas sensors, which mainly rely on the direct absorption spectroscopy [70–73]. Instead of measuring the spectral attenuations, the PTgas spectroscopy analyzes the trace gas by detecting the accumulated phase changes. The PTgas spectroscopy adapts a pump-probe detection scheme. The periodic gas absorption of intensity-modulated pump beam would induce localized temperature, density and pressure distribution changes, and thus modulate the refractive index of gas molecules within the HC-PBF. A probe beam with its nominal wavelength tuned away from the gas absorption line would experience and accumulate the PT phase modulation when propagating along the same HC-PBF. A fibre-optic interferometry with highly precise phase sensitivity is utilized to detect the phase changes of probe beam. The photothermal interferometer (PTI) with HC-PBFs has achieved an ultra-sensitivity of 2 ppb or  $2.3 \times 10^{-9} \text{ cm}^{-1}$  of  $\text{C}_2\text{H}_2$  in 1530.37 nm by the use of 10-m-long HC-PBFs, preceding any of previously reported HC-PBF gas sensors [70]. Meanwhile, it also achieve an unprecedented dynamic range of nearly six orders of magnitude. Both the sensitivity and dynamic range have been enhanced

by nearly three orders of magnitude than previously reported results on HC-PBF gas sensors.

## 1.2 Research motivations

### 1.2.1 Principles of PT phase modulation and optimized performance of PTI with HC-PBFs

Even though, the experimental and theoretical demonstration of PT gas spectroscopy have been fully exploited in free-space optics [77–79]. It is supposed to be quite different for PT phase modulation in HC-PBF since the much more confined light beam and different boundary condition, especially when the beam radius is comparable with the confined boundary. For further design and improvement of PT gas spectroscopy in HC-PBF, the theoretical analysis is necessary to comprehend the mechanism of PT phase modulation in HC-PBF. Therefore, the first part of my motivation is quite straightforward:

**Mechanism and dynamics of PT phase modulation in HC-PBFs.** The use of pulsed pump beam helps us make an observation and understanding of dynamics and mechanism of PT phase modulation in HC-PBF. It would do a favor in the future exploration and optimization of PT gas spectroscopy. A numerical model has been proposed in the thesis to model and explain the PT phase modulation and meanwhile give a theoretical expectation of PT phase modulation efficiency, which is critical for the further optimized works of PT gas spectroscopy. The corresponding experimental works were also carried out to verify the theoretical model. The great agreement between the experimental results and simulation works suggests that the heat transfer or conduction process is dominant for PT spectroscopy. The optimized pulse duration of pump beam is given for the practical employment.

**Optimized performance of PTI in HC-PBFs.** In the previous PT gas spectroscopy system, a Mach-Zehnder interferometer (MZI) has been proposed to detect the PT phase modulation[70]. However, the use of MZI requires an electronic feed-back serve-control to stabilize the interferometry system, which makes the system complex and uneasy to operate. It has to re-match the fibre lengths of sensing and reference arms when the length of sensing HC-PBF has been changed. On the other hand, the unavoidable mismatch lengths between the two arms would turn the laser phase noise into intensity fluctuations of interferometry output [80]. Thus for a practical application, a passively stabilized system has to be constructed with comparable sensitivity. Furthermore, the frequency-dependent response of PT gas spectroscopy has been demonstrated in free-space optics [77]. However, for a HC-PBF gas cell, the phenomena could be quite different. Thus the works has to be done for finding best choices of pump modulation frequency which would maximize the performance of PT gas spectroscopy. The passively stabilized Sagnac interferometer using a  $3 \times 3$  optical coupler has been modified to overcome the limitation of high loss HC-PBF gas cell and etalon-effect in the fibre loop and high phase sensitivity has been achieved. The works of this part are a significant step towards the practical application of PT interferometry.

### 1.2.2 Distributed PT gas spectroscopy with HC-PBFs

The capability of detecting events in arbitrary locations along an optical fibre is a unique and overwhelming advantage of fibre-optic sensors. In some applications, such as surveillances of natural gas pipelines and oil wellbores, distributed detection of gas concentration over a long haul or an extended area is often needed and necessary. However, little work has been reported on distributed gas detection with optical fibres.

Sumida et al reported a distributed hydrogen sensor by use of a silica-core fibre coated with  $Pt/WO_3$  thin film as hydrogen sensitive cladding [81]. The complex fabrication process and propagation loss caused by metal cladding however limit the sensing length to tens of centimeters. Jin et al studied a distributed gas detection based on the optical time domain reflectometry (OTDR) with a HC-PBF. By exploiting both backscattering due to imperfection in surface membranes and gas absorption-induced spectral attenuation, they demonstrated the detection of acetylene gas over  $\sim 75$ -m-long HC-PBF. However, even with a very large number of averages (up to 64,000 times), the detectable gas concentration is only a few percent of acetylene with a spatial resolution of several meters [53]. The coherent mixing or interference of HC-PBF supported modes was identified as a major factor that affects the stability and noise performance of the sensor and the minimum detection limit was not addressed. The possibility of distributed gas sensing with photothermal gas spectroscopy has been proposed in [70]. However, no experiment was conducted yet. Garcia-Ruiz et al demonstrated a distributed gas sensor based on the PT effect in a small solid-core photonic crystal fibre (PCF) [82]. Evanescent-wave absorption of gas molecules raises the local temperature of the index-guiding PCF, which was detected with a chirped-pulse phase-sensitive OTDR system. However, only a qualitative demonstration of gas presence was reported with no claims on the detection limit and spatial resolution. The length of sensing PCF is  $\sim 10$  m.

**Distributed photothermal gas spectroscopy with HC-PBFs.** HC-PBFs appear to be an ideal gas cell which make them an ideal long-haul distributed platform for trace gas detection with low optical loss. It is possible to build a distributed photothermal gas sensing with high sensitivity. The presence of gas at arbitrary locations can absorb the intensity-modulated pump beam. A phase-sensitive OTDR system can be applied to probe the PT phase modulation along the fibre where the gas presents. By considerate designing the HC-PBF gas cell, the primary demonstration of distributed photothermal gas sensing with a long HC-PBF has been achieved. The

theoretical expectation and limited factors have been addressed, which may help a lot in the future works. The experimental results present a good sensitivity, which are a good movement towards a practical all-fibre distributed gas sensing.

## 1.3 Thesis outline

The thesis mainly focuses on the development of photothermal gas spectroscopy in HC-PBF, from its basic theoretical investigation to its applications, and would be organized as follows:

**Chapter 2** introduces the literature review on basic concepts of gas spectroscopy and related highly sensitive detection methods. The wavelength modulation spectroscopy will be discussed. The concepts and techniques introduced in this chapter will be a basis for the works of following chapters.

**Chapter 3** reviews the principles and development of photothermal techniques. The basics of fibre-optic interferometer will be presented. Furthermore, the theoretical deduction of photothermal interferometry in free-space optics from a variety of sources will be summarized and given in a generally unified way, which would help a lot in optimizing the photothermal interferometry and giving a theoretical expectation of sensitivity performance in the free-space optics. The advantages of using HC-PBFs for PTI gas sensors will be presented by comparing with that using open-path gas cells and direct absorption spectroscopy in HC-PBFs.

**Chapter 4** presents the studies on the mechanism and dynamics of PT phase modulation in HC-PBF. A numerical model will be built to explain the heat conduction process in the HC-PBF gas cell using a pulsed pump beam. The PT induced phase modulation coefficient will be given, which is a theoretical expectation for the calculation on the sensitivity of PT spectroscopy in HC-PBF. The influence factors of PT efficiency in HC-PBF will be discussed. The model fits well with the

experimental measured results. Also, pulsed PT interferometry in HC-PBF as an gas sensor will be demonstrated.

**Chapter 5** will further discuss the optimized performance of PT interferometry in HC-PBF. The frequency-dependent PT efficiency will be exploited both theoretically and experimentally. To make the PT interferometry compatible to the in-situ field applications, a PT Sagnac interferometry working with passively stabilization will be demonstrated with high sensitivity.

**Chapter 6** gives a primary presentation on the distributed PT gas spectroscopy with long HC-PBFs. The theoretical expected performance of distributed sensing using PT spectroscopy will be discussed and a general applicable equation to estimate the PT phase modulation along the HC-PBF will be provided. The experimental demonstrations of both quasi-distributed and distributed sensing present high sensitivity and the capability of long-haul gas detection. Other possible improvements of distributed PT interferometry will be discussed.

**Chapter 7** demonstrates a summary on our thesis and further works will be addressed.

# Chapter 2

## Background knowledge

The detection of gas molecules with high sensitivity and selectivity indicates that by using specific techniques, the minimum detectable gas absorption could be as better as possible while the discrimination of gas species with 'finger-print' selection. The concepts and origins of gas spectroscopic technique form a basic understanding of gas detection.

In this chapter, we review some basic concepts of gas spectroscopic techniques which are the fundamental knowledge for our following works.

### 2.1 Background of ro-vibration spectra

#### 2.1.1 Light-matter interaction

The light-matter interaction could most likely manifest as one of the changes of three characteristics: electric dipole moment (absorption/emission), induced polarization (Raman scattering, inelastic) and elastic scattering (Rayleigh scattering), as shown in Fig.2.1. The Rayleigh scattering from molecules could only change the propagation direction of photons but the energy ( $h\nu_0$ ) of incident photons remains unchanged while the Raman scattering could induce an energy exchange between the molecules

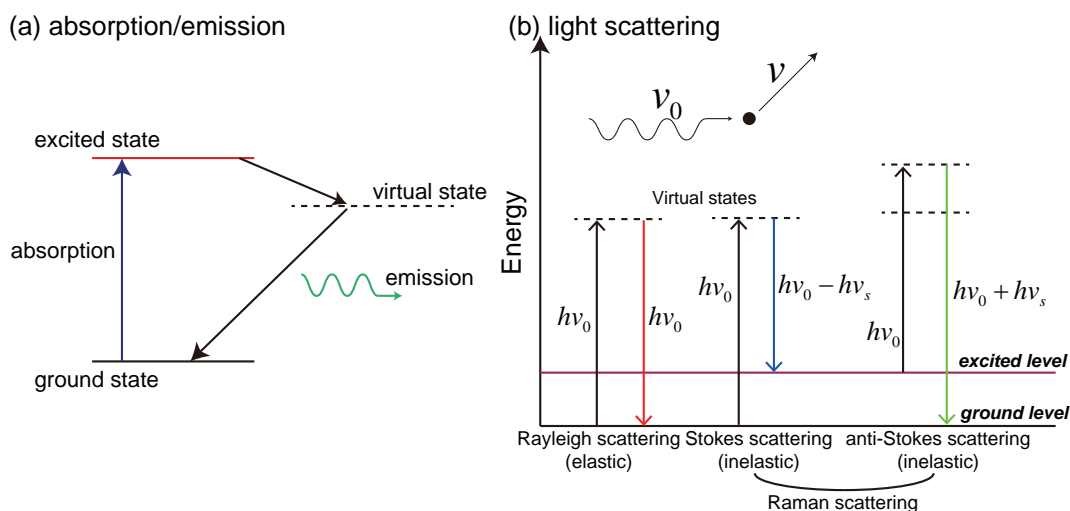


Fig. 2.1 Illustration of light-matter interaction process.  $h = 6.63 \times 10^{-34} \text{ J} \cdot \text{s}$  is the Planck's constant [83];  $\nu_0$ : input laser frequency;  $\nu_s$ : Stokes frequency shift.

and the incident photons, resulting in a possible energy decrease ( $h\nu_0 - h\nu_s$ , where  $\nu_s$  is the frequency of Stokes shift) or increase ( $h\nu_0 + h\nu_s$ ) [83].

For ro-vibration spectra, it involves the transition between different energy levels accompanying a process of absorption/emission. The rotational and vibrational state changes of molecule would induce a state change of electric dipole moment and thus the possible energy changes with absorbing or emitting photons to back to its equilibrium as shown in Fig. 2.1(a). Those processes would lead to a change of internal energy of molecules. In a common way, the internal energy of a gas molecule could be stored in three of modes: electronic, rotation and vibration. As illustrated in the Fig. 2.2, the energy levels of atomic or molecular system are discrete and the absorption/emission spectra are also in a discrete manner. On the other hand, the orders of magnitudes of transitions between different type of energy state generally follows:  $\Delta E_{\text{rot}} < \Delta E_{\text{vib}} < \Delta E_{\text{elec}}$ . The rotational energy transitions usually occur in the micro-wave region while the ro-vibrational transitions correspond to infrared (IR) region. The rovibronic energy transitions involving all of the three kinds of energy state changes usually take place in UV/Vis region. It is worth to note that the vibrational energy changes are generally accompanied by rotational energy changes

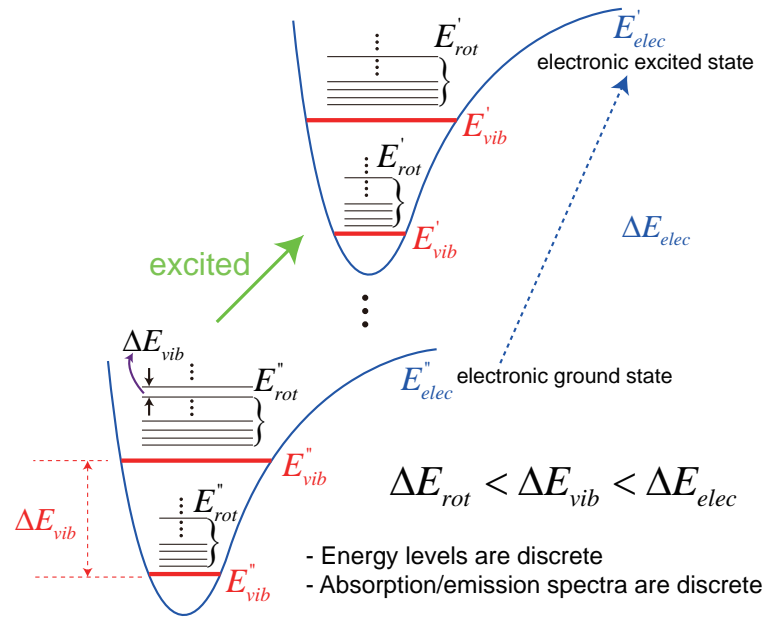


Fig. 2.2 Illustration of different energy levels.  $E''$  and  $E'$  indicate the lower and higher electronic energy levels, respectively [83].

while the electronic energy changes are generally accompanied by vibrational and rotational energy changes [83].

### 2.1.2 Diatomic molecular spectra

The heteronuclear diatomic molecules could be recognized as being formed by a pair of permanent net positive/negative charges located in opposite ends of molecule and as a simplicity, it is reasonable to assume that the atoms are point masses (with diameter of nuclei  $d \approx 10^{-13} \text{ cm}$ ) and separated by an equilibrium distance  $r_e$ , where  $r_e$  remains constant or named as 'rigid rotor' (RR), as illustrated in Fig.2.3.

In quantum mechanics, such a system would have an angular momentum of  $\Upsilon \Omega_{rot}$  where  $\Omega_{rot}$  is the rotational angular velocity. The allowable magnitudes of angular momentum are then quantized as:

$$\|\Upsilon \Omega_{rot}\| = \sqrt{J(J+1)}\hbar, (\hbar = h/2\pi, J = 0, 1, 2, 3, \dots) \quad (2.1)$$

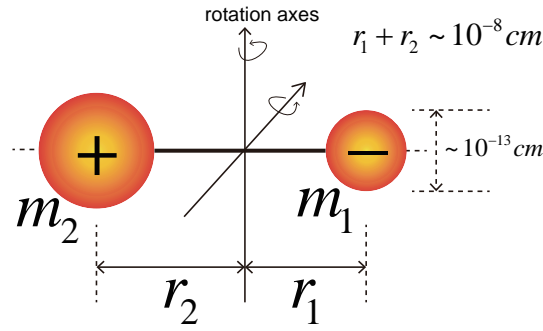


Fig. 2.3 Diatomic molecule with rigid rotor approximation [83].

where the moment of inertia  $\Upsilon = \sum m_i r_i^2 = \mu_m r_e^2$ ,  $i = 1, 2$  and  $\mu_m = m_1 m_2 / (m_1 + m_2)$  in a classical mechanics definition.  $\mu_m$  is the reduced mass and  $r_e$  is the equilibrium separating distance between nuclei.  $J$  is an integer called as a quantum number, which is used to characterize the total angular momentum. Then it yields a rotational energy by considering the moment of inertia [83]:

$$E_{rot} = \frac{1}{2} \Upsilon \Omega_{rot}^2 \quad (2.2)$$

$$= \frac{1}{2\Upsilon} (\Upsilon \Omega_{rot})^2 \quad (2.3)$$

$$= \frac{1}{2\Upsilon} J(J+1) \hbar^2 \quad (2.4)$$

$$= J(J+1) \frac{\hbar^2}{8\pi^2 \Upsilon} \quad (2.5)$$

$$= E_J \text{ (in unit of Joules.)} \quad (2.6)$$

The rotational energy  $F(J)$  should be defined in the unit of  $cm^{-1}$  as:

$$F(J)[cm^{-1}] = \frac{E_J[J]}{hc} \quad (2.7)$$

$$= \left[ \frac{h}{8\pi^2 \Upsilon c} \right] J(J+1) \quad (2.8)$$

By defining a rotational constant  $B_J[cm^{-1}] = h/(8\pi^2\Upsilon c)$ , the final expression of rotational energy could be in the form of:

$$F(J) = B_J J(J+1), J = 0, 1, 2, \dots \quad (2.9)$$

The absorption spectra actually are related to some specific allowable transitions between the energy levels, which known as *selection rules*. The selection rules are determined by the transition probability or probability that a molecule could occupy a space. The probability could be found by solving the time-dependent form of *Schrödinger's* equation:

$$\frac{d^2\Theta(x)}{dx^2} + \frac{2m}{\hbar^2}[E - U(x)]\Theta(x) = 0 \quad (2.10)$$

The Eq. 2.10 describes a atom or molecule with mass of  $m$  moving in a potential field of  $U(x)$ . The complex solution of Eq. 2.10 is the wave function  $\Theta(x)$  and multiplied by its complex conjugate, forming  $\Theta\Theta^*$  is the probability that a atom or molecule would occupy a specified region  $x \rightarrow x + dx$ .

The transition probability from a initial state  $n$  to a final quantum state  $m$  could be found by the integral over the whole space of interest:

$$\text{Transition probability} \propto \int \Theta_m \mu \Theta_n^* d\tau \rightarrow \Delta J = \pm 1 \quad (2.11)$$

where  $\mu$  is the dipole moment. Thus it indicates that the change in rotational quantum number could only be  $\pm 1$ . For pure rotational transition we may restrict it to only +1:

$$\Delta J = J' - J'' = +1 \quad (2.12)$$

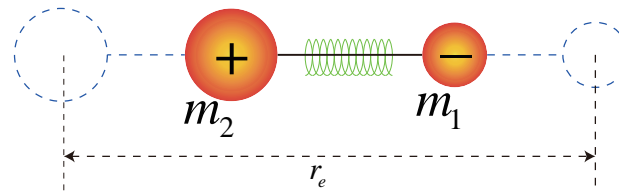


Fig. 2.4 Simple harmonic oscillator model of a linear diatomic molecule.  $r_{min}$  indicates the minimum compression distance between the two charges [83].

This is the *selection rule* of rotational transition. Thus the rotational transition frequencies could be obtained by following the selection rule:

$$\bar{\nu}_{J' \leftarrow J''} = B_J(J'' + 1)(J'' + 2) - B_J(J'')(J'' + 1) \quad (2.13)$$

$$= 2B_J(J'' + 1) \quad (2.14)$$

The rotation energy spacing would increase as the involved energy level increased. On the other hand, the line spacing between any two of the adjacent pure rotational transition would be constant as  $2B$ . The line spacing parameter is useful in spectroscopy since it could be a basics to find the  $\Upsilon$  and  $r_e$  in rigid rotor model. By this way, the quantum mechanism model could be related and verified by a classic mechanism model. From the notation of Eq. 2.9, there should be a maximum energy of every group of rotational transition.

In a similar manner, the vibration spectra could also be interpreted as a simple harmonic oscillator (SHO), as shown in Fig. 2.4.

In SHO, the characteristics of classical mechanics could be expressed in the form of [83]:

$$\text{Force} : k_s(r - r_e) \quad (k_s : \text{Hookie's constant}) \quad (2.15)$$

$$\text{Fundamental Freq} : \nu_{vib} = \frac{1}{2\pi} \sqrt{k_s/\mu_m}, \mu_m = \frac{m_1 m_2}{m_1 + m_2} \quad (2.16)$$

$$\text{Angular Frequency} : \Omega_{vib}[cm^{-1}] = \nu_{vib}/c \quad (2.17)$$

$$\text{Potential Energy} : U = \frac{1}{2} k_s (r - r_e)^2. \quad (2.18)$$

In quantum mechanics, it may has the following expression [83]:

$$\text{Vibration Quantum Number} : \nu = 0, 1, 2, \dots \quad (2.19)$$

$$\text{Vibration Energy} : G(\nu)[cm^{-1}] = \Omega_{\text{vib}}(\nu + 1/2) \quad (2.20)$$

$$\text{Selection Rules} : \Delta\nu = \nu' - \nu'' = +1. \quad (2.21)$$

Thus it is obviously that the adjacent vibration quantum states have the same energy difference  $G(\nu + 1) - G(\nu) = \Omega_{\text{vib}}$  or line spacing, has nothing to do with the quantum number  $\nu$ .

However, due to the vibration-rotation coupling and centrifugal distortion, the real diatomic oscillator could not strictly follow a SHO model. Instead, the practical anharmonic oscillator (AHO), which includes the nonlinear oscillating influence, would be much more appropriate for the practical model as:

$$G(\nu) = \Omega_{\text{vib}}(\nu + 1/2) + \Omega_{\text{vib}}x_{\text{vib}}(\nu + 1/2)^2 + \dots + H.O.T; \quad (2.22)$$

where  $x_{\text{vib}}$  is the coefficient dependent on the influence strength of second order oscillating while H.O.T is the abbreviation of higher order terms. From the Eq. 2.22, it indicates that the spacing (i.e. energy difference) between the two adjacent vibration lines (i.e. energy levels) would be decreased and some weak transition which may not strictly follow the selection rules of Eq. 2.21 could possibly occur. However, the energy barrier of those weak transition would increase dramatically as the  $\Delta\nu$  increases. Therefore, there are relatively weaker overtone vibration transitions (first overtone  $\Delta\nu = +2$ , second overtone  $\Delta\nu = +3$ ) accompanying the fundamental vibration transition ( $\Delta\nu = +1$ ). The vibration potential then could be a Morse function as:

$$U = D_{eq}[1 - \exp(-\zeta(r - r_e))]^2 \quad (2.23)$$

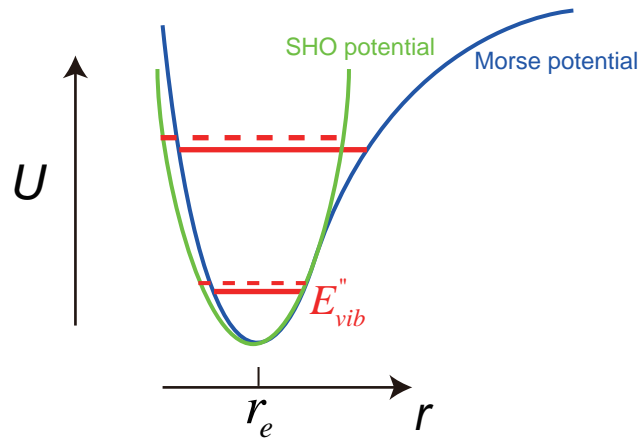


Fig. 2.5 Potential energy for SHO and AHO model with vibration states;  $U$ : potential energy for vibrational states [83].

where  $D_{eq}$  is the bond-dissociation energy (in  $cm^{-1}$ ) and  $\zeta = 1.2177 \times 10^7 \Omega_{vib} \sqrt{\mu_m/D_{eq}}$  is the modified factor. The potential energy between those two kinds of model could be illustrated as Fig. 2.5.

On the other hand, the RR model of pure rotational spectra also require a further modification with a centrifugal distortion constant  $D_v$  and the rotation constant should be dependent on the vibrational state as  $B_v$ . The sub-script of  $v$  indicates the vibrational quantum number dependence. The rotation energy should be revised as:

$$F_v(J) = B_v J(J+1) - D_v J^2(J+1)^2. \quad (2.24)$$

As a simple illustration of ro-vibration spectra, we only consider a Born-Oppenheimer approximation with the regard that the vibration and rotation transition are independent. The total energy of ro-vibration could be [83]:

$$T(v, J) = RR + SHO \quad (2.25)$$

$$= F(J) + G(v) \quad (2.26)$$

$$= B_v J(J+1) + \omega_e(v + 1/2) \quad (2.27)$$

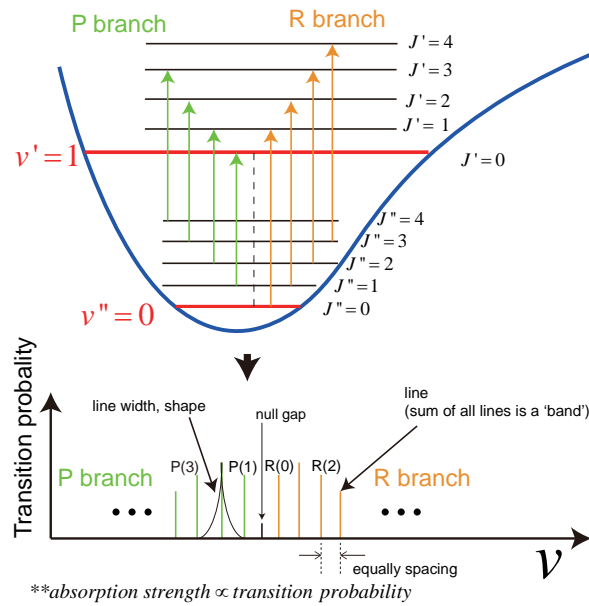


Fig. 2.6 Illustration of ro-vibration transitions and its corresponding spectra [83].

with selection rules of:

$$\Delta v = +1 \quad (2.28)$$

$$\Delta J = \pm 1 \quad (2.29)$$

Thus the line position of ro-vibration transition could be determined by  $\bar{\nu} = T(v', J') - T(v'', J'')$ . Thus there could be two groups of rotational transition for each vibration transition:

$$\text{P branch} = \Delta J = -1 \quad (2.30)$$

$$\text{R branch} = \Delta J = +1 \quad (2.31)$$

The ro-vibration spectra could be illustrated as Fig. 2.6 with regards to the ro-vibration transition. It can be concluded from the figure and discussions above, there are two branches, namely P and R branch in each absorption band. The line spacings between any of two adjacent absorption lines are equal and there are local maxima of each P or R branch. Even though there could be some modifications by

considering the other complex factors, the absorption lines of a gas molecule could be well approximately understood by the description here.

For the transition  $v = 0 \rightarrow v = 1$  is the fundamental transition,  $v = 0 \rightarrow v = i$  ( $i > 1$ ) is the overtone transition and the transition from an already excited vibrational state to another higher state (further excited) is called a hot transition. Typically there are five types of bands (vibrational transitions): fundamental bands ( $v_i, \Delta v = v' - v'' = 1$  for *ith* mode), first overtone ( $2v_i, \Delta v = v' - v'' = 2$ ), second overtone ( $3v_i, \Delta v = v' - v'' = 3$ ), combination bands (e.g.  $v_1 + v_2$  with  $\Delta v_1 = \Delta v_2 = 1$ ;  $2v_1 + v_2$  with  $\Delta v_1 = +2$  and  $\Delta v_2 = +1$ ) and difference bands ( $v_1 - v_2$  with  $\Delta v_1 = \pm 1$  and  $\Delta v_2 = \mp 1$ ). The combination transition could be observed when two or more fundamental transitions occur simultaneously.

In ro-vibration spectroscopic technique, the degrees of freedom (DOF) usually refers to the vibration modes [84]. For a linear polyatomic molecule, the DOF is  $3N_{num} - 5$  while it is  $3N_{num} - 6$  for nonlinear one, where  $N_{num}$  is the number of nuclei in molecule. Fig. 2.7 presents the fundamental vibration modes of  $C_2H_2$ . The types of the transition bands are usually classified as the vibration modes ( $v_i$ , the *ith* vibrational mode). The  $C_2H_2$  is a linear structure molecules with 4 nuclei and therefore there should be  $3 \times 4 - 5 = 7$  vibrational DOF. However, there are two types of doubly degenerated modes:  $v_4$  and  $v_5$ .

Mode	Description	Symmetry	Normal Mode
$v_1$	symmetric C-H stretch	$\Sigma_g^+$	$\overleftarrow{H} - C \equiv C - \overrightarrow{H}$
$v_2$	symmetric C≡C stretch	$\Sigma_g^+$	$H - \overleftarrow{C} \equiv \overrightarrow{C} - H$
$v_3$	asymmetric C-H stretch	$\Sigma_u^+$	$\overleftarrow{H} - C \equiv C - \overleftarrow{H}$
$v_4$	symmetric bend (degenerate)	$\Pi_g$	$\begin{array}{c} \uparrow H - C \equiv C - H \\ \downarrow \quad \quad \downarrow \end{array}$
$v_5$	asymmetric bend	$\Pi_u$	$\begin{array}{c} \uparrow H - C \equiv C - H \\ \downarrow \quad \quad \downarrow \end{array}$

Fig. 2.7 Illustration of fundamental vibration modes of acetylene [85].

On the other hand, in polyatomic molecules, the vibrational transitions are represented in the form of DOF. For example, the transition  $(0,0,0) \rightarrow (0,0,2)$  indicates the vibrational state  $\nu_3$  is excited from  $\nu_3 = 0$  to  $\nu_3 = 2$  and this is the molecule's first overtone transition while such a molecule has three discrete mode of vibrations (DOF). The transition  $(0,1,1,1) \rightarrow (0,1,2,2)$  indicates a combination band with frequency of  $\nu_3 + \nu_4$  and with 4 vibrational DOF. The transition  $(0,0,0,0) \rightarrow (0,1,1,2)$  indicates a combination band with frequency  $\nu_2 + \nu_3 + 2\nu_4$ . It is also possible to deduce the energy of overtone or combinational transition from the fundamental transition [86]. For example,  $H_2O$  has three fundamental vibrational frequencies:  $\nu_1$  ( $3652\text{ cm}^{-1}$ ),  $\nu_2$  ( $1595\text{ cm}^{-1}$ ) and  $\nu_3$  ( $3756\text{ cm}^{-1}$ ). The observed transition  $3151.4\text{ cm}^{-1}$  could be the overtone transition  $2\nu_2 = 3190\text{ cm}^{-1}$ . The difference of  $48.6\text{ cm}^{-1}$  may result from the anharmonic oscillation. Another observed transition  $6874\text{ cm}^{-1}$  could be a combination transition  $2\nu_2 + \nu_3 = 6945.8\text{ cm}^{-1}$ .

### 2.1.3 Parameters of gas spectroscopy

As mentioned in Eq. 1.1 in Chapter 1, the gas absorption of light beam follows the well-known Beer-Lambert law with gas absorption coefficient  $\alpha(\nu)$ , which is related to gas concentration, light wavelength and type of gas species. The absorption coefficient could be expressed in the form of:

$$\alpha(\nu) = N\sigma(\nu) = CN_{tot} \cdot S_0 \cdot g(\nu) \quad (2.32)$$

where  $N(\text{molecules}/\text{cm}^{-3})$  is the number of absorption gas molecules in unit volume,  $\sigma(\nu)(\text{cm}^2/\text{molecule})$  is the absorption cross section per molecule,  $C$  is the relative molar fraction with definition of  $C = N/N_{tot}$ ,  $N_{tot}(\text{molecules}/\text{cm}^{-3})$  is the total molecular number density,  $S_0(\text{cm}^{-1}/(\text{molecule} \cdot \text{cm}^{-2}))$  is the line strength or spectral line intensity and  $g(\nu)$  is the lineshape function with normalization of

$\int_{-\infty}^{+\infty} g(\nu) d\nu = 1$ . The typical definition of lineshape function could be illustrated in Fig. 2.8.

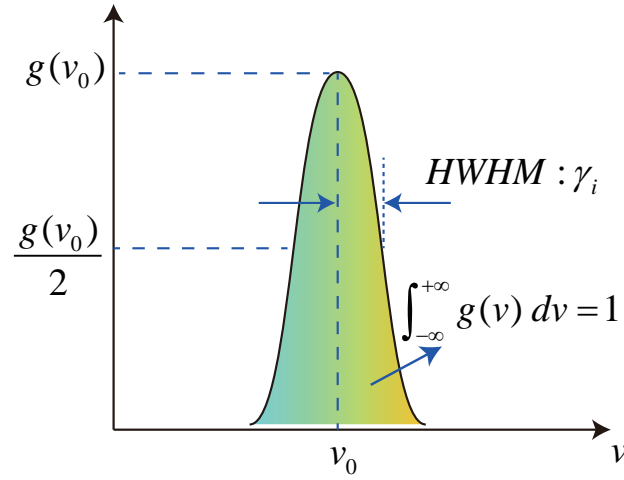


Fig. 2.8 Illustration of lineshape function.  $\gamma_i$  is the half-width-half-maximum (HWHM) of a lineshape,  $i$  indicates the different lineshape function in the following discussion.

The total molecular number density  $N_{tot}$  in temperature  $T(K)$  and pressure  $p(atm)$  could be expressed as:

$$N_{tot} = N_L \frac{273.15}{T} \cdot p \quad (2.33)$$

where  $N_L$  is the Loschmidt number with value of  $2.68676 \times 10^{19} \text{ molecule/cm}^3$ , at 273.15 K and 1 atm. In ambient condition ( $T = 296 K, p = 1 atm$ ),  $N_{tot} = 2.479 \times 10^{19} \text{ molecule} \cdot \text{cm}^{-3}$ .

The line strength  $S_0$  is related to Einstein's A and B coefficient with  $S_0 \propto N_1 B_{12} \cdot (h\nu/c)$ , for a transition from lower state 1 to upper state 2.  $N_1$  is the function of population located in the lower state 1. The  $B_{12}$  indicates the transition probability from lower state to upper state, which is in the unit of  $J^{-1} m^3 s^{-2}$  and in a relationship to  $A_{21}(s^{-1})$  of:

$$\frac{B_{12}}{A_{21}} = \frac{1}{8\pi h} \left(\frac{c}{\nu}\right)^3 \frac{g_2}{g_1} \quad (2.34)$$

the  $g_1$  and  $g_2$  are the statistical weights of level 1 and 2 (or sometimes called as degeneracy factor), which define the relationship between  $B_{12}$  and  $B_{21}$  with  $g_1 B_{12} = g_2 B_{21}$ .

For the practical spectroscopy, the absorption spectrum is not a line with infinite sharp but with specific lineshape, which is the results of line broadening. The line broadening is the mixing results of measurement uncertainty and external perturbations on the transition process. The basic broadening is the result of measurement uncertainty, or natural broadening due to the lifetime of exciting states. This determine the minimum possible linewidth and shape of an absorption line. According to the Heisenberg Uncertainty Principle, the measured transition energy should have the uncertainty as:

$$\Delta E \tau_{\text{trans}} \geq \frac{h}{2\pi} \quad (2.35)$$

where  $\tau_{\text{trans}}$  is the lifetime of a transition, which is related to the lifetime of lower state  $\tau''$  and upper state  $\tau'$ . The natural broadening is homogeneous and characterized as a Lorentz profile.

There are three main lineshape profile: Gaussian, Lorentz and Voigt profile. The Gaussian profile is an inhomogeneous broadening resulting from the random thermal motion of gas molecules (also called as a Doppler broadening or Doppler profile). The Gaussian lineshape function is typically in the form of:

$$g_D(\nu) = \frac{1}{\gamma_D} \sqrt{\frac{\ln 2}{\pi}} \exp\left[-\ln 2 \cdot \left(\frac{\nu - \nu_0}{\gamma_D}\right)^2\right] \quad (2.36)$$

with half-width of half maximum (HWHM):

$$\gamma_D = \nu_0 \sqrt{\frac{2k_B T \ln 2}{mc^2}} = 3.51812 \times 10^{-7} \nu_0 \sqrt{\frac{T}{M}} \quad (2.37)$$

where  $\nu_0(\text{cm}^{-1})$  is the center wavenumber and  $M$  is the molecular weight in atomic mass unit. The peak value of Doppler profile is:

$$g_D(\nu_0) = \frac{1}{\gamma_D} \sqrt{\frac{\ln 2}{\pi}} \quad (2.38)$$

The Lorentz profile is a homogeneous broadening resulting from the natural broadening (as discussed above about lifetime-induced broadening) and collision broadening. It is typically dominant at the elevated pressure  $\leq 0.1 \text{ atm}$ . The collisions between the molecules can affect the transitions between the energy levels. In general experimental condition, the natural broadening can be ignored. The Lorentz profile is in the form of:

$$g_L(\nu) = \frac{1}{\pi} \frac{\gamma_L}{(\nu - \nu_0)^2 + \gamma_L^2} \quad (2.39)$$

with peak value of:

$$g_L(\nu_0) = \frac{1}{\pi \gamma_L} \quad (2.40)$$

In most practical cases, the Doppler broadening is dominant at low pressure, high temperature and small wavelength region condition while the collision broadening is the most significant at high pressure ( $\leq 0.1 \text{ atm}$ ), low temperature and large wavelength region condition. But in many conditions, the real line profile are the integrated results of both two broadening resulting a Voigt profile. The Voigt profile is the convolution between the Doppler and Lorentz profile:

$$g_V(\nu) = \int_{-\infty}^{+\infty} g_D(u) g_L(\nu - u) du \quad (2.41)$$

Or in a easy-to-calculating form:

$$g_V(\nu) = g_D(\nu_0) \frac{a}{\pi} \int_{-\infty}^{+\infty} \frac{\exp(-y^2)}{a^2 + (w - y)^2} dy = g_D(\nu_0) \cdot V(a, w) \quad (2.42)$$

where  $V(a, w)$  is the Voigt function,  $a$  is the Voigt parameter and  $w$  is the dimensionless line position parameter and  $y$  is the integral parameter:

$$a = \sqrt{\ln 2} \gamma_L / \gamma_D \quad (2.43)$$

$$w = \sqrt{\ln 2} \cdot (v - v_0) / \gamma_D \quad (2.44)$$

$$y = \sqrt{\ln 2} \cdot u / \gamma_D \quad (2.45)$$

The HWHM of Voigt lineshape function can be estimated as:

$$\gamma_V = 0.5346 \gamma_L + \sqrt{0.2166 \gamma_L^2 + \gamma_D^2} \quad (2.46)$$

The peak value of Voigt lineshape could be [83]:

$$g_V(v_0) = g_D(v_0) \cdot V(a, 0) \quad (2.47)$$

$$= g_D(v_0) \cdot \exp(a^2) [1 - \operatorname{erf}(a)] \quad (2.48)$$

$$= \sqrt{\frac{\ln 2}{\pi}} \cdot \frac{1}{\gamma_D} \cdot \{\exp(a^2) [1 - \operatorname{erf}(a)]\} \quad (2.49)$$

where  $\operatorname{erf}(a)$  is the error function with parameter of  $a$ . As  $a$  increase, the Voigt profile tends to be more 'Lorentzian' while as  $a$  decrease the Voigt tends to be more 'Gaussian'. The peak value of Voigt value tends to decrease with the increased  $a$  monotonously while the linewidth of Voigt profile tends to increase as  $a$  increases monotonously. On the other hand, for the same value of HWHM, the Lorentzian profile has a slower decrease speed (small gradient) on the both wing sides than that of Gaussian profile. Under normal conditions ( $T = 296 K$  and  $p = 1 atm$ ), we usually adapt Lorentzian profile as the line shape for most of gas absorption spectroscopy.

### 2.1.4 Ro-vibration spectra of acetylene

In a practical application, the absorption coefficients of gas molecules usually are explored through the public available HITRAN database [85, 87]. In a typical output data form, the following parameters are usually adapted to calculate the desired absorption coefficient: the line position or wavenumber of absorption  $\nu(cm^{-1})$ , line strength  $S_0$ , the air-broadened HWHM  $\gamma_{air}$  and the self-broadened HWHM  $\gamma_{self}$ . In weak absorption approximation with very low gas concentration buffered by  $N_2$  or air, the HWHM of Lorentzian profile could be assumed to be equal to that of air broadening  $\gamma_{air}$ .

For example, taking the P(9) absorption line as an example. The P(9) absorption line is the transition in  $\nu_1 + \nu_3$  combination band from a rotational state  $J'' = 9$  in ground vibrational state to another rotational state  $J' = 8$  in excited vibrational state, resulting  $\Delta J = -1$  and labelled as P(9) line. For P(9) absorption line of  $C_2H_2$  with  $\nu = 6534.363450cm^{-1}$ ,  $S_0 = 1.21 \times 10^{-20} cm^{-1}/(molecule \cdot cm^{-2})$  and  $\gamma_L = \gamma_{air} = 0.0820 cm^{-1}$ , we have the peak value of Lorentzian profile as Eq. 2.40:  $g_L(\nu_0) = 1/(\pi \cdot \gamma_L) = 3.8818 cm$ . Then for a relative  $C = 1 ppm$  (parts per million in molar or volume fraction) gas concentration, the absorption coefficient for P(9) line of  $C_2H_2$  is:

$$\alpha(\nu_0) = C \cdot N_{tot} \cdot S_0 \cdot g_L(\nu_0) \quad (2.50)$$

$$= C \cdot 2.479 \times 10^{19} [molecules/cm^3] \cdot 1.21 \quad (2.51)$$

$$\times 10^{-20} [cm/molecule] \cdot 3.8818 [cm] \quad (2.52)$$

$$= 1.1654 C [cm^{-1}] \quad (2.53)$$

$$= 1.1654 \times 10^{-6} [cm^{-1}] \quad (2.54)$$

The absorption cross-section could be:  $\sigma(\nu_0) = S_0 \cdot g_L(\nu_0) = 4.7 \times 10^{-24} [m^2]$ . The molar extinction coefficient or molar attenuation coefficient should be  $\epsilon(\nu_0) =$

$N_A \cdot S_0 \cdot g_L(\nu_0) = \sigma(\nu_0) \cdot N_{tot} [m^2/mol]$ , where  $N_A = 6.0221 \times 10^{23} \text{ molecules/mol}$  is the Avogadro constant. The absorbance of gas absorption should be defined as:

$$A = -\ln\left(\frac{I_t(\nu)}{I_0}\right) = \alpha_0(\nu)CL \quad (2.55)$$

which is related to the length of gas absorption.

The typical absorption lines of  $\nu_1 + \nu_3$  band of  $C_2H_2$  are shown in Fig. 2.9. Both the maximum absorption of P and R branches occur at the 9th line (P(9) at 1530.37 nm and R(9) at 1520.086 nm).

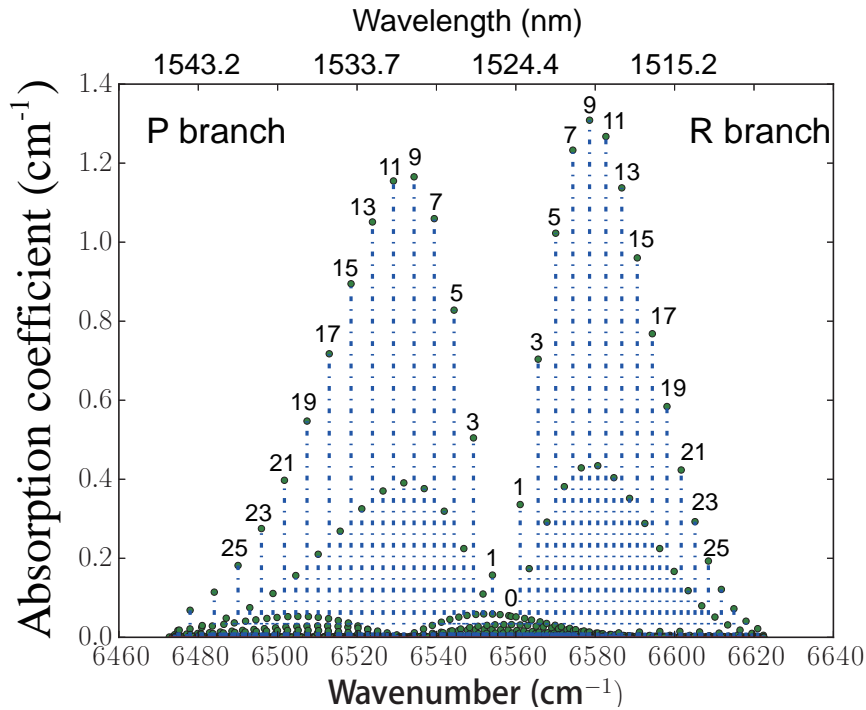


Fig. 2.9 Absorption lines of  $\nu_1 + \nu_3$  band of  $C_2H_2$  in the wavelength range of 1510-1545 nm .

The obtained absorption spectrum in Fig. 2.9 is the plot of absorption lines without taking the lineshape profile into consideration. In fact, by use of Lorentz lineshape function with the input of  $\gamma_{air}$ , the absorption spectrum with line-profile can be obtained. As illustrated in Fig. 2.10, the absorption spectrum with line profile around P(9) absorption line can be obtained. Also, the Lorentzian line-fit, as shown

in Fig. 2.10(b), can also be used to compare the difference between the absorption spectrum and Lorentzian profile. From the line-fit, the HWHM linewidth is about  $0.0829\text{ cm}^{-1}$  can be obtained, which is closed to  $0.0820\text{ cm}^{-1}$  of HITRAN data.

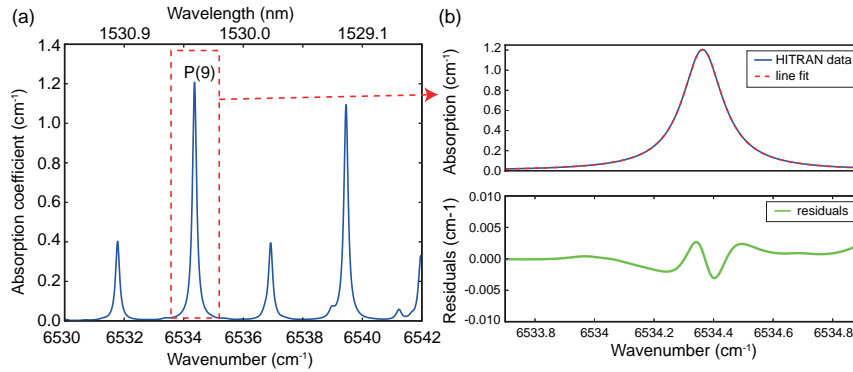


Fig. 2.10 (a) absorption spectrum with line profile in the vicinity of P(9) absorption line; (b) the Lorentzian line-fit for P(9) absorption line. The lower part is the fit residuals.

## 2.2 Wavelength modulation spectroscopy

To increase the detection sensitivity of trace gas, it usually follows the two directions: one is to increase the absorption signal level while the other is to reduce the background noise (ideally, down to quantum noise limit) [3]. As shown in Eq. 1.1, the increase of effective gas absorption length, such as using high finesses cavity or long HC-PBF, could enhance the signal level. However, the noise performance varies from the different detection methods.

In a conventional direction absorption spectroscopy using a single-pass gas cell, following Beer-Lambert law, the transmitted light power experiences an attenuation directly proportional to the factor of  $\alpha L$ , where  $\alpha$  is the gas absorption with the definition the same as  $\alpha(\nu)$  and  $L$  is the length of gas cell. Without any amplitude modulation or other noise background, the minimum detectable absorption signal

could reach a shot noise limit with a detection bandwidth of  $B$  [3]:

$$(\alpha L)_{min} = \frac{2eB^{1/2}}{\eta P_0} \quad (2.56)$$

where  $e$  is the elementary charge with value of  $1.60217662 \times 10^{-19}C$ ,  $\eta[A/W]$  is the photo-detector responsivity and  $P_0$  is the incident light power. It could reach a shot-noise limited detectable absorption as good as  $1 \times 10^{-8}$  at bandwidth of  $1/2\pi$  Hz (i.e. 1-s averaging time),  $P_0 = 1mW$ ,  $\eta \sim 0.8A/W$  at  $1.064\mu m$ . However, due to the existence of various noises which dominate over the shot-noise limit, such a sensitivity is far to be achieved, especially in the low-frequency ranges [3]. In order to reduce the background noise integrated during the detection, modulation techniques, either amplitude modulation or frequency modulation, are usually adapted to work at the high detection frequency and with narrow detection bandwidth [88, 89].

Frequency modulation spectroscopy (FMS) is one of the most sensitive spectroscopic detection methods applied for gas sensing [2, 90]. The FMS usually uses an external phase modulator, driven at radio-frequency with low modulation depth, to achieve fast optical frequency modulation. After passing through a gas-absorption cell, by monitoring the phase and amplitude of heterodyne beat radio-frequency signals between the sidebands and carrier frequency (aligned with the center of absorption line), both the features of absorption and dispersion in the vicinity of gas absorption line can be observed. Since the noises (including the laser  $1/f$  excess noise) at radio-frequencies is small, the FMS can achieve high detection sensitivity. Also, if the modulation depth is small and modulation frequency is smaller than the absorption linewidth, the whole absorption spectrum at the spectral feature of interest can be recovered by scanning the tunable diode laser source or phase modulation frequencies [91]. For FMS, the shot noise limited absorption signal could be down to [3, 4]:

$$(\alpha L)_{min} = \left(\frac{2eB}{\eta P_0}\right)^2 \frac{\sqrt{2}}{J_0(m)J_1(m)} \quad (2.57)$$

where  $J_0(J_1)$  is the zero (first) order Bessel function with the parameters of modulation index  $m$  (unity or less). The maximum value of  $J_0(m)J_1(m)$  could be 0.34 at  $m \approx 1.1$ . Thus the frequency modulation spectroscopy could deteriorate by a factor of  $\sim 4$  loss in terms of sensitivity with a identical optical power, compared with the direction absorption limit in Eq. 2.56. The reasons for such a loss may arise from that part of the optical power in the carrier frequency have to convert to sidebands, which results a power reduction.

Besides the method of reducing noises, the utilization of multi-pass high finesses cavity is attractive to enhance the absorption length and amplify the absorption signal [27, 92]. By carefully designing a cavity with finesses of  $\mathfrak{F}$ , the shot noise limit could be enhanced as [3]:

$$(\alpha L)_{min} = \frac{\pi}{2 \times \mathfrak{F}} \left( \frac{2eB}{\eta P_0} \right)^2 \frac{\sqrt{2}}{J_0(m)J_1(m)} \quad (2.58)$$

Thus, for a frequency modulation spectroscopy ,with modulation index of  $m = 0.5$  and  $\eta = 0.85 A/W$ ,  $P_0 = 5 mW$ , 1-s averaging time, the minimum detectable absorption is  $(\alpha L)_{min} = 2.2 \times 10^{-8}$  for a single pass cell while it could be down to  $(\alpha L)_{min} = 3.5 \times 10^{-13}$  with a cavity of finesses  $\mathfrak{F} = 10^5$  [3]. For experimental achievement, up to now, the most sensitive detection scheme reported is the works conducted with noise-immune cavity-enhanced optical heterodyne molecular spectroscopy (NICE-OHMS) method achieving sensitivity of  $1 \times 10^{-14} cm^{-1}$ , in terms of gas absorption coefficient, with 1s averaging time (only 1.5 times worse than that of calculated shot noise limit) [3, 4].

Wavelength modulation spectroscopy (WMS) shares the similar principle with FMS while has smaller modulation depth  $m \leq 1$  and lower modulation frequency which is much smaller than the absorption linewidth. WMS can directly modulate the wavelength (or optical frequency) of laser source at  $kHz$  rates by injection of

current. In some cases, the availability of instruments may simply determine the choice of FMS or WMS. In our implementations, we focus on WMS.

### 2.2.1 Principles of WMS

The modulation methods are attractive for a sensitive detection. For a electrical field  $E = E_0 \exp[i(2\pi\nu_0 t + m \cos(\omega t))]t$  with modulation depth of  $m$  at modulation frequency of  $\omega$ , if a large modulation index  $m \gg 1$  and lower modulation frequency  $\omega \ll \gamma_L$  ( $\gamma_L$  is the Lorentzian HWHM) are used, the modulation spectroscopy is called as a wavelength modulation spectroscopy. If  $m \leq 1$  and  $\omega \gg \gamma_L$ , then it is frequency modulation spectroscopy (FMS) [91, 93–95].

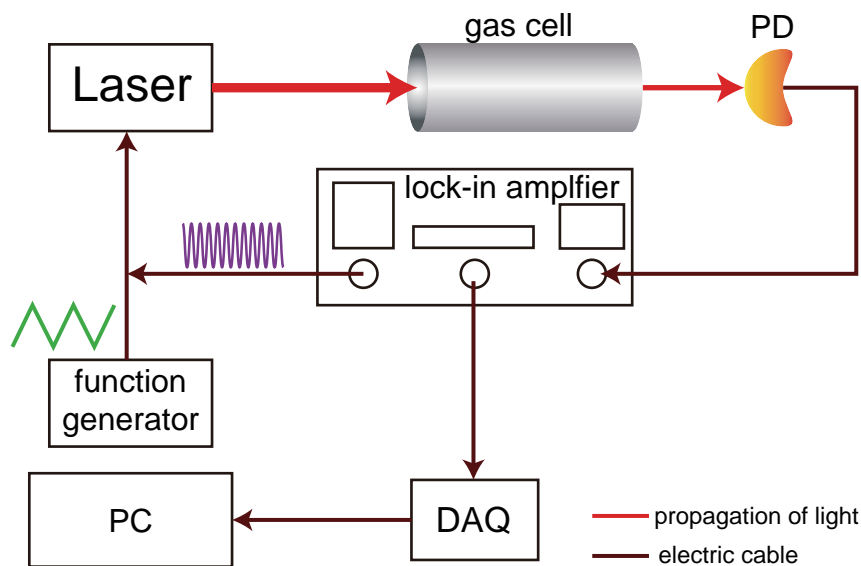


Fig. 2.11 Illustration of WMS methods. PD: photo-detector; DAQ: data-acquisition card; PC: personal computer.

WMS has been widely applied in the trace gas analysis due to its intrinsic advantages. For a practical WMS in near IR wavelength region, a distributed-feedback (DFB) laser is often used. The wavelength of DFB laser is scanned across the gas absorption line at a slow frequency in a saw-tooth (or triangular) waveform through a thermoelectric controller, while its wavelength (intensity) is simultaneously modulated sinusoidally at a fast speed through an electric current tuning, as shown

in Fig. 2.11. The modulated laser field then interacts with gas molecules and the output signals could be detected by the use of a lock-in amplifier working at high harmonics. Thus, the WMS can work at high modulation frequency, avoiding the disturbance from the lower frequency noise source, such as laser excess noise ( $1/f$  noise). Since the signal strength and waveform of WMS are directly related to the absorption strength and lineshape, the two unique characteristics of trace gas could be obtained simultaneously. The derivative relationship with gas absorption lineshape also makes the WMS capable of discriminating the absorption signals from the broadband featureless noise, such as window absorption [96–99]. Meanwhile, the broadening wings of absorption line tends to fall off much more slowly compared with the central part, resulting a smaller corresponding signals at second-harmonics ( $2f$ ) and making the WMS could be much more attractable to reduce the influence from pressure-broadening wings [83].

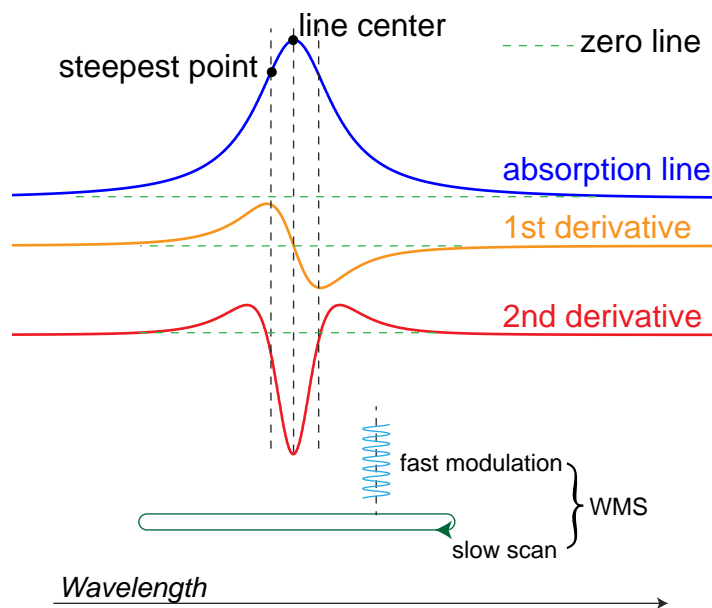


Fig. 2.12 Schematic drawing for illustrating the principles of WMS.

In a pure WMS, with a schematic drawing shown in the Figure. 2.12. where no additional intensity modulation on the laser beam, assuming a Lorentzian absorption

lineshape as:

$$\alpha(x) = \frac{CN_{tot}S_0}{\pi\gamma_L} \frac{1}{1+x_v^2} = \alpha_0 \frac{1}{1+x_v^2}. \quad (2.59)$$

where  $x_v$  is the normalized laser frequency,  $\gamma_L$  is the HWHM of Lorentzian lineshape,  $\alpha_0$  is the peak absorption coefficient. The time-dependent laser frequency could be expressed as:

$$v(t) = v + \Delta v \cos(\omega t) \quad (2.60)$$

with fast modulation frequency of  $\omega$  and maximum frequency deviated from the instant central laser frequency.  $v$  corresponds to the slow-scanning of wavelength modulation. The normalized laser frequency could be defined as:

$$x_v = (v(t) - v_0) / \gamma_L \quad (2.61)$$

$$= ((v - v_0) + \Delta v \cos(\omega t)) / \gamma_L \quad (2.62)$$

$$= \bar{x}_v + m \cos(\omega t) \quad (2.63)$$

where  $\bar{x}_v = (v - v_0) / \gamma_L$  is the instant normalized optical frequency (corresponding to the slow-scanning),  $m = \Delta v / \gamma_L$  is the modulation depth. From the theory of Arndt [100], the signals at the detector output could be decomposed into a series of Fourier series (assuming  $\alpha_0 = 1$ ):

$$S(\bar{x}_v) = \sum_{n=0}^{\infty} H_n(\bar{x}_v) \cos(n\omega t) \quad (2.64)$$

The harmonics terms is in a complex number form:

$$H_n(\bar{x}_v) = \frac{1}{2} \frac{1}{m^n} \epsilon_n i^n \frac{\{\sqrt{(1 - i\bar{x}_v)^2 + m^2} - (1 - i\bar{x}_v)\}^n}{\sqrt{(1 - i\bar{x}_v)^2 + m^2}} + c.c. \quad (2.65)$$

where  $i$  is the imaginary unit,  $n$  indicates the  $n$ -th order of harmonics,  $c.c$  means the complex conjugate parts which could be ignored in the following calculation and

$\varepsilon_0 = 1, \varepsilon_n = 2(n = 1, 2, \dots)$ . The expression is the fundamental expression for the following analysis after removing imaginary parts.

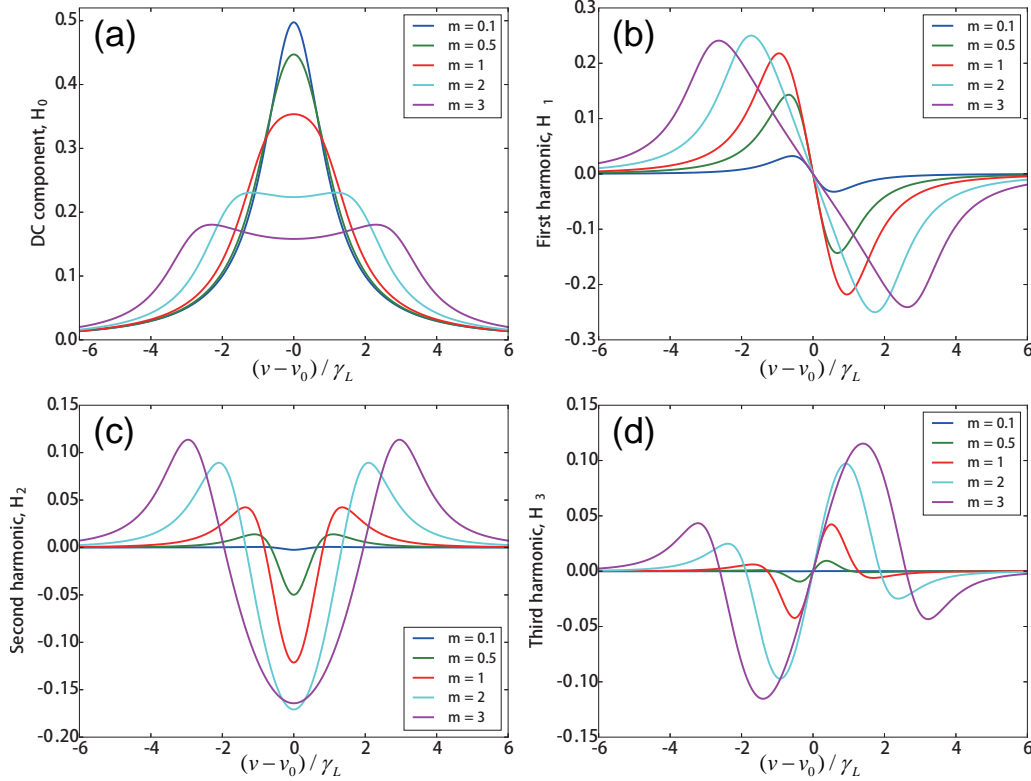


Fig. 2.13 The first four orders of harmonics with different modulation depth.

The first four orders (with  $n = 0, 1, 2, 3$ ) are plotted against the normalized frequency with different modulation depth in Fig. 2.13. It has shown that the waveforms of harmonics are broadened with the increased modulation depth. The wings of waveform tend to run away from the absorption line center while the modulation depth is increased. The odd harmonics presents a zero-value while the second harmonics appear its maximum value at the line center.

## 2.2.2 Optimized parameters for WMS

The maximum ( $H_{n,max}$ ) and amplitude ( $H_{n,ampl}$ ) could be defined as illustrated in the Fig. 2.14. From the Fig. 2.13, both the maximum and amplitude varies as  $m$  changes.

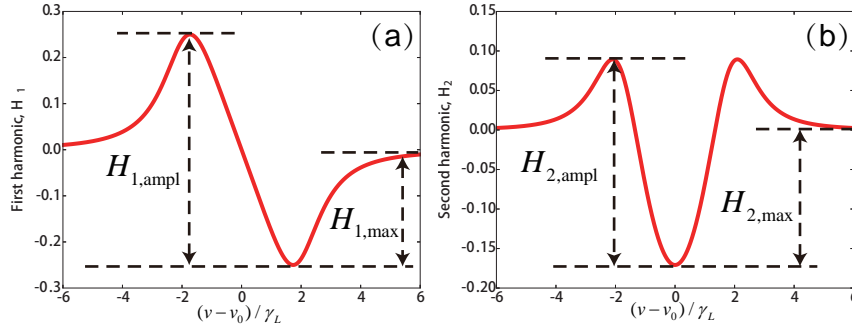


Fig. 2.14 The definition of maximum and amplitude of first and second harmonics.

The optimized modulation depth  $m$  to achieve a best harmonic signal is essential for WMS detection. The theoretical investigation reveals that the maximum value of first harmonics  $H_1$  occurs at:

$$\Delta = \pm \frac{\sqrt{3m^2 + 4} - 1}{\sqrt{3}} \quad (2.66)$$

where  $\Delta = (v - v_0)/\gamma_L$  is the deviation from the line center. The maximum value could be achieved with a dependence on the modulation depth  $m$ :

$$H_{1,max} = \frac{\sqrt{3}}{2m} \frac{\sqrt{3m^2 + 4} - 2}{\sqrt{\sqrt{3m^2 + 4} - 1}} \quad (2.67)$$

The maximum of the second harmonics occur at the line center  $\Delta = 0$  with a maximum of:

$$H_{2,max} = \frac{2}{m^2} \left( 2 - \frac{m^2 + 2}{\sqrt{m^2 + 1}} \right) \quad (2.68)$$

It has been clear from the theoretical investigations that for pure WMS, the optimized values  $m$  where the best  $H_{n,max}$  happens are 2.00, 2.20, 3.59 and 4.12 for the first four orders of harmonics. For even order of harmonics, the optimized values  $m$  where the best  $H_{n,ampl}$  happens are different from that of  $H_{n,max}$  while it remain the same for the odd order of harmonics. For 2n- and 4th-order of harmonics, the optimized of  $H_{n,ampl}$  happens at  $m = 3.09$  and  $m = 4.85$ , respectively.

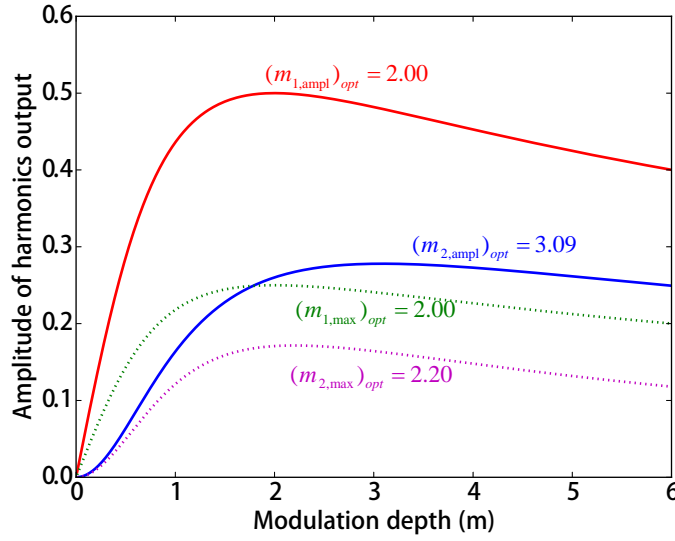


Fig. 2.15 The optimized  $m$  for the 1st- and 2n-order harmonics.

In practical application, it is not easy to achieve a pure WMS. In WMS, the modulation of wavelength would induce undesired residual intensity modulation (RIM), or sometimes referred as residual amplitude modulation (RAM), which may distort the output waveforms of WMS and deteriorate the performance of WMS. Here, the RIM or RAM is called as intensity modulation (IM), discriminating from the definition of wavelength modulation. In a detail analysis, there is a phase shift between the wavelength modulation and intensity modulation. The phase shift ( $\psi$ ) depends on the laser structure and modulation frequency, but for a DFB it typically varies from 0 at lower frequencies to  $-\pi$  at higher frequencies [98]. The theoretical analyzing of WMS combined with IM has been deduced in [95, 97, 101]. The results from Schilt [98] are much compatible with the results from Arndt [100]. The signals at different harmonics are similar to Eq. 2.65 with a coefficient difference of  $\mathfrak{R} = -I_0 * a_0 / \sqrt{\gamma_L \cdot \pi}$ , where the  $I_0$  is the optical intensity at the line center while  $a_0$  is an constant for a specific measurement defined in Eq. (A10) in Schilt's paper.

## **2.3 Summary**

This chapter gives a literature review of gas spectroscopy. The basic concepts of gas spectroscopy have been discussed, which would help us understanding the future works on the gas spectroscopy and the nature of photothermal. Furthermore, the WMS spectroscopic technique has been discussed theoretically and the optimized condition for a best signal-to-ratio has been demonstrated. Those concepts and spectroscopic techniques are basics for the further research investigations.



# Chapter 3

## Photothermal gas spectroscopy

### 3.1 Photothermal spectroscopy

#### 3.1.1 Photothermal effect

Photothermal (PT) effect is actually a result of non-radiation relaxation process involving in the population inversion, which is induced by the optical absorption [102]. In detail, optical absorption of photons in gas molecules would lead to the population inversion, resulting the molecular transition from lower state to upper state. Due to the unstable of excited state or collected virtual state, the relaxation from upper state to lower state would occur in a short time scale. Most time, in normal ambient condition, the collision and natural lifetime are the main reasons for the relaxation. Both spontaneous relaxation (radiative or fluorescence generated) and non-radiative relaxation could happen. The non-radiation process would reduce the energy of molecules in the upper state through thermal relaxation, i.e. generating heat as illustrated in Fig. 3.1. The generated heat could change the density, temperature and pressure of surrounding materials. All of those changes can finally manifest themselves as refractive index changes of sample materials.

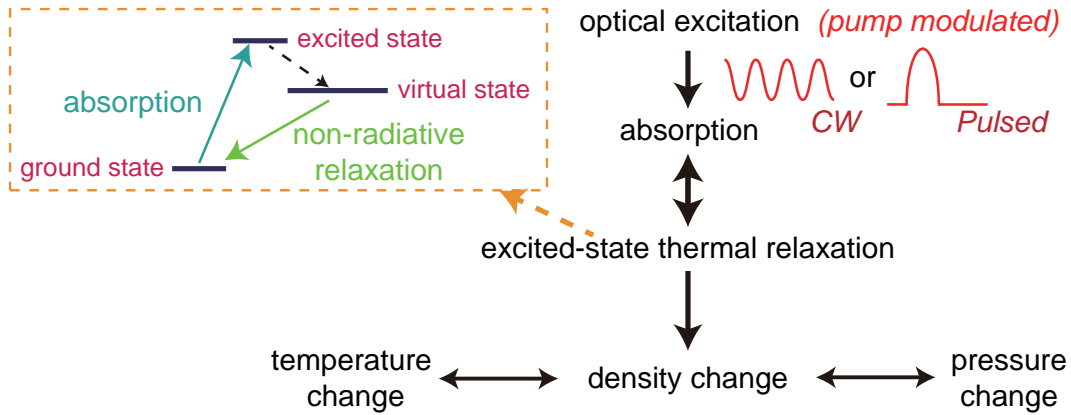


Fig. 3.1 Illustration of process involved in the photothermal spectroscopy. The upper corner shows the non-radiative relaxation process. The modulated continuous wave or a pulsed wave is usually adapted as the pump source. CW: continuous-wave.

### 3.1.2 Detection of photothermal effect

Depending on the measurand of subsequent macroscopic manifestation of PT effect, usually, there are a variety of methods [3, 102]: temperature changes (photothermal calorimetry), pressure variation and/or volume expansion (photoacoustic spectroscopy), density variation or refractive index change (photothermal lens, deflection, diffraction and interferometry). The photothermal technique has been widely applied in many different applications but here we may focus on the photothermal spectroscopy.

In a simple model to investigate the photothermal effect in the free-space optics (dimension of gas cell is much larger than the beam radius of light), the mass diffusion and heat convection are usually negligible [102]. Thus the temperature rise of absorbing gas samples could be obtained by solving the heat conduction equation as:

$$\frac{\partial T}{\partial t} - D_T \nabla^2 T = \frac{q_H}{\rho C_p} \quad (3.1)$$

where  $D_T = \kappa / \rho C_p$  (in unit of  $m^2/s$ ) is the thermal diffusivity.  $\kappa$  (in unit of  $W/(m \cdot K)$ ),  $\rho$  [ $kg/m^3$ ] is the density of medium and  $C_p$  [ $J/(kg \cdot K)$ ] is the specific heat.  $q_H$  [ $W/m^3$ ] is the heat generation source due to the optical absorption.

The photothermal lens is formed by the photothermal effect induced temperature gradient [103, 104]. A Gaussian intensity distribution (in cross-section) passes through the absorbing medium and absorption would induce the heat generation, resulting in a non-uniform temperature distribution. Due to the temperature-dependent refractive index, a photothermal lens could be formed as shown in the Fig. 3.2 [105–107]. Since the most of thermo-optic coefficient is negative (temperature rise would induced expansion of medium), the photothermal lens are usually a diverging lens with negative focal length.

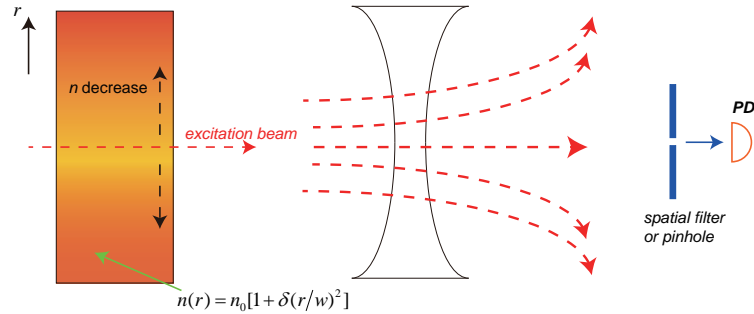


Fig. 3.2 Illustration of photothermal lens generation. The left side represents its equivalent diverging lens. PD: photo-detector.

By investigating the Eq. 3.1, it has been revealed that the quadratic terms in the expansion of refractive index  $n(r)$  will be dominant and for a thin region of sample length  $L$ , the focal length  $f_\infty$  of the equivalent lens in a steady state is determined by the radial heat conduction as:

$$f_\infty = \frac{n_0 \pi \kappa w^2}{P_0 \alpha L (dn/dT)} \quad (3.2)$$

where  $\kappa [W/(m \cdot K)]$  is the thermal conductivity,  $w$  is the beam radius (optical amplitude in Gaussian beam falls down to  $1/e$  of its maximum),  $P_0 [W]$  is the optical power of pump beam,  $\alpha [cm^{-1}]$  is the absorption coefficient of medium and  $dn/dT [K^{-1}]$  is the thermo-optic coefficient.

If the pump beam is switched on at the time  $t = 0$ , then the time-dependent focal lens would be:

$$f(t) = f_{\infty} \left[ 1 + \frac{t_c}{2t} \right] \quad (3.3)$$

where  $t_c$  is the characteristic thermal conduction time constant given by:

$$t_c = \frac{w^2}{4D_T} \quad (3.4)$$

Following the Eq. 3.2, it is obviously that measuring the focal length, either in the transient condition or in a steady state, the optical absorption coefficient  $\alpha$  then could be determined.

To improve the detection sensitivity of absorbance, a two-laser thermal lens measurement was proposed by Grabiner [108]. The system adapts a pump-probe configuration. The pump beam is chopped and passes through the absorbing medium while the probe beam is continuous laser source to travel through the same medium to measuring the laser intensity loss due to the divergence, which results from the thermal lens. However, such an arrangement of pump-probe configuration could enhance the detection sensitivity, mainly attributable to the reasons: (1) the pump laser now can directly focus on the medium which would result in a much more larger laser intensity to generate a much more steep thermal lens; (2) the use of lock-in amplifier could enable a narrow detection bandwidth which could ensure a lower detection noise. It has been exploited that the detection limits of thermal lens are as good as  $10^{-7}$  to  $10^{-8} \text{ cm}^{-1}$  for liquid and gas analysis [106] using 10 to 200 mW continuous pump source.

The photothermal deflection methods was initially applied for the surface analysis. The optical absorption of pump source heats up the liquid or gas medium above a solid surface. The heated gas or liquid serves as a prism and deflects the probe beam incident tangent to the surface. A beam position sensor is usually adapted to

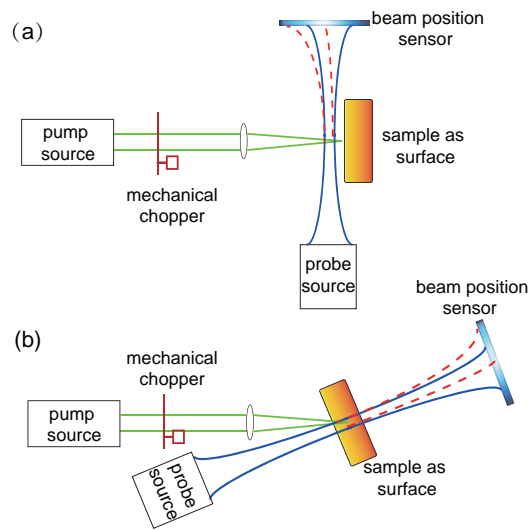


Fig. 3.3 Illustration of photothermal deflection spectroscopy: (a) transverse geometry; (b) collinear geometry.

detect the changes of probe beam. There are two types of photothermal deflection spectroscopy geometry: transverse and collinear, as illustrated in Fig. 3.3, depending on the relative position of pump and probe beam. The pump beam could be intensity-modulated by an optical chopper, enabling the use of lock-in amplifier to increase the signal-to-noise ratio. The photothermal deflection spectroscopy could present a same detection sensitivity performance as good as that of two-laser photothermal lens spectroscopy [102].

## 3.2 Photothermal interferometry

The photothermal interferometry (also called as phase-fluctuation spectroscopy, PT phase-shift spectroscopy) is an ultra-sensitive trace-gas analyzing methods [77, 109]. The optical absorption of gas molecules could result in sample heating and subsequently cause the refractive index changes of the medium. Using an optical interferometer, the refractive index changes of probe beam, which propagates through the same gas sample, could be measured and mapped to the characteristics of gas molecules. The refractive index changes of gas molecules can be related to the

temperature changes caused by the PT effect in the form of:

$$\Delta n = -(n_0 - 1) \frac{\Delta T}{T_{\text{abs}}} \quad (3.5)$$

where  $\Delta T = T - T_{\text{abs}}$  is the temperature changes compared with the ambient temperature. In fact,  $dn/dT = -(n_0 - 1)/T_{\text{abs}}$  is the thermo-optic coefficient. Thus, by calculating the PT induced temperature changes, we may be able to estimate the optical phase changes accumulated by the probe beam.

A typical PT interferometry could be illustrated as Fig. 3.4 by the use of a Mach-Zehnder interferometer (MZI) [77]. A PZT is used for the stabilization of interferometer. It has been shown that the minimum detectable gas absorption down to  $1.8 \times 10^{-9} \text{ cm}^{-1}/W$  (optical power  $W$  indicates the averaged pump power) could be achieved with an interferometer of phase sensitivity as good as  $5.3 \times 10^{-6} \text{ rad}/\sqrt{\text{Hz}}$  with an optical interferometer in free-space optics (with optical lens for optical alignment) [77]. With a much larger pump power, a detection sensitivity of  $10^{-10} \text{ cm}^{-1}$  in terms of absorption coefficient could be achieved [77].

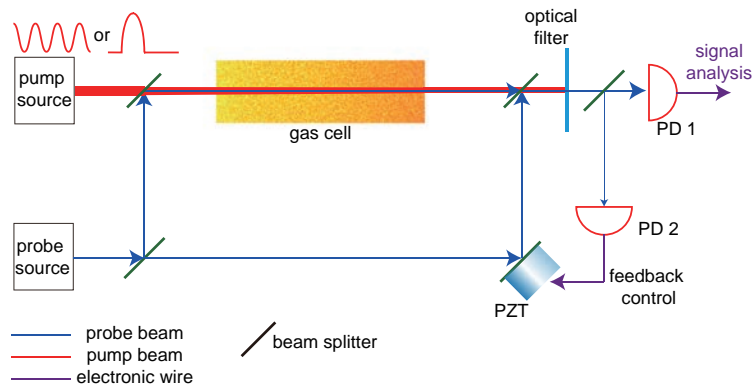


Fig. 3.4 Illustration of PT interferometry using a Mach-Zehnder interferometer. The thicknesses of the line could somehow indicate the relative strength of electric field. PZT: piezo-electric transducer.

To find the PT induced localized temperature rise, the Eq. 3.1 is usually used to solve with some general assumptions: in free-space optics, the beam radius of pump and probe source is considered as much smaller than the geometric dimension

of gas cell, thus the Eq. 3.1 could be considered with a infinite boundary condition. On the trace-gas analysis, the weak-absorption assumption is of the interest and thus the temperature remain invariant along the directions of beam propagation. Furthermore, due the small temperature rise and infinite boundary constraints, the temperature far away from the central axis could be considered as constant as the ambient temperature  $T_{abs} = 293.15K$ .

At the beginning of following sections, the principles of optical interferometry will be presented. In fact, the optical interferometry in free-space optics shares the same basic principles with fibre-optic interferometry. However, since our work focuses on the fibre-optic sensors, we will only give a literature review on the fibre-optic interferometry. It can be a useful reference for the work in construction of optical interferometer in free-space optics. Thereafter, the literature review and summary of general solutions for different types  $q_H$  of pump beam in free-space optics are discussed. The numerical analysis based on the analytic or semi-analytic solutions discussed here would be investigated at the final section.

### 3.2.1 Fibre-optic interferometry

Optical interferometry is basically based on the interference between optical waves and is a powerful technique for the detection of small phase shift. The detected phase shift can be a result of various external disturbances, e.g. temperature, strain, stress and pressure, on the light path. Thus the optical interferometry can be a highly sensitive optical sensing system for different types of physical parameters. Optical fibre can serve as not only the transmission cables but also sensing elements. With additional advantages, such as compactness, low-cost and EMI, the fibre-optic sensors have been widely developed and applied in a broad sense [15, 110].

In a common sense, there a two basic types of fibre-optic sensors based on the usage of optical fibre: the intensity and phase detection type. For the intensity type,

the optical power attenuation is measured while in the phase type the optical phase changes is much more concerned. For an intensity-detection type, the fibre only serves as a light waveguide while the fibre also serves as a intimate sensing element in the phase-detection type. The optical phase detection could be used to detect very small external perturbation (pressure, strain, acoustic wave, temperature wave) imposed on the propagation path of light beam [15, 16, 18–20, 111–114].

Usually, a fibre-optic interferometer is a technique in which the interference of electro-magnetic wave occurs and is often used to detect the extreme small accumulated differential optical phase shifts caused by the measurand. The typical interferometry includes Mach-Zehnder, Michelson, *Fabry – Pérot* and Sagnac interferometer.

### Principles of interferometer

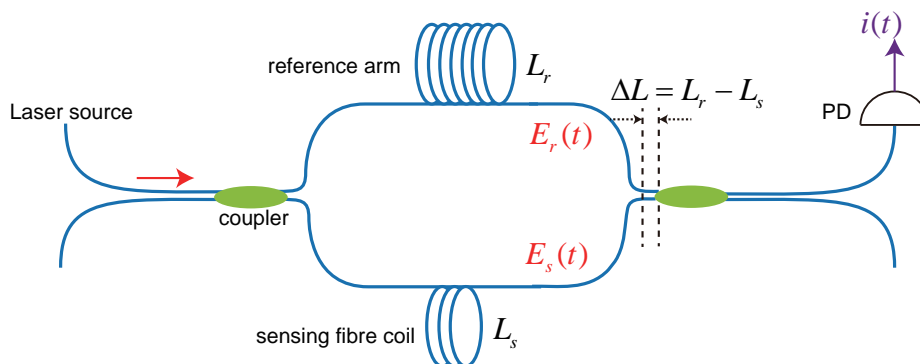


Fig. 3.5 Illustration of Mach-Zehnder interferometer.

Both of the Mach-Zehnder and Michelson interferometer are results of two-beam interference formed by a dual-path way. A typical Mach-Zehnder interferometer (MZI) is illustrated in Fig. 3.5. A highly coherent laser source is launched and divided into two beams through an fibre-optic coupler. The two beams passes through the sensing and reference arms, respectively. Then the beams would re-combine at another fibre-optic coupler and interfere with each other at a photo-detector, which would generate the output signals [115]. The optical phase delay could be defined in

the form of:

$$\phi = n_0 k L = \beta L \quad (3.6)$$

where  $n_0$  is the refractive index of optical fibre,  $k = 2\pi/\lambda$  is the angular wavenumber of light in vacuum,  $\beta = n_0 k$  is the propagation constant in the optical fibre,  $\lambda$  is the wavelength of light and  $L$  is the physical length of fibre. In fact,  $nL$  is also called as the optical path length. It could be found that any change(s) of  $n$ ,  $k$ ,  $L$  would lead to a phase shift, i.e. the change of  $\phi$ . Typically the external disturbance would induce a variations of  $n$  and  $L$  while  $k$  is often related to the laser frequency jitters or optical dispersion. The electrical field in the sensing arm could be expressed in the form of:

$$E_s(t) = E_A e^{i(\Omega_0 t + \phi_A + \Delta\phi(t))} \quad (3.7)$$

where  $E_A$  is the electrical strength in the sensing arm,  $\Omega_0$  is the angular frequency of optical wave,  $\phi_A$  is the initial phase or static phase factor of sensing arm and  $\Delta\phi(t)$  is an induced phase shift or change, corresponding to the measurand. For a similar definition, the electrical field in the reference arm could be:

$$E_r(t) = E_B e^{i(\Omega_0 t + \phi_B)} \quad (3.8)$$

If the photo-detector is a squared-lay detector, the output of the detector is the interference of signal (the interference of electrical wave could only occur on the photo-detector, not at the fibre-optic coupler or within optical fibre in our system [116]):

$$i_1(t) = \Gamma R \zeta \alpha_c \langle E_s(t) E_r(t) \rangle \quad (3.9)$$

where  $\langle \rangle$  is the time-averaging product with the definition of:

$$\langle E_s(t) E_r(t) \rangle = \frac{1}{2} \text{Re}[E_s^* E_r] \quad (3.10)$$

$\Gamma$  is the degree of coherent between the two waves,  $\zeta$  is the polarization-related factors, and the absolute value of the both two parameters are in the range of  $[0, 1]$ . Only the physical length difference between the two arms of MZI is much smaller than the coherent length of laser source could lead to  $|\Gamma| = 1$  and the identical linear polarization state could lead to  $\zeta = 1$ .  $R[A/W]$  is the responsivity of photo-detector, usually in the value range of  $[0.6, 1]$ . The  $\alpha_c$  is the power loss coefficient that the coupling from two arms to the photo-detector happens. Here we consider complete interference and lossless systems with unit responsivity of photo-detector, resulting in:

$$i_1(t) = \langle E_s(t)E_r(t) \rangle \quad (3.11)$$

$$\propto [E_s(t) + E_r(t)]^*[E_s(t) + E_r(t)] \quad (3.12)$$

$$= |E_A|^2 + |E_B|^2 + E_A E_B e^{-i(\Omega_0 t + \phi_A + \Delta\phi(t))} e^{i(\Omega_0 t + \phi_B)} \quad (3.13)$$

$$+ E_A E_B e^{i(\Omega_0 t + \phi_A + \Delta\phi(t))} e^{-i(\Omega_0 t + \phi_B)} \quad (3.14)$$

$$\rightarrow |E_A|^2 + |E_B|^2 + 2E_A E_B \cos[(\phi_A - \phi_B) + \Delta\phi(t)] \quad (3.15)$$

$$\rightarrow I_A + I_B + 2\sqrt{I_A I_B} \cos[(\phi_A - \phi_B) + \Delta\phi(t)] \quad (3.16)$$

The Eq. 3.16 indicates the final output signal from the photo-detector in the form of light intensity  $I_{A,B}$  with a relationship between light intensity and electric field strength as  $I = c\epsilon_0 n_0 |E|^2 / 2$  ( $\epsilon_0$  is the vacuum permittivity and  $c$  is the light speed in vacuum). It includes a DC term and an AC terms. The AC term is related to the time-dependent phase shift  $\Delta\phi(t)$ . If assuming a sinusoidal phase shift  $\Delta\phi(t) = m \sin(\omega_m t)$  and also  $\phi_d = \phi_A - \phi_B$ , the AC term of interferometric output signals has the form of:

$$i_{ac} = i_0 \cos[\phi_d + m \sin(\omega_m t)] \quad (3.17)$$

The signals could be expanded in the Bessel function as:

$$i_{ac} = i_0 \{ \cos(\phi_d) [J_0(m) + 2 \sum_{n=1}^{\infty} J_{2n}(m) \cos(2n\omega_m t)] \} \quad (3.18)$$

$$+ \sin(\phi_d) [2 \sum_{n=0}^{\infty} J_{2n+1}(m) \sin((2n+1)\omega_m t)] \} \quad (3.19)$$

where  $J_n(m)$  is the Bessel function of order  $n$  with argument of  $m$ . Through this way, the phase shift could be converted into an intensity output of the interferometer from the photo-detector.

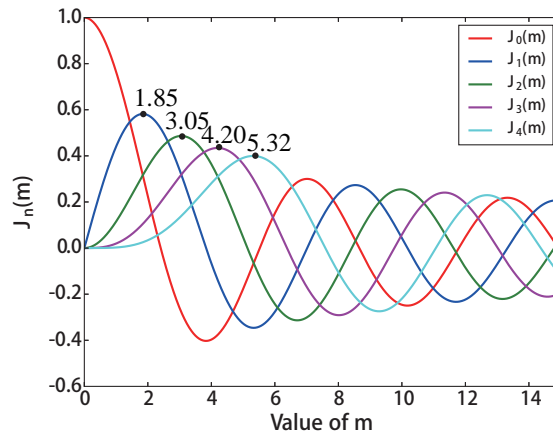


Fig. 3.6 The first kind Bessel function against the modulation depth  $m$ . The number on the line indicates the value of  $m$  where the first maximum of Bessel function could be achieved.

It is clear that the amplitude  $m$  of phase shift ( $m$  can be considered as modulation depth) is always of main interest. The output of  $m$  is first of all determined by the Bessel function  $J_n(m)$ . As shown in the Fig. 3.6, the Bessel function is usually periodic as  $m$  changes. However, it could still be able to achieve a linear conversion with the condition that  $|m| \ll 1$  and the value of Bessel function could be  $J_0(m) \sim 1$ ,  $J_1(m) = m/2$  and so does higher orders in a similar linear relationship to  $m$ . On the other hand, there are periodic local maximum for  $J_n(m)$  which may be helpful to calibrate the phase shifter. The visibility of interferometric output could be defined

as:

$$V = \frac{I_{max} + I_{min}}{I_{max} - I_{min}} \quad (3.20)$$

$$= \frac{2\sqrt{I_A I_B}}{I_A + I_B} \quad (3.21)$$

Thus the output of interferometer could be expressed in a simple form as  $i_v = 1 + V \cos[(\phi_A - \phi_B) + \Delta\phi(t)]$ .

To achieve linear and maximum conversion of phase signal  $\Delta\phi(t)$  to output intensity signal  $i$ , the DC phase shift  $\phi_d$  is of considerable importance. As illustrated in the Fig. 3.7, if  $\phi_d = (2N + 1)\pi/2$ ,  $N = 0, 1, 2, \dots$ , then the output signal could be maximized while if  $\phi_d = N\pi$ ,  $N = 0, 1, 2, \dots$ , then the output signal would vanishes. The working points of interferometer at  $\phi_d = (2N + 1)\pi/2$  are also called as the quadrature points. However, all the conditions follow the basics that  $|m| \ll 1$ , or we say working at the linear principle. Strictly speaking, the 1% dynamic range of an interferometer could be achieved as long as  $|m| \leq 0.1\pi$ . For  $|m| > 0.1$ , significant distortion of interferometric signal compared with the input phase signal would happen as shown in the bottom of Fig. 3.7.

All the two-beams interferometer, including Michelson, Sagnac and low-finesses *Fabry – Pérot* interferometer, follows the similar principles discussed above. The process of retrieving input phase signals, both amplitude  $m$  and input frequency  $\omega_m$ , is usually called a demodulation process of interferometer. On the other hand, it is a common way to manifest external disturbance as strain applied on the optical fibre. Ignoring the radial stress applied on the optical fibre, the elasto-optical coefficient could be defined as [16, 117]:

$$\xi = 1 - \frac{1}{2}n^2 p_{12} \quad (3.22)$$

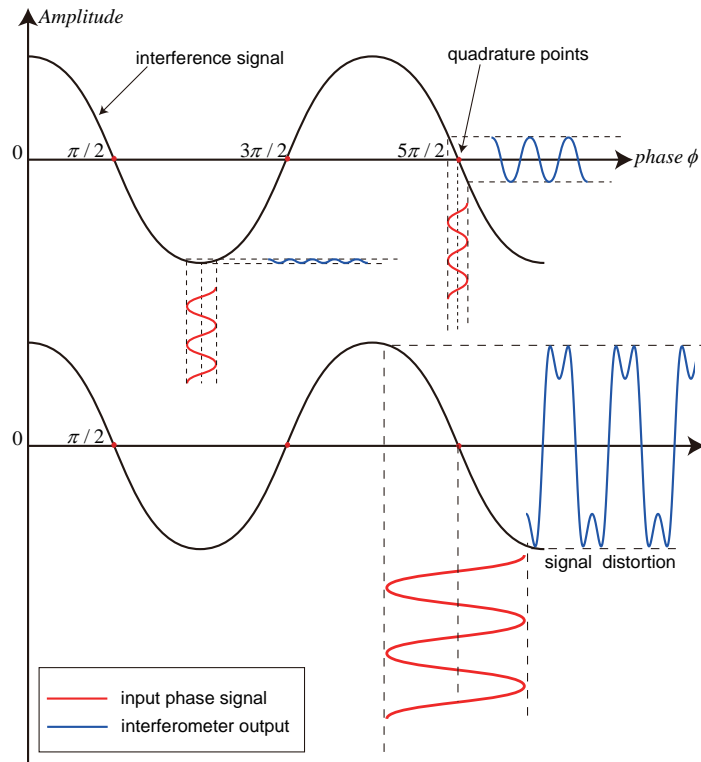


Fig. 3.7 The illustration of interferometric output amplitude as a function of phase signal.

where  $p_{12}$  is the strain-optic coefficient (for silica  $p_{12} = 0.27$  [16]). The strain is the ratio between the deformation to the initial dimension of optical fibre, or  $\varepsilon = \Delta L/L$ .

Then it follows:

$$\frac{d\phi}{\phi} = \xi \varepsilon \quad (3.23)$$

$$d\phi = \frac{2\pi n L \xi \varepsilon}{\lambda} \quad (3.24)$$

### Stabilization of inteferometers

In a practical system, due to the undesired environmental phase perturbations (temperature drift, polarization fading and mechanical perturbation), the bias phase  $\phi_d$  terms in Eq. 3.17 is not stable and the fluctuations may cause the measuring errors while meanwhile deviates from the quadrature points. There are a variety of techniques

to demodulate the phase signal  $\Delta\phi(t)$  with relatively low errors and they may be categorized as active and passive demodulation methods [117–119].

### Part I: Active homodyne stabilization

Active stabilization is one of most generally used, easy to operate scheme in the fibre-optic interferometry. It enables the two interfering beams passing through the different optical paths keeping at a constant phase bias, minimizing the phase drifts which may degraded the performance of the interferometry as discussed above. The active stabilization is usually based on a negative feedback servo-loop control, where the phase drifts from the pre-set desired value could be converted into an error signal and then sent back to the mother-system, usually via a optical fibre-wounded piezoelectric transducer (PZT), to compensate the variations of phase, as illustrated in Fig. 3.8. To achieve a maximizing and linear conversion from the phase signal to intensity signal of interferometric output, it is common locking the phase bias of interferometer at the quadrature points  $\phi_d = (2N + 1)\pi/2$ ,  $N = 0, 1, 2, \dots$  [120–126].

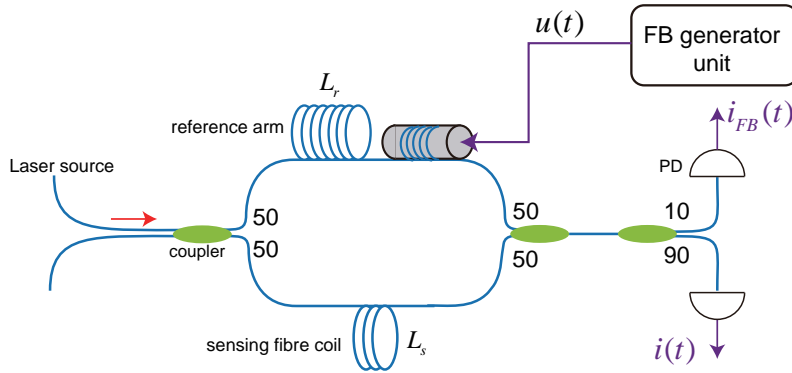


Fig. 3.8 Illustration of active homodyne stabilization of MZI. The number on the coupler indicates the power coupling coefficients. FB: feedback.

Considering the output interferometric output signals as:

$$P = P_1 + P_2 + 2\sqrt{P_1 P_2} \cos[\phi_d + \phi_n + \Delta\phi - \phi_c] \quad (3.25)$$

where  $\phi_d$  is the desired phase bias, usually in the quadratic working points.  $\phi_n$  is a slow varying components which is the results of picking up external perturbation,

like temperature.  $\Delta\phi$  is the desired phase signals.  $\phi_c$  is the feedback compensation signals generated by a PZT. Near the quadrature points, the AC terms becomes proportional to the phase signals (without the existence of phase signals, which could be achieved by passing output signals into a low-pass filter):

$$V_{ac} = V_0(\phi_d + \phi_n - \phi_c) \quad (3.26)$$

$$= V_0(\phi_\varepsilon - \phi_c) \quad (3.27)$$

where  $V_{ac}$  and  $V_0$  has been translated into voltage signals proportional to the optical power. Ideally, in quadrature, it has to be  $V_{ac} = 0$  where phase drifts  $\varepsilon$  could be cancelled out by the compensation signal  $\phi_c$ . The output of  $V_{ac}$  could be obtained from the data-acquisition card (DAQ) and then sent feedback to a analog control, generating a voltage signal to drive PZT unit. The phase  $\phi_c$  generated by the PZT could be made exactly to cancel  $\phi_\varepsilon$ . At last, the error signals  $V_{ac}$  could be locked at zero. Such a feedback signal is the integral of  $V_{ac}$  as:

$$V_{fed} = g \int_0^{\tau_{int}} V_{ac}(t') dt' \quad (3.28)$$

where  $\tau_{int}$  is the integration time. The differential equation for the signal  $V_{fed}$  is in the form of:

$$\frac{dV_{fed}}{dt} + g_0 R_v V_0 V_{fed} = g_0 V_0 \phi_\varepsilon \quad (3.29)$$

where  $R_v [rad/Volts]$  is the volts to radians constant of PZT and  $g_0$  is the gain factor of feedback loop. The parameter  $g_0 R_v V_0$  is the gain bandwidth product of the feedback circuit.

This approach is often referred as a PI (proportional-integral) control process with  $\phi_\varepsilon = \phi_c$  serves as a output control signals and  $V_{ac}$  (deviates from the zero value) serves as the error signals. One of the major disadvantages is that the output voltages of a practical system is limited and if the upper limited of voltages is approached,

the feedback system has to be reset. Such a reset would result in an glitch of output signals [15].

There is an alternative approach using PID (proportional-integral-derivative) control [125], which has been adapted in the first demonstration of PT gas spectroscopy with HC-PBFs [70]. The general idea is similar to that of a PI control, but incorporating a derivative term, which predicts the behavior of the system and improves the time setting and stability. If the output error signals is  $P_x$  while the ideal output signals is  $P$ , corresponding to the output visibility  $V_x$  and  $V$ , respectively. The error signals could be defined in a dimensionless way:

$$e_0(t) = (I_x - I)/V = (V_x - V)/V = V_x/V - 1 \quad (3.30)$$

By passing through a low pass filter to discriminate the error signal from the phase signal while extracting the single tone of a specific frequency  $\nu_{osc}$ . Typically, the low-frequency drift noise spectrum of fibre-optic interferometer exhibits bandwidth of  $\sim 300Hz$ . The choice of  $\nu_{osc} = 200Hz$  may be sufficient. Combining the error signal and single tone, the signals over a period of  $\nu_{osc}$  could be obtained in the form  $e(t) = e_0(t)\cos(\nu_{osc}t)$ , which would be fed as the error signals of the PID control. The output of control signals applying PZT to generate a  $\phi_c$  compensation terms may be in the form of:

$$u(t) = K_p e(t) + K_i \int_t^{t+T} e(t') dt' + K_d \frac{de(t)}{dt} \quad (3.31)$$

where  $K_p, K_i$  and  $K_d$  are the proportional, integral and derivative gain, respectively. The whole process of feedback servo loop control could be achieved by using LabView analog circuit. This method provides a phase stability better than  $0.1^\circ$  and bandwidth of  $3kHz$ .

The active tracking and stabilization has a good noise performance since the most of electronic noise are typically in the level of  $0.1 - 1\mu rad$ , corresponding to

the phase changes of  $\sim 10^{-7}$  of an optical wavelength or the equivalent physical fibre length change of  $\Delta L \sim 10^{-13}m$  with  $\lambda \sim 1\mu m$  [119].

### **Part II: Passive stabilization**

Even though it is much easier to stabilize the interferometer using an active control with a high performance, but it is rarely used in an real industrial systems. The first reason is that the limited dynamic range of feedback elements make it must suffer from the resetting problem, which may occur many times a second in real application while only a few time per day in lab. Another major limit is that such a system is very difficult to interrogate a multiplexing system which contains more than one sensing arrays. The passive scheme could approach high phase detection sensitivity with all-fibre (no electronic circuit) and no-requirement of servo control. The stabilization of the system could be achieved passively by elegant design or modulation of the system. The electro-optic modulation methods, using the output of interferometer and algorithms to achieved desired phase, including the phase-generated carrier (PGC) homodyne [127], PGC synthetic heterodyne [128, 129], and differential delay heterodyne [130]. The all-fibre optical approaches includes a  $3 \times 3$  loop coupler [131–134], polarization discrimination [135], frequency-shifter Sagnac loop [136, 137], phase-bias modulation Sagnac scheme [138]. Here, the  $3 \times 3$  Sagnac phase demodulation system would be used in our future works and would be introduced in a detail way. The choice of using  $3 \times 3$  coupler is that it is electronic elements free and easy-to-operate without any servo-control.

A typical  $3 \times 3$  Sagnac loop could be illustrated as the Fig. 3.9. A light source (usually a broadband source to reduce the backscattering/reflection phase noise) is launched into the fibre loop through a  $3 \times 3$  coupler and divided into two beams as clock-wise (CW) and counter-clock-wise (CCW). Due to the fibre delay line, the time that CW and CCW beams reaches the sensing part is different and considering the time-varying modulated phase signals at the sensing part, at a specific time  $t$ , there

would be a phase modulation difference between the CW and CCW experiencing at the sensing part.

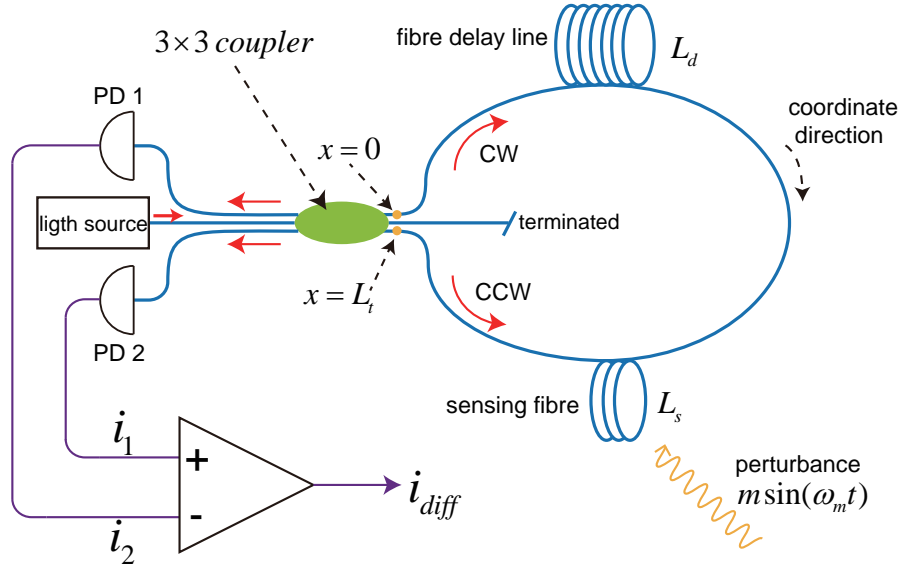


Fig. 3.9 Illustration of  $3 \times 3$  Sagnac interferometer.

The instantaneous phase of the CW and CCW beam could be obtain through the integrations [80]:

$$\phi_{CW} = \int_0^{L_t} \beta \left[ x, t - (L_t - x) \frac{n_0}{c} \right] dx, \quad (3.32)$$

$$\phi_{CCW} = \int_0^{L_t} \beta \left( x, t - \frac{xn_0}{c} \right) dx \quad (3.33)$$

where  $\beta$  is the propagation constant and  $x$  is the coordinates along the fibre in a clock-wise way.  $L_t$  is the total length of the fibre loop,  $c$  is the light speed in vacuum and  $n$  is the refractive index of fibre. Assuming a sinusoidal phase modulation, then the phase signal could be expressed as:

$$\beta(x, t) = \beta_0 + \delta\beta \sin(\omega_m t) \quad (3.34)$$

where  $\omega_m$  is the phase modulation frequency and  $\delta\beta$  is the modulation constant. In real deduce, the phase modulation could be expressed in the form of phase

modulation instead of  $\beta$  modulation. They have a relationship of  $\Delta\phi(x, t) = \beta(x, t) \times L_s$ , where  $L_s$  is the physical fibre length of sensing part.

Through the integration, the phase difference between the CW and CCW beams could be:

$$\Delta\phi(t) = \phi_{CW} - \phi_{CCW} \quad (3.35)$$

$$= \delta\phi \cos\left[\omega_m\left(t - \frac{L_t n}{2c}\right)\right] \quad (3.36)$$

with:

$$\delta\phi = \delta\beta \frac{2c}{\omega_m n} \left\{ \cos\left[\frac{\omega_m n}{2c}(L_t - 2L_s)\right] - \cos\left(\frac{\omega_m n}{2c}L_t\right) \right\} \quad (3.37)$$

$$= \delta\beta \frac{2c}{\omega_m n} \sin\left[\frac{\omega_m n(L_t - L_s)}{2c}\right] \sin\left[\frac{\omega_m n}{2c}L_s\right] \quad (3.38)$$

$$= \delta\beta L_s \sin\left[\frac{\omega_m n(L_t - L_s)}{2c}\right] \quad (3.39)$$

$$= 2\delta\phi_0 \sin\left(\omega_m \frac{\tau_d}{2}\right) \quad (3.40)$$

where  $\delta\phi_0 = \delta\beta L_s$  is the amplitude of phase modulation signal and  $\tau_d = n(L_t - L_s)/c$  is the delay time due to the fibre delay line with length approximately  $L_d = L_t - L_s$ . There is a weak modulation assumption with  $\sin(s) \sim s$  if  $s \ll 1$ . The modulation depth is now could still be held as  $m = \delta\phi$ . The modulation phase signals thus could be expressed in a simple but not loss of meaning form as  $\Delta\phi(t) = m\cos(\omega_m t)$ .

For a practical  $3 \times 3$  with loss and asymmetry, the output current signals at the port of 1 and 3 could be:

$$i_1 = R(P_0 + \Delta P) \{1 + \cos[\Delta\phi(t) - 120^\circ + \phi_{\Delta'}]\} \quad (3.41)$$

$$i_2 = RP_0 \{1 + \cos[\Delta\phi(t) + 120^\circ]\} \quad (3.42)$$

where  $\Delta P$  and  $\phi_{\Delta'}$  is the averaging power difference and phase asymmetric factor between the two output ports, respectively. Using a balanced detection, the subtraction

of the two output signals could lead to a differential output signals as:

$$i_{\text{diff}} = R\Delta P \quad (3.43)$$

$$+\Delta P\{1 + \cos[\Delta\phi(t) - 120^\circ + \epsilon_0]\} \quad (3.44)$$

$$+2RP_0\sin[\Delta\phi(t) + \phi_{\Delta'}]\sin(\phi_{\Delta'} + 120^\circ) \quad (3.45)$$

where  $\phi_{\Delta} = 2\phi_{\Delta'}$ . In most practical cases  $\phi_{\Delta} \ll 120^\circ$  and  $\Delta P/P_0 < 0.1$ , thus for a small phase modulation, the first and second term of the right hand side serves as a low noise source, which we may ignore in the following discussion. The expression now could be simplified as:

$$i_{\text{diff}} = 2RP_0\sin(120^\circ)\sin[\Delta\phi(t) + \phi_{\Delta}] \quad (3.46)$$

$$= \sqrt{3}RP_0\sin[m\cos(\omega_m t) + \phi_{\Delta}] \quad (3.47)$$

$$= \sqrt{3}RP_0\{\sin(\phi_{\Delta})[J_0(m) + 2\sum_{n=1}^{\infty}(-1)^n J_{2n}(m)\cos(2n\omega_m)] \quad (3.48)$$

$$-\cos(\phi_{\Delta}) \cdot 2\sum_{n=0}^{\infty}(-1)^n J_{2n+1}(m)\cos[(2n+1)\omega_m]\} \quad (3.49)$$

As described above, it works in a similar way as that of MZI. However, as observed in the equation, the phase modulation depth  $m$  (i.e.  $\delta\phi = 2\delta\phi_0\sin(\omega_m \frac{\tau_d}{2})$ ) is finally related to the fibre delay time  $\tau_d$ . To optimized the phase detection sensitivity, the detected modulation frequency  $\omega_m$  of phase modulation should meet the requirement that:

$$\omega_m \frac{\tau_d}{2} = (2N+1)\frac{\pi}{2}, N = 0, 1, 2, \dots \quad (3.50)$$

It makes that  $\sin(\omega_m \frac{\tau_d}{2}) = 1$ . Such frequencies of  $\omega_m$  is the proper frequencies of Sagnac interferometer. For a fibre delay length of  $2\text{km}$  or delay time of  $10\mu\text{s}$ , the first proper frequency is  $\sim 50\text{kHz}$  for the first harmonic detection.

The use of  $3 \times 3$  loop coupler in Sagnac interferometer could achieve near shot-noise limit. The best reported minimum detectable phase is  $2.5 \times 10^{-7}\text{rad}/\sqrt{\text{Hz}}$ ,

which is near the shot-noise limit, with a multi-mode (transverse mode) laser diode [ref]. One of the advantages using Sagnac interferometer is that it is capable of remote and multiplexing networking while with a high sensitivity, as reported in [139].

### Noise properties

In a practical system, the noise sources that dominate over all noise could varies and require experimental-based investigations. However, there are several noises source that could set a lower bound of phase detection.

#### Part I: Shot noise

Shot noise is a quantum limit noise, arising from the random probably occurrence of photon absorption event in a photo-detector and characterizing as the discreteness of photons and electrons. The shot noise is not the noise of a laser intensity itself but related to the input laser field on the photo-detector. The shot noise could be simply expressed in the form of electric current as [116]:

$$\langle i_{\text{shot}} \rangle = \sqrt{eRP_0B} \quad (3.51)$$

with input optical power of  $P_0$ , bandwidth  $B$  of photo-detector and responsivity  $R$  of photo-detector. The coefficient  $e$  is the elementary charge. As indicated, the shot noise has a root-square relationship with the optical power.

#### Part II: Thermal noise of resistor

The thermal noise, or Johnson-Nyquist noise, is the noise due to the voltages applied on the load resistor. It could be a basic noise limit of any electronic circuit as a form of [116]:

$$\langle i_T \rangle = \sqrt{\frac{4k_BTB}{R_T}} \quad (3.52)$$

where  $k_B$  is the Boltzmann's constant,  $T$  [in K] is the absolute temperature and  $R_T$  is the load resistance. The thermal noise of resistor is also not related to the light field itself.

### Part III: Laser noise

The laser noise (excess noise from laser source) could be classified as intensity and frequency noise. The laser intensity noise is the results of the amplitude fluctuations of a laser source. If considering the output of laser power as [116]:

$$P(t) = P_0 + \Delta P(t) \quad (3.53)$$

where  $P_0$  is the time-averaging power and  $\Delta P(t)$  is the instantaneous variation of optical power. The mean squared deviation of the optical power fluctuations could be characterized as:

$$\overline{(P(t) - P_0)^2} = \overline{(\Delta P(t))^2} = \int_0^\infty S_{\Delta P}(f) df \quad (3.54)$$

where  $S_{\Delta P}(f)$  is a form of spectral density function  $S_{\Delta P}(\omega)$ :

$$S_{\Delta P}(f) = 2\pi S_{\Delta P}(\omega), (\omega = 2\pi f) \quad (3.55)$$

considering the responsivity of photo-detector as  $R$ , the output current of the detector is  $i(t) = RP(t)$ . Thus the current fluctuations of detector output could be:

$$\langle i_P \rangle = R \sqrt{S_{\Delta P}(f) B} \quad (3.56)$$

with  $B$  is the detection bandwidth of detector. The relative intensity noise (RIN) is defined as a unit bandwidth of:

$$\text{RIN} = \frac{S_{\Delta P}(f)(B = 1\text{Hz})}{P_0^2}. \quad (3.57)$$

For a single mode semiconductor laser, the RIN could be in a level of  $10^{-16}$  (or -160 dB). The responsivity of a detector could be:

$$R = \frac{e\eta}{h\nu} \quad (3.58)$$

where  $\nu = c/\lambda$  is the laser frequency,  $h$  is Planck constant and  $\eta$  is the quantum efficiency (electrons generated by a single photon). Then for a photo-detector with detection bandwidth of  $B = 10^9 \text{ Hz}$ , input power  $P_0 = 3 \text{ mW}$ ,  $\text{RIN} = 10^{-16} \text{ Hz}^{-1}$ ,  $\lambda = 1.3 \mu\text{m}$  and quantum efficiency of  $\eta$ , the fluctuations due to the laser intensity noise is  $\langle i_p \rangle = 5.95 \times 10^{-7} \text{ A}$ .

Furthermore, by using a balanced detection methods, the laser intensity noise could be greatly reduced [140, 141].

Laser frequency noise is a result of laser frequency drift. The laser frequency noise could be translated into an intensity noise of interferometric output through unbalanced path of two arms of an interferometer and thus it is directly proportional to the optical path difference of the interferometer arms. There are two main ways to reduce the laser frequency noise: balancing the optical path of arms and enhancing the frequency stability of laser source. Since the complete balanced optical path is not practical to achieve, using a feedback control to minimize the laser frequency fluctuation is a not bad choice [16]. On the other hand, using a common path interferometer (e.g. Sagnac interferometer) could largely balance the optical paths of two beam and thus it could be a choice.

#### **Part IV: Polarization fading**

The interference between the light beams should meet the same polarization requirement to achieve the best visibility. However, since the unavoidable asymmetric physical dimension and also the external perturbation, the state of polarization (SOP) of a light beam travelling along the fibre could vary from time to time and resulting a mismatch of SOP between the interfered beams, which results in reduced visibility,

or called as polarization fading. The polarization fading phenomena is a common problem for all fibre-optic interferometers and could be reduced by several methods, like using polarization discrimination scheme [135, 139], using depolarized light source [142, 143].

### 3.2.2 PTI with open-path gas cells

The PTI sensors have been primarily proposed and demonstrated with optical interferometer in free-space optics [144]. There have been many published literature with derived results to explain and calculate the magnitude of PT phase modulation (or the PT induced temperature changes). Here we give a summary of the most of works that have been done to calculate or estimate the magnitude of temperature changes resulting from PT effect. This part is expected to provide a unified or generalized results for the estimation of PT phase modulation. The numerical results are also presented to discuss some key parameters that may affect the efficiency of PT effect, that will be crucial for the reasons of choosing HC-PBFs as our gas cells.

#### Part I: Analytical and semi-analytical results with different pump source

##### Pulsed pump beam

The pulsed pump beam could be expressed in the form of:

$$Q(r,t) = \frac{2\alpha E_0}{\pi w^2 t_0} e^{-2r^2/w^2}, 0 \leq t \leq t_0 \quad (3.59)$$

$$= 0, t > t_0 \quad (3.60)$$

where  $E_0 [J]$  is the pulse energy,  $t_0$  is the pulse width. The peak light intensity could be in the form of  $I_0 = \frac{2P_0}{\pi w^2}$  with peak pump power  $P_0 = E_0/t_0$ .

Carslaw and Jaeger [145] have gave the Green's function for the Eq. 3.1, yielding a temperature rise at radius  $r$  and time  $t$  for a unit line heat source at  $r'$  and time zero

in an infinite medium:

$$G(r', r, t - t'') = \frac{1}{4\pi\kappa(t - t'')} \exp\left[\frac{-(r^2 + r'^2)}{4D_T(t - t'')}\right] \times I_0\left[\frac{rr'}{2D_T(t - t'')}\right] \quad (3.61)$$

where  $I_0(x)$  is the modified Bessel function of first kind and zero order,  $D_T$  is the thermal diffusivity.

Thus the temperature rise due to the heat source  $q_H = Q(r, t)$  could be found through the integral:

$$T(r, t) = \int_0^t dt'' \int_0^\infty 2\pi r' dr' Q(r', t'') G(r', r, t - t'') \quad (3.62)$$

In fact, this integral form could be used to solve all types of pump source, including pulsed, CW (continuous-wave) with or without modulation. But generally, it would be cumbersome to do such an integral.

It can be obtained the results for pulse source as:

$$\Delta T(r, t) = \frac{\alpha E_0}{\pi\kappa t_0 2r} \{Ei(-2r^2/w^2) - Ei[-2r^2/(w^2 + 8D_T t)]\}, 0 \leq t \leq t_0 \quad (3.63)$$

$$\Delta T(r, t) = \frac{\alpha E_0}{\pi\kappa t_0 2r} (Ei\{-2r^2/[w^2 + 8D_T(t - t_0)]\} - Ei[-2r^2/(w^2 + 8D_T t)]), t > t_0 \quad (3.64)$$

where  $Ei(z)$  is the exponential integral:

$$E_1(z) = -Ei(-z) = \int_z^\infty \frac{e^{-t}}{t} dt \quad (3.65)$$

$$= \mu_{\text{Euler}} + \ln|z| + \sum_{k=1}^{\infty} \frac{z^k}{kk!}, \text{ Taylor expansion} \quad (3.66)$$

where  $\mu_{\text{Euler}} = 0.5772$  is an Euler's constant. Some definition using  $E_1(z) = -Ei(-z)$ . Here  $E_1(z)$  has a identical definition as that of function *expint* in MATLAB software.

In [102], a simple form integration of Eq. 3.63 and Eq. 3.64, leading to a final solution as:

$$\Delta T(r,t) = [\alpha P(t)] \otimes \frac{2}{\pi \rho C_p} \frac{1}{w^2 + 8D_T t} e^{-2r^2/(8D_T t + w^2)} \quad (3.67)$$

$$= [\alpha P(t)] \otimes \Delta T_H(r,t) \quad (3.68)$$

with  $P(t)$  [W] is a time-dependent optical power (in fact, it could in the any form, such as pulse or cw modulated we discussed later) and  $\otimes$  indicates doing convolution.

For very short pulses (pulse duration much more less than  $t_c$ ), it has been shown that  $\Delta T(r,t) = \alpha P_0 \Delta T_H(r,t)$  with  $P_0$  is the peak optical power of pulse.

On the other hand, for very short pulse Davis [77] gave a similar solution with a consideration of thermal relaxation time  $\tau$  as the form of:

$$\Delta T'(r,t) = [1 - \exp(-t/\tau)] \alpha P_0 \Delta T_H(r,t) \quad (3.69)$$

In Davis's deduction, the assumption that  $\tau \ll w^2/8D_t$  is made which is equivalent to the assumption of infinite medium. It has to be noted that the source form in Davis's deduction is  $q_H = \frac{N(r,t)E_{vib}}{\rho C_p \tau} \exp(-t/\tau)$ . The term  $\exp(-t/\tau)$  indicates that the thermal relaxation occurs and exponentially decay. The other part of heat source could has a relationship with our definition as:

$$N(r,t) = \frac{2N_{tot} \sigma P(t)}{\pi w^2 E_{vib}} e^{-2r^2/w^2} \quad (3.70)$$

where  $\alpha = N_{tot}\sigma$  is the absorption coefficient of the medium and  $E_{vib} = h\nu$  is the vibrational energy (in our study, the selection rule allows only  $\Delta v = 1$  as we have discussed).

### CW Gaussian beam

In Davis's deduction [77], the wall effect of cylindrical gas cell with radius size  $b$  has been taken into consideration. For an impulse reaction to a heat source, the Green's function of Eq. 3.1 could be expressed as:

$$\Delta T(r,t) = \frac{T_0[1 - \exp(-t/\tau)]}{b^2} \sum_{n=1}^{\infty} \frac{J_0(rx_n)\exp(-D_T x_n^2 t)}{J_1^2(bx_n)} \times \int_0^b J_0(r'x_n)\exp(-2r'^2/w^2)r'dr'dt' \quad (3.71)$$

where  $T_0 = I_0\alpha/\rho C_p$  with  $I_0$  is the peak light intensity of pump beam.  $x_n$  is the  $n$ th root of  $J_0(bx_n) = 0$ ,  $n = 1, 2, 3, \dots$

For an infinite medium  $b \gg w$  and on-axis region  $r \ll b$ , it could result in a cw-unmodulated beam as:

$$\Delta T(r,t) = \frac{T_0 w^2}{4b^2} \sum_{n=1}^{\infty} \frac{J_0(rx_n)}{J_1^2(bx_n)} \exp(-x_n^2 w^2/8) \times \int_{-\infty}^t \{1 - \exp[-(t-t')/\tau]\} \times \exp[-D_T x_n^2(t-t')] dt' \quad (3.72)$$

or in a summation form, easy to calculate numerically:

$$\Delta T(r,t) = \frac{T_0 w^2}{4D_T} \sum_{n=1}^{\infty} \frac{J_0(r\beta_n/b)\exp(-\beta_n^2 w^2/8b^2)}{\beta_n^2(1 + \beta_n^2 D_T \tau/b^2)J_1^2(\beta_n)} \quad (3.73)$$

$$= \frac{T_0 w^2}{4D_T} \sum_{n=1}^{\infty} \frac{J_0(r\beta_n/b)\exp(-\beta_n^2 w^2/8b^2)}{\beta_n^2 J_1^2(\beta_n)}, \quad (D_T \tau/b^2 \ll 1) \quad (3.74)$$

where  $\beta_n = x_n b$ . In Eq. 3.74,  $D_T \tau/b^2 \ll 1$  has been made. For air,  $D_T = 2 \times 10^{-5} m^2/s$  and typically for  $C_2H_2$ ,  $\tau \sim 74ns$ . For a typical free-space optics

geometry,  $b$  in the dimension of  $mm$ , which resulting satisfaction of  $D_T \tau / b^2 \ll 1$ . Even for a gas cell with radius of  $5 \mu m$  (as in HC-PBFs), the  $D_T \tau / b^2 \sim 0.06 \ll 1$  could still meet the approximation. From the deduction made above, it could be seen that the temperature rise near the axis is parabolic, which agrees well with the deduction in PT lens spectroscopy [107].

The most summation will converge for  $n < b/w$  [77], thus for near axis  $r \ll w$ , the temperature rise could be:

$$\Delta T(r \ll w, t) = \frac{T_0 w^2}{4D_T} \sum_{n=1}^{\infty} \frac{(1 - r^2 \beta_n^2 / 4b^2)}{\beta_n^2 J_1^2(\beta_n)} \exp(-\beta_n^2 w^2 / 8b^2). \quad (3.75)$$

For on-axis temperature rise, just let  $r = 0$  in Eq. 3.75. On the other hand, there is another deduction results which is equivalent to Eq. 3.75 as [77]:

$$\Delta T(r \ll w, t) = \frac{T_0 w^2}{16D_T} [2 \ln(b/r) + E_1(2b^2/w^2) - E_1(2r^2/w^2)]. \quad (3.76)$$

where  $E_1(z) = -E_i(-z)$  is the exponential integral. Eq. 3.76 is equivalent to Eq. 3.75, except for the expression form [77].

Also, it has been shown that the CW pump induced temperature rise could be obtained by doing the integral of Eq. 3.63 with assuming that  $t_0 \rightarrow \infty$ . The on-axis temperature rise could have been approximately in a simple form, ignoring the influence from the boundary of gas cell [146]:

$$\Delta T(r = 0, t) = \frac{P_{0,CW} \alpha t_c}{\pi w^2 \rho C_p} \ln(1 + 2t/t_c) \quad (3.77)$$

with  $P_{0,CW}$  is the averaging optical power of CW pump source. As indicated in Eq. 3.77, as  $t \rightarrow \infty$ , the temperature rise could tend to be infinite. It is the results of assumption that the gas sample is infinite and thus the temperature tends to rise within the gas sample without any energy exchange with the other medium and external environment. However, this is impossible to obtain since the heat energy

transfer could happen between the gas sample and gas cell (imposed boundary), and then with the external environment. But it is still possible to deduce from Eq. 3.77 that the temperature rise tends to increase slowly when  $t \rightarrow \infty$  as expected.

On the other hand, in fact, for  $t \ll t_c$ ,  $\ln(1 + 2t/t_c) \approx 2t/t_c$ , i.e. for short pulses, there could be  $\Delta T(r = 0, t) \propto \frac{2P_0 t}{\pi w^2 \rho C_p}$ , a result similar to that discussed in pulsed beam case.

### CW Sinusoidal modulated pump source

Considering a general free-space optics with  $w \ll b$ , following Eq. 3.72, it has:

$$\begin{aligned} \Delta T(r, t) &= \frac{T_0 w^2}{4b^2} \sum_{n=1}^{\infty} \frac{J_0(rx_n)}{J_1^2(bx_n)} \exp(-x_n^2 w^2 / 8) \\ &\times \int_{-\infty}^t \{1 - \exp[-(t - t')/\tau]\} \\ &\times \exp[-2D_T x_n^2 (t - t')] \sin(\omega_m t') dt'. \end{aligned} \quad (3.78)$$

where  $\omega_m$  is the intensity modulation frequency of pump beam. Subject to the condition that  $\tau \omega_m \ll 1$ , indicating the operation of modulation frequency are much smaller than  $GHz$ , it results in:

$$\begin{aligned} \Delta T(r, t) &= \frac{T_0 w^2}{4b^2} \sum_{n=1}^{\infty} \frac{J_0(rx_n)}{J_1^2(bx_n)} \\ &\times \exp(-x_n^2 w^2 / 8) \frac{\sin(\omega_m t - \phi_n)}{\sqrt{(2D_T x_n^2)^2 + \omega_m^2}} \end{aligned} \quad (3.79)$$

with  $\tan(\phi_n) = \omega_m / 2D_T x_n^2$ .

Further considering that  $\omega_m \ll 5.783D_T/b^2$ , it may has the solution form of:

$$\Delta T(r, t) = \frac{T_0 w^2}{8D_T} \sin(\omega_m t) \sum_{n=1}^{\infty} \frac{J_0(r\beta_n/b)}{\beta_n^2 J_1^2(\beta_n)} \exp(-\beta_n^2 w^2 / 8b^2). \quad (3.80)$$

The condition  $\omega_m \ll 5.783D_T/b^2$  should be discussed. For typical value of  $b = 10\text{mm}$ , it should work at  $\omega_m \ll 1\text{Hz}$  while for  $b = 100\text{mm}$ , it should be  $\omega_m \ll 0.01\text{Hz}$ .

For higher modulation frequency  $\omega_m \gg (8D_T)/b^2$  and  $\tau \ll w^2/8D_T$ , considering that  $w \ll b$ , there would be:

$$\begin{aligned} \Delta T(r,t) = & \frac{T_0 w^2}{16D_T} \int_{w^2/8D_T}^{\infty} \exp(-2r^2/8D_T x) \{1 - \exp[-(x - w^2/8D_T)/\tau]\} \\ & \times \sin\{\omega_m(t + \frac{w^2}{8D_T}) - \omega_m x\} dx \end{aligned} \quad (3.81)$$

with  $x = t - t' + w^2/8D_T$ . The condition  $\tau \ll w^2/8D_T$  is usually satisfied with  $w$  in dimension of millimeter with  $\tau$  in the order of nano-second. Even when  $w \sim 4\mu\text{m}$  as that in HC-PBFs,  $w^2/8D_T \sim 10^{-7} \gg \tau$  still satisfy the requirement.

For the temperature rise on-axis with  $r \ll w$ ,  $\exp(-2r^2/w^2) \approx 1$  and neglecting the transient term, it would result in:

$$T(r \ll w, t) = \frac{T_0 w^2 F}{16D_T} \sin(\omega_m t - \phi) \quad (3.82)$$

$$F = \sqrt{[Ci(\frac{w^2 \omega_m}{8D_T})]^2 + [\frac{\pi}{2} - Si(\frac{w^2 \omega_m}{8D_T})]^2} \quad (3.83)$$

$$\phi = \arctan(\cot F - w^2 \omega_m / 8D_T) \quad (3.84)$$

where  $Ci$  and  $Si$  are cosine and sine integrals, respectively. It could be seen that the temperature rise is generally modulation frequency dependent. For  $\omega_m \gg (8D_T/w^2)$ ,  $F \approx 8D_T/w^2 \omega_m$ , and  $\cot F \approx 1/F$ , it would follow:

$$T(r \ll w, t) = \frac{T_0}{2\omega_m} \sin(\omega_m t) \quad (3.85)$$

For practical application, it has been deduced that the maximum temperature rise for a light with intensity of  $I_0$  and intensity modulation frequency of  $\omega_m$  could be:

$$\Delta T_{max} = \frac{I_0 \alpha \sin(\omega_m t)}{2 \omega_m C_p \rho} \quad (3.86)$$

i.e. the results of Eq. 3.85, or in terms of pulse energy  $E_0$  [J] as:

$$\Delta T_{max} = \frac{2E_0 \alpha}{\pi w^2 \rho C_p} \quad (3.87)$$

Eq. 3.86 and Eq. 3.87 are usually applied for the theoretical estimation of magnitude of photothermal-induced phase modulation in free-space optics (assuming that  $b \gg w$ ) [77, 147–153].

## Part II: Numerical Analysis

### Intensity dependence

If using the magnitude of temperature rise to define the efficiency of PT effect, we may draw a few conclusions here. The intensity dependence for pulse or modulated pump are quite different from that of CW unmodulated pump. From Eq. 3.69 and Eq. 3.85, it is clear to see that  $\Delta T \propto I_{\text{pump}} = P_0/(\pi w^2)$ , i.e. the PT effect is directly proportional to the light intensity of pump for short pulses or CW modulated excitation (the CW modulate excitation also show the modulation frequency dependence). However, for the CW unmodulated of pump beam, the PT effect presents as  $\Delta T \propto P_0 \alpha / (4\pi \kappa)$ , as indicated by Eq. 3.77, which is independent of the light intensity of pump beam but inversely proportional to the thermal conductivity of gas medium. However, as discussed, this results violate the practical fact that the energy exchange between the gas cell and the external environment must exist. Similar to the discussion of Eq. 3.77, Eq. 3.75 could reach a similar conclusion with  $b \gg w$ .

### Influence of gas cell sizes

In a general way, for smaller  $b/w$  value, the heat generated within the gas cell may exchange with the gas cell and then external environment, which makes that the heat could not be accumulated or deposited within the gas cell and results in a relative low efficiency of PT effect, as illustrated in Fig. 3.10, plotted through the Eq. 3.75. For the fixed ratio of  $b/w$  (changing the value of  $w$  or  $b$  but remain  $b/w$  unchanged), there is no significant changes of photothermal-induced temperature rise for CW unmodulated beam source. Thus it may conclude that with smaller beam radius (larger light intensity for same optical power), the PT effect could be much larger. But for smaller  $b/w$ , the boundary of gas cell would impose a significant influence on the PT effect within gas medium, which may break the validity of all analytical deduction presented above.

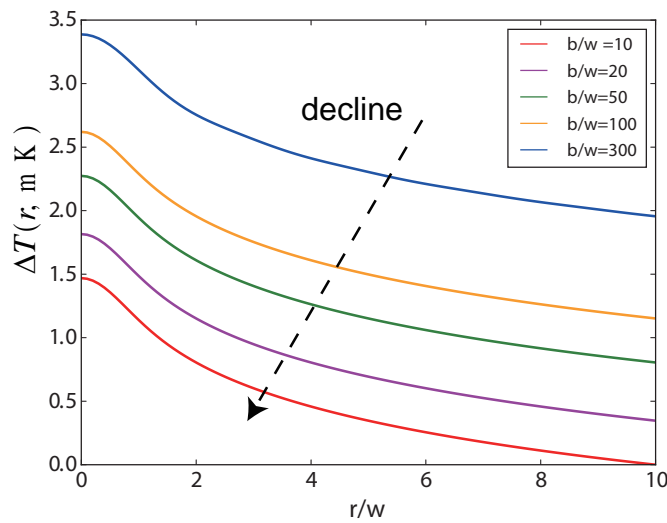


Fig. 3.10 Illustration about the influence of size of gas cell as function of  $r/w$ . The simulation assumes that the radius of pump beam is fixed at  $w = 0.5\text{mm}$  and different ratio of  $b/w$ . The vertical value indicates the relative temperature rise. The pump beam is a CW unmodulated laser.

### Pulse duration dependence

From Eq. 3.69, the pulse dependence of PT effect could be expected. As illustrated in Fig. 3.11, increasing the pulse width could increase the temperature

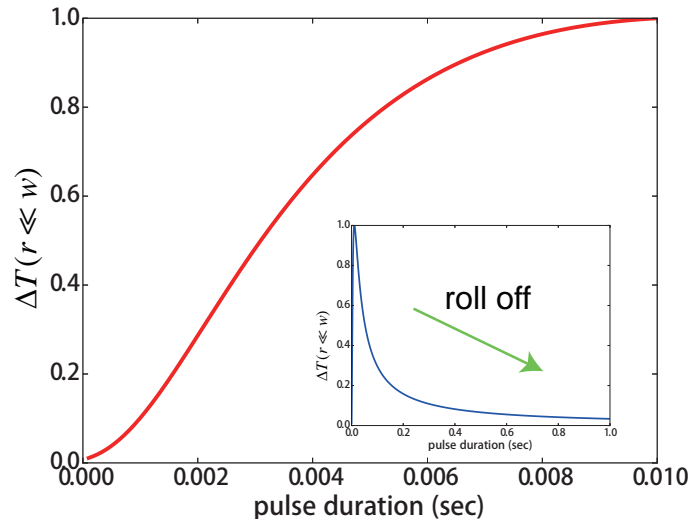


Fig. 3.11 Illustration about the pulse durations dependence of PT effect with short pulses. The beam radius is  $0.5\text{mm}$  with  $t_c \sim 0.03\text{s}$ .

changes caused by PT effect when  $t_0 < 0.01\text{s}$ . However, as illustrated in the inset of Fig. 3.11, further increase the pulse width could cause the degraded of PT effect.

### CW modulation frequency dependence

Similar to the pulse duration dependence, there is also CW modulate frequency dependence of PT effect. From Eq. 3.82, the PT modulation amplitude could be illustrated as Fig. 3.12 as the function of modulation frequency  $f_m = 2\pi\omega_m$ . The increasing the modulation frequency could reduce the temperature rise induced by the PT effect. For smaller modulation frequency, the photothermal-induced temperature rise could be inversely proportional to the modulation frequency.

## 3.3 PTI with HC-PBFs

### 3.3.1 HC-PBFs as ideal gas cell for photothermal spectroscopy

The detection of PT signal in PTI system is actually the measurement of optical phase modulation experienced by probe beam. From the previous sections, we can

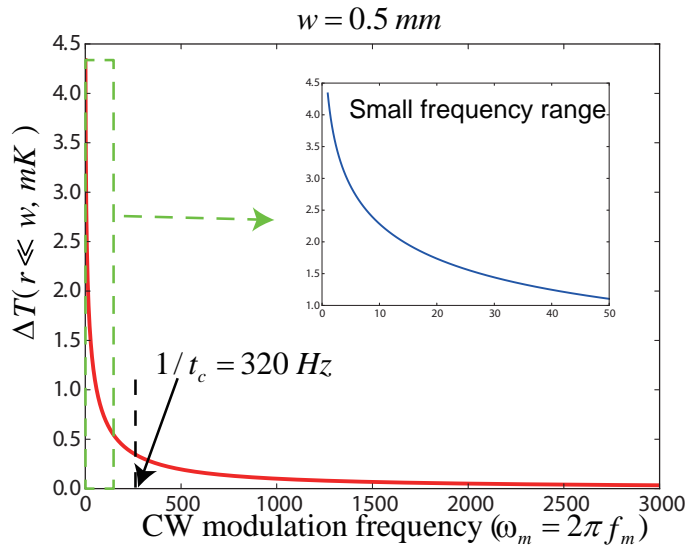


Fig. 3.12 Illustration about the CW modulation frequency dependence of PT effect. The beam radius is  $0.5\text{mm}$  with  $1/t_c \sim 320\text{Hz}$ .

find out that the optical phase modulation of probe beam can be in the form of:

$$\Delta\phi_{\text{probe}} \propto I_{\text{pump}} \cdot \alpha \cdot L \cdot \frac{dn}{dT} \quad (3.88)$$

Therefore, the PT phase modulation is directly proportional to the light intensity of pump beam, the gas absorption strength, the absorption length and also the thermo-optic coefficient. To achieve a better PT signal, we can try to increase one or few of those parameters.

In practice, increasing the interaction length and/or optical light intensity are usually adapts. PTI has been primary developed in free-space optics [77]. Experiments in free-space optics have been suffered from unavoidable beam divergence, resulting in the spread out of beam and rolling off of light intensity. There could be a tradeoff between a small beam size (large light intensity) and interaction length. Allowing for a large light intensity, i.e. a smaller beam size, the light beam will usually be focused on a small spot through optical lens. For a Gaussian beam propagating in free-space optics and focused to a beam diameter of  $2r_0$ , the beam cross-section will be twice of that in focused spot area (beam radius will be  $\sqrt{2}$  of focused spot radius)

after propagating through a Rayleigh length  $z_R = \pi r_0^2/\lambda$ . If the beam diameter of focused spot is  $8\ \mu\text{m}$ , then it will have  $z_R \sim 21\ \mu\text{m}$ . Smaller focused spot size indicates smaller Rayleigh length. Therefore, using optical lens to increase the light intensity will compromise the length of gas absorption. The use of capillary as an open gas cell (meanwhile a waveguide) is somehow a solution. The effective length of a capillary could be defined as a  $1/e$  intensity loss length as [154]:

$$L_{1/e} \approx \left(\frac{2\pi}{z_{01}}\right)^2 \frac{(d/2)^2}{\lambda^2} \frac{\sqrt{n_0^2 - 1}}{n_0^2 + 1} \quad (3.89)$$

where  $z_{01}$  is the first zero of the Bessel function  $J_0$ ,  $\lambda$  is the light wavelength,  $n_0$  is the refractive index of the glass and  $b$  is the bore diameter of the capillary. For an un-coated fused silica capillary  $d = 10\ \mu\text{m}$ , the effective interaction length could be only  $0.1\ \text{mm}$  for  $\lambda = 1550\ \text{nm}$ . Even though a larger bore radius could increase the effective interaction length, it could significantly reduce the peak light intensity for a given launched optical power. For  $a = 75\ \mu\text{m}$ , the length could be as acceptable as  $1.5\ \text{m}$ , but the peak light intensity drops by a factor of 225. Hence, the use of capillary still suffers from comprising either light intensity or interaction length. In fibre-optics, the most common open-path gas cells is formed by a pair of GRIN lens. The typical beam diameter of GRIN lens is about  $0.5\ \text{mm}$ . The light can be collimated through the GRIN lens but the propagation distance of collimated light beam can be limited to be tens of centimeters. Even though the cascaded GRIN lens can increase the length of absorption lens, it cost the complexity of the system and also the total optical loss can be increased.

Therefore, in free-space optics, the gas cells is far from the ideal requirement of achieving good PT signal with both long interaction length and large light intensity. But the HC-PBFs can be a solution to such a dilemma. HC-PBFs have a periodic photonic crystal structure with a central air defect in its cross section, which forms a photonic bandgap to confine the light beam at the hollow core. In its photonic crystal

structure, the lattice constant is in the order of light wavelength and index contrast is large enough due to the large air-filling ratio. Thus, HC-PBFs can confine both light and gas molecules within the central air-core (or call it hollow-core) over a long distance with low loss while provides nearly 100% light-gas overlap. The mode-field diameter (MFD) of HC-PBFs is very small (for HC-1550-02 type, the MFD is about  $11\ \mu\text{m}$ ) and can be maintained over a long range without beam divergence.

### 3.3.2 Advantages of PTI in HC-PBFs

HC-PBFs can provide a larger light intensity for a given optical power and meanwhile longer interaction length, making it an ideal gas cell for PTI sensors. It could be possible to achieve a better trace-gas detection sensitivity by using HC-PBFs in photothermal interferometry. The photothermal interferometry using HC-PBFs was firstly proposed by W. Jin [70]. By the use of all-fibre MZI and a 10-m-long HC-PBFs, a gas absorption sensitivity of  $2.3 \times 10^{-9}\ \text{cm}^{-1}$  has been achieved. Due to large linear working range of optical interferometer, it can also achieve a detection dynamic range (in the range where the output PT signal maintains a linear relationship to the gas concentration) up to 1.6%.

Compared with the PTI in free-space optics, the PTI using HC-PBFs can achieve all-fibre gas sensing with characteristics of compactness, EMI and potential for remote/distributed sensing. In addition, there are several advantages to use HC-PBFs for PTI sensors:

- The primary demonstration of working modulation frequency of PT spectroscopy in HC-PBFs is tens of kHz while that in free-space optics could only be in a range  $< 100\ \text{Hz}$ , or even smaller  $< 1\ \text{Hz}$  depending on the transverse geometric size of open-path gas cell, for an optimized condition. Such a feature enables PTI working in a frequency range where environmental noise can be

much lower and some spectroscopic methods (e.g. WMS) could be utilized to increase the signal-to-noise ratio and also map-out the absorption spectrum.

- It is quite easy to achieve a very high light intensity with only moderate pump power in HC-PBFs. High light power could be delivered into HC-PBF to demonstrate better detection sensitivity. In our primary PTI system, the used peak pump power is usually in tens of milliwatts, which is enough to achieve a comparable sensitivity in free-space optics. In some cases of free-space optics, higher light intensity may cause severe self-focusing effect [43]. However, higher optical power could be launched into HC-PBFs without arising significant nonlinear phenomena.
- The length of gas absorption can be extended in a large scale with low loss, resulting a better detection sensitivity.
- The operation wavelength of both pump and probe beams are in the telecom-band, enabling the incorporation of our PT gas sensors with the conventional well-developed silica-fibre system and devices, which can make the PTI system being low-cost.
- PTI using HC-PBFs has full potential for distributed PT spectroscopic detection. In such a distributed gas sensing, HC-PBFs can serve as both a light transmission cable and a ideal gas sensing platform to detect the trace gas at any locations along single long HC-PBFs.

Compared with other gas sensors based on HC-PBFs, PTI can achieve nearly three orders of magnitude enhancement in both detection sensitivity and dynamic range. The other gas sensors based on HC-PBFs have demonstrated a limit of detection down to  $10^{-6} \text{ cm}^{-1}$  gas absorption, which is far from our expectation when using a HC-PBF with long absorption length. The main limit of direct absorption spectroscopy based on HC-PBFs is believed to be limited by the mode interference in

HC-PBFs, which is a consequence of light interferences between modes in HC-PBFs [53]. The mode interference in HC-PBFs makes the small gas absorption signal indistinguishable from noise background.

The possible reasons that PTI in HC-PBFs can achieve a better detection sensitivity may attribute to the following reasons.

- **The use of pump-probe configuration:** The PT effect induced temperature changes is small. Since most fraction of light power are located in the fundamental mode, the excited high order modes can only generate very small temperature changes.

On the other hand, the refractive index changes of probe beam depend on the surface integral over the hollow-core cross-section between the temperature distribution (resulting from absorption of pump beam) and modal field profile (in form of power distribution) of probe beam. The PT induced temperature changes has a transverse distribution resembling the optical mode field profile of pump beam. If both the temperature distribution and mode field profile are Gaussian distribution (fundamental mode), it can achieve a largest surface integral or best PT phase modulation when the heat conduction is assumed to be the dominant process in PT effect. The mode field profile in the form of power distribution for the fundamental mode  $LP_{01}$  and lowest high order mode  $LP_{11}$  of HC-PBFs can be illustrated in Fig. 3.13. The surface integral between the two modes can be very small. The PT induced temperature changes due to higher order modes of pump beam have small surface integral with the fundamental modal field of probe beam. The PT induced temperature changes due to fundamental modes of pump beam can also have small surface integral with the higher order mode field of probe beam. Even though the photothermal induced temperature changes due to higher order modes can have large surface integral with the higher modal field of probe beam, both of the two integral

source have a very small fraction of power and thus can be ignored. Therefore, in pump-probe configuration, the high order modes have little influence on the PT phase modulation of probe beam.

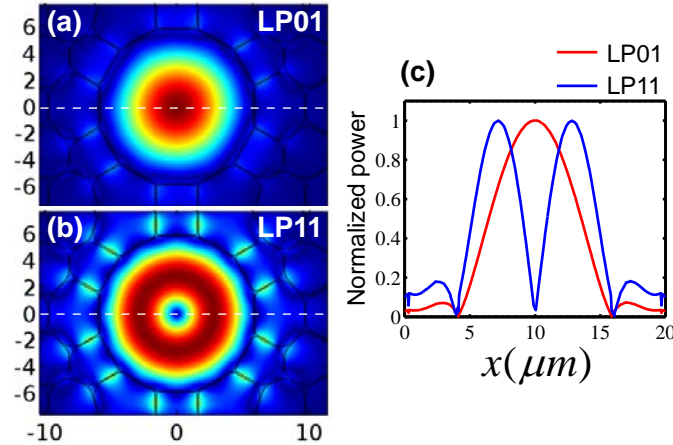


Fig. 3.13 Mode field profile in the form of power distribution of (a) fundamental mode  $LP_{01}$  and (b) lowest high order modes  $LP_{11}$  mode with both axial direction along the fibre geometry in unit of  $\mu m$ ; (c) the normalized power distribution of both mode fields (red line is of  $LP_{01}$  and blue line is of  $LP_{11}$ ), indicated by the dashed lines in (a)(b).

- **The use of optical interferometer for high-precision phase detection:** Optical interferometer can be used to detect very small phase shift and it is a powerful technique to detect small signals with high detection sensitivity. Therefore, small PT phase modulation can be detected to map out the gas absorption signals. The use of high-precision optical interferometer is crucial for PTI sensors.

On the other hand, the phase-sensitive detection can enhance the signal-to-noise ratio. In direct absorption spectroscopy using HC-PBFs, the mode interference between the fundamental modes and high order modes can happen at the photo-detector which may be a severely noise source, especially when the amplitude of signal is close to the noise floor. In MZI system, interferences of probe beam mainly comes from: fundamental modes of both sensing and reference arms, high order modes of sensing arm and fundamental mode of

reference arm, high order modes and fundamental mode of sensing arm. As discussed above, the higher order modes of sensing arm will experience small PT phase modulation. The interference between the two fundamental modes can have a much better PT phase modulation, compared with that between high order modes of sensing arm and fundamental mode of reference arm. Through this way, there could be an enhancement of signal-to-noise ratio. It has to be mentioned that the interference between high order modes of sensing arm and fundamental mode of either sensing or reference arm may not generate effective PT phase modulation but could possibly be a noise source of optical interferometer. However, since only small fraction of power located in the high order modes, such a noise floor could be dominated over by other noise sources of optical interferometer.

- **Taking full advantages of using HC-PBFs as gas cells:** Other gas sensors with HC-PBFs based on direct absorption spectroscopy only utilize the long absorption length for using HC-PBFs as gas cells. However, in PTI with HC-PBFs, it takes the full advantages of HC-PBFs. Both the long absorption length and large light intensity can be exploited simultaneously, that make PTI with HC-PBFs much outstanding.
- **The use of intensity/wavelength modulation approach:** Since the wavelength of the probe beam is fixed, there is no spectral instability due to the scanning of wavelength and mode interference in HC-PBF. On the wavelength where probe beam is fixed, the mutual coupling between the higher order modes and fundamental modes may happen due to the environmental changes (e.g., stress, bending, twist or any other disturbance that may cause the index profile variations along the direction of light propagation). By detecting the PT signal at higher modulation frequency with lock-in amplifier, the noise arising

from the mode couplings can be greatly reduced or avoided since most of such mode couplings are slow-varying noises.

Even though the advancement of PTI using HC-PBFs have been demonstrated, there are still a number of issues required to be explored. The PT effect in free-space optics is found to be dominated by the heat conduction process. However, considering the small core size where strong temperature exchange between the air and silica boundary could happen and there could be some different results of heat conduction. Therefore, it is necessary to find out the mechanism of PT effect in HC-PBFs. On the other hand, the use of MZI for PTI system is far from the requirements for practical applications. It is necessary to develop a passively stabilized PTI system with high detection sensitivity to promote the practical applications of PTI using HC-PBFs. Furthermore, it is possible to develop other PTI-based systems/devices. The following sections of this thesis are going to solve those issues.

### **3.4 Summary**

This chapter demonstrates a basic review of the development of photothermal techniques. The nature of PT effect and principles of fibre-optic interferometry have been investigated, which would help us understand the future modeling on the photothermal spectroscopy. The general and unified analytic solutions for pulsed, CW and modulated pump beams have been demonstrated and the influence factors on the PT signal generations have been exploited. The photothermal interferometry in HC-PBFs has also been introduced and discussed. The advantages of PTI using HC-PBFs have been discussed and some problems required to be answered in the further investigations have been addressed.



## **Chapter 4**

# **Mechanism and dynamics of PT phase modulation in HC-PBFs**

In our first demonstration of PT gas spectroscopy in HC-PBFs [70], the pump beam was a continuous intensity modulated light source. Considering that the most high energy source available on the commercial market are the pulsed light source, it could possibly achieve a better performance using high power pulsed light source. On the other hand, due to the much more confined core size, the PT phase modulation could be quite different from that in free-space optics. Thus it is necessary to investigate the mechanism and dynamics of PT gas spectroscopy in HC-PBFs and discuss the possibility using a pulsed light source.

In this Chapter, we report a numerical model to simulate and explain the mechanisms and dynamics of PT phase modulation in HC-PBFs both theoretically and experimentally.

## 4.1 Mathematical modeling

### 4.1.1 Theoretical model

The geometry of our simple model may be classified into three regions: the central circular hollow-core with the dimension same as the used HC-PBFs gas cell filled with target gas, a fused silica solid bound with a thickness identical to the silica ring surrounding the air-core of HC-PBFs, an extending gas molecules region filled with target gas where all the conditions are under standard temperature and pressure condition. Due to the large air filling ratio ( $> 90\%$ , [65]), the micro-structure cladding the HC-PBFs could be simplified as a pure air region with the assumption of weak absorption in hollow-core. The heat source is a pump beam propagating through the central hollow-core, resulting in a refractive index modulation. A probe beam would propagate through the same path and accumulate the phase modulation in the same fibre. For a collimated free-space optics, as shown in Fig. 4.1(b), the boundary dimension is much larger than the pump beam radius or heat source. A schematic illustration of the cross-section of hollow-core fibre HC-1550-02 is shown in Fig. 4.1(c).

To further simplify the complexity of our numerical model, some assumptions and approximations should be discussed and analyzed. Here we only consider the pump pulse with pulse duration ranging from a few ns to a few  $\mu s$ , which is of the interest during our experiments and also suitable for the most applications.

Firstly, we ignore the temporal process of gas molecules to be excited from the ground vibrational state to higher vibrational state. This process is usually in the time scale of  $ps$ , and could be ignored for our investigating pulse durations.

Secondly, only the vibration to rotation and translation ( $V \rightarrow R, T$ ) processes are considered. As mentioned in the previous Chapter, the most overtone or fundamental tone transition in the infrared region occurs at the ro-vibrational spectra. The transition

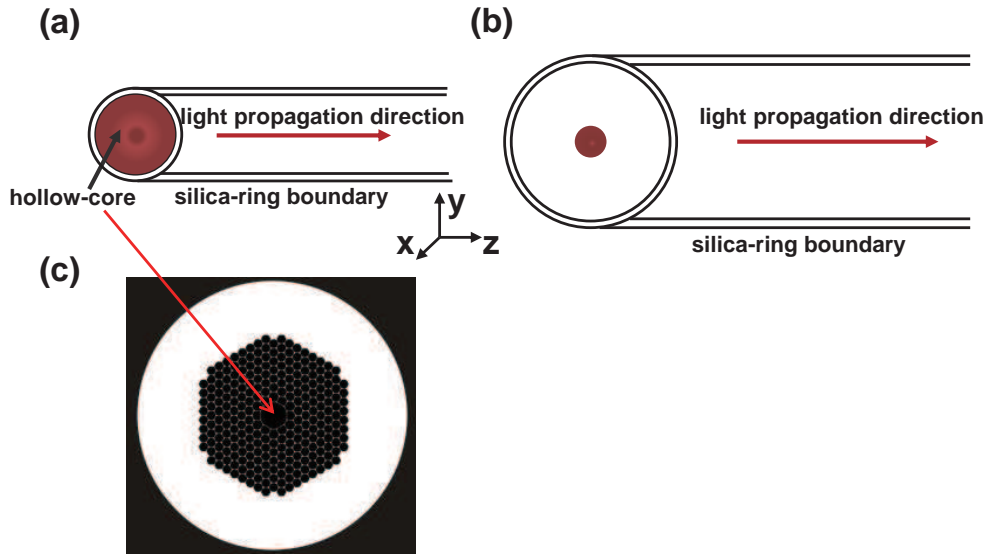


Fig. 4.1 Geometric of modeling the PT phase modulation in (a) HC-PBFs and (b) free-space optics. The red-filled part in the core center is the gas-filled place. The thick boundary indicates the silica glass. (c) image of cross-section of commercial available hollow-core fibre HC-1550-02 from NKT.

may be involved with a rotation state in ground vibration state to another rotation state in excited vibration state. For target gas of interest (i.e.  $C_2H_2$  with  $N_2$  as buffering), under the condition of standard temperature and pressure (s.t.p), the  $V \rightarrow R, T$  thermal relaxation time could be  $\tau \sim 74ns$  [102, 155]. It has to be noted that the thermal relaxation time is not the lifetime of upper state. The linewidth of the gas absorption should be determined by the life time of upper and lower state and determined by the faster process. Thus it will be found that the P(9) absorption line has a linewidth of  $0.082\text{ cm}^{-1}$ , corresponding to the lifetime of  $0.4ns$ , which is much faster than the thermal relaxation process. As we know, the thermal relaxation time indicates the time taken for the molecules to relax from virtue state and deposit the heat into the surroundings.

Thirdly, typically we only consider the weak absorption ( $\alpha L \ll 1$ ), resulting an invariability of pump intensity and also heat generation along the propagation direction of light. It could simplify our model into a simple two dimension models, as shown in Fig. 4.2(a). Even under strong absorption, it could still be extended to

adapt the condition by dividing the optical path into infinitesimal slices, within each slice the weak absorption assumption could be held.

Fourthly, the thermal dynamics within HC-PBFs could still be valid as a continuum regime. For s.t.p condition, the Knudsen number ( $Kn = \Lambda/d$ , where  $\Lambda$  is the mean free path of gas molecules and  $d$  is the diameter of gas cell) is in the orders of  $10^{-6}$  for  $N_2$  gas (the concentration of  $C_2H_2$  is much smaller) in a 1-mm-diameter tube. For a HC-PBFs with hollow-core diameter of  $d = 11\mu m$ , the Knudsen number is about 0.008 for  $N_2$  gas. It has been shown that with  $Kn$  from 0.001 and 0.1, the continuum regime assumption is still valid within most of the fluid region while in the region adjacent to the boundary between fluid and solid, the slip flow condition should be considered for a more accurate model [156]. However, as the fundamental mode profile of the pump (and probe) beam in a HC-PBFs is approximately of a Gaussian shape (as illustrated in Fig. 4.2 (a)), and the light intensity near the core/cladding boundary region is significantly lower than that at the core center. It means that the temperature change near the boundary is much smaller than that near the center, and its effect on the phase modulation of probe beam should be very small. Hence, the exact flow condition near the boundary would have very little effect on the overall phase modulation and may not need to consider for purpose of calculating phase modulation.

Fifthly, the thermal conduction is regarded as the dominant heat dissipation process. Under the condition of the same or similar beam radius ( $w_p$ ) for the pump and probe beams and ignoring the mutual influence between conduction and convection processes, the natural convection velocity around laser radiation region may be estimated by [157]:

$$v_{\text{convect}} = \left( \frac{2\alpha I_{\text{pump}} w_p^2 g}{\rho C_p T_{\text{abs}}} \right)^{1/3} \quad (4.1)$$

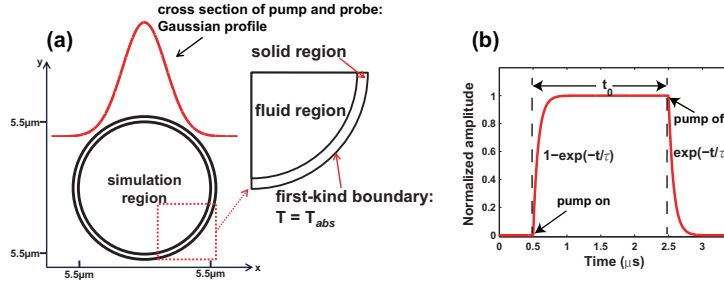


Fig. 4.2 Detail of the computed models. (a) The gas sample is enclosed within the central air core by a  $\sim 70\text{nm}$  thick fused silica solid boundary. The intensity profiles of both pump and probe beam are assumed identical as Gaussian beams and have the same beam radius. (b) the temporal form of heat source as a function of time and thermal relaxation time. In this illustration, the pulse duration is  $t_0 = 2\mu\text{s}$  and the thermal relaxation time is  $\tau = 74\text{ns}$  for  $\text{C}_2\text{H}_2$  under s.t.p condition.

where  $\alpha [\text{cm}^{-1}] = \alpha_0 C$  with  $\alpha_0 [\text{cm}^{-1}]$  is the peak absorption coefficient of the absorptive gas for a relative concentration of 100% at s.t.p, which equals to  $1.165 \text{cm}^{-1}$  for the P(9) absorption line of  $\text{C}_2\text{H}_2$ .  $C$  is a relative gas concentration.  $I_{\text{pump}}$  is pump laser intensity,  $g (= 9.8 \text{m/s}^2)$  is the acceleration of gravity,  $\rho (= 1.165 \text{kg/m}^3)$  is  $\text{N}_2$  gas density,  $C_p (= 1040 \text{J/(kg} \cdot \text{K)})$  is the specific heat of  $\text{N}_2$  gas molecules and  $T_{\text{abs}} (= 293.15 \text{K})$  is the ambient temperature.

The thermal conduction velocity may be estimated by [77]:

$$v_{\text{cond}} = \frac{\kappa}{\rho C_p w_p} = D_T / w_p \quad (4.2)$$

where  $\kappa (= 0.0256 \text{W/(m} \cdot \text{K)})$  is the thermal conductivity of  $\text{N}_2$  buffer gas,  $D_T = \kappa / \rho C_p \approx 2.0 \times 10^{-5} \text{m}^2/\text{s}$  is the thermal diffusivity of the buffer gas. Under s.t.p condition, in a HC-PBFs with beam radius of  $\sim 4.03 \mu\text{m}$  [158], the natural convection velocity is estimated to be  $\sim 1 \times 10^{-4} \text{m/s}$  with a peak pump power of 25 mW and 100 ppm (parts per million by volume)  $\text{C}_2\text{H}_2$  gas while the thermal conduction velocity is  $5 \text{m/s}$ . This would give a thermal conduction time of the order of  $\mu\text{s}$  and a convection time of the order of ms. For pump pulse duration from ns to  $\mu\text{s}$ , the natural convection process would not be fast enough to catch up with the PT signal

change. Therefore, within our observation time, the natural convection process could be ignored.

On the other hand, as we have discussed on above, the heat generation inside the hollow-core fibre can result in the changes of temperature, density and pressure distributions. All of those changes can manifest themselves as the changes of refractive index. However, as we have calculated, the mass diffusion will occur at a very low speed to cause a density changes and therefore we ignore the density changes resulting from mass diffusion process. The pressure change can generate acoustic wave through thermal expansion process and cause a density change, resulting in refractive index change. However, the acoustic wave will propagate at a very fast speed compared with the heat conduction speed. The propagation speed of acoustic wave can be as fast as  $\sim 300\text{ m/s}$  in gas medium, if the radius of HC-PBF is  $\sim 5.5\ \mu\text{m}$ , then the time that acoustic wave can reach its equilibrium can be much smaller than  $20\text{ ns}$ , which is much faster than thermal relaxation process of gas molecules and also the used parameters of pump pulse durations in our model. Therefore, we can also ignore the influence of acoustic or pressure wave on the modulation of refractive index.

From the assumptions and approximations above, the PT phase modulation in HC-PBFs may be simplified as a process of heat transfer. The temperature rise could be obtained by solving the heat transfer equations [159]:

$$\rho C_p \frac{\partial T}{\partial t} + \rho C_p \mathbf{u} \cdot \nabla T = \nabla \cdot (\kappa \nabla T) + Q(r, t) \quad (4.3)$$

where  $\mathbf{u}$  is a nearly zero velocity field and  $Q(r, t)$  ( $\text{W}/\text{m}^3$ ) is heat generation source per volume.

Even though it is similar to that of free-space optics, the heat transfer equation could be used to find the magnitude of temperature rise and hence the PT phase modulation, but due to the limit and constraint of the very small core size (nearly

equal to the beam radius), the solutions discussed in Chapter 3 may no longer valid for the calculating in the case of HC-PBFs.

The absorption of pump beam could induce a transition from ground state to an excited state, which is not stable and could be relaxed through a non-radiative process, i.e. thermal relaxation, and generating heat. With the weak absorption assumption, the heat source  $Q(r,t)$  could be related to the pump light intensity and beam radius in the form of:

$$Q(r,t) = \alpha I_{\text{pump}} \exp(-2r^2/w_{\text{pump}}^2) \cdot S(t) \quad (4.4)$$

$$= \alpha \cdot P_{\text{pump}} \cdot \Xi_{\text{pump}}(r) \cdot S(t) \quad (4.5)$$

where  $I_{\text{pump}} = 2P_{\text{pump}}/\pi w_{\text{pump}}^2$  is the peak light intensity of the pump beam and a Gaussian profile with a beam radius (peak power down to  $1/e^2$  of its maximum) of  $w_{\text{pump}}$  has been assumed with the peak power of  $P_{\text{pump}}$ .  $S(t)$  is the time-varying function of pulse waveform, and  $\Xi_{\text{pump}}(r)$  is the area-normalized light intensity function and manifest in the form of [160]:

$$\Xi_{\text{pump}}(r) = \frac{2}{\pi w_{\text{pump}}^2} \exp(-2r^2/w_{\text{pump}}^2) \quad (4.6)$$

For weak absorption assumption where only small temperature rise occurs, the temperature of outside of silica boundary could be assumed to be fixed as that of first-boundary condition for a derivative equation [161]. Due to the continuity, the temperature between the central air core and silica boundary should be varying as the same, and all the thermal properties (including the thermo-optic coefficient  $\partial n/\partial T$ , thermal conductivity and heat capacity) of gas material are also regarded as constant considering the very small temperature changes. With these conditions, Eq. 4.3 may be solved numerically and temperature changes  $\Delta T(r,t)(= T(r,t) - T_{\text{abs}})$  could be obtained.

The Lorentz-Lorentz relation could help to obtain the temperature induced refractive index in gas molecules [161]:

$$\begin{aligned}\Delta n &= -(n_0 - 1) \frac{\Delta T(r, t)}{T_{\text{abs}}} \\ &= \frac{\partial n}{\partial T} \Delta T(r, t)\end{aligned}\quad (4.7)$$

where  $\partial n / \partial T = -(n_0 - 1) / T_{\text{abs}}$  is the thermo-optic coefficient. With the refractive index  $n_0 = 1.00029$  of air under s.t.p conditions,  $\partial n / \partial T \approx -0.989 \times 10^{-7} / K$ . As indicated, a larger thermo-optic coefficient  $\partial n / \partial T$  of surrounding material or buffer gas could result in a larger refractive index modulation with the same temperature changes. Under the assumption of constant pressure, the refractive index changes could also be expressed in terms of density changes, which has a similar expression as that in terms of temperature changes [70, 77].

The total refractive index changes is the integral over the modal area of probe beam, which is identical to that of pump beam, and could be expressed in the form of [160]:

$$\Delta n_{\text{eff}} = \frac{\iint \Delta n \cdot \bar{\Psi}^2 dA}{\iint \bar{\Psi}^2 dA}\quad (4.8)$$

where  $\bar{\Psi}$  is the electrical field profile of probe beam in the HC-PBFs. The fundamental mode of the probe beam is also approximately Gaussian and may be expressed as:

$$\bar{\Psi}^2 = E_0^2 \exp(-2r^2 / w_{\text{probe}}^2)\quad (4.9)$$

where  $E_0$  is the electrical field strength and the integration of the electrical field satisfies  $\iint \bar{\Psi}^2 dA \approx E_0^2 \pi w_{\text{probe}}^2 / 2$ .

Finally, the complete total PT phase modulation imposed on the probe beam may could be expressed in the form of:

$$\Delta \phi(t) = \frac{2\pi L}{\lambda} \cdot \Delta n_{\text{eff}} = \frac{2\pi L}{\lambda} \cdot \frac{\partial n}{\partial T} \int \Delta T(r, t) \Xi_{\text{probe}}(r) \cdot 2\pi r dr\quad (4.10)$$

where  $L$  is the length of HC-PBFs (here in this paper, for simulations and experiments,  $L = 0.62m$ ),  $\lambda$  is the optical wavelength of the probe beam.  $\Xi_{\text{probe}}(r)$  is the area-normalized intensity profile of probe beam, which has the same expression as Eq.4.6 but with  $w_{\text{pump}}$  replaced by  $w_{\text{probe}}$ . In this chapter, without arising confusion and due to the same waveguide where the pump and probe beam travelling, we may express the beam radius in a unified way as  $w_{\text{pump}} = w_{\text{probe}} = w_p$ .

### 4.1.2 Computed results

The waveform of pulsed heat generation source  $S(t)$  used in numerical model is illustrated in the Fig. 4.2(b). After the pulsed pump is switched on, the heat generated would rise exponentially to a flat level following  $1 - \exp(-t/\tau)$  with the thermal relaxation time  $\tau$  of the absorption gas molecules. When the pulsed pump is switched off, the heat generation would follow an exponential decay in the form of  $\exp(-t/\tau)$  [79].

Fig. 4.3(a) demonstrates the temperature rise  $\Delta T(r,t)$  temporal behavior in a sensing HC-PBFs filled with 100 ppm  $C_2H_2$  calculated by our numerical model. The pulsed pump has a pulse duration  $2\mu s$  and a peak pump power of 25 mW, and its nominal central wavelength is fixed to the P(9) absorption line of  $C_2H_2$   $\nu_1 + \nu_3$  vibration combination band at 1530.371 nm. The magnitude of  $\Delta T(r,t)$  is usually very small while the maximum of  $\Delta T(r,t)$  appears at the center of the fibre, which is less than 2 mK. The arrows in the Fig. 4.3(b) indicate the direction of heat flux, showing that the heat flux tends to dissipate outwards radially until reach a thermal equilibrium state.

Fig. 4.3(c) presents phase modulation dynamics against the different pulse durations from 40 ns to 4  $\mu s$ , and the peak magnitude of PT phase change as the function of the pump pulse duration for a given peak pump power is illustrated in Fig. 4.3(d). Both are the computed results. The peak magnitude of PT phase

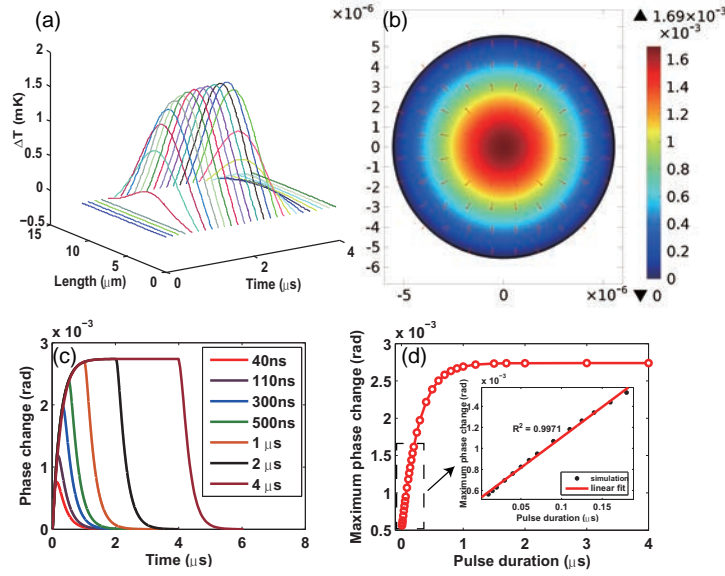


Fig. 4.3 The results of numerical modeling. The HC-PBFs has a core radius of  $5.5 \mu\text{m}$  and a beam radius of  $4.03 \mu\text{m}$ . The pulse duration is  $2 \mu\text{s}$  for (a) and (b). It has been assumed that the peak pump power is 25 mW and length of HC-PBFs is 0.62 m filled with 100 ppm  $\text{C}_2\text{H}_2$  in  $\text{N}_2$ . (a) temporal changes of  $\Delta T(r, t)$ ; (b) two-dimension of temperature changes at the time of  $1.5 \mu\text{s}$  after launching the pump beam. (c) The PT phase modulation against time with different pulse durations; (d) the peak magnitude of PT phase modulation with different pulse duration.

change appear to increase approximately linearly as the increasing pump pulse durations until  $\sim 200$  ns. This value of time span is approximately equal to the thermal conduction time from the center of core to a quarter of the beam radius  $t_{c1} = (w_p/4)/v_{\text{cond}} = w_p^2/4\beta \sim 193$  ns, resemble to that in free-space optics [77]. However, when the pump pulse duration is beyond  $\sim 1.2 \mu\text{s}$ , the peak magnitude of phase modulation does not increase significantly with increasing pulse duration, indicating an optimal pulse duration of  $\sim 1.2 \mu\text{s}$  to achieve a maximum PT signal. This pulse duration agrees approximately with the thermal conduction time from center of the air core to the hollow-core boundary, which could be estimated as  $t_{c2} = a/v_{\text{cond}} \sim 1.1 \mu\text{s}$ , where  $a$  is the core radius of hollow core. This feature time indicates that the thermal conduction within the gas sample plays a essential and dominant role in the dynamics of PT phase modulation in the HC-PBFs.

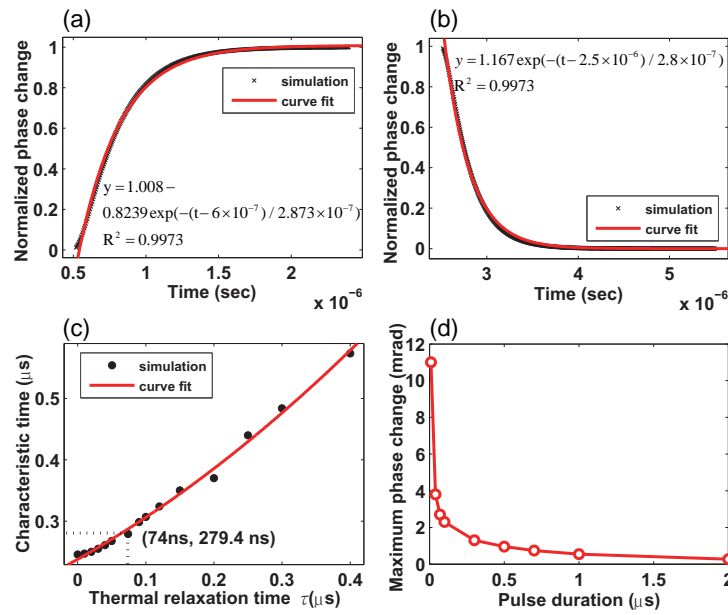


Fig. 4.4 Simulation results with curve fitting demonstrate both the (a) leading and (b) trailing part, showing the dynamics of PT phase modulation. (c) the influence of  $\tau$  on the characteristic time constant; (d) The peak magnitude of PT phase modulation with a fixed pulse energy of 5 nJ for different pump pulse durations. All other parameters of simulation are identical to that of Fig. 4.3.

On the other hand, through curve fitting the trailing and leading part of the PT phase modulation with a  $2 \mu\text{s}$  pulse duration of pump pulse (Fig. 4.4(a) and Fig. 4.4(b)), a pair of characteristic time of 287 ns and 280 ns respectively could be obtained. Those two featured time constant indicate the characteristic time that the magnitude of photothermal-induced phase change will rise to  $1 - 1/e$  or decay down to  $1/e$  of its maximum value. These values are about one quarter the value of  $t_{c2}$  (i.e.,  $t_{c2} \sim 275 \text{ ns}$ ), indicating that the thermal conduction could be the main mechanism that dominates and determines the rise and falling behavior of the PT phase modulation.

It is possible that the thermal relaxation time  $\tau$  of gas molecules could also affect the characteristic time performance for leading and trailing edge of the PT phase modulation signals. With other parameters remain unchanged and only changing the thermal relaxation time  $\tau$  from 5 ns to 400 ns (typically, under the condition of s.t.p, not larger than  $1 \mu\text{s}$ ), using the same curve fitting methods to find the characteristic

time of the exponential PT phase modulation curve as indicated in the Fig. 4.4(c). It is obviously that varying  $\tau$ , the characteristic time could be changed from 240 ns to 550 ns. For our application with  $\tau = 74\text{ns}$ , the characteristic time is  $\sim 280\text{ns}$  with thermal conduction dominates. However, for gas molecules with  $\tau \gg t_{c2}/4$ ,  $\tau$  could cause significant curve broadening, which could explain partially the slight difference between our numerically solved results and the calculated characteristic time  $t_{c2}/4$ . For  $\tau \gg t_{c2}$ , the optimal pulse duration may be different from the results we present here. Furthermore, it also indicates that by observing the characteristic time of PT phase modulation, it could possibly using PT phase modulation in HC-PBFs to observe and measure the thermal relaxation time constant  $\tau$ .

For the  $C_2H_2$  gas absorption at P(9) line and the probe beam of 1553 nm, the magnitude of PT phase modulation is calculated to be 2.739 mrad with peak pump power of 25 mW, 100 ppm gas concentration and 0.62-m-long sensing HC-PBFs. The normalized magnitude of PT phase modulation coefficient is  $1.767 \times 10^{-6} \text{rad} \cdot \text{ppm}^{-1} \cdot \text{mW}^{-1} \cdot \text{m}^{-1}$  in terms of gas concentration of  $C_2H_2$  or  $1.517 \text{rad} \cdot \text{cm} \cdot \text{mW}^{-1} \cdot \text{m}^{-1}$  in terms of absorption coefficient.

By far, we only consider the results with different pump pulse durations under the condition of a given peak pump power. However, if we assume a fixed pulse energy of 5 nJ but with different pump pulse duration, the maximum magnitude of PT phase modulation against the pulse durations could be shown as Fig. 4.4(d). In our numerical simulation, the pulse repetition rate is slow enough to ensure that there is no overlap between any two pump pulse signals. Now, it demonstrate an opposite results that the magnitude of PT phase modulation would be larger for shorter pump pulse duration. For pulse duration of 10 ns, the maximum magnitude of PT phase modulation with a 5 nJ pulse energy can be 0.011 rad for 0.62-m-long HC-PBFs and 100 ppm  $C_2H_2$  gas concentration. The normalized phase modulation coefficient could be  $0.03548 \text{rad} \cdot \text{ppm}^{-1} \cdot \mu\text{J}^{-1} \cdot \text{m}^{-1}$ . For a pulse with higher energy, e.g. 100 nJ, a maximum magnitude of PT phase modulation of  $\sim 0.3$  rad with 1-m-long sensing

HC-PBFs and 100 ppm gas concentration could be achieved. For a typical highly precise fibre-optic interferometry with a minimum detectable phase of  $1 \mu\text{rad}/\sqrt{\text{Hz}}$ , the minimum detectable gas concentration of  $\text{C}_2\text{H}_2$  could be down to 1 ppb. However, it must be noted that if the pulse energy is too high (e.g. at the order of  $\mu\text{J}$  to  $\text{mJ}$  with nano-second pulse duration), the temperature rise within the central hollow core could be so large that a fixed temperature boundary condition would not be valid any more and the further revision of the model should be required, sometimes the whole micro-structure cladding of hollow-core fibre should be taken into consideration.

From the previously discussion and Eq. 4.3, with a given peak power, the maximum heat generation  $Q_{\text{max}}(r,t)$  is directly inversely proportional to the beam radius of pump beam. Hence we may expect that a larger PT phase modulation could be achieved with a smaller spot size. However, as we have discussed in Chapter 3, the silica boundary surrounding the central hollow core could impose a stringent constraint on the magnitude or efficiency of PT phase modulation. If we remain the beam radius of the pump and probe beam unchanged but increasing the hollow-core size, as well as using the corresponding optimized pulse durations of  $\sim a/v_{\text{cond}}$ , the peak magnitude of PT phase modulation for different hollow-core size was numerical solved and is demonstrated in the Table. 4.1. Other parameters are identical to those of discussion previously. As expected, the peak magnitude of PT phase modulation would increase as increasing the diameter of the hollow-core. Thus we may conclude that the silica boundary has important influence on the efficiency of PT phase modulation within HC-PBFs, and the results that we discussed in the Chapter 3 for free-space optics may not be suitable for the case of our PT spectroscopy in HC-PBFs. The influence of the smaller core-size of hollow core could be explained as a faster thermal conduction of silica as compared to the gas molecules. Due to the smaller core size, the energy exchange between the gas molecules and the silica boundary could be efficient and the heat generated by the PT effect may dissipate outwards before it can be accumulated to reach a higher level.

On the other hand, in the view of solving the differential equation, a much smaller boundary constraint means that the solutions of the equation could be significantly affected by the outside condition, especially the boundary condition. Furthermore, the smaller core size is the reason that the thermal conduction of PT in HC-PBFs could be much faster than that in the free-space optics and explain the phenomena that the pump pulse duration of PT phase modulation in HC-PBFs is quite different from that in free-space optics, as discussed in the Fig. 3.11. Thus, in terms of hollow core size, a larger hollow core could result in a better PT signal with a given pump power and fixed beam radius. However, in real application, for a waveguide, the beam radius is usually related to the dimension of waveguide, e.g. the hollow-core size. Therefore, there could possibly an optimized choice of core size and beam radius, or an optimized hollow-core fibre for a best performance of PT spectroscopy.

Table 4.1 Maximum phase changes for different sizes of cores

Core Size ( $\mu m$ )	Maximum phase changes (mrad)
5.5	1
9.5	5.2
20	8.5
50	12

As discussed above, the analytical or semi-analytical solutions in the free-space optics [77, 102, 161] may not longer suitable for analyzing the PT phase modulation in HC-PBFs. On the other hand, our model could still be extended to simulating the PT phase modulation in the free-space optics.

## 4.2 Experiments with pulsed pump beam

### 4.2.1 Experimental set-up

To study the dynamics of PT phase modulation, we built up an experimental set-up as shown in the Fig. 4.5. The pump source is an external-cavity laser (ECDL) which

is amplified by an erbium-doped amplifier (EDFA) and then intensity modulation by an acoustic-optic modulation (AOM). The pulse repetition of pump beam is 500 Hz, sufficient slow to avoid the overlap between any two pulses in our system. The 0.62-m-long HC-PBFs (HC-1550-02 from NKT Photonics) is filled with 7500 ppm  $C_2H_2$  in  $N_2$ . The central nominal wavelength of ECDL is calibrated through a standard  $C_2H_2$  gas cell and fixed at the P(9) absorption line of  $C_2H_2$  at 1530.371 nm.

An all-fibre Sagnac interferometer using a  $3 \times 3$  loop coupler is used to demodulate the PT phase modulation in the HC-PBFs. Any two adjacent output ports of the  $3 \times 3$  loop coupler have a fixed phase bias as  $2\pi/3$  and by using a balance detector, the system output is approximately linearly proportional to the PT phase modulation [132], achieving a maximum and linear conversion from phase signal to output light intensity signal. A super-luminescent light emitting diode (SLED) with a measured 3-dB bandwidth of 41 nm nominally centered at 1545 nm is utilized as the broadband probe source. After launching into the  $3 \times 3$  loop coupler, the probe beam could be divided into two opposite directions (clock-wise, CW and counter-clock-wise, CCW), travelling along the same fibre loop. Due to the existence of a 2-km-long delay fibre (SMF), the time that CW and CCW reach the sensing HC-PBFs could be different and with a time delay of  $\sim 10 \mu s$ .

The output waveforms of Sagnac interferometer could be different for the varying pulse durations of pump-induced phase modulation due to the  $10 \mu s$  fibre delay. As indicated in Fig. 4.6, the output waveform of Sagnac interferometer depends on the pump pulse duration  $t_0$  and the loop delay time  $t_d$ . For  $t_0 < t_d$ , the system output appears to be two identical shaped pulses but with reverse signs. For pulse duration  $t_0 > t_d$ , there is overlap between the two output pulses and the interferometric output pulses would present as all the same pulse width as  $10 \mu s$  no matter what  $t_d$  is. The overlap parts of CW and CCW would cancel out the phase modulation signals. Thus for  $t_0 > t_d$ , the pulse shape of outputs would be all the same for all  $t_0$  except that the distance between the two pulses would increase as the value of  $t_0 - t_d$ . The Fig.

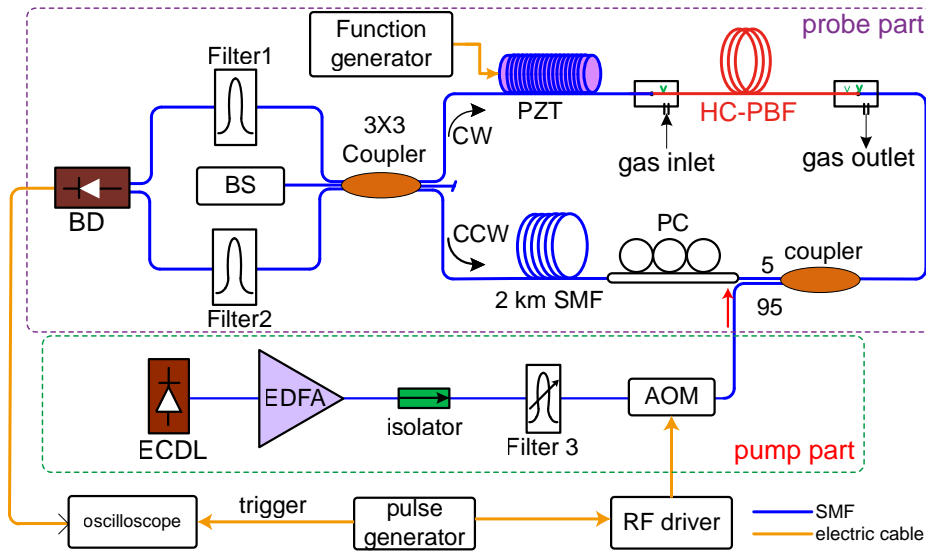


Fig. 4.5 Pump-probe configuration of experimental set-up with a modified Sagnac interferometer. The length of HC-PBFs is 0.62 m. The pump source is an external-cavity diode laser (ECDL) with nominal central wavelength of 1530.371 nm. Filter 3: filters out the undesired ASE noise output from EDFA; Filter 1, 2: filters out the residual pump beam and allow the pass of probe beam; BS: broadband source (probe, at 1553.33 nm); PC: polarization controller; BD: balanced detector; AOM: acoustic-optic modulator for intensity modulation of pump beam.

4.7 shows the measuring outputs of our system with pump pulse duration of  $2\ \mu\text{s}$  and  $40\ \mu\text{s}$ . Here in our experiments, we focus on the case that the pump duration is considerably shorter than the loop delay time  $t_d$  (here  $t_d \sim 10\ \mu\text{s}$  corresponding to a 2-km-long single-mode fibre, SMF); this ensures that the dynamics of PT phase modulation due to a single pump pulse could be observed clearly from the output waveform.

Fig. 4.8(a) shows the output waveforms from BD for pump pulse duration from 100 ns to  $2\ \mu\text{s}$ . The HC-PBFs are 0.62-m-long and filled with 7500 ppm  $\text{C}_2\text{H}_2$  in nitrogen and the peak pump power delivered to the HC-PBFs is 20.2 mW. The output signal closely resembles that predicted by the numerical model and the signal amplitude increases with pulse duration up to  $\sim 1.2\ \mu\text{s}$  and become flat for longer pulse duration, agreeing well with the numerical results in Fig. 4.3.

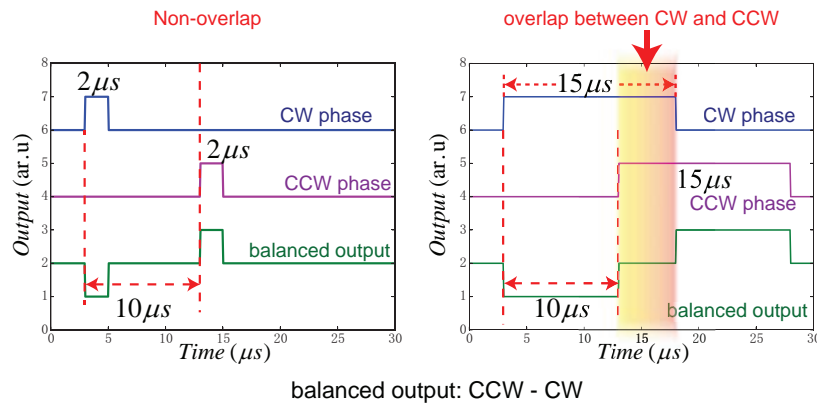


Fig. 4.6 Simulated output Sagnac interferometer with the pulse durations of  $2\ \mu\text{s}$  and  $15\ \mu\text{s}$ . The phase modulation is simulated as the PT-induced pulsed phase modulation.

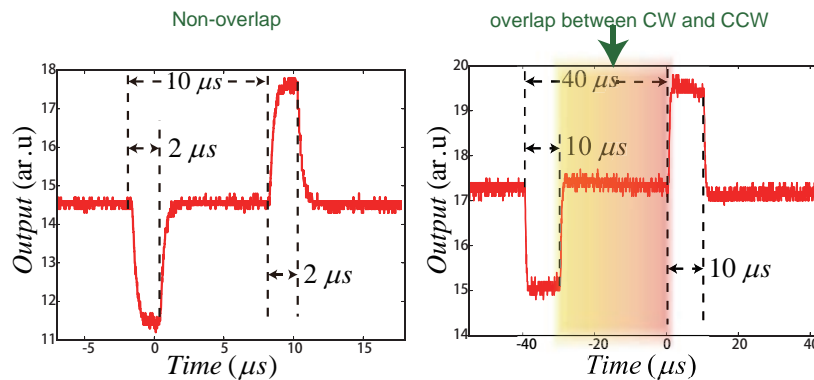


Fig. 4.7 Experimental measuring the interferometric outputs with pulse duration of  $2\ \mu\text{s}$  and  $40\ \mu\text{s}$ .

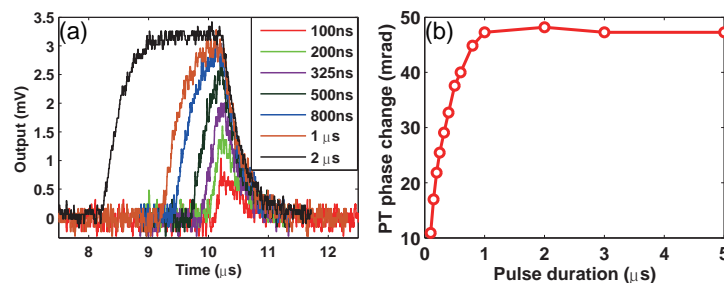


Fig. 4.8 Waveform output from interferometer.(a) output for the same peak pump power but different pulse durations;(b) the peak magnitude of measured PT phase modulation for different pump pulse duration. The peak pump power is  $20.2\ \text{mW}$ . The gas sample is  $0.62\text{-m}$ -long HC-PBFs filled with  $7500\ \text{ppm}\ \text{C}_2\text{H}_2$  gas.

### 4.2.2 Comparison between the measured results and computed results

The phase to intensity conversion of our Sagnac system may follow the calibration process: an piezoelectric-transducer (PZT) wrapped with tens of meters long SMF as our standard phase modulator, connected into the Sagnac loop adjacent to the sensing HC-PBFs. The  $\pi$  (in terms of amplitude) of phase difference between the CCW and CW beams with modulation frequency of 50 kHz could be generated by applying appropriate driving voltage on the PZT and the output of BD could be directly observed in the oscilloscope [132, 137]. Under the assumption of linear conversion between the driving voltage and magnitude of phase modulation of PZT, the phase conversion of our system could be determined as 132 mV/rad. However, for pulsed phase modulation, there is a factor of 2 loss compared to that of continuous wave modulation and hence a phase conversion coefficient of 66 mV/rad could be obtained. The peak magnitude of PT phase modulation, corresponding to the peak output amplitude (in voltages) in Fig. 4.8(a) could be determined as  $3.102mV/66mV \times 1rad = 0.047 rad$ .

Thus the maximum magnitude of PT phase modulation of different pump pulse durations could be calculated, corresponding to the measured output voltage signals, shown in Fig. 4.8(b). It can be observed that in our experimental results, the maximum PT efficiency is at a critical pulse duration of  $1.2\mu s$ , remains more or less fixed for pulse durations beyond that. The measured results agree well with our numerically obtained results in Fig. 4.3.

Since the gas concentration we used here is  $C = 7500ppm$ , the assumption of weak absorption may no longer valid strictly and the averaged pump power should be re-considered and calibrated as  $20.2 \times [1 - \exp(-\alpha L)]$ , i.e.  $\sim 8.4$  mW for 0.62-m-long gas cell. The numerical model obtaining the maximum magnitude of phase modulation is 0.069 rad for pulse duration  $< 2\mu s$  and a deviation of  $\sim 38\%$  between

the experimental value of 0.047 rad and the theoretical expected value. Such a deviation may attribute to (i) the phase calibration process using a PZT in our system may not be precise; (ii) some other complex processes are ignored in our model which may also affect partially our results; (iii) the beam radius and core size of HC-PBFs could not be determined in a very precise way while the core size may have a significant influence on the PT effect; (iv) the efficiency of heat yield - we have simply assumed that all the relaxation processes in  $V \rightarrow R, T$  manifest as thermal relaxation process, converting to heat, but it is just an ideal situation.

The PT phase modulation process obtained through experimental measurement are plotted in Fig. 4.9(a) and Fig. 4.9(b) for two pump pulse durations of 325 ns and 2  $\mu$ s, respectively, with the corresponding simulation results. The thermal relaxation time  $\tau = 74$  ns. To observe the leading and trailing edge in a better and unified way, the magnitude of PT phase modulation has been normalized to its maximum. It could be observed that there is a good agreement between the experimental results and our numerical modeling results, indicating that our model is good enough and reasonable to explain the PT phase modulation in HC-PBFs.

Fig. 4.9(c) and Fig. 4.9(d) shows the leading and trailing edges of the measured output signals of PT phase modulation with the pump pulse duration of 2  $\mu$ s with curve fitting. The characteristic time constant for both edges are 294 ns and 315 ns, respectively, agree well with our predicted value of  $t_{c2}/4 \sim 275$  ns and numerical solved value  $\sim 280$  ns.

### 4.2.3 Trace gas detection with pulsed PT spectroscopy

The sensitivity of the pulsed PTI system was evaluated with same setup as shown in Fig. 4.5 but the oscilloscope is replaced by a boxcar averager (SRS250). The sensitivity of boxcar averager is 1V/5mV and gate width is about 300 ns. The pump pulse duration is set to be  $\sim 3$   $\mu$ s with repetition rate of 500 Hz. The peak pump

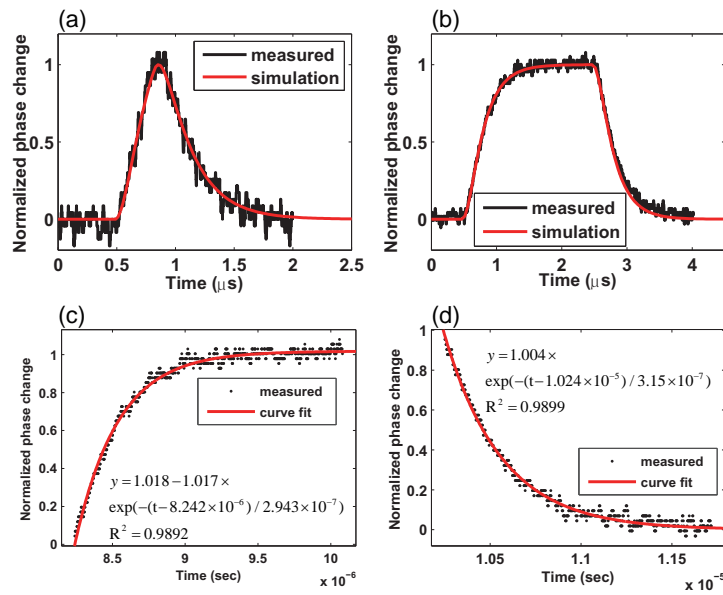


Fig. 4.9 Comparison between the numerical modeling results and the experimental results for the PT phase modulation with pump pulse duration of (a) 325 ns and (b)  $2\mu s$ . Curve fitting results of (c) leading and (d) trailing part of experimentally measured PT phase modulation signal with pulse duration of  $2\mu s$ .

power launched into HC-PBFs is 20.2 mW. The  $C_2H_2$  gas concentration is 7500 ppm.

Fig. 4.10(a) shows the output from the boxcar for the averaging times ( $N$ ) of 10 and 10000. The  $1\sigma$  noise level is reduced significantly with larger number of averages but the signal level remains approximately the same. The slight change ( $\sim 0.06\text{ dB}$ ) in the averaged signal amplitude is believed due to the stability of our phase detection system. The measurements with 10 and 10 K averages were conducted with a time interval of  $\sim 20\text{ min}$ , and the stability of our Sagnac demodulation system was previously measured to be  $\sim 0.87\text{ dB}$  over a 6-hour period [162], due to possibly polarization fading. The relationship between the signal-to-noise (SNR) ratio and the number of averaging ( $N$ ) is calculated and shown in Fig. 4.10(b). Curve fitting shows that the SNR is linearly proportional to  $\sqrt{N}$ , indicating that the noise in our measurement is approximately white [163]. With averaging times of 10000, the signal output from the BD is  $\sim 3.34\text{ mV}$  and  $1\sigma$  noise level is 0.00147 mV. The SNR is about 2272. The lower detection limit in terms of noise equivalent minimum detectable gas concentration can then estimated to be  $\sim 3.3\text{ ppm}$  for a SNR of unity.

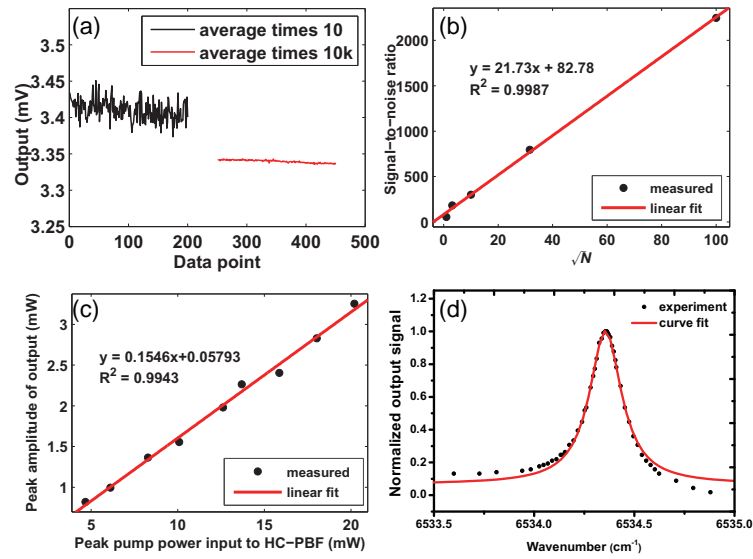


Fig. 4.10 Sensitive trace gas detection with pulsed pump beam PT spectroscopic technique. (a) Boxcar averager output with average times of 10 and 10k; (b) the linear performance of SNR against  $\sqrt{N}$ ; (c) Output from BD against the peak pump power with the same pulse duration of  $3 \mu\text{s}$ ; (d) the spectral line measurement, compared with the Lorentzian curve fit.

For the pump pulse duration of  $3 \mu\text{s}$ , the peak amplitudes of the PT modulation for varying pump power level is also measured and plotted in Fig. 4.10(c). As expected, it follows a linear relationship, indicating that the system performance would be further improved by increasing the peak pump power level.

The absorption line profile (Lorentzian shape) could also be measured by using our system as shown in Fig. 4.10(d). The pump wavelength is tuned from  $1530.27 \text{ nm}$  to  $1530.47 \text{ nm}$  (or  $6533.94 \text{ cm}^{-1} \rightarrow 6534.79 \text{ cm}^{-1}$  in terms of wavenumber). The output signals have been normalized to its maximum value. By the Lorentzian curve fitting, the half width half maximum (HWHM) as  $0.09757 \text{ cm}^{-1}$  could be obtained, agreeing well with the database value  $0.0820 \text{ cm}^{-1}$  (HITRAN [87]).

### 4.3 Discussion about the results

We have investigated the PT phase modulation process in a pulsed PT interferometry with HC-PBFs both theoretically and experimentally. A straightforward and easy to understand theoretical model has been solved by finite element method. The experimentally observed dynamics of PT process matches well with the our theoretical model for the pump pulse durations from ns to a few  $\mu s$ . There are still some discussions should be addressed:

I) With a given peak pump power, the maximum magnitude of PT phase modulation would increases as increasing the pump pulse duration and finally reaches a more or less constant level after approaching a pulse duration of  $\sim 1.2 \mu s$ . The maximum magnitude of PT phase modulation is found linearly proportional to the peak pump power, the length of HC-PBFs and gas absorption. For our HC-PBFs (HC-1550-02, NKT), the normalized phase modulating coefficient could be  $1.767 \times 10^{-6} \text{ rad} \cdot \text{ppm}^{-1} \cdot \text{mW}^{-1} \cdot \text{m}^{-1}$  (for P(9) line of  $C_2H_2$ ) in terms of gas concentration or  $1.517 \text{ rad} \cdot \text{cm} \cdot \text{mW}^{-1} \cdot \text{m}^{-1}$  in terms of absorption coefficient.

II) For pulse duration of the order of  $1 \mu s$ , the thermal conduction is identified as the main mechanism responsible for the phase modulation dynamics. The characteristic time constant for both leading and trailing time behavior with optimal pulse duration was experimentally determined to be around 300 ns, agree well with the calculated value of  $t_{c2}/4 \sim 275 \text{ ns}$  and is also affected by the thermal relaxation time  $\tau$  of gas molecules. The pulse duration required to achieved maximum phase modulation (optimal pulse duration) is approximately  $\sim 1.2 \mu s$ , determined by thermal conduction time of  $a/v_{\text{cond}} \sim 1.1 \mu s$ .

III) Gas detection experiments with a 1530.371 nm pump laser with peak power of 20.2 mW, pulse duration of  $3 \mu s$  and 500 Hz repetition demonstrated a noise equivalent  $C_2H_2$  concentration of  $\sim 3.3 \text{ ppm}$  with averaging times of 10000. This

value would be further reduced by using a higher peak pump power and a larger number of averaging times.

IV) For a fixed pulse energy, the maximum phase modulation was theoretically evaluated and found to increase with reducing pulse duration. It is theoretically possible to achieve ppb level lower detection limit for  $C_2H_2$  in  $N_2$  with pulse energy of  $\sim 100$  nJ , pulse duration of 10 ns and sensing HC-PBFs of  $\sim 1$  m. However, for very high pulse energies, the temperature change near the core/cladding boundary could be large and the first-kind of boundary conduction may not be accurate anymore and further investigation is needed.

V) Under the condition of constant pump power level, smaller spot size (mode field diameter) enhances pump light intensity in the core, which would enhance the PT phase modulation. On the other hand, smaller core size would mean that thermal conduction is fast and the phase modulation could be reduced for a fixed pulse duration because of the fast thermal dissipation. Ideal HC-PBFs with appropriate core size should exist to achieve maximum phase modulation.

VI) We only investigated pulse duration in the range of few tens of ns to  $\mu s$ . For much longer (e.g., millisecond) or shorter (e.g., picoseconds) pulse duration, the phase modulation could be affected by other processes and further investigation is needed.

## 4.4 Maximum allowable laser power

In our discussions of the whole thesis work, we only consider the temperature rises much smaller than 1 K for the valid modeling assumptions with a fixed/constant boundary temperature condition. However, for a maximum allowable laser power of the pump beam, there are also some other issues needed to be considered:

i) **Constant temperature boundary conditions:** in our calculations, a pulsed pump beam with peak light power 25 mW can generate an maximum temperature

rise as large as  $\Delta T_{max} \sim 2mK$  in 100 ppm  $C_2H_2$  gas concentration. If we assume that the maximum allowable temperature rise is about  $1, K$  for the valid conditions of constant temperature boundary conditions, then the maximum allowable peak laser power of pulsed pump is about 12.5 W in 100 ppm  $C_2H_2$  gas concentration. For higher gas concentration, it obviously lowers the maximum allowable laser power of pump beam.

ii) **Maximum PT phase modulation allowed in optical interferometry for linear operation:** the normalized PT phase modulation coefficient is about  $1.767 \times 10^{-6} rad \cdot ppm^{-1} \cdot mW^{-1} \cdot m^{-1}$ , as we have presented in the previous section of this Chapter. If we assume that the sensing fibre length is 1 meter, the gas concentration is about 100 ppm  $C_2H_2$  and the maximum allowable magnitude of phase modulation is about  $0.1\pi$ , then the maximum allowable peak pump power is  $\sim 1.8W$ . This assumption can guarantee a linear and maximum conversion from the measured PT phase modulation signal to the output light intensity signal of fibre-optic interferometry. Of course, some other phase demodulation approaches, such as phase generated carrier methods, could increase the dynamic range of precise phase detection and lead to a much larger maximum allowable pump power, however, partially at the cost of phase sensitivity of the system.

iii) **Optical saturation:** the optical saturation could possibly result in a different performance of PT phase modulation and therefore could an upper limit of pump beam power. In HC-PBF with beam radius of  $5 \mu m$ , for  $C_2H_2$  gas molecules, the absorption cross-section is about  $4.7 \times 10^{-24} m^2$  and lifetime of upper-state is 100 ns at  $P(9)$  line ( $1530.371 nm$ ), the optical saturation power is about  $\sim 21.7W$ . This saturation power is strongly dependent on the gas absorption cross-section and lifetime of upper-state.

The maximum allowable laser power of pump beam can be determined by those factors. However, as indicated above, only when the optical power is much larger than several watts, it is possible to cause a different mechanism/dynamics of PT

phase modulation inside HC-PBF, which may require considerations of modified boundary conditions and other physical phenomena. Furthermore, if the temperature rise is significant and the heat exchange along the optical axis (or light propagation direction), then it is better that we need to consider a three-dimensional model, instead of two-dimensional one. Meanwhile, it is possibly required to take the whole periodic air-silica photonic crystal structure into the consideration. Such a three-dimensional model will dramatically increase the burdens of computation resources and time. But even so, we can still cut the solving regions into small slices, similar to a differential operator for integration, where the two-dimensional calculation is still valid. Therefore, even at high pump power, our model can still be revised to allow the calculation of PT phase modulation.

## 4.5 Summary

Gas detection with HC-PBFs and pulsed PT interferometry spectroscopy are studied theoretically and experimentally. A theoretical model is developed and used to compute the gas-absorption-induced temperature and phase modulation in HC-PBFs filled with low-concentration of  $C_2H_2$  in nitrogen. The PT phase modulation dynamics for different pulse duration, peak power and energy of pump beam are numerically modelled, which are supported by the experimental results obtained around the P(9) absorption line of  $C_2H_2$  at 1530.371 nm. Thermal conduction is identified as the main process responsible for the phase modulation dynamics. For a constant peak pump power level, the phase modulation is found to increase with pulse duration up to  $\sim 1.2 \mu s$ , while it increases with decreasing pulse duration for a constant pulse energy. It is theoretically possible to achieve ppb level detection of  $C_2H_2$  with  $\sim 1$  m length HC-PBFs and a pump beam with  $\sim 10$  ns pulse duration and  $\sim 100$  nJ pulse energy.



## **Chapter 5**

# **Performance optimization of PT gas spectroscopy**

In the first demonstration of PT gas spectroscopy with HC-PBFs, the MZI has been adapted. However, the MZI configuration requires a electrical servo-control to actively stabilized the system which makes the system much more cumbersome and complex, not suitable for the application in real in-situ detection. On the other hand, the servo-loop could only stabilized the system at a low frequency while in industrial application, the ambient environmental conditions could change a few times per second, which may cause the frequent resetting of servo-loop. Thus it is necessary to develop a passively stabilized PT interferometry with high sensitivity.

Furthermore, it has been shown that the continuous-wave modulation frequency of pump beam could greatly affect the output PT signal. It is expected that the possible frequency dependence of PT phase modulation in HC-PBFs may exist. Thus, it needs to investigate such a phenomena which is important for the future design of PT gas sensors using HC-PBFs.

In this Chapter, we report the results of our further experimental and theoretical investigations on the frequency-dependent characteristics of PT phase modulation in a HC-PBFs and demonstrate sensitive and stable operation of a HC-PBFs gas sensor

over a period of several hours, an important step toward the practical application of the PT HC-PBFs sensors.

## 5.1 Frequency dependence of PT phase modulation in HC-PBFs

In Chapter 4, we have studied the use of pulsed pump beam for PTI sensors. It has been demonstrated that the PT phase modulation has a strong dependence on the pulse durations of pump beam. When using a continuous-wave beam with its intensity modulated periodically in sinusoidal/squared waveform, there could also be a modulation-frequency dependent PT signal.

The frequency-dependent characteristics of PT phase modulation is experimentally studied with the setup shown in Fig. 5.1. It is similar to the one used in [70] but the modulation scheme of the pump is different. Instead of wavelength modulation, here the wavelength of the pump is fixed to the center of the P(9) absorption line of  $C_2H_2$  while its intensity is periodically modulated by an acoustic-optic modulator (AOM). Such an arrangement ensures that the PT phase modulation is at the pump modulation frequency, which makes it easier to measure experimentally the frequency dependence of the phase modulation by simply viewing the interferometer output with an electrical spectrum analyzer (ESA).

The gas cell used here is a 0.62-m-long HC-PBFs with its two ends fusion-spliced to single-mode fibres (SMFs), and it is placed in one arm of the Mach-Zehnder interferometer (MZI). Fifteen side holes were drilled along the HC-PBFs gas cell by the use of a femtosecond laser [65], and 7500 ppm  $C_2H_2$  gas buffered by  $N_2$  was filled to the HC-PBFs gas cell by self-diffusion via the side holes. The interferometer is stabilized at quadrature by active servo-control [70], which enables efficient and linear conversion from PT phase modulation into the interferometer output

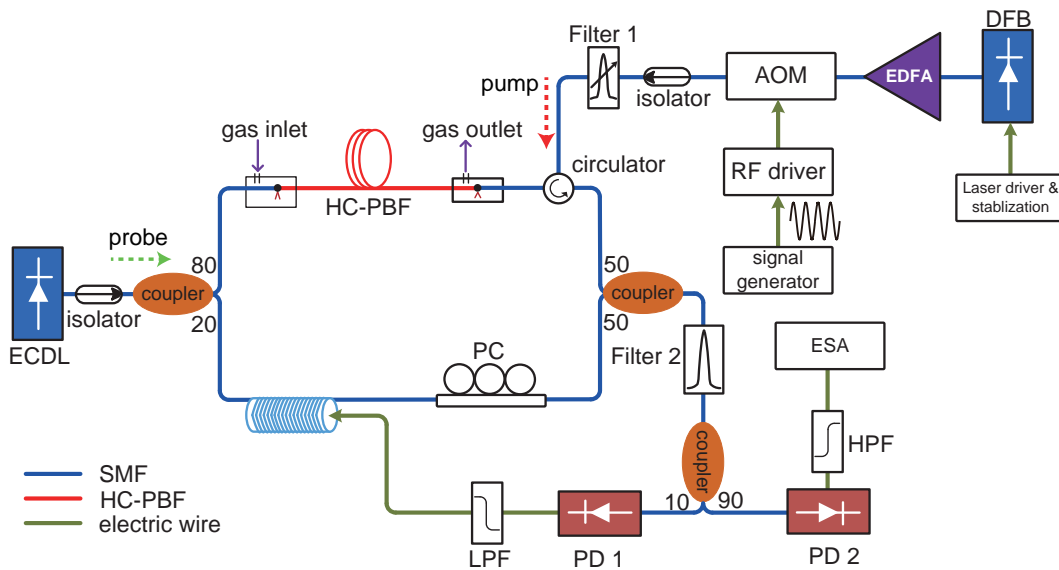


Fig. 5.1 Experimental set-up for the measuring the frequency-dependence of PT phase modulation in a gas-filled HC-PBFs. HPF, LPF: high- and low-pass filter; PD1 and PD2: photo-detector.

intensity. By varying the frequency of pump intensity modulation and recording its corresponding magnitude of the output signal, the frequency response can be obtained. Fig. 5.2(a) shows the measured phase modulation (red circles) against the pump modulation frequency. The vertical axis is normalized against the maximum value that occurs approximately at  $\sim 30$  kHz. The magnitude of PT phase modulation shows no significant change at low frequency, drop to  $\sim 90\%$  of the maximum value at  $\sim 330$  kHz, and reduces quickly from  $\sim 440$  kHz to  $\sim 2$  MHz. This frequency-dependent characteristics is very different from that in a free-space system in that the magnitude of PT phase modulation increases approximately linearly with the reducing modulation frequency down to a few kHz level [77].

Theoretical investigation of the phase modulation was also carried out by modeling the HC-PBFs with a cylindrical tube with its inner diameters equals to that of the hollow-core. Under the assumption that the heat conduction of gases within hollow-core is the dominant heat transfer process, the dynamics of PT phase modu-

lation may be studied by use of the following heat conduction equation [164]:

$$\rho C_p \frac{\partial T}{\partial t} + \rho C_p \mathbf{u} \cdot \nabla T = \nabla \cdot (\kappa \nabla T) + Q \quad (5.1)$$

where all the parameters are identical to that in [164] except that the sinusoidally modulated heat source should be expressed as:

$$Q(r, t) = \alpha C I_{\text{pump}} \exp(-2r^2/w_{\text{pump}}^2) \quad (5.2)$$

$$\times [1 + \cos(\omega_p t)]/2. \quad (5.3)$$

where  $I_{\text{pump}}$  is the peak pump intensity and  $w_{\text{pump}}$  is the beam radius of pump.  $\alpha$  is the absorption coefficient of target gas sample at 100% relative concentration and  $C$  is the gas concentration in volume ratio.  $\omega_p = 2\pi f_p$  is the modulation frequency of pump beam.

The computed results of PT phase modulation as function of time for pump modulation frequency of 600 kHz and 3.7 MHz are shown respectively in insets (i) and (ii) of Fig. 5.2(a). The parameters are identical to the experimental conditions except that the gas concentration is 100 ppm. The peak-to-peak magnitude of PT phase modulation ( $A_{\text{p-p}}$ ) at 600 kHz is about 4 times larger than that at 3.7 MHz. For higher modulation frequency, the heat conduction could not catch up with the heat generation, resulting in heat accumulation in the fibre core and hence an obvious rise of DC level at the onset of pump modulation and a smaller value of  $A_{\text{p-p}}$  at the steady state. The computed phase modulation magnitude (normalized against its maximum value) as function of frequency is also shown in Fig. 5.2(a). The modulation efficiency drops to 90% at  $\sim 330$  kHz, agreeing well with the experimental results. At higher frequencies, the deviation between the computed and the experimental results become significant probably partly due to the Kerr nonlinearity occurring in the section of SMF within MZI via which the high pump power is delivered to

the HC-PBFs gas cell. In the experiment, the length of SMF in the sensing arm is about 10 m, and the pump power levels in the SMF sections before and after the HC-PBFs are estimated to be  $\sim 45.6$  mW and  $\sim 9.1$  mW, respectively. The Kerr phase modulation is estimated to be  $\sim 1.2$  mrad, which is opposite in sign to the PT phase modulation and results in smaller total modulation as observed in the experiments. At 2.5 MHz, the magnitude of PT phase modulation is estimated to be  $\sim 4$  mrad with 14.6 mW peak pump power and 7500 ppm  $C_2H_2$ .

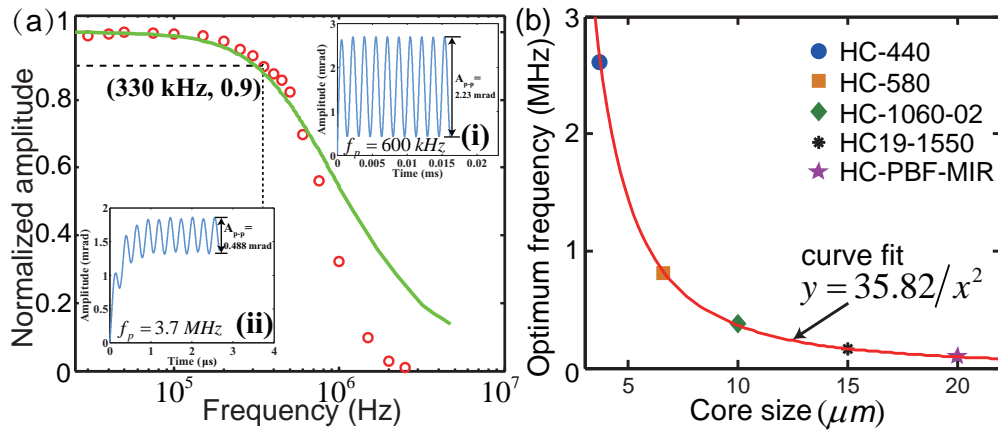


Fig. 5.2 (a) Frequency dependent of PT phase modulation in HC-PBFs. The light-green solid line is the simulation results while the red dot is the measured results. The inset (i) and (ii) are the simulated results in time-domain for modulation frequency of 600 kHz and 3.7 MHz, respectively. (b) Simulation results of optimum frequencies for some HC-PBFs. HC-PBFs-MIR means an HC-PBFs with a large core size for mid-infrared guidance, while the others are HC-PBFs available in NKT Photonics.

On the other hand, for HC-1550-02 fibre, the normalized PT phase modulation coefficient for a CW sinusoidal modulated pump source is  $0.76 \text{ rad} \cdot \text{cm} \cdot \text{mW}^{-1} \cdot \text{m}^{-1}$  in terms of gas absorption coefficient or  $8.85 \times 10^{-7} \text{ rad} \cdot \text{ppm}^{-1} \cdot \text{mW}^{-1} \cdot \text{m}^{-1}$  in terms of gas concentration for  $C_2H_2$  detection.

The frequency dependent PT phase modulation would be primarily determined by the core size of the HC-PBFs and the thermal conductivity of buffer gas. As shown in Fig. 5.2(b), the optimum frequencies depend on the core sizes of hollow-core waveguides. The results by use of  $N_2$  as buffer gas are close to that by use of air.

The results presented here would be a useful reference for selecting the frequency of pump modulation for the design of an optimized PT sensing system.

## 5.2 Optimized PT Sagnac interferometry with HC-PBFs

### 5.2.1 Experimental set-up

The MZI requires active servo-control to maintain stable operation at quadrature and adjustment/calibration is necessary every time when the system is switched on and when the HC-PBFs gas cell is replaced. This is not preferred for practical applications and the use of electronic feedback also compromises its ability for remote detection and for operating in higher EMI environment.

To overcome this limitation, we further studied on the use of a modified balanced-homodyne Sagnac interferometer (Fig. 5.3) for phase detection, aiming to achieve stable operation without using active servo control. A Sagnac interferometer is a single fibre interferometer in which counter-propagating beams travel along the same fibre but in opposite directions. This minimizes the effect of environment on the phase difference between the counter-propagating beams and improves the stability of the detection system. The use of a  $3 \times 3$  coupler in combination with the use of balanced detector (BD) enables an output signal that is directly linearly proportional to phase difference between the counter propagating beams [132], i.e. the PT phase modulation. This linear relationship is independent of the length of the gas cell (assuming it is much shorter than the total length of Sagnac loop), and allowing the use of the same system for phase demodulation of different HC-PBFs gas cells. In our experiments with the Sagnac configuration, an amplified, wavelength-modulation DFB laser was used as the pump source, which generates PT phase modulation in the HC-PBFs. The probe beam was divided into clock-wise (CW) and counter-clock-

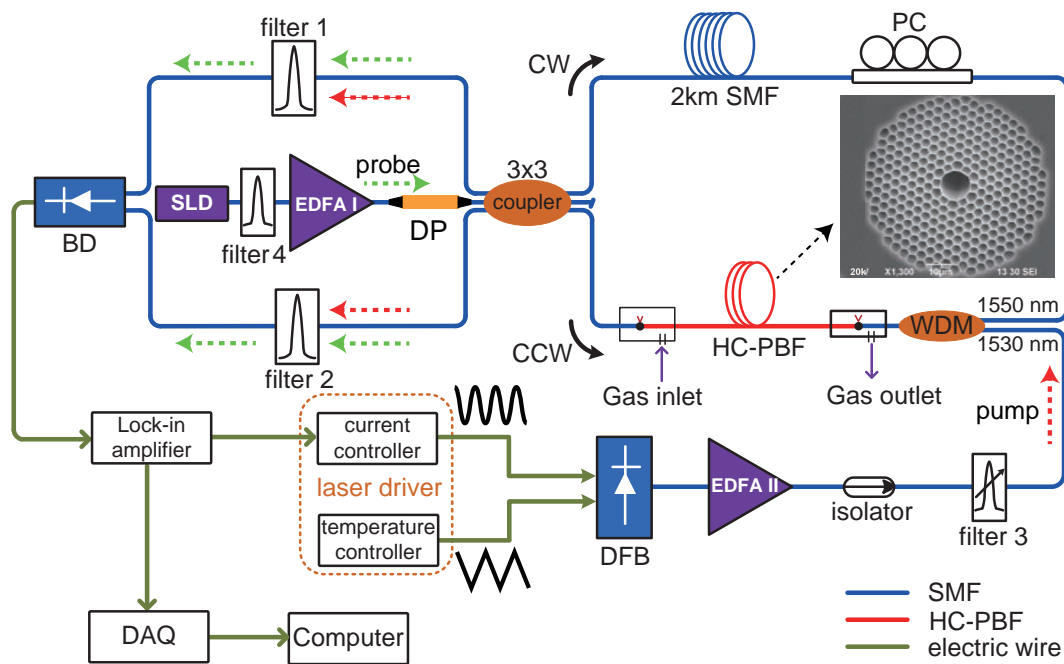


Fig. 5.3 The experimental set-up of PT gas spectroscopy. Filter 1, 2: bandpass filters centered at the probe wavelength to filter out the residual pump; Filter 3: bandpass filter centered at the pump wavelength to filter out the undesired ASE noise; Filter 4: bandpass filter to select a narrow band light from the SLD, which is subsequently amplified and used as the probe beam. BD: balanced photo-detector; DAQ: data-acquisition card; PC: polarization controller; DP: fibre-optic depolarizer. Inset: cross-section of HC-1550-02.

wise (CCW) beams. A 2-km SMF was used as a delay fibre so that the CW and CCW beams pass through the HC-PBFs with a time delay of  $\sim 10 \mu\text{s}$  and the phase difference is maximized by operating at the proper frequency of Sagnac loop, i.e.  $\sim 50 \text{ kHz}$ , which is also within the optimum frequency ( $< 330 \text{ kHz}$ ) for PT phase modulation, as discussed above.

The probe beam is from a super-luminescent diode (SLD) filtered by a Fabry-Perot (FP) filter (Filter 4) and amplified by an Er-doped fibre amplifier (EDFA I). The wavelength of this filter is centered at 1553.33 nm with a bandwidth of  $\sim 1.2 \text{ nm}$ . Filters 1 and 2 have approximately the same passing bands that pass the probe but reject the residual pump beam that is tuned to the P(9) line of  $\text{C}_2\text{H}_2$  at 1530.37 nm. The use of pre-amplifier EDFA I ensures sufficient probe light power reaching the BD, considering the large splicing loss between the SMF and HC-PBFs ( $\sim 4.5 \text{ dB}$  per joint). The use of such a probe source instead of a highly coherent laser source significantly reduces the coherent backscattering/reflection noises in the Sagnac system [165]. A depolarizer is placed before launching probe beam into the Sagnac loop to reduce the polarization fading.

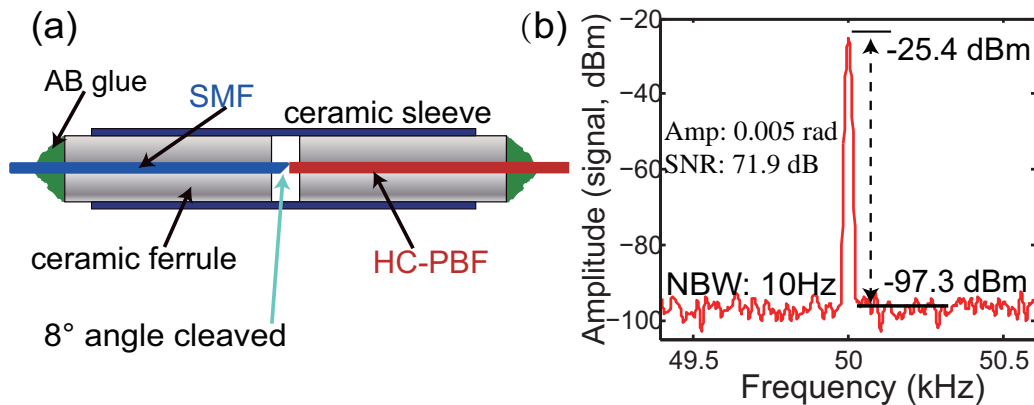


Fig. 5.4 (a) Schematic drawing of gas cell;(b) ESA output of PZT phase modulator with amplitude of 5 mrad.

### Fabrication of HC-PBFs gas cell

To minimize the effect of large Fresnel reflection occurring at SMF and HC-PBFs joints, an  $8^\circ$  angle was introduced at the end of SMF before it is mechanically spliced to the HC-PBFs, as shown in Fig. 5.4(a). The fibre are inserted into a ferrule and then aligned inside a ceramic sleeve with a side slit. A gap of  $\sim 5 \mu\text{m}$  is introduced between the SMF and HC-PBFs, which allows gas to be pressured into the hollow-core. The transmission loss of this gas cell is  $\sim 9$  dB while back-reflection is reduced down to  $\sim -35$  dB. The two mechanical joints are then sealed respectively in two T-shaped steel tubes with one port of the tubes used for the purpose of gas filling.

### 5.2.2 Experiments results

Gas detection experiments were then conducted by filling with 100 ppm  $\text{C}_2\text{H}_2$  into the 1.1-m-long HC-PBFs gas cell. In the previous experiments, we used a higher gas concentration (say 7500 ppm). The reasons that we choose a high or low gas concentration were determined by two factors: the available gas cylinder in our lab and the purpose of our experiments. In previous experiments, what we care most about is the modulation frequency or pulse duration dependent PT phase modulation, therefore a higher gas concentration is better for our observation when the PT phase modulation is working under low efficient way. On the other hand, even the gas concentration is as large as 7500 ppm, the absorption-induced temperature rise is still in the rational regime of our model. In this section, to measure the LOD of our system, we then turn to use a low gas concentration which makes the results much more reasonable for prediction the LOD of our system. The gas filling was done by applying  $\sim 3$  atm pressure difference between gas inlet and outlet for  $\sim 10$  min to ensure the complete filling, even though the theoretical time required is much shorter [65]). The gas pressure was then set to ambient condition and experiments were conducted at room temperature. During the experiments, the wavelength of DFB

pump laser was scanned with a slow sawtooth signal (0.005 Hz) via temperature tuning while it is simultaneously modulated with a faster sinusoidal wave ( $\sim 24.4$  kHz) through current injection, which ensures that the second harmonic of the phase modulation matches to the proper frequency of the Sagnac loop. It should be stated that the current modulation used here mainly modulates the wavelength of the DFB laser (with a smaller residual amplitude modulation), which is different from the pure intensity modulation produced by an AOM in Fig. 5.1. The wavelength modulation could generate multiple harmonics when the nominal wavelength is scanned across the absorption line. Fig. 5.5(a) shows the recorded second harmonic lock-in output when the pump DFB laser is scanned across the P(9) line of  $C_2H_2$  at 1530.37 nm. The depth of DFB wavelength modulation is chosen to be as  $\sim 2.2$  times the linewidth of P(9) line of  $C_2H_2$  to achieve the best signal-to-noise ratio (SNR). The time constant of lock-in amplifier is set to 1s with 18 dB/Oct slope, corresponding to a noise equivalent bandwidth of 0.094 Hz.

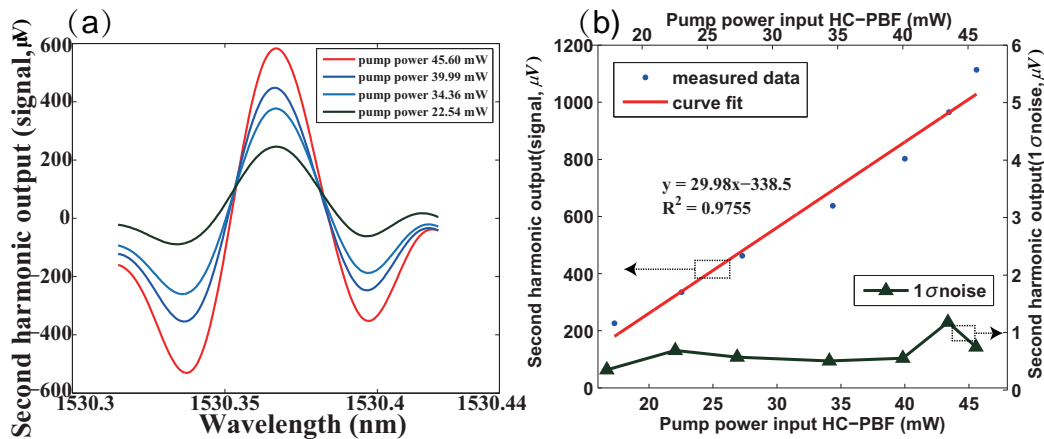


Fig. 5.5 (a) Second harmonic lock-in amplifier output waveform when pump wavelength is scanned across the P(9) line 1530.37 nm with different pump power. The  $C_2H_2$  gas concentration is  $\sim 100$  ppm, pressured into  $\sim 1.1$ -m-long HC-PBFs (HC-1550-02, NKT Photonics). (b) Second harmonic output signal amplitudes and  $1\sigma$  noises as function of peak pump power levels. The noises were measured with the wavelength of pump beam fixed but tuned away from the absorption line. The  $1\sigma$  value was calculated from a recording over  $\sim 2$  min.

For peak pump power of 45.6 mW, the signal amplitude is  $\sim 1113.8 \mu V$  with  $1\sigma$  noise level of  $\sim 0.74 \mu V$ . Thus the noise equivalent minimum detectable gas concentration (NEC) is  $\sim 67$  ppb for SNR = 1. The NECs with pump modulation frequencies of  $\sim 74.2$  kHz, 124.5 kHz and 175.2 kHz, corresponding to the second harmonics being matched to 3, 5 and 7 times the proper frequency of the Sagnac loop, were also measured and they are respectively  $\sim 69$  ppb,  $\sim 148$  ppb and  $\sim 76$  ppb, close to that of 24.4 kHz. In theoretical expectation, for 45.6 mW peak pump power, 1.1-m-long HC-PBFs and the system phase sensitivity of  $4 \times 10^{-7}$ , the calculated minimum detectable gas concentration should be  $\sim 9.4$  ppb for pure intensity modulation pump source. However, due to WMS methods, there could a factor of 4 deterioration in the detection sensitivity [3], and hence the expected minimum detectable gas concentration should be  $\sim 37.6$  ppb. The measured results is about 1.8 times worse than our theoretical expectation, which may result from the residual amplitude modulation during the wavelength modulation process [98].

The second harmonic output of signal and  $1\sigma$  noise level as functions of the peak pump power are shown in Fig. 5.5(b). The second harmonic amplitude of lock-in amplifier follows approximately a linear relationship with the peak pump power, while the  $1\sigma$  noise level presents no significant increase. This implies that further increase the pump power could further improve the NEC.

We also conducted the Allan deviation analysis based on the measured second harmonic lock-in output over one hour period when the wavelength of pump is fixed and tuned away from the absorption line. As shown in Fig. 5.6(a), the Allan deviation decreases with the integration time in the form of  $y \propto 1/\sqrt{t}$ . We may conclude that the white noise is dominant within the integration time of our measurement [90]. For integration time of 145s, the Allan deviation is  $0.2 \mu V$ , corresponding to the sensitivity of  $\sim 18$  ppb. These results are comparable to the HC-PBFs PT gas sensors with MZI configuration [70], however it is achieved without the use of electronic servo loop to stabilize the interferometer.

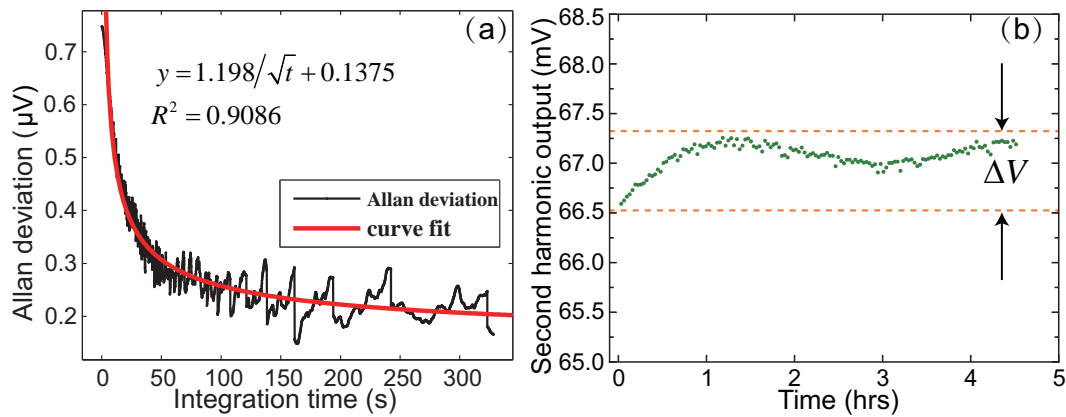


Fig. 5.6 (a) Allan deviation measurement results. The red solid line is the curve fit result with  $y = A/\sqrt{t} + B$ . (b) Results of stability test over several hours. The gas concentration is 1000 ppm. The wavelength of the pump beam is periodically scanned across the absorption line, and the maximum value of R-output of lock-in amplifier is recorded and plotted against the time. The measurement was conducted under the normal laboratory condition and environment.

The stability of the gas sensor was tested with 1000 ppm gas concentration and the results are shown in Fig. 5.6(b). The second harmonic output of lock-in amplifier varies  $<1\%$  over a 4.5-hours-period under laboratory environment and the performance could be further improved by using polarization maintaining fibres in the system.

## 5.3 Discussion on noise properties of PT Sagnac interferometer

### 5.3.1 Theoretical analysis

As we have discussed previously, there are a variety kind of noise sources that would limit our minimum detectable phase (MDP) sensitivity. Here, a few main limited noises sources for our Sagnac interferometer. For all the calculation, we assume that the input optical power at the BD is  $P_0 [W]$  (which could be measured in the experiments) for each channel (assuming equal). Then the differential output current

of BD is about:

$$i_{\text{diff}} = 2\sqrt{3}RP_0 \cdot \Delta\phi \quad (5.4)$$

where  $R$  is the responsivity of our detector in the unit of  $R = 0.9A/W$  typically.  $\Delta\phi$  is the magnitude of phase modulation signal. The factor of 2 results from the measured magnitude of phase modulation is half of the real generated magnitude of phase modulation.

### Shot noise

The root-mean-squared (rms) current output of shot noise could be expressed as [132]:

$$i_{\text{shot}} = 2\sqrt{eRP_0B} \quad (5.5)$$

Comparing with the Eq. 5.4, the MDP limited purely by shot noise is:

$$2\sqrt{eRP_0B} = 2RP_0\sqrt{3}\Delta\phi \quad (5.6)$$

$$\rightarrow \Delta\phi = \sqrt{\frac{4eB}{3RP_0 \times 2}} \quad (5.7)$$

### Thermo-dynamic noise

The thermo-dynamic noise in optical fibre may also called as the fundamental thermal noise of fibre, arising from the random thermal fluctuations within optical fibre (or explained in another description: thermal fluctuations in refractive index of fibre) [166, 167]. The rms (root-mean-squared) value of phase noise normalized to detection bandwidth could be expressed in the form of:

$$\frac{\Delta\phi}{\sqrt{B}} \approx \frac{2T}{\lambda} \left( \frac{\partial n}{\partial T} + n\alpha_T \right) \times \sqrt{\pi \frac{k_B L}{\kappa} \left\{ \frac{[k_{\text{max}}^2 + (\frac{\omega}{v})^2]^2 + \frac{\omega^2}{D_T}}{[k_{\text{min}}^2 + (\frac{\omega}{v})^2]^2 + \frac{\omega^2}{D_T}} \right\} \left[ 1 - \text{sinc}\left(\frac{\omega_p L}{v}\right) \right]} \quad (5.8)$$

where  $k_B$  is the Boltzmann's constant,  $k_{max} = 2/W_0$  and  $k_{min} = 4.81/d$  are the coefficient related to the fibre-optic parameters:  $W_0$  mode field radius and  $d$  cladding diameter of the fibre, respectively. The  $\partial n/\partial T$  is the thermo-optic coefficient of silica fibre.  $\omega_p$  is the angular frequency of phase modulation and  $v = c/n_0$  is the light speed in the fibre.  $D_T$  is the thermal diffusivity.  $\alpha_T$  is the linear thermal expansion coefficient.  $\kappa$  is the thermal conductivity and  $T_{abs}$  is the absolute temperature. All parameters are listed in the Table. 5.1.

Table 5.1 Parameters for calculation of thermo-dynamic phase noise

Property	Value	Unit
$k_B$	$1.38 \times 10^{-23}$	$m^2 \cdot kg \cdot s^{-2} \cdot K^{-1}$
$W_0$	$5.2 \times 10^{-6}$	m
$d$	$125 \times 10^{-6}$	m
$\partial n/\partial T$	$8.1 \times 10^{-6}$	$K^{-1}$
$T_{abs}$	295	K
$\alpha_T$	$5.5 \times 10^{-7}$	$K^{-1}$
$D_T$	$8.2 \times 10^{-7}$	$m^2/s$
$\kappa$	1.37	$W/(m \cdot K)$
$n_0$	1.468	1
$L$	$2 \times 10^3$	m
$\lambda$	$1.553 \times 10^{-6}$	m
$B$	1	1

The numerical calculated spectral density of thermo-dynamic noise in the frequency range of  $0 \sim 400 kHz$  in our Sagnac interferometer is shown in the Fig. 5.7. It has been observed that the thermo-dynamic noise of our Sagnac interferometer has a maximum value  $0.8 \mu rad/\sqrt{Hz}$  at 14.19 kHz while it is about  $0.3 \mu rad/\sqrt{Hz}$  at the proper frequency of  $50 kHz$ . The thermo-dynamic noise increases from the lower frequency to its maximum value and then fall off quickly to the higher frequency region. Increasing the total Sagnac loop fibre length could lead to an increased thermo-dynamic noise.

### Phase noise from backscattering

One of the most attractive advantages of Sagnac interferometer is that it is completely balanced (at least ideally) with zero optical path different between

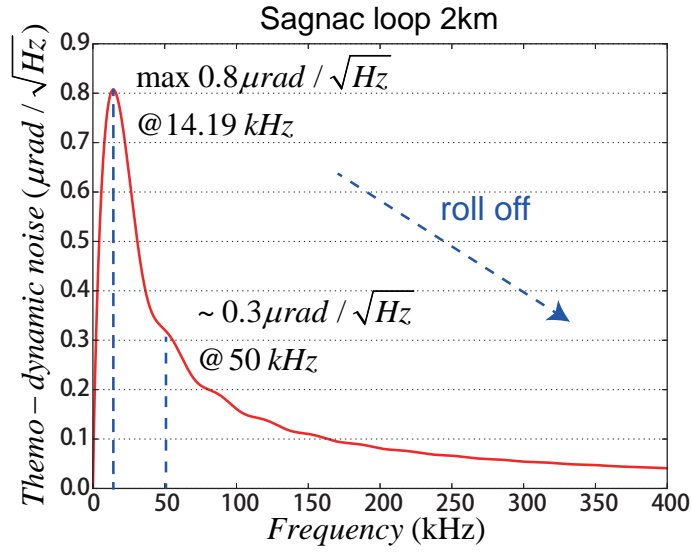


Fig. 5.7 Simulated results of thermo-dynamic phase noise in optical fibres with Sagnac loop length of 2 km.

the two interfering beams. The conversion from laser phase (frequency) noise to interferometric output intensity noise could be eliminated and thus it can be much more immune to the environmental perturbation induced drifts. However, the laser phase fluctuations could still have chance to be translated into an intensity noise due to the parasitic interferences induced by the Rayleigh backscattering within optical fibres or the reflection from the fibre joints, both of the groups of the interfering waves experience a different optical path when being combined. Such noises could disperse into a broadband phase noise [80].

In our Sagnac system, with the help of balanced detection, the source amplitude noise could be greatly reduced [140] and thus the relative intensity noise (RIN) could be ignored in our system. On the other hand, the bandwidth of our probe beam is around  $\Delta\lambda \sim 1.2 \text{ nm}$ . If we define the optical coherent length in such a way [116]:

$$\begin{aligned}
 L_c &= c\tau_c \\
 &= \frac{c}{\Delta\nu} \\
 &= \frac{\lambda^2}{\Delta\lambda}
 \end{aligned} \tag{5.9}$$

where  $\tau_c$  is the coherent time and  $\lambda = 1.553 \mu m$  is the wavelength of probe beam. The calculated coherent length is about  $\sim 2 mm$ , which is sufficient for our current system design to eliminate the possible strong reflection and also its resulting phase noise. Thus we only need to consider the Rayleigh backscattering induced phase noise.

In our system, the coherent length is much shorter than the loop length ( $\sim 2 km$ ) and only frequencies  $\omega\tau_c \ll 1$  are considered. Thus from the deduce of [80], the two-sided power spectrum could be expressed in the form of:

$$W_{RS}(\omega) \approx P_{in}^2 S \alpha_f \tau_c e^{-2\alpha_f L} \left\{ 2L(|k_1|^2 + |k_2|^2 - 2|k_1||k_2| \cdot \cos[\phi_1 + \phi_2] \frac{\sin(\omega_p L/v)}{\omega_p L/v}) + v\delta(\omega_p)(|k_1|^2 + |k_2|^2 - 2|k_1||k_2|\cos[\phi_1 + \phi_2]) \right. \quad (5.10)$$

where the assumption that the fibre attenuation is mainly due to the Rayleigh scattering has been made.  $|k_{1,2}|$  and  $\phi_{1,2}$  are the power coupling coefficient and phase shift of  $3 \times 3$  coupler. The complex coupling coefficient of coupler is  $k_{1,2} = |k_{1,2}|e^{j\phi_{1,2}}$ .  $\delta(\omega_p)$  is a  $\delta$ -function.  $S$  is the Rayleigh backscattering coefficient, which could be calculated by:

$$S = \frac{3}{2(\omega_0/v)^2 w^2} \quad (5.11)$$

where  $\Omega_0$  is the optical angular frequency of probe light beam and  $w$  is the beam radius.  $\alpha_f$  is the attenuation constant of fibre. For single-sided noise power spectrum, it should be equal to  $\sqrt{2W_{RS}(\omega)}$ . All parameters used for simulation are listed on the Table. 5.2.

This is for ideal  $3 \times 3$ . We may consider a simple case with incident probe power into Sagnac loop  $P_{in} = 1W$ , even though this is not practical in real experimental condition. The calculated results of Rayleigh backscattering induced results is

Table 5.2 Parameters for calculation of Rayleigh backscattering phase noise

Property	Value	Unit
$ k_1 $	$1/(3\sqrt{3})$	1
$ k_2 $	$1/(3\sqrt{3})$	1
$\phi_1$	$-\pi/6$	rad
$\phi_2$	$\pi/6$	rad
$v$	$2 \times 10^8$	m/s
$\lambda$	$1.553 \times 10^{-6}$	m
$\tau_c$	$2.54 \times 10^{-12}$	s
$\alpha_f$	$4.6 \times 10^{-5}$	$m^{-1}$
$w$	$5.2 \times 10^{-6}$	m
$L$	$2 \times 10^3$	m
$B$	1	1

plotted against the frequency is as shown in Fig.5.8. For non-ideal coupler, with  $|k_1| = 0.180$ ,  $|k_2| = 0.178$ ,  $\phi_1 = 75^\circ$ ,  $\phi_2 = -19^\circ$ , it is also plotted. Even it is  $9.3 \times 10^{-9} \text{rad}/\sqrt{\text{Hz}}$  with input optical power  $P_{in} = 1 \text{W}$ , for much lower input power, the Rayleigh backscattering noise could be much lower but we still adapt value of  $9.3 \times 10^{-9} \text{rad}/\sqrt{\text{Hz}}$  as a general illustration.

It should be noted that the phase noise induced by the Rayleigh backscattering has a strong dependence on both the coherent time of laser source and the length of Sagnac loop. For shorter fibre, e.g. 500 m, the phase noise could be up to  $\sim 5 \mu\text{rad}/\sqrt{\text{Hz}}$  for almost all detection frequencies when an unideal  $3 \times 3$  coupler and laser source with linewidth of  $100 \text{MHz}$  (coherent time 3 ns) are used. But for an ideal coupler, such a phase noise demonstrate strong frequency dependence and at lower frequencies the magnitude of phase noise could be reduced. Therefore, theoretically, it is possible to build up a Sagnac interferometry with very short-length fibre loop and single-frequency laser source to achieve phase sensitivity down to  $\mu\text{rad}/\sqrt{\text{Hz}}$ . But usually, for most sensing applications, e.g. fibre-optic gyroscope, it is not practical. The broadband laser diode sources are usually preferred.

### Electronic noise

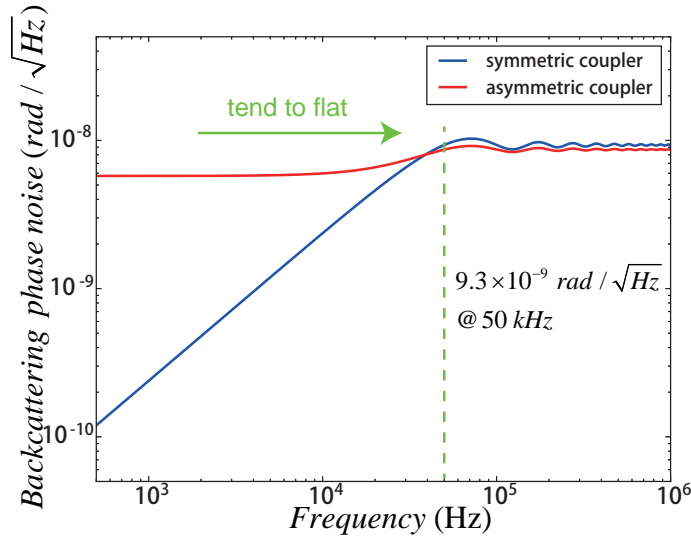


Fig. 5.8 Simulated results of Rayleigh backscattering phase noise in optical fibres with Sagnac loop length of 2 km and spectral bandwidth of 1.2 nm of probe beam.

The electronic noise could be measured by turning off the probe and pump beams while turning on the balanced detector and also the electric-spectrum analyzer (ESA). Assuming the measuring value is  $i_{\text{elect}}$  (which is measured as  $1.4 \text{ pA}/\sqrt{\text{Hz}}$ ). Then the electronic noise limited phase sensitivity could be:

$$\Delta\phi = \frac{i_{\text{elect}}}{2RP_0\sqrt{3}} \quad (5.12)$$

### 5.3.2 Comparison between experimental and theoretical results

The performance of the Sagnac system with the 1.1-m-long HC-PBFs gas cell was firstly tested with a calibrated phase modulator made by wounding  $\sim 10.75$ -m-long SMF around a piezoelectric transducer (PZT). The PZT phase modulator was placed near the HC-PBFs gas cell to generate phase modulation of 5 mrad and the corresponding ESA output is shown in Fig. 5.4(b). The minimum detectable phase (MDP) is estimated to be  $\sim 4 \times 10^{-7} \text{ rad}/\sqrt{\text{Hz}}$  at 50 kHz, close to the thermodynamic phase noise in optical fibres [134].

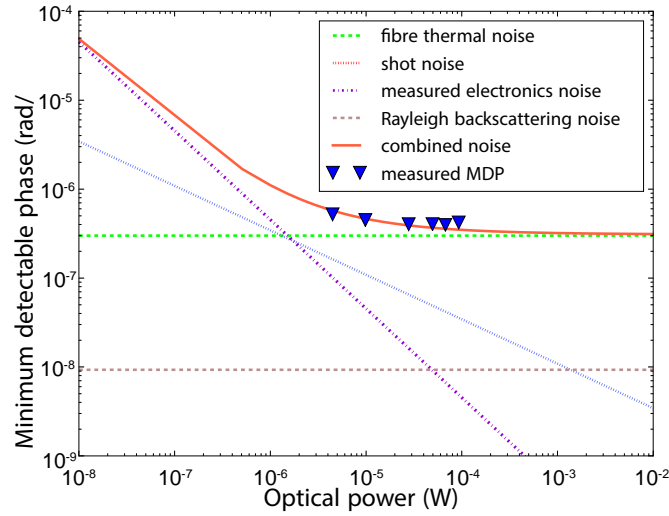


Fig. 5.9 Noise properties of Sagnac interferometer with simulated results and experimental measured results.

The confirmation of noise dominant mechanism could be conducted by comparing the measured results with the simulated results. From the description above, the calculated shot noise, thermo-dynamic phase noise and Rayleigh backscattering phase noise are shown in Fig. 5.9. The measured electronic phase noise has been also presented. The measured MDP is conducted by a calibrated PZT with the corresponding measured optical power  $P_0$  (averaged value of two input ports of BD).

## 5.4 Models of PT phase modulation in open-path gas cells

In Chapter 4 and 5, we have demonstrated the numerical model to find the mechanism, dynamics, frequency-dependence and magnitude of PT phase modulation of PT phase modulation in HC-PBFs for gas spectroscopy. As we have discussed above, both of the theoretical analysis in terms of concepts and numerical modeling agree well with the experimental results, using pulsed or CW modulated pump beam. Our model is easy to solve and find the magnitude of PT phase modulation within HC-PBFs.

Few further extended discussion are summarized here for a better understanding and proof of our simulation model.

Still, our simulation could be extended to simulate the heat conduction or PT phase modulation in the free-space optics.

First of all, the magnitude of PT phase modulation coefficient of our simulation agrees well with the previously measured experimental value: In [147], with a gas cell of inner radius of  $R = 2\text{ mm}$  and beam radius of pump as small as  $w = 0.5\text{ mm}$ , the frequency modulation is  $f_p = 27\text{ Hz}$ , he measured that the signal output amplitude is  $10\text{ }\mu\text{V}$  for 10 ppb  $\text{C}_2\text{H}_4$  (absorption coefficient of  $\alpha = 32.17\text{ cm}^{-1}$  for  $P_{10}(14)$  line and 100% gas concentration), which corresponds to a magnitude of PT phase modulation of  $1.43 \times 10^{-4}\text{ rad}$  (with phase response of system  $70\text{ mV/rad}$ ), using a light intensity of  $250\text{ W/cm}^2$ . The normalized PT phase modulation coefficient is  $1.4488\text{ rad} \cdot \text{cm} \cdot \text{mW}^{-1} \cdot \text{m}^{-1}$  for probe beam at  $\lambda_{\text{probe}} = 632\text{ nm}$  or  $0.5895\text{ rad} \cdot \text{cm} \cdot \text{mW}^{-1} \cdot \text{m}^{-1}$  for probe beam at  $\lambda_{\text{probe}} = 1553.33\text{ nm}$ . With the same parameters provided, the normalized PT phase modulation coefficient using our numerical model could be calculated to be  $0.617\text{ rad} \cdot \text{cm} \cdot \text{mW}^{-1} \cdot \text{m}^{-1}$  for the probe wavelength of  $1553.33\text{ nm}$ . All the coefficients are normalized to the gas absorption coefficient ( $\text{cm}$ ), peak pump power ( $\text{mW}$ ) and length of light-gas interaction ( $\text{m}$ ). The result of our numerical model agrees well with the experimental result reported in [147].

Second, the frequency dependence of free-space optics could also be exploited through our numerical modeling. In fact, the working frequency at  $f_p = 27\text{ Hz}$  of CW pump beam modulation is not the best working frequency for the experimental discussion above [147]. The calculated normalized PT phase modulation coefficient is about  $2.049\text{ rad} \cdot \text{cm} \cdot \text{mW}^{-1} \cdot \text{m}^{-1}$  working at  $f_p = 1\text{ Hz}$ , which is more than 3 times as that of working in  $f_p = 27\text{ Hz}$ . The CW pump modulation frequency dependence or pulse duration dependence has been discuss in Chapter 3 with the analytical and semi-analytical solutions. Our simulation results with  $w = 0.5\text{ mm}$  is illustrated in the Fig. 5.10. It agrees well with the analytical analysis of Fig. 3.12 in Chapter 3.

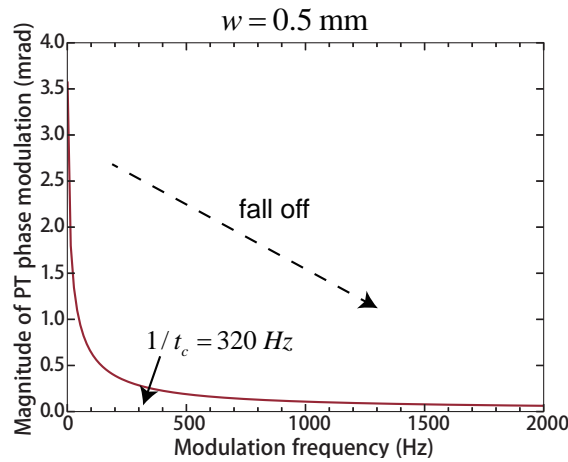


Fig. 5.10 Parameters for the calculation of frequency-dependence of PT phase modulation in the free-space optics with beam radius of  $w = 0.5 \text{ mm}$ .

However, estimating magnitude of phase modulation using Eq. 3.86 and Eq. 3.87 would not appropriate for PT phase modulation in HC-PBFs, which would lead to a nearly  $\sim 4$  orders of magnitude difference compared with our measured and computed results in HC-PBFs.

It is obviously that the performance of frequency dependence of PT phase modulation in HC-PBFs is quite different from that in free-space optics. In HC-PBFs, there is a nearly flat-response band (the magnitude of PT phase modulation shows no significant change with varying pump modulation frequency) for pump modulation frequency  $< 330 \text{ kHz}$  and then the magnitude of PT phase modulation would roll off quickly down to  $\text{MHz}$ . But for that in free-space optics, the flat-response band is not that straightforward or even cannot be observed in the most cases and then the PT phase modulation efficiency may fall off quickly down to  $1 - 2 \text{ kHz}$ .

Such a characteristic make the PT gas spectroscopy much more attractive since it can work at a higher modulation frequency where the ambient broadband noise is typically lower and some spectroscopic methods (like WMS) could be possibly used to increase the signal-to-noise ratio.

Even though we have discussed that the PT phase modulation is directly proportional to the pump light intensity, however, it has shown that the normalized phase modulation coefficient in HC-PBFs is  $0.7573 \text{ rad} \cdot \text{cm} \cdot \text{mW}^{-1} \cdot \text{m}^{-1}$  (pump modulation frequency  $< 330 \text{ kHz}$ ), which is quite close to that of free-space optics.

The main factor that affect the PT efficiency in HC-PBFs may be the silica boundary constraint. As we have discussed in Fig. 3.10 of Chapter 2, for free-space optics, the ratio between the diameter of gas cell and the pump beam radius  $b/w$  would impose a effect on the final output magnitude of PT phase modulation. As  $b/w$  decrease, or gas cell tends to similar in geometry dimension to the beam radius, the PT efficiency could reduce. However, in that analytical calculation, only down to  $b/w \sim 10$  was considered. For smaller value of  $b/w$ , some basic assumptions for analytic analysis break down and not suitable for calculate the accurate results. However, the influence of boundary constraint could still be expected. As illustrated in the Table. 4.1 in Chapter 4, increasing the core size of hollow-core with a fixed beam radius could further increase the magnitude of PT phase modulation.

Thus, it may conclude that: (i) due to the smaller core size of HC-PBFs waveguide, much larger light intensity of pump beam could be achieved and hence larger PT phase modulation coefficient could be achieved with a moderate pump power; (ii) also due to the smaller core size of HC-PBFs and also comparable boundary constraint, the heat conduction is fast enough to dissipate the heat generated by PT effect, making the accumulating heat within hollow-core much more difficult and hence resulting in a lower PT efficiency. (iii) due to the smaller core size of HC-PBFs, a fast heat dissipation could be achieved and a fast heat changes could be accessible. Thus it makes that the PT phase modulation in HC-PBFs could work in a higher CW modulation frequency.

In a summary, comprehensively considering the influence from the core size, compromising the coefficient of PT phase modulation nearly equal to that of free-

space optics and also makes the PT phase modulation in HC-PBFs could work in a higher modulation frequency.

## 5.5 Summary

In this chapter, we studied the dependence of PT phase modulation in an acetylene-filled HC-PBFs on the frequency of pump modulation and found the modulation efficiency exhibits no significant change for modulation frequency up to  $\sim 330$  kHz, and reduces to  $\sim 10\%$  of the maximum at a couple of MHz. This would be useful for designing PT gas sensors. We also studied the use of a Sagnac interferometer with  $3 \times 3$  loop coupler and balanced detection to achieve stable phase demodulation. With a 1.1-m-long HC-PBFs gas cell optimized to reduce reflections at the HC-PBFs/SMF joints, and the Sagnac interferometer for phase demodulation, we demonstrated a gas sensor with NEC down to  $\sim 67$  ppb  $C_2H_2$  with a modulated pump of 45.6 mW in peak power and 1s time constant. The NEC could go down to  $\sim 18$  ppb for 145s integration time. These values of NEC are comparable to that of the stabilized MZI but this system achieves stable operation without the need of electronic servo control, enabling remote detection and multiplexed sensor networking via fibre-optic telemetry links.



# Chapter 6

## Distributed gas sensing with optical fibre photothermal interferometry

To further extending the application of PT interferometry, in this Chapter, we report a spectroscopic distributed gas detection system based on PT interferometry with a HC-PBFs. The system uses a modulated pump to generate periodic PT phase modulation and a dual-pulse heterodyne OTDR is used for the detection of distributed phase modulation. The system is capable to detect low level of trace gas along a long length of HC-PBFs.

### 6.1 Basic principles

#### 6.1.1 Distributed PT phase modulation along a HC-PBFs

An intensity-modulated pump beam and a probe beam are propagating in the same gas-filled HC-PBFs, as shown in Fig. 6.1 and Fig. 6.2(a). If the nominal wavelength of the pump is tuned to an absorption line of a trace gas contained within the HC-PBFs, the pump absorption will heat up the gas, change the distribution of gas temperature, pressure and density within the HC-PBFs, modulate the effective

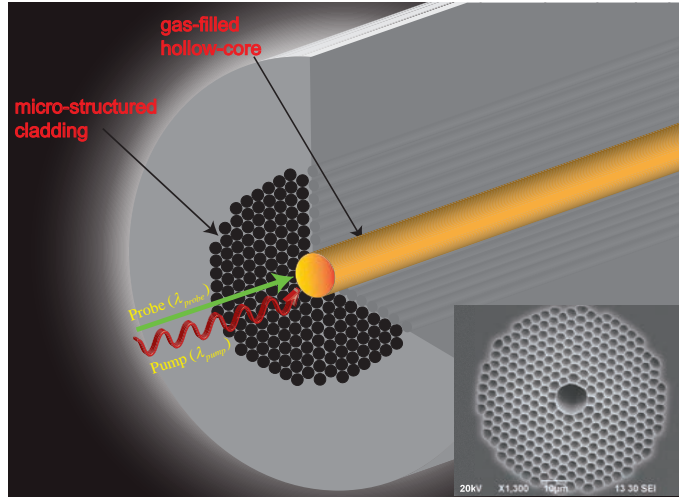


Fig. 6.1 Schematic drawing of a HC-PBFs with a pump and a probe beam propagating within it. Inset: scanning electron microscope (SEM) cross-sectional image of a commercial HC-PBFs (NKT HC-1550-02) [168].

refractive index (RI) and hence the accumulated phase of the probe beam [70, 144]. Assuming weak absorption, the magnitude of PT phase modulation over a section  $[z, z + dz]$  along the gas-filled HC-PBFs may be expressed as [164]:

$$\Delta\phi_p = P_0 \cdot e^{-\alpha_f z} \cdot e^{-\alpha_0 C z} \cdot \Delta\bar{\phi}_0 \cdot \alpha_0 C \cdot dz \quad (6.1)$$

where  $P_0$  is the peak pump power input to the HC-PBFs,  $\alpha_f$  is the power attenuation coefficient propagating along the optical fibre,  $\alpha_0$  is the gas absorption coefficient for pure (100%) target gas and  $C$  is the relative gas concentration.  $\Delta\bar{\phi}_0$  is a normalized phase modulation coefficient, representing the magnitude of phase modulation produced for  $1 \text{ cm}^{-1}$  gas absorption, 1 mW peak pump power and 1-m-long sensing HC-PBFs. We use the normalized coefficient here so that Eq. (6.1) is independent of the strength of the absorption lines, which could be significantly different for different absorption lines and gas species.

Due to the intrinsic fibre loss and pump absorption, the pump power level reduces with increasing propagation distance, resulting in a reduction in the magnitude of PT phase modulation per meter down the sensing HC-PBFs. Taking the P(9) absorption

line of  $C_2H_2$  at 1530.37 nm as an example,  $\alpha_0 = 1.165 \text{ cm}^{-1}$ . For the HC-1550-02 fibre, if pump beam is intensity-modulated sinusoidally with a frequency  $< 330 \text{ kHz}$  [169] and the probe wavelength is around 1550 nm,  $\Delta\bar{\phi}_0$  has been determined to be  $\Delta\bar{\phi}_0 = 0.76 \text{ rad} \cdot \text{cm} \cdot \text{mW}^{-1} \cdot \text{m}^{-1}$  [164]. Assuming a fibre attenuation of 24 dB/km [46], a peak pump power level of 100 mW, and 10 ppm  $C_2H_2$  balanced by  $N_2$  is uniformly distributed along the fibre. The magnitude of PT phase modulation per unit length at  $z = 0$  is calculated to be 1.8 mrad/m accounting for round-trip phase modulation, and reduces down to 0.4 mrad/m at the end of 200 m length of HC-PBFs. If the fibre attenuation could be reduced down to 1.2 dB/km, which is the currently reported lowest loss for HC-PBFs [48], the magnitude of PT phase modulation would be 1.3 mrad/m after 200 m and 0.11 mrad/m at the end of 2 km.

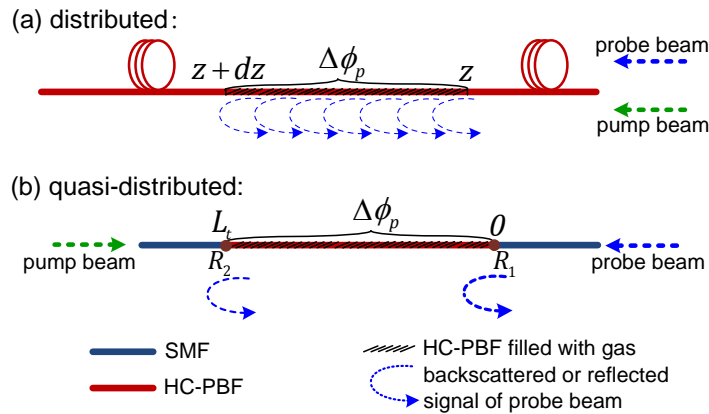


Fig. 6.2 (a) PT phase modulation due to pump absorption over a section  $[z, z + dz]$  of HC-PBFs. The backscattered probe beams shown as dashed blue lines are used to detect the distributed phase modulation, forming the basis for distributed gas sensing. (b) PT phase modulation over a length ( $L_t$ ) of sensing HC-PBFs sandwiched between the two SMFs. The back-reflected probe beams at the HC-PBFs/SMF joints are used to detect the phase modulation, which forms the basis for quasi-distributed gas sensing. The line thickness of backscattered/reflected signal indicates the relative signal strength.

The same principle can be applied to quasi-distributed sensing (Fig. 6.2(b)) in which discrete sensing HC-PBFs sections are connected in series by single-mode fibres (SMFs) for light transmission. In such a case, the magnitude of PT phase modulation over a length ( $L_t$ ) of gas-filled HC-PBFs can still be estimated with Eq.

(6.1) by replacing  $dz$  with  $L_t$ , and  $P_0 e^{-\alpha_c z} e^{-\alpha_0 C z}$  with the peak pump power inputting into the particular section of the sensing HC-PBFs (assuming weak absorption and negligible fibre loss for the relatively short length of the sensing HC-PBFs). For multiple sensing sections (HC-PBFs sensors) serially connected by SMFs, the pump power into the sensors down the fibre cable would reduce considerably due to the connection loss between the HC-PBFs and SMF [45]. Assuming the length of each HC-PBFs sensor is 28 m (the length used in our experiments in Section 5) and it is filled with 10 ppm  $C_2H_2$  balanced by  $N_2$ , the magnitude of PT phase modulation (round-trip) for first sensing section is estimated to be 49.6 mrad with 100 mW peak input pump power. Considering the state-of-the-art splicing loss achieved between the SMF and HC-PBFs, we may assume a 4-dB loss for each sensor (mainly from the two HC-PBFs/SMF splicing joints[45]), and the PT phase modulation would then be reduced down to 19.7 mrad at the 2nd sensor and  $5 \mu\text{rad}$  at the 11th sensor. If the loss per sensor could be reduced down to  $\sim 2$  dB, the PT phase modulation would be  $\sim 0.78$  mrad at the 10th sensor and  $\sim 7.8 \mu\text{rad}$  at the 20th sensor.

### 6.1.2 Detection of PT phase modulation

The distributed phase modulation may be detected by exploiting backscattering of the HC-PBFs (Fig. 6.2(a)) in combination with the phase-sensitive OTDR or time-resolved optical frequency domain reflectometry (OFDR) [170, 171]. The backscattering in a HC-PBFs is mainly caused by surface scattering due to random fluctuations of the core dimensions and has a value of  $\sim 1.5 \times 10^{-6} m^{-1}$  [172]. A variety of phase-sensitive OTDR configurations have been reported for acoustic/vibration detection, including interferometry-assisted OTDR [173], heterodyne phase-sensitive OTDR [174] and chirped pulse phase sensitive OTDR [175]. They all in principle could be used to detect the distributed PT phase modulation. However, to our knowledge, most of the previous reports were concentrated on the detection

of events like intrusions and did not focus much on the quantification of phase modulation along the fibre, and little or no information is available on the minimum detectable phase modulation.

For quasi-distributed sensing, the accumulated phase modulation of probe beam over each of the sensing sections (sensors) may be determined by examining the interference between the reflected probe waves occurring at the HC-PBFs/SMF splicing joints (Fig. 6.2(b)). The optical power reflections ( $\sim 4\%$ ) are much stronger than the backscattered signals and this allows the use of the various techniques developed for multiplexed acoustic sensor (hydrophone) arrays to perform de-multiplexing and de-modulation [110, 127, 134, 176, 177]. These techniques are well developed with phase detection resolution down to the level of  $10^{-5}$  to  $10^{-6}$   $rad/\sqrt{Hz}$  [134].

We here use a dual-pulse heterodyne phase sensitive OTDR technique [178, 179] to detect the PT phase modulation. The system is capable of detecting distributed phase modulation along a sensing HC-PBFs via backscattered probe beam or quasi-distributed phase modulation at multiple sensors by utilizing the reflections at HC-PBFs/SMF joints. The phase detection resolutions for the two scenarios are on the order of  $10^{-3}$  and  $10^{-4}$   $rad/\sqrt{Hz}$ , respectively. Based on the calculated magnitude of PT phase modulation in Section 2.1, such a phase detection resolution would enable distributed detection of trace-gas over a distance of kilometers or quasi-distributed gas detection with tens of sensors with a pump power of hundreds of mW.

In real applications, gas concentration would not be uniform along the sensing HC-PBFs and the required detection limit could vary significantly for different applications. However, the formulation and discussion provided here would provide useful references to the design of different PT distributed gas sensing systems.

## 6.2 Experimental set-up

The setups for the distributed and quasi-distributed sensing experiments are similar and shown schematically in Fig. 6.3. The system comprises three main blocks: the pump, probe and sensing blocks. The pump block provides a modulated pump beam that is fed into the sensing fibre to produce distributed PT phase modulation along the gas-filled HC-PBFs. Here we use a distributed-feedback laser (DFB) with a nominal central wavelength at 1530.37 nm, corresponding to the P(9) absorption line of  $C_2H_2$ . The pump is amplified by an erbium-doped amplifier (EDFA 2) and the accompanying ASE noise is filtered out by an optical filter (Filter 2) centered at the pump wavelength with a 3-dB pass-band of  $\sim 1$  nm. The amplified pump is modulated in intensity by an acoustic-optic modulator (AOM 3).

The probe block is a dual-pulse heterodyne phase-sensitive OTDR, and the details can be found in [178, 179]. A narrow linewidth probe laser with wavelength around 1550 nm is used. The wavelength of the probe is selected to be away from the gas absorption line and its optical frequency is denoted as  $f_0$ . The probe beam is separated into two by an optical fibre coupler, and the two beams are then pulsed and frequency-shifted by the amount of  $f_1$  and  $f_2$ , respectively, by AOM 1 and AOM 2. Subsequently, the probe pulses with frequency difference  $\Delta f = f_1 - f_2$  are temporally offset by  $\tau_d = L_d/v$  through a fibre delay line of length  $L_d$  ( $v$  is light speed in the delay fibre), and combined by a second optical fibre coupler. The pair of probe pulses are then combined with the modulated pump by a wavelength-division multiplexer (WDM) and launched into the sensing fibre. The operating windows of the WDM are centered at 1550 nm and 1531 nm, respectively, both with 3-dB bandwidth of  $\sim 15$  nm. The same WDM is also used to separate the backscattered/reflected pump and probe, and the residual pump beam is removed by an optical filter (Filter 1) before the photo-detector (PD).

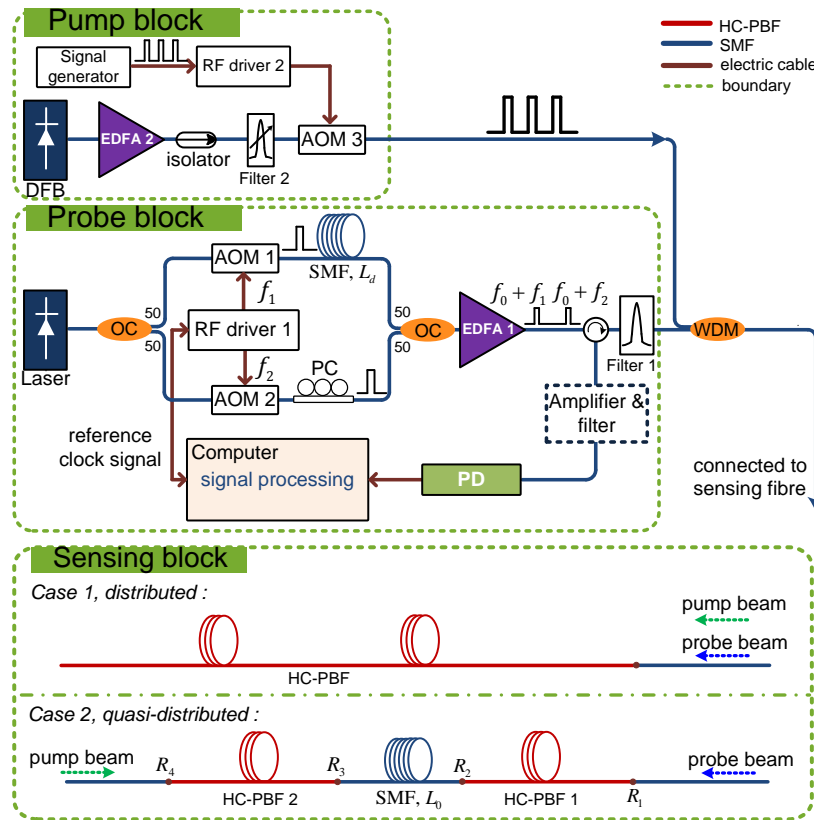


Fig. 6.3 Schematic of the experimental set-up. The sensing could be either distributed (Case 1) or quasi-distributed sensing manner (Case 2). The green dashed arrows indicate the pump directions. AOM: acoustic-optic modulator; SMF: single-mode fibre; EDFA: erbium-doped amplifier; PD: photo-detector; PC: polarization controller; DFB: distributed feedback laser. WDM: wavelength-division multiplexer. OC: optical fibre coupler.

The backscattered or reflected signals of the two probe pulses would interfere with each other and generate a heterodyne signal at the PD. The frequency of this signal equals to the beat frequency  $\Delta f$ , and the phase of the signal contains the information of PT phase modulation with its magnitude proportional to the gas concentration and the pump power level. The information about the spatial location, magnitude and frequency of PT phase modulation are recovered by post-processing the heterodyne signals, which will be described in Section 4.

For distributed sensing based on backscattered probe beams, the heterodyne signal at the PD output is the result of interference between the pair of the backscattered probe waves with a time delay of  $\sim \tau_d$ . The spatial resolution of the dual

pulse OTDR system may be estimated by  $(\tau_d + w_p)v_{\text{PBF}}/2$  with  $w_p$  representing the probe pulse width and  $v_{\text{PBF}}$  is the light speed in the HC-PBFs. Considering the relatively weak backscattered power level, an optical amplifier and filter module (the dashed-line rectangular box in the Fig. 6.3) may need to be used to boost the signal level before the PD.

For quasi-distributed sensing, the heterodyne signal is the result of interference between the two back-reflected pulses at the HC-PBFs/SMF joints, and the length of the sensing HC-PBFs needs to match with that of the temporal offset of the probe pulses to observe the interference signals. Since the reflected signals are considerably larger than the backscattering signals, the amplifier and filter module before the PD may not be necessary.

It should be pointed out that, for both distributed and quasi-distributed sensing systems, the pump and probe could be either co-propagating or counter-propagating. Since the magnitude of PT phase modulation depends on the pump power level, a variety of pumping schemes such as co-, counter-, or even bi-direction pumping could also be used to enhance the magnitude and uniformity of PT phase modulation along the sensing fibre [180–184].

### 6.3 Signal processing

Taking a quasi-distributed system with  $H$  sensors (the  $i$ th HC-PBFs sensor is labelled as  $S_i, i = 1, 2, \dots, H$ ) as an example, the sequences of the probe pulses at different locations of the system are shown in the Fig. 6.4 (for  $H = 2$ ). For each electric pulse (trigger, as shown in Fig. 6.4(a)) applied to the RF driver 1 in Fig. 6.3, dual probe pulses with different frequencies are generated (Fig. 6.4(b)) and launched into the sensing fibre. For each trigger pulse  $n$  ( $n = 1, 2, \dots, N$ ), the waveform (the reflected optical signals from the sensing block) at the output of the PD contains  $H$  groups of pulses, each corresponding to a particular sensor (for two sensors, the groups are

labelled as  $S_1, S_2$  in Fig. 6.4(c)). Under the condition that the optical path lengths of the sensors match well with the delay fibre length  $L_d$ , there will be three pulses in each of the groups, as illustrated in the Fig. 6.4(c). The front pulse is the first probe pulse reflected from the splicing joint  $R_1$  (see Fig. 6.3) with the optical frequency of  $f_0 + f_2$  while the rear pulse is the second probe pulse reflected from the splicing joint  $R_2$  with the optical frequency of  $f_0 + f_1$ . The middle pulse is the coherent beating of the first probe pulse reflected from  $R_2$  and the second probe pulse reflected from  $R_1$ . The phase of the beat signal, with frequency of  $\Delta f = |f_2 - f_1|$ , is the optical phase difference between the dual pulses, which contains the information about the PT phase modulation accumulated over the length of sensor  $S_i$ . By extracting the middle pulses of the groups, the beat frequency component  $\Delta f$  can be obtained and then PT phase modulation can be recovered [179].

The PD output is then sampled at a much faster rate than the repetition rate of the probe pulses, and the sampling is triggered by a clock signal that is synchronized with the AOM-driving pulse (generated by RF driver 1) (Fig. 6.4(d)). For each trigger pulse, the PD output waveform is sampled  $M$  times, and the start of the sampling is signified by a positioning pulse that has a fixed time delay with respect to the trigger pulse. This positioning pulse is used to correlate the subsequent sampled time-series data to locations along the sensing fibre. For a sequence of  $N$  trigger pulses (generating  $N$  pairs of probe pulses), a matrix with dimension of  $A = N \times M$  is then created. The row  $N$  indicates the number of repetitions of the probe pulses and the column  $M$  indicates the number of sampled data points within a single repetition period  $T_{\text{rep}}$ , as shown in Fig. 6.4(d). However, for quasi-distributed sensing system, not all these data need to be used. We only need to select  $H$  columns at the sampling positions  $m_i, i = 1, 2$  (for  $H = 2$ ), corresponding to the beat frequency component (middle pulse) of each sensor. Hence, the useful data matrix is reduced to  $N \times H$ , with  $H$  representing the number of sensors, and  $N$  the total number of sampling data points for an individual sensor.

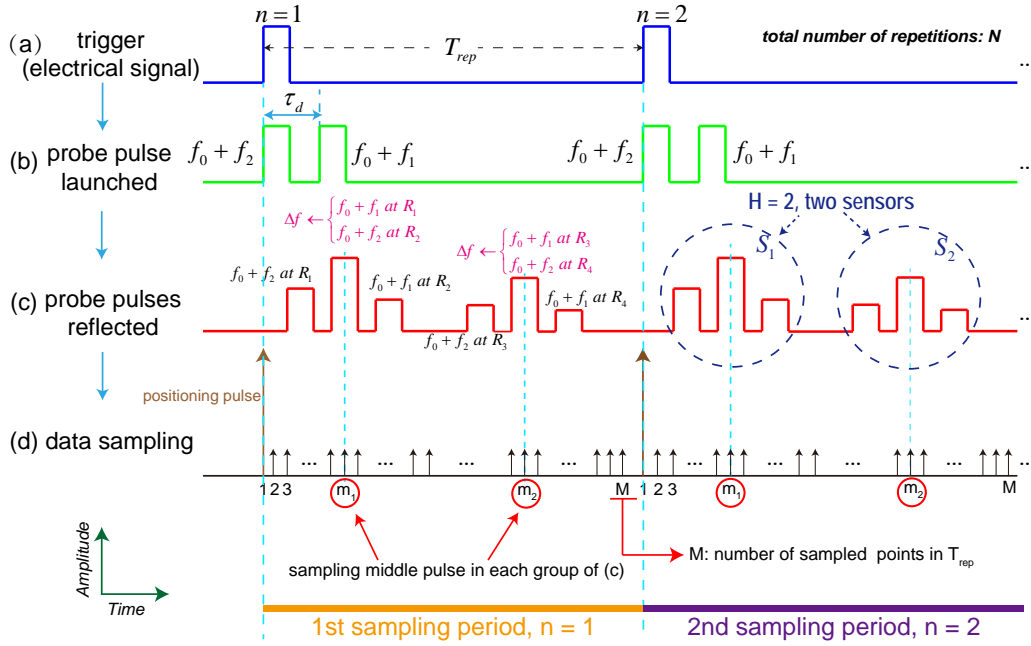


Fig. 6.4 Illustration of pulse sequence at different locations in the system and sampling at the system output, for quasi-distributed sensing system. (a) trigger pulses for AOM; (b) dual pulses launched in to the sensing block with a temporal offset; (c) pulse waveform reflected from the sensing block; (d) data sampling at the PD output. The left-bottom corner indicates the coordinate directions.

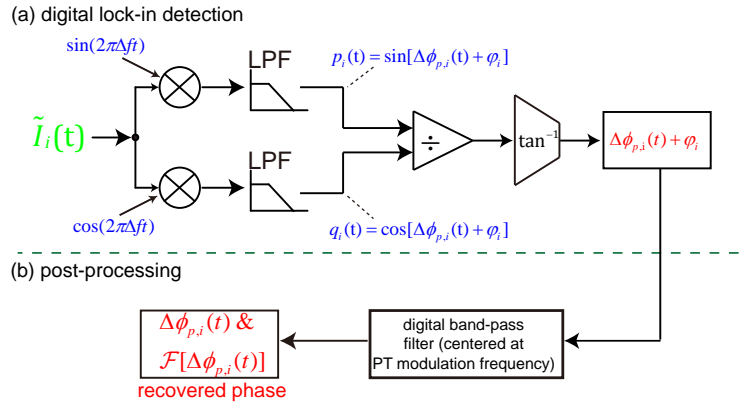


Fig. 6.5 Illustration of digital lock-in detection and subsequent processing to obtain the PT phase modulation signals [185].

The  $i$ th column of the data matrix is then a sampled version of the analog beating signal of sensor  $S_i$ , which is an interferometric signal given by:

$$\tilde{I}_i(t) = I_i \{ 1 + v_i \cos[2\pi\Delta f t + \Delta\phi_{p,i}(t) + \phi_i] \} \quad (6.2)$$

where  $I_i$  is the average signal level,  $v_i$  is the fringe visibility and  $\varphi_i$  is the initial phase and  $\Delta\phi_{p,i}(t)$  is the PT signal, whose magnitude is proportional to the gas concentration and pump power at sensor  $S_i$ , as indicated in Eq. (6.1). The frequency of  $\Delta\phi_{p,i}(t)$  is the modulation frequency of the pump beam. The time  $t$  is a digitized time sequence.

The recovery of the PT phase modulation (i.e. determining  $\Delta\phi_{p,i}(t)$ ) is implemented with an algorithm that may be briefly described as a digital lock-in detection, as shown in Fig. 6.5: the interferometric signal is mixed with the orthogonal components of a sinusoidal signal with frequency of  $\Delta f$ , followed by low pass filters to generate a pair of orthogonal signals  $p_i(t) = \sin[\Delta\phi_{p,i}(t) + \varphi_i]$  and  $q_i(t) = \cos[\Delta\phi_{p,i}(t) + \varphi_i]$ . Then, a digital arc tangent algorithm is used to determine the phase term  $\Delta\phi_{p,i}(t) + \varphi_i$ , which contains the information of the PT phase modulation [186]. By applying a digital band-pass filter centered at the PT modulation frequency, the PT phase modulation  $\Delta\phi_{p,i}(t)$  can be recovered and its frequency spectrum can be obtained by using Fourier transform.

For distributed sensing, the signal processing is similar to that in quasi-distributed sensing, as illustrated in Fig. 6.6. However, for each trigger pulse or sampling period  $T_{\text{rep}}$ , there will be two backscattered OTDR traces, corresponding to two probe pulses backscattered from the sensing fibre. The traces have a frequency difference  $\Delta f$  and a temporal offset  $\tau_d$ , and interference between them generates a continuous trace of beat signal with its phase containing the PT phase modulation distributed along the fibre, as shown in the Fig. 6.7. To recover this distributed phase modulation, all the sampled data points during each repetition period  $T_{\text{rep}}$  need to be used and the final data matrix dimension will be  $A = N \times M$ . The phase of the beat signal recovered from each column of data correlates to the gas concentration over a specific section along the sensing fibre.

The frequency resolution of the spectrum is determined by the total number of data points used to perform Fourier transform. Here we use a Kaiser-Bessel data

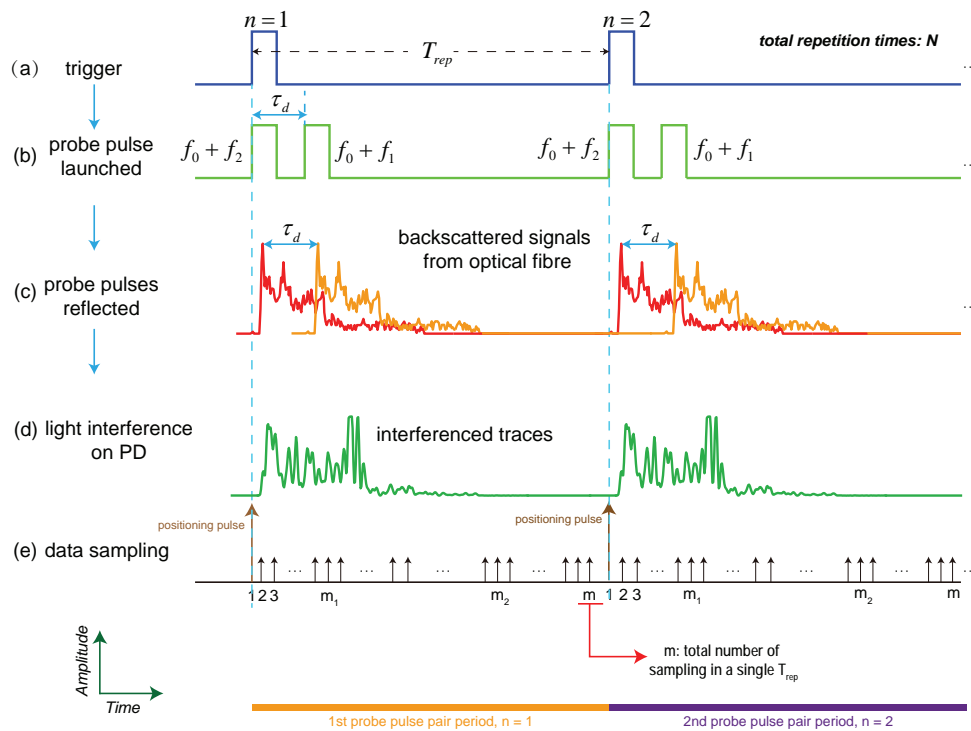


Fig. 6.6 Illustration of signal processing in distributed sensing system.

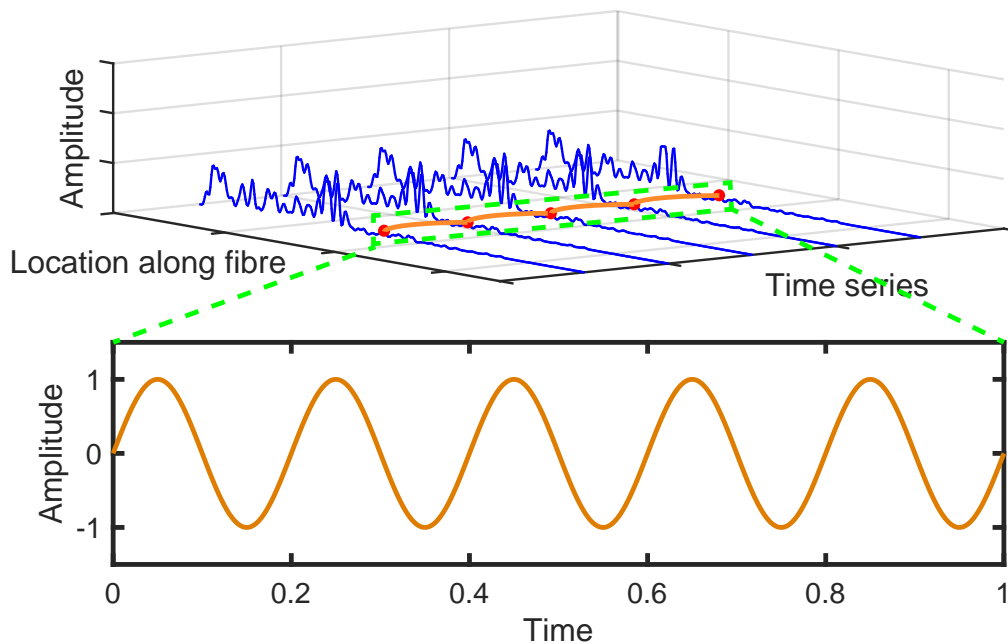


Fig. 6.7 Schematic of procedure to obtain time-dependent phase modulation signals in distributed sensing system.

window with parameter  $\alpha \sim 1.08$  as the narrow-band digital band-pass filter, the effective noise bandwidth (ENBW) would be  $\sim 1.1$  times of the frequency resolution

[187]. For the quasi-distributed experiment (Section 5), the number of data points used for Fourier transform is 1071104 with a final sampling rate of 10 kHz, giving an ENBW of  $\sim 0.01$  Hz [187]. For the distributed experiment (Section 6), the number of data points is 16926 with a sampling rate of 20 kHz, giving an ENBW of  $\sim 11.8$  Hz.

## 6.4 Quasi-distributed sensing experiment

A quasi-distributed system with two sensors was tested with the dual-pulse heterodyne phase detection system. As shown in Fig. 6.3 (Case 2, quasi-distributed), two sections of the HC-PBFs are connected via SMFs to form the sensing cable. The length of each HC-PBFs section (sensor) is about  $L_t \sim 28$  m. The SMF between the two HC-PBFs sensing sections is sufficiently long so that the reflected pulses from the different sensors are separated in time domain. The pump beam is square-wave modulated in intensity with an AOM at the frequency of 630 Hz and is launched into the sensing fibre from the opposite direction with respect to the probe beam.

The probe beam is a low noise fibre laser (NKT Koheras Basik E15) with narrow linewidth ( $< 0.1$  kHz). It is pulsed by the two AOMs with frequency shifts of  $f_1 = 100.05$  MHz (AOM 1) and  $f_2 = 100$  MHz (AOM 2), respectively, giving an optical frequency difference of  $\Delta f = 50$  kHz. The pulse widths of the probe pulses are  $w_p \sim 140$  ns and the repetition rate is  $f_{\text{rep}} = 200$  kHz. The length of the delay SMF in unbalanced Mach-Zehnder interferometer (MZI) is  $\sim L_d = 38$  m, approximately twice of the optical path length of the sensing HC-PBFs. This ensures that the dual pulses overlap at the PD after experiencing reflections at the front and rear ends of the HC-PBFs sensors, generating the beat signals.

In preparation of HC-PBFs gas cells, both ends of HC-PBFs were mechanically spliced to SMF and the  $C_2H_2$  were pressured into the HC-PBFs by applying a pressure difference on one end of the HC-PBFs. The mechanical splicing method

will be described in the following sections. For proof-of-concept purpose, we use 28-m-long HC-PBFs gas cell and it is necessary to pressure the gas over 2 days to make ensure that the HC-PBFs could be sufficiently filled by  $C_2H_2$ . However, uniformity of gas distribution may still exist along the HC-PBFs. For a fast response and practical gas cell, the micro-holes could be drilled along the HC-PBFs, which will be discussed in Section 7. The light-gas interaction length (i.e., 28-m-long HC-PBFs here) should be matched with the time delay  $\tau_d$  between the two probe pulses. Smaller  $\tau_d$  enables a shorter HC-PBFs gas cell.

The measured output from the PD is shown in Fig. 6.8, which agrees with the expected pulse waveform as shown in Fig. 6.4(c). The  $1.28\ \mu s$  time delay between the two groups of pulses corresponds to the length of the SMF (i.e.,  $L_0 \sim 128\ m$  as shown in Fig. 6.3) between the two HC-PBFs sensors.

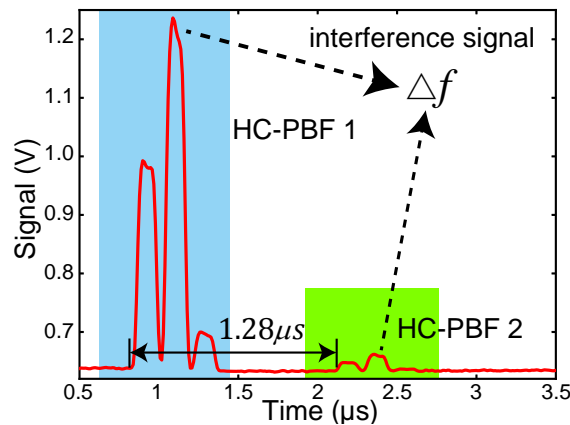


Fig. 6.8 A typical measured output from the PD for a quasi-distributed sensing system with two HC-PBFs sensors.

By following the signal processing procedures outlined in Section 4, the phase modulation corresponding to the two HC-PBFs sensors can be obtained. Figs. 6.9(a) and 6.9(b) show respectively the frequency spectrums of HC-PBFs 1 filled with  $\sim 2700\ \text{ppm } C_2H_2$  and HC-PBFs 2 filled with  $\sim 44\ \text{ppm } C_2H_2$ , both buffered with  $N_2$ . The signal-to-noise ratio (SNR) are 65 dB and 73 dB for HC-PBFs 1 and HC-PBFs 2, respectively. The noise floor is measured when the pump beam is turned off.

The pump and probe beams are counter-propagating in the sensing fibre, and the peak pump power delivered to HC-PBFs 2 and HC-PBFs 1 are estimated to be  $\sim 55$  mW and  $\sim 7.8$  mW, respectively. For HC-PBFs 2, the LOD in terms of noise-equivalent gas concentration for SNR = 1 is  $\sim 10$  ppb with an ENBW of 0.01 Hz or  $5.5 \text{ ppb} \cdot \text{W} / \sqrt{\text{Hz}}$  when normalized to 1 W peak pump power and 1 Hz ENBW. For HC-PBFs 1, it is  $\sim 1.5$  ppm or  $117 \text{ ppb} \cdot \text{W} / \sqrt{\text{Hz}}$ . It should be mentioned that since HC-PBFs 1 is filled with higher concentration of  $C_2H_2$  gas, the pump light is heavily absorbed and the effective absorption length is only  $L_{\text{eff}} \sim 3.2 \text{ m}$ , as estimated by using  $L_{\text{eff}} = [1 - \exp(-\alpha_0 C L_t)] / (\alpha_0 C)$  [188].

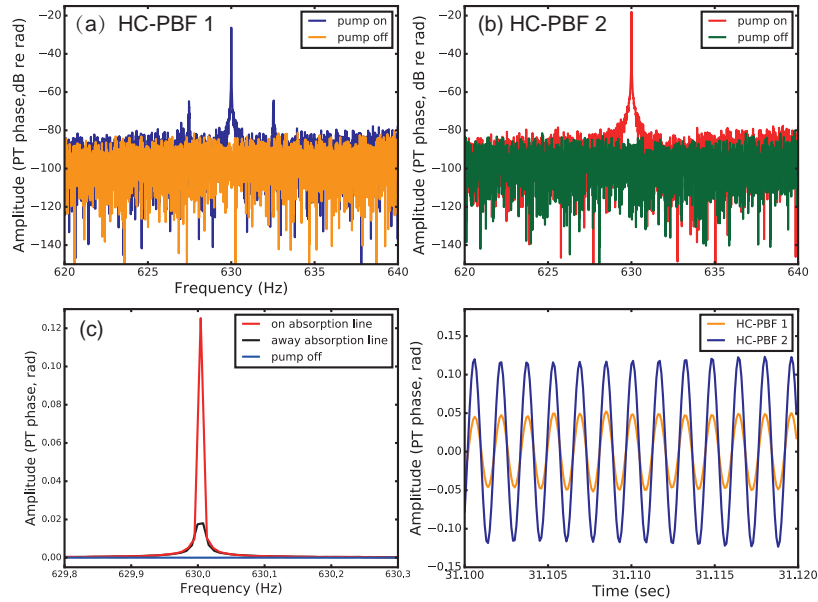


Fig. 6.9 The recovered frequency spectrums of the recovered PT phase modulation for (a) HC-PBFs 1 with 7.8 mW pump power and  $\sim 2700$  ppm  $C_2H_2$  in  $N_2$ , (b) HC-PBFs 2 with 55 mW pump power and  $\sim 44$  ppm  $C_2H_2$  in  $N_2$ . The dB re rad is define as  $20 \log_{10}(x \text{ rad} / 1 \text{ rad})$ . The measured magnitude of PT phase modulation is 0.05 rad (-26 dB re rad) for HC-PBFs 1 and 0.13 rad (-17.7 dB re rad) for HC-PBFs 2; (c) The spectrum of the recovered phase modulation for HC-PBFs 2 when the pump was tuned to the center of the absorption line, away from the absorption line, and turned off. (d) The time domain waveforms of the recovered PT phase modulation for the two sensors.

The frequency spectrums of the recovered phase modulation for HC-PBFs 2 with different pump settings are shown in Fig. 6.9(c) in a linear scale. As can be seen,

tuning the wavelength of pump away from the absorption line does not reduce the signal down to the noise floor. This could result from the residual Kerr-induced cross-phase modulation, due to the mismatch between the length of the sensing HC-PBFs  $L_t$  and the delay fibre  $L_d$ , as well as background absorption. However, the magnitude of undesired phase modulation is considerably smaller (at least 5 times smaller for the case shown in Fig. 6.9(c)) than that of PT phase modulation, and it would not seriously affect the estimation of the LOD.

The minimum detectable phase modulation of the dual-pulse detection system may be determined from the noise floor when the pump is switched off. From Figs. 6.9(a) and 6.9(b), this noise floor is  $\sim -91$  dB re rad (with respect to 1 rad) with a ENBW of  $\sim 0.01$  Hz, corresponding to a phase sensitivity of  $\sim 2.8 \times 10^{-4} \text{ rad}/\sqrt{\text{Hz}}$ , for both HC-PBFs sensors. Assuming that the 28-m-long HC-PBFs is filled with low concentration  $C_2H_2$  uniformly and the pump power levels delivered to HC-PBFs 1 and HC-PBFs 2 are respectively 7.8 mW and 55 mW, the theoretical LODs may be determined by comparing the magnitude of PT phase modulation calculated from Eq. (6.1) with that noise floor, giving  $\sim 724 \text{ ppb}/\sqrt{\text{Hz}}$  for HC-PBFs 1 and  $\sim 103 \text{ ppb}/\sqrt{\text{Hz}}$  for HC-PBFs 2, or  $\sim 5.7 \text{ ppb} \cdot W/\sqrt{\text{Hz}}$  for both sensors. The theoretical LOD is close to that experimentally measured result for HC-PBFs 2 but deviates from that measured in HC-PBFs 1. The discrepancy may be resulted from the inhomogeneous gas distribution along the HC-PBFs.

By using a reference interferometer to minimize the common mode noise from the laser sources and external disturbance [15], it is possible to achieve a  $\sim 20$  dB reduction in noise floor within the frequency range of 20 Hz to 1 kHz [179]. This would improve the phase detection limit down to  $10^{-5} \text{ rad}/\sqrt{\text{Hz}}$  and could significantly improve LOD for gas detection.

## 6.5 Distributed sensing experiment

Distributed gas detection system was performed with a similar experimental setup. The pump beam is, however, modulated at 500 Hz and made to co-propagate with probe beam along the sensing fibre (see Fig. 6.3, Case 1, distributed). The peak pump power delivered to the sensing HC-PBFs is  $\sim 62.5$  mW. The probe source is a single frequency laser source (RIO ORION laser module) with wavelength centered at 1550 nm. The two independent backscattered traces, corresponding to the two probe pulses, interfere with each other to generate beat frequency components [178]. An EDFA and an optical filter are used before PD to amplify the weak backscattered signals as shown in the dashed-box in Fig. 6.3. The pulse widths of probe beams are  $w_p \sim 50$  ns and the length of delay SMF is  $L_d \sim 36$  m, corresponding to a spatial resolution  $\sim 30$  m in HC-PBFs. Other parameters are the same as the quasi-distributed experiments.

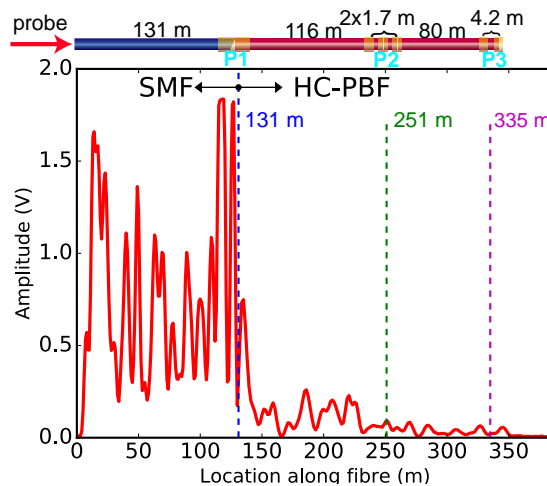


Fig. 6.10 Measured interfering backscattering traces with pump power was turned off. There are three sections labelled as P1, P2 and P3, corresponding to the spatial locations respectively at 131 m, 251 m and 335 m with the lengths of 131 m SMF, 120 m HC-PBFs and 84 m HC-PBFs. The upper diagram is the illustration of fibre alignment of sensing block. At P1, the mechanical splicing between an angle-cleaved SMF and HC-PBFs is used. A  $\sim 116$  m long HC-PBFs is then mechanical spliced to a  $\sim 3.4$  m short HC-PBFs (P2), which consists two  $\sim 1.7$  m gas-filled HC-PBFs. Another  $\sim 80$  m long HC-PBFs was mechanically spliced at P2, whose end was connected by a  $\sim 4.2$  m gas-filled HC-PBFs at P3.

The sensing fibre comprises five segments of HC-PBFs with respective lengths of  $\sim 116$ ,  $\sim 1.7$ ,  $\sim 1.7$ ,  $\sim 80$  and  $\sim 4.2$  meters, as shown at the top of Figs. 6.10 and 6.11. These segments are connected in series by mechanical splicers, giving a total sensing distance  $\sim 200$  meters. At the splicing joint, a small gap (less than  $4\ \mu\text{m}$ ) is left between the two HC-PBFs, and the details about the mechanical splicing can be found in [189]. The back-reflections from the joints between the HC-PBFs are measured to be on the order of  $10^{-6}$ , comparable with the magnitude of backscattering coefficient from the HC-PBFs [172, 190]. The sensing HC-PBFs is mechanically spliced to  $\sim 131$ -m-long SMF for connection to the detection system. The end of SMF is angle-cleaved to minimize Fresnel reflection back into SMF while the end of HC-PBFs is normal-cleaved with a flat end face [191]. The power reflection from the SMF/HC-PBFs joint is measured to be  $\sim -35$  dB.

Fig. 6.10 shows signal trace detected at the PD output before signal processing, when the pump is off and the HC-PBFs is not filled with  $\text{C}_2\text{H}_2$ . The large signal due to Fresnel reflection can be clearly observed at around P1, which is the joint between SMF and HC-PBFs and at the spatial location of 131 m, followed by the backscattered signals from HC-PBFs.

Gas detection experiments were conducted by filling  $\sim 498$  ppm of  $\text{C}_2\text{H}_2$  gas balanced by  $\text{N}_2$  into short sections of HC-PBFs around spatial location P2 (251 m) and P3 (335 m), as shown in Fig. 6.11. At P2, the gas was pressurized (with  $\sim 3$  atm pressure difference) into the HC-PBFs via the gap of the middle splicing joint, while the gaps of the other two joints were open to atmosphere. At P3, the gas was pressurized into the HC-PBFs via the far end of the fibre with the gap at the splicing joint left open to atmosphere. With such a setup, we believe that the gas would mainly be filled into the short-lengths (i.e.,  $2 \times 1.7 = 3.4\ \text{m}$  around P2 and  $4.2\ \text{m}$  around P3) of the HC-PBFs. According to [67], the pressure-pumped gas-filling process could take  $\sim 0.5$  min and  $\sim 3.5$  min to fill 1.7-m-long and 4.2-m-long HC-PBFs, respectively. For other sections of HC-PBFs, since there is no pressure

difference, the self-diffusion processes would take  $\sim 16$  hrs for filling 1-m HC-PBFs [39]. Hence the sensing lengths could be determined by the lengths of the HC-PBFs around P2 and P3 where the gas pressure differences are applied and the magnitude of PT phase modulation within these sections of HC-PBFs can be calculated by use of Eq. (6.1).

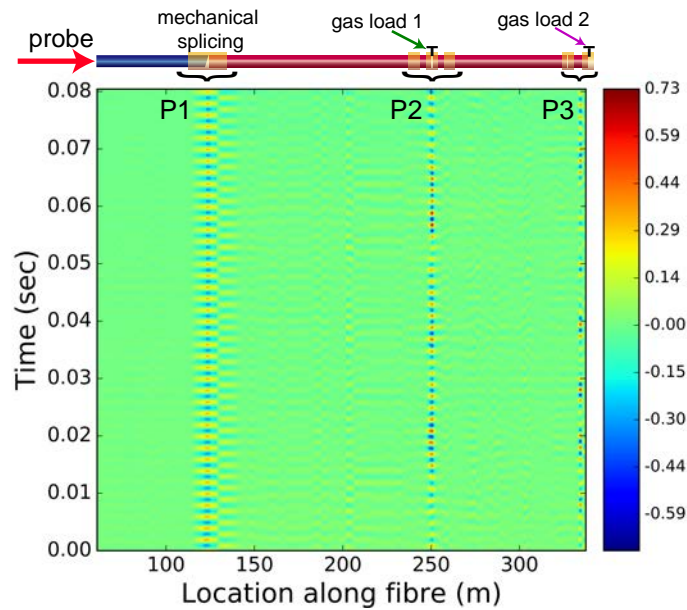


Fig. 6.11 The phase distribution along the sensing fibre. The upper diagram shows the fibre alignment and segments of sensing fibre. The position P1, P2 and P3 corresponds to the spatial location of 131 m, 251 m and 335 m, respectively. The displayed spatial locations range from 60 m to 338 m.

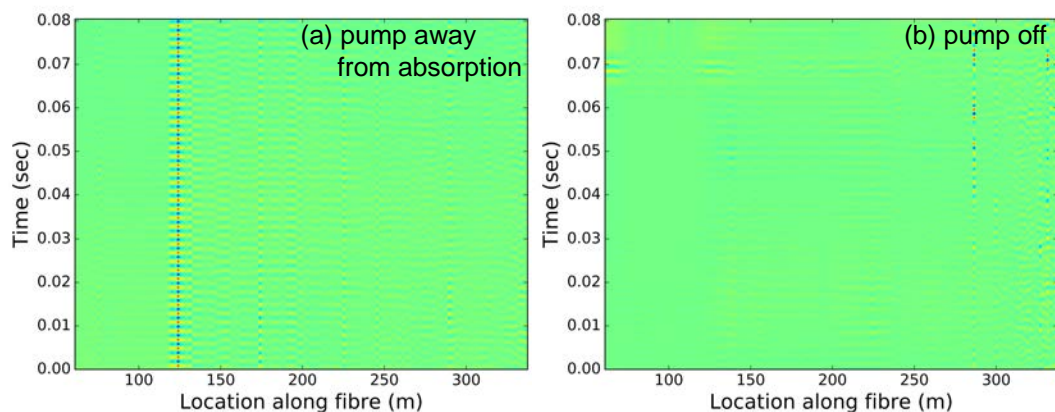


Fig. 6.12 The phase distributed along the sensing fibre with: (a) pump wavelength tuned away from the absorption line; (b) pump beam turned off. The figures share the same color legend as that in Fig.6.11.

The Fig. 6.11 shows the recovered phase distribution map over the entire 200-m-long HC-PBFs. The presence of gas absorption around P2 and P3 can be clearly observed. The signals around P1 are the result of Kerr-induced cross-phase modulation.

To verify that the phase modulation signals observed in Fig. 6.11 are the results of gas absorption, the phase distributions along the fibre were measured again when pump wavelength is tuned away from the absorption line and when pump is turned off. The results are shown in Figs. 6.12 (a) and 6.12(b), respectively. With the pump wavelength away from the absorption line, the phase modulation signals around P2 and P3 disappear while that around P1 remains. Turning off the pump beam results in the disappearance of all the phase modulation signals. Obviously, the phase modulation signals around P2 and P3 are due to gas-absorption-induced PT phase modulation.

The location and time-varying phase information in the presence of gas absorption can be observed simultaneously in a three dimension display. Fig. 6.13 shows an example of demonstration for the recovered phase modulation signal around P2. The projection in the left coordinate plane shows the location information while that in the rear coordinate plane shows the time-varying phase information. The information about other locations can be also displayed in a similar way.

The recovered phase modulation signals at P2 and P3 are extracted out and further analyzed. Figs. 6.14(a),(c) and (b), (d) shows respectively the time waveforms and frequency spectrums of the signals for the two locations P2 and P3. The LODs can be evaluated from the spectrums by comparing the signal levels with the noise floors measured with pump tuned away from the gas absorption, which is not much different from that measured when the pump is switched off. At P2, the signal and noise floor levels are 0.35 rad (3.4-m-long HC-PBFs) and 0.012 rad, giving a SNR of 29 with a ENBW of 11.8 Hz and a normalized LOD of  $\sim 5.0 \text{ ppm}/\sqrt{\text{Hz}}$  or

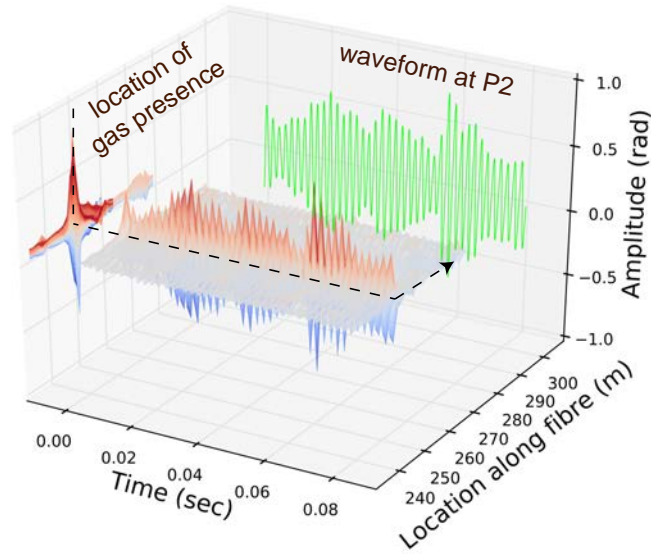


Fig. 6.13 The three dimension demonstration of gas presence at the spatial location P2.

$\sim 312 \text{ ppb} \cdot W / \sqrt{\text{Hz}}$ . Similarly, at P3, the SNR is 9.5 (4.2-m-long HC-PBFs), giving a normalized LOD of  $\sim 15.5 \text{ ppm} / \sqrt{\text{Hz}}$  or  $\sim 970 \text{ ppb} \cdot W / \sqrt{\text{Hz}}$ .

From Figs. 6.14(c) and 6.14(d), the minimum detectable phase modulation of the current detection system can be estimated to be  $\sim 2.93 \times 10^{-3} \text{ rad} / \sqrt{\text{Hz}}$  and  $\sim 4.8 \times 10^{-3} \text{ rad} / \sqrt{\text{Hz}}$  for P2 and P3, respectively. If we assume that 3.4-m-long and 4.2-m-long HC-PBFs around P2 and P3 are uniformly filled with low concentration  $C_2H_2$  balanced by  $N_2$ , by using Eq. (6.1) with peak pump power of 62.5 mW, the theoretical expected LODs are  $\sim 7.8 \text{ ppm} / \sqrt{\text{Hz}}$  (or  $448 \text{ ppb} \cdot W / \sqrt{\text{Hz}}$ ) and  $\sim 10.3 \text{ ppm} / \sqrt{\text{Hz}}$  (or  $\sim 664 \text{ ppb} \cdot W / \sqrt{\text{Hz}}$ ) at P2 and P3, respectively. The theoretical expected LODs are close to that of the measured results and therefore we believe that the gas were mainly filled into the two short HC-PBFs segments around P2 and P3, rather than other sections of HC-PBFs. This means that the lengths of our gas-filled HC-PBFs are much shorter than the spatial resolution  $\sim 30 \text{ m}$  of phase detection system. If the length of gas-filled HC-PBFs matches with the spatial resolution, the LOD of our gas detection system can be further improved.

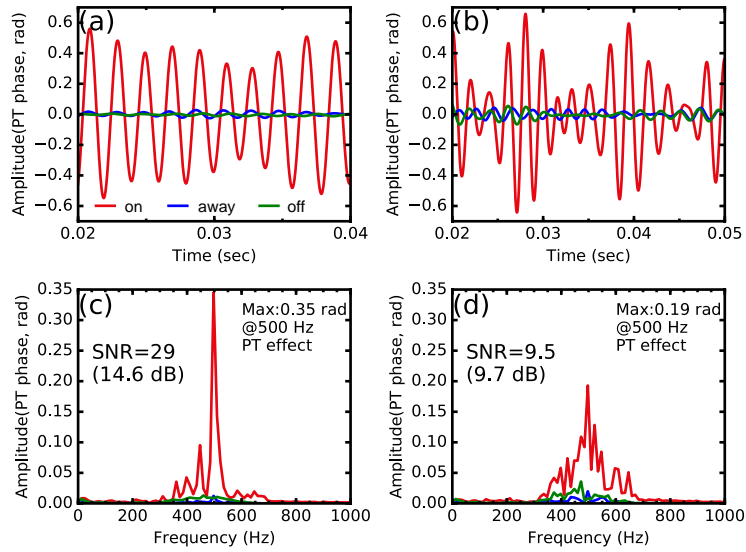


Fig. 6.14 The PT phase modulation signals in time and frequency domain (a) (c) for spatial location at P2 and (b) (d) for spatial location at P3. The signals have been filtered by a digital band-pass filter with central frequency of 500 Hz and bandwidth of 200 Hz. In (c), the signal level is 0.35 rad and the noise floor is 0.012 rad and 0.013 rad when the pump is tuned away from gas absorption and switched off, respectively. In (d), the signal level is 0.19 rad and noise floors are 0.02 rad and 0.01 rad, respectively. The all plots share the same legend shown in (a) as on: aligned to the center of absorption line, away: away from absorption and off: switched off.

## 6.6 Discussion

For the further development of distributed gas detection system with PT interferometry, some important issues need to be addressed:

(i) **Spatial resolution:** the spatial resolution of the current dual-pulse heterodyne OTDR system is  $\sim 30$  m, determined by the probe pulse width and the length of the delay fibre to offset the pulses. The use of narrower pulses in combination of a shorter delay fibre would improve the spatial resolution. However, the magnitude of backscattering signal is pulse-width relevant [192, 193] and a narrower probe pulse would result in a weaker backscattering signal, affecting the SNR at the PD. Since the length of the delay fibre approximately determines the sensing length over which the PT phase modulation is examined by the dual-pulse approach, the use of shorter

delay fibre also reduces the magnitude of the accumulated phase modulation being detected.

(ii) **LOD**: increasing the pump power can increase the magnitude of PT phase modulation and hence improves the SNR and LOD. By using a bi-directional pump scheme, the pump power level can be made more uniform and hence more uniform LOD over the entire sensing distance. The nonlinear threshold of HC-PBFs is significantly higher than that of the conventional SMFs [192, 194, 195], which would enable higher pump power delivered to the HC-PBFs to achieve distributed gas detection with high sensitivity over a long distance.

The SNR could be further enhanced by operating at a higher modulation frequency. It has been shown that the pump intensity could be modulated at a frequency of up to 330 kHz without compromising the efficiency of PT phase modulation [169]. In our current distributed sensing experiment, the pump modulation frequency is 500 Hz, which lies in the low frequency region where the flicker noise or environmental noise may be dominant [16]. The maximum detectable frequency is limited by the relatively low beat frequency (50 kHz) and the pulse repetition rate (200 kHz) of the current dual-pulse detection system. To operate at a higher modulation frequency, the beat frequency and the repetition rate need to increase correspondingly to ensure accurate recovery of the PT phase modulation. This could be at the cost of reducing sensing distance, since the maximum measurable length is inversely proportional to the repetition rate of probe pulse [196, 197].

(iii) **Response time**: the current sensing cable is made of several segments of HC-PBFs connected in series for the reasons that we can easily determine the locations where the trace-gas is loaded into the HC-PBFs and the length of gas-filled HC-PBFs. Future work would use a single long HC-PBFs as the sensing fibre, with many micro-size holes drilled along the fibre by using, for example, a femtosecond laser [65]. It is possible to drill hundreds and more holes along a HC-PBFs with low loss [71] and the response time will be determined by the spacing between the holes

[39]. There are other types of fibres such as negative curvature hollow-core fibres [198] and suspended-core fibres [199, 200] that would allow continuous opening of the fibre core to the outside but more research is needed to access the potential of these fibres for distributed gas detection.

(iv) **Phase detection technique:** here we use a dual-pulse heterodyne phase-sensitive OTDR system to perform distributed phase detection. There are other schemes that are actively being investigated for distributed acoustic sensing (DAS) [201–204] and could be used for detecting the PT phase modulation. Similar to PT gas detection, DAS could be understood as a method to detect the dynamic phase modulation along the fibre. The only difference is that the DAS accounts for the external acoustic-wave 'hitting' the fibre, which induces phase modulation of probe beam. However, the PT phase modulation accounts for the internal gas-absorption-induced phase modulation. The fact that the fixed modulation waveform (e.g., pure sinusoidal wave with a known frequency) for PT gas sensing, as compared with the unpredictable ones for the DAS, would allow better performance in terms of phase detection resolution/accuracy.

(v) **Implications of laser power levels:** Currently we used a periodically modulated continuous-wave laser with peak power of 62.5 mW, corresponding to a peak light intensity of  $2.5 \times 10^5 \text{ W/cm}^2$  in the hollow-core. With such an intensity level, the temperature rise in the central hollow-core filled with 1% concentration  $\text{C}_2\text{H}_2$  is small and below 1 K. For longer distance sensing that requires higher pump power and if applications also involve higher gas concentration, the temperature rise could be significant to cause burning or even explosion. The LOD of the distributed sensing system depends on the averaged power level of the backscattered probe beam. For current system, we used a pulse probe source with  $\sim 35$  mW peak power input HC-PBFs, 50 ns pulse duration and 200 kHz repetition rate, and achieved satisfactory results. Increasing sensing distance will cause lower backscattered power level of the probe beam from the far end, which would require the use of a probe source with

higher power or an optical receiver with higher sensitivity. These would be topics for future study.

(vi) **Capability of multi-gases sensing:** At this time, we only demonstrate the capability of gas sensing for single gas components. However, it is feasible that our system can be extended to multi-gases sensing. Absorption lines of many gas molecules (like  $C_2H_4$ ,  $CH_4$ ) can occur nearly the C-band, there are possible overlaps of gas absorption lines between different gas molecules. By use of different modulation frequencies for different gas molecules at different absorption lines, with the help of curve analysis and algorithms, we still believe that we can achieve high-sensitive detection of the mixture composed of a variety of gas components.

## 6.7 Summary

An optical fibre distributed spectroscopic gas detection system based on PTI is described. The system uses a HC-PBFs as the sensing fibre and a dual-pulse heterodyne phase-sensitive OTDR to detect the absorption-induced PT phase modulation along the fibre. The use of low-loss HC-PBFs enables strong spectroscopic light-gas interaction within the hollow-core over a long distance, allowing label free distributed gas detection with high sensitivity and avoiding complex procedures to coat fibres with gas-sensitive materials. The use of PTI with a modulated pump beam enables zero-background gas detection with significantly higher sensitivity over the previous direct absorption-based sensors. Experiment with a two-sensor quasi-distributed system demonstrated a LOD down to  $\sim 10$  ppb acetylene with a pump power level of  $\sim 55$  mW and a noise bandwidth of 0.01 Hz. Distributed sensing experiment with  $\sim 200$ -meter-long HC-PBFs demonstrated a LOD of  $\sim 5$  ppm with  $\sim 63$  mW pump power and 10 Hz noise bandwidth. The spatial resolution of the current distributed sensing system is limited to  $\sim 30$  m by the dual-pulse OTDR, but it is possible to reduce down to 1 meter or smaller by optimizing the system parameters. The PTI

system operates at telecom wavelength band and could be developed for distributed gas sensing over long distances (kilometers) with high sensitivity and selectivity.

# Chapter 7

## Conclusions and future work

### 7.1 Conclusions

In this thesis, the mechanism and dynamics of PT phase modulation in HC-PBFs have been investigated both theoretically and experimentally. A numerical model has been proposed to explain well the experimental results using a pulsed pump source. The modulation frequency dependence of PT signal in HC-PBFs has also been analyzed and the theoretical predictions agree well with the measured results. Furthermore, an optimized PT interferometry has been demonstrated with a modified Sagnac phase demodulation system. To extend the applications of PTI, the distributed PT gas spectroscopy has been primarily presented.

Firstly, the mechanism and dynamics of PT phase modulation in HC-PBFs was investigated and a numerical model was proposed. Both the theoretical analysis and experimental results show that the thermal conduction is the dominant process for PT phase modulation in HC-PBFs. Using a pulsed pump source, it has been found that the PT signal would increase as increasing the pump pulse durations until  $1.2\mu s$ , which is determined by the thermal conduction time from center of hollow core to the silica boundary. After this critical value of  $1.2\mu s$ , the PT signal demonstrates no significant changes. Therefore we may conclude that  $1.2\mu s$  is the optimized

value of pump pulse duration. The normalized magnitude of PT phase modulation is calculated to be  $1.517 \text{ rad} \cdot \text{cm} \cdot \text{mW}^{-1} \cdot \text{m}^{-1}$  in terms of gas absorption coefficient or  $1.767 \times 10^{-6} \text{ rad} \cdot \text{ppm}^{-1} \cdot \text{mW}^{-1} \cdot \text{m}^{-1}$  in terms of  $C_2H_2$  gas concentration with absorption at P(9) line. On the other hand, the leading and trailing parts of PT signal using pulsed pump source is affected by the thermal relaxation time of gas molecules and also the thermal conduction time. Furthermore, the core size of hollow core could also impose a stringent effect on the efficiency of PT phase modulation in HC-PBFs. With larger core size while the beam radius remain fixed, it yields a larger PT signal under the same pump power and length of sensing fibre. The probe wavelength indicated in this thesis is assumed to be 1553.33 nm for all our analysis and experiments.

Secondly, an optimized PT interferometry has been demonstrated. At the beginning, the pump modulation frequency dependence of PT phase modulation was analyzed in both theory and experiments. Using different CW modulation frequencies of pump source, the PT signal will remain nearly unchanged until the modulation frequency increase up to  $\sim 330 \text{ kHz}$ . For modulation frequency larger than  $\sim 450 \text{ kHz}$ , the PT signal will decrease dramatically as the increase of modulation frequency. This is the basic choice for our further design of PT interferometry. A modified Sagnac interferometer using a  $3 \times 3$  loop coupler has been proposed to achieve a stable operation while remain high sensitivity. It has been shown that with peak pump power of  $\sim 45.6 \text{ mW}$  and modulation frequency of 25 kHz at proper frequency of Sagnac interferometer, the minimum detectable gas concentration can be down to 67 ppb for  $C_2H_2$  detection using a 1.1-m-long HC-PBFs and 1-s integration time. The long term stability over  $\sim 5 \text{ hrs}$  has been tested and the maxima-to-minima amplitude fluctuation is about  $\sim 1\%$ . Meanwhile, the normalized magnitude of PT phase modulation is determined to be  $8.85 \times 10^{-7} \text{ rad} \cdot \text{ppm}^{-1} \cdot \text{mW}^{-1} \cdot \text{m}^{-1}$  in terms of  $C_2H_2$  gas concentration or  $0.76 \text{ rad} \cdot \text{cm} \cdot \text{mW}^{-1} \cdot \text{m}^{-1}$  in terms of gas absorption coefficient, for PT phase modulation in HC-PBFs using CW intensity

modulated pump source and with modulation frequency  $< 330\text{kHz}$ . For PT phase modulation in free-space optics, we also compared our numerical model with the experimental results and the normalized magnitude of PT phase modulation could be  $0.617 \cdot \text{rad} \cdot \text{cm} \cdot \text{mW}^{-1} \cdot \text{m}^{-1}$  for a typical system with GRIN lens and pump beam radius of 0.5 mm. The reasons to choose HC-PBFs as an ideal gas cell for PT interferometry have been discussed.

Finally, the distributed gas sensing with optical fibre PT interferometry has been presented. The dual-pulse heterodyne phase sensitive system has been adapted to both quasi-distributed and distributed gas detection. For quasi-distributed sensing, by using 28-m-long HC-PBFs as a sensor, the minimum detectable gas concentration could be down to  $\sim 10\text{ppb}$  with only 55 mW peak pump power or  $5.5\text{ppb} \cdot \text{W} / \sqrt{\text{Hz}}$ . For distributed sensing, the minimum detectable gas concentration is  $\sim 5\text{ppm}$  with peak pump power of 62.5 mW or  $\sim 312\text{ppb} \cdot \text{W} / \sqrt{\text{Hz}}$ . Both the sensitivities can be further improved. The detectable sensing length of HC-PBFs can be extended to over km. The spatial resolution of the distributed sensing system is currently  $\sim 30\text{m}$  and can be further optimized and possibly down to 1 m. The use of other micro-structure fibre, e.g. the suspended-core fibres, can also be applied as an distributed gas sensing platform, which makes our system can be developed in a broad sense. The currently demonstrated distributed gas sensing system is adaptable with the other distributed acoustic sensing system using conventional silica fibre, which makes our system much more attractive and extendable.

## 7.2 Future work

There are still some future works that should be addressed:

(i) Design the PT devices with HC-PBFs: since the PT effect can result in a phase modulation with a relatively fast speed, it could be possible to design a PT devices using HC-PBFs, e.g. optical switch, phase modulator.

(ii) Improving the PT efficiency: current PT phase modulation in HC-PBFs presents relatively low PT phase modulation. Improvement of PT efficiency can benefit the further development of PTI sensors.

(iii) All-fibre distributed PT gas sensing: currently the use of HC-PBFs actually consists of several segments fibre which is not ideal for a concept of single fibre distributed sensing. It is possible to achieve such a distributed sensing using just a single HC-PBFs as long as kilo-meters.

## References

- [1] P. Werle, F. Slemr, K. Maurer, R. Kormann, and B. Mücke R .and Jänker. “Near-and mid-infrared laser-optical sensors for gas analysis”. In: *Optics and lasers in engineering* 37.2 (2002), pp. 101–114. DOI: [10.1016/S0143-8166\(01\)00092-6](https://doi.org/10.1016/S0143-8166(01)00092-6).
- [2] J.L. Hall. “Nobel Lecture: Defining and measuring optical frequencies”. In: *Reviews of Modern Physics* 78.4 (2006), p. 1279. DOI: [10.1103/RevModPhys.78.1279](https://doi.org/10.1103/RevModPhys.78.1279).
- [3] J. Ye, L.S. Ma, and J.L. Hall. “Ultrasensitive detections in atomic and molecular physics: demonstration in molecular overtone spectroscopy”. In: *JOSA B* 15.1 (1998), pp. 6–15. DOI: [10.1364/JOSAB.15.000006](https://doi.org/10.1364/JOSAB.15.000006).
- [4] L.S. Ma, J. Ye, P. Dube, and J.L. Hall. “Ultrasensitive frequency-modulation spectroscopy enhanced by a high-finesse optical cavity: theory and application to overtone transitions of  $C_2H_2$  and  $C_2HD$ ”. In: *JOSA B* 16.12 (1999), pp. 2255–2268. DOI: [10.1364/JOSAB.16.002255](https://doi.org/10.1364/JOSAB.16.002255).
- [5] T. Udem, R. Holzwarth, and T.W. Hansch. “Optical frequency metrology”. In: *Nature* 416.6877 (2002), pp. 233–237. DOI: [10.1038/416233a](https://doi.org/10.1038/416233a).
- [6] J. Ye, L.S. Ma, and J.L. Hall. “Ultrasensitive high resolution laser spectroscopy and its application to optical frequency standards”. PhD thesis. COLORADO UNIV AT BOULDER, 1996.
- [7] K.K. Lehmann and A.M. Smith. “Where does overtone intensity come from?” In: *The Journal of chemical physics* 93.9 (1990), pp. 6140–6147. DOI: [10.1063/1.458985](https://doi.org/10.1063/1.458985).
- [8] C. Wang and P. Sahay. “reath analysis using laser spectroscopic techniques: breath biomarkers, spectral fingerprints, and detection limits”. In: *Sensors* 9.10 (2009). DOI: [10.3390/s91008230](https://doi.org/10.3390/s91008230).
- [9] M.R. McCurdy, Y. Bakhirkin, G. Wysocki, R. Lewicki, and F. K. Tittel. “Recent advances of laser-spectroscopy-based techniques for applications in breath analysis”. In: *Journal of Breath Research* 1.1 (2007). DOI: [10.1088/1752-7155/1/1/014001](https://doi.org/10.1088/1752-7155/1/1/014001).
- [10] H. Nakstad and J. T. Kringlebotn. “Oil and gas applications: Probing oil fields”. In: *Nature Photonics* 2 (2008). DOI: [10.1038/nphoton.2008.18](https://doi.org/10.1038/nphoton.2008.18).
- [11] J.A. Wahr, K.K. Tremper, S. Samra, and D.T. Delpy. “Near-infrared spectroscopy: theory and applications”. In: *Journal of cardiothoracic and vascular anesthesia* 10.3 (1996), pp. 406–418. DOI: [10.1016/S1053-0770\(96\)80107-8](https://doi.org/10.1016/S1053-0770(96)80107-8).
- [12] L.B. Kreuzer. “Ultralow gas concentration infrared absorption spectroscopy”. In: *Journal of Applied Physics* 42.7 (1971), pp. 2934–2943. DOI: [10.1063/1.1660651](https://doi.org/10.1063/1.1660651).

- [13] A. Fried and D. Richter. *Infrared absorption spectroscopy*. Ed. by Dwayne Heard. UK: Oxford, 2006.
- [14] D. Heard. *Infrared absorption spectroscopy*. John Wiley Sons, 2008.
- [15] T.G. Giallorenzi, J.A. Bucaro, A. Dandridge, G.H. Sigel, J.H. Cole, S.C. Rashleigh, and R.G. Priest. “Optical fiber sensor technology”. In: *IEEE transactions on microwave theory and techniques* 30.4 (1982), pp. 472–511. DOI: [10.1109/TMTT.1982.1131089](https://doi.org/10.1109/TMTT.1982.1131089).
- [16] C.K. Kirkendall and A. Dandridge. “Overview of high performance fibre-optic sensing”. In: *Journal of Physics D: Applied Physics* 37.18 (2004), R197.
- [17] B. Culshaw. “Optical fiber sensor technologies: opportunities and-perhaps-pitfalls”. In: *Journal of lightwave technology* 22.1 (2004), pp. 39–50. DOI: [10.1109/JLT.2003.822139](https://doi.org/10.1109/JLT.2003.822139).
- [18] K.T.V. Grattan and T. Sun. “Fiber optic sensor technology: an overview”. In: *Sensors and Actuators A:Physical* 82.1 (2000), pp. 40–61. DOI: [10.1016/S0924-4247\(99\)00368-4](https://doi.org/10.1016/S0924-4247(99)00368-4).
- [19] B. Lee. “Review of the present status of optical fiber sensors”. In: *Optical fiber technology* 9.2 (2003), pp. 57–79. DOI: [10.1016/S1068-5200\(02\)00527-8](https://doi.org/10.1016/S1068-5200(02)00527-8).
- [20] A.D. Kersey. “A review of recent developments in fiber optic sensor technology”. In: *Optical fiber technology* 2.3 (1996), pp. 291–317. DOI: [10.1006/oft.1996.0036](https://doi.org/10.1006/oft.1996.0036).
- [21] K. Benuehll. *Fundamentals of molecular spectroscopy*. 1985.
- [22] H.L. Ho, W. Jin, and M.S. Demokan. “Quantitative measurement of acetylene by using external-cavity tunable diode laser”. In: *In Photonics East 99*. International Society for Optics and Photonics., 1999.
- [23] W. Jin, Y.Z. Xu, M.S. Demokan, and G. Stewart. “Investigation of interferometric noise in fiber-optic gas sensors with use of wavelength modulation spectroscopy”. In: *Applied optics* 36.28 (1997), pp. 7239–7246. DOI: [10.1364/AO.36.007239](https://doi.org/10.1364/AO.36.007239).
- [24] G. Stewart, A. Mencaglia, W. Philp, and W. Jin. “Interferometric signals in fiber optic methane sensors with wavelength modulation of the DFB laser source”. In: *Journal of lightwave technology* 16.1 (1998), p. 43.
- [25] J. Sa, Y. Chen, G. Zhang, Z. Zhou, and L. Cui. “Gas cell based on cascaded GRIN lens for optical fiber gas sensor”. In: *In Proc. of SPIE Vol 6723* (2007), pp. 67234I–1. DOI: [10.1117/12.783642](https://doi.org/10.1117/12.783642).
- [26] H.L. Ho, J. Ju, and W. Jin. “Fiber optic gas detection system for health monitoring of oil-filled transformer”. In: *In Proc. of SPIE Vol 7503* (2009), 75030T–1. DOI: [10.1117/12.834904](https://doi.org/10.1117/12.834904).
- [27] B.A. Paldus and A.A. Kachanov. “An historical overview of cavity-enhanced methods”. In: *Canadian Journal of Physics* 83.10 (2005), pp. 975–999. DOI: [10.1139/p05-054](https://doi.org/10.1139/p05-054).
- [28] C.D. Hussey and J.D. Minelly. “Optical fibre polishing with a motor-driven polishing wheel”. In: *Electronics Letters* 24.13 (1988), pp. 805–807. DOI: [10.1049/el:19880548](https://doi.org/10.1049/el:19880548).

- [29] J. Lou, L. Tong, and Z. Ye. “Modeling of silica nanowires for optical sensing”. In: *Optics Express* 13.6 (2005), pp. 2135–2140. DOI: [10.1364/OPEX.13.002135](https://doi.org/10.1364/OPEX.13.002135).
- [30] G. Brambilla. “Optical fibre nanotaper sensors. Optical Fiber Technology”. In: *Optical Fiber Technology* 16.6 (2010), pp. 331–342. DOI: [10.1016/j.yofte.2010.08.009](https://doi.org/10.1016/j.yofte.2010.08.009).
- [31] G. Stewart, W. Jin, and B. Culshaw. “Prospects for fibre-optic evanescent-field gas sensors using absorption in the near-infrared”. In: *Sensors and Actuators B: Chemical* 38.1-3 (1997), pp. 42–47. DOI: [10.1016/S0925-4005\(97\)80169-4](https://doi.org/10.1016/S0925-4005(97)80169-4).
- [32] H.L. Ho, Y.L. Hoo, W. Jin, J. Ju, D.N. Wang, R.S. Windeler, and Q. Li. “Optimizing microstructured optical fibers for evanescent wave gas sensing”. In: *Sensors and Actuators B: Chemical* 122.1 (2007), pp. 289–294. DOI: [10.1016/j.snb.2006.05.036](https://doi.org/10.1016/j.snb.2006.05.036).
- [33] T.M. Monro et al. “Sensing with suspended-core optical fibers”. In: *Optical Fiber Technology* 16.6 (2010), pp. 343–356. DOI: [10.1016/j.yofte.2010.09.010](https://doi.org/10.1016/j.yofte.2010.09.010).
- [34] L. Tong, R.R. Gattass, J.B. Ashcom, and S. He. “Subwavelength-diameter silica wires for low-loss optical wave guiding”. In: *Nature* 426.6968 (2003), p. 816. DOI: [10.1038/nature02193](https://doi.org/10.1038/nature02193).
- [35] Y. Cao, W. Jin, L.H. Ho, and Z. Liu. “Evanescent-wave photoacoustic spectroscopy with optical micro/nano fibers”. In: *Optics Letters* 37.2 (2012), pp. 214–216. DOI: [10.1364/OL.37.000214](https://doi.org/10.1364/OL.37.000214).
- [36] J.B. Jensen et al. “Photonic crystal fiber based evanescent-wave sensor for detection of biomolecules in aqueous solutions”. In: *Optics Letters* 29 (2004), pp. 1974–1976. DOI: [10.1364/OL.29.001974](https://doi.org/10.1364/OL.29.001974).
- [37] W. Chengli et al. “Negative curvature fibers”. In: *Advances in Optics and Photonics* 9.3 (2017), pp. 504–561. DOI: [10.1364/AOP.9.000504](https://doi.org/10.1364/AOP.9.000504).
- [38] T.A. Birks, J.C. Knight, and P.S.J. Russell. “Endlessly single-mode photonic crystal fiber”. In: *Optics Letters* 22.13 (1997), pp. 961–963. DOI: [10.1364/OL.22.000961](https://doi.org/10.1364/OL.22.000961).
- [39] Y.L. Hoo, W. Jin, C. Shi, H.L. Ho, D.N. Wang, and S.C. Ruan. “Design and modeling of a photonic crystal fiber gas sensor”. In: *Applied Optics* 42.18 (2003), pp. 3509–3515. DOI: [10.1364/AO.42.003509](https://doi.org/10.1364/AO.42.003509).
- [40] P.J. Russell. “Photonic-crystal fibers”. In: *Journal of lightwave technology* 24.12 (2006), pp. 4729–4749.
- [41] J.C. Knight, J. Broeng, T.A. Birks, and P.S.J. Russell. “Photonic band gap guidance in optical fibers”. In: *Science* 282.5393 (1998), pp. 1476–1478. DOI: [10.1126/science.282.5393.1476](https://doi.org/10.1126/science.282.5393.1476).
- [42] J. D. Joannopoulos, S. G. Johnson, J. N. Winn, and R. D. Meade. *Photonic crystals: molding the flow of light*. Princeton University Press, 2011.
- [43] P.J. Russell. “Photonic crystal fibers”. In: *Science* 299.5605 (2003), pp. 358–362. DOI: [10.1126/science.1079280](https://doi.org/10.1126/science.1079280).

- [44] R.F. Cregan, B.J. Mangan, J.C. Knight, T.A. Birks, P.S.J. Russell, P.J. Roberts, and D.C. Allan. “Single-mode photonic band gap guidance of light in air”. In: *Science* 285.5433 (1999), pp. 1537–1539. DOI: [10.1126/science.285.5433.1537](https://doi.org/10.1126/science.285.5433.1537).
- [45] L.M. Xiao, M.S. Demokan, W. Jin, Y. Wang, and C.L. Zhao. “Fusion splicing photonic crystal fibers and conventional single-mode fibers: microhole collapse effect”. In: *Journal of lightwave technology* 25.11 (2007), pp. 3563–3574.
- [46] NKT. *HC-1550-02 data sheet*. online.
- [47] C.M. Smith, N. Venkataraman, M.T. Gallagher, and D. Muller. “Low-loss hollow-core silica/air photonic bandgap fibre”. In: *Nature* 424.6949 (2003), p. 657. DOI: [10.1038/nature01849](https://doi.org/10.1038/nature01849).
- [48] P.J. Roberts et al. “Ultimate low loss of hollow-core photonic crystal fibres”. In: *Optics Express* 13.1 (2005), pp. 236–244. DOI: [10.1364/OPEX.13.000236](https://doi.org/10.1364/OPEX.13.000236).
- [49] B. Mangan et al. “Low loss (1.7 dB/km) hollow core photonic bandgap fiber”. In: *In Optical Fiber Communication Conference, Optical Society of America*. PD24 (2004).
- [50] T. Birks. “Reducing losses in photonic crystal fibres”. In: *In Optical Fiber Communication Conference, Optical Society of America* p.OFC7 (2006).
- [51] T.P. Hansen et al. “Air-guiding photonic bandgap fibers: spectral properties, macrobending loss, and practical handling”. In: *Journal of Lightwave Technology* 22.1 (2004), p. 11.
- [52] F. Benabid, F. Couny, J.C. Knight, T.A. Birks, and P.S.J. Russell. “Compact, stable and efficient all-fibre gas cells using hollow-core photonic crystal fibres”. In: *Nature* 434.7032 (2005), p. 488. DOI: [10.1038/nature03349](https://doi.org/10.1038/nature03349).
- [53] W. Jin, H.L. Ho, Y.C. Cao, J. Ju, and L.F. Qi. “Gas detection with micro- and nano-engineered optical fibers”. In: *Optical Fiber Technology* 19.6 (2013), pp. 741–759. DOI: [10.1016/j.yofte.2013.08.004](https://doi.org/10.1016/j.yofte.2013.08.004).
- [54] B. Culshaw et al. “Fibre optic techniques for remote spectroscopic methane detection—from concept to system realisation”. In: *Sensors and actuators B: chemical* 51.1 (1998), pp. 25–37. DOI: [10.1016/S0925-4005\(98\)00184-1](https://doi.org/10.1016/S0925-4005(98)00184-1).
- [55] W. Jin, H.F. Xuan, and H.L. Ho. “Sensing with hollow-core photonic bandgap fibers”. In: *Measurement Science and Technology* 21.9 (2010), p. 094014. DOI: [10.1088/0957-0233/21/9/094014](https://doi.org/10.1088/0957-0233/21/9/094014).
- [56] Y.L. Hoo, W. Jin, H.L. Ho, J. Ju, and D.N. Wang. “Gas diffusion measurement using hollow-core photonic bandgap fiber”. In: *Sensors and Actuators B: Chemical* 105.2 (2005), pp. 183–186. DOI: [10.1016/j.snb.2004.05.059](https://doi.org/10.1016/j.snb.2004.05.059).
- [57] T. Ritari, J. Tuominen, H. Ludvigsen, J.C. Petersen, T. Sorensen, T.P. Hansen, and H.R. Simonsen. “Gas sensing using air-guiding photonic bandgap fibers”. In: *Optics Express* 12.17 (2004), pp. 4080–4087. DOI: [10.1364/OPEX.12.004080](https://doi.org/10.1364/OPEX.12.004080).
- [58] J.A. Nwaboh, J. Hald, J.K. Lyngso, J.C. Petersen, and O. Werhahn. “Measurements of CO<sub>2</sub> in a multipass cell and in a hollow-core photonic bandgap fiber at 2 μm”. In: *Applied Physics B* 110.2 (2013), pp. 187–194. DOI: [10.1007/s00340-012-5047-0](https://doi.org/10.1007/s00340-012-5047-0).

- [59] A.M. Cubillas, M. Silva-Lopez, J.M. Lazaro, M.N. Conde O.M. and Petrovich, and J.M. Lopez-Higuera. “Methane detection at 1670-nm band using a hollow-core photonic bandgap fiber and a multiline algorithm”. In: *Optics Express* 15.26 (2007), pp. 17570–17576. DOI: [10.1364/OE.15.017570](https://doi.org/10.1364/OE.15.017570).
- [60] J.P. Parry et al. “Towards practical gas sensing with micro-structured fibres”. In: *Measurement Science and Technology* 20.7 (2009), p. 075301. DOI: [10.1088/0957-0233/20/7/075301](https://doi.org/10.1088/0957-0233/20/7/075301).
- [61] A.M. Cubillas et al. “Photonic crystal fibres for chemical sensing and photochemistry”. In: *Chemical Society Reviews* 42.22 (2013), pp. 8629–8648. DOI: [10.1039/c3cs60128e](https://doi.org/10.1039/c3cs60128e).
- [62] Y. Qu, Z.H. Kang, Y. Jiang, and J.Y. Gao. “Multiline absorption spectroscopy for methane gas detection”. In: *Applied Optics* 45.33 (2006), p. 8537. DOI: [10.1364/ao.45.008537](https://doi.org/10.1364/ao.45.008537).
- [63] K. Yamamoto, Hideo Tai, M. Uchida, S. Osawa, and K. Uehara. “Long-distance Simultaneous Detection Of Methane And Acetylene By Using Diode Lasers in Combination With Optical Fibers”. In: *IEEE photonics technology letters* 4.7 (1992), pp. 804–807. DOI: [10.1109/ofs.1992.763102](https://doi.org/10.1109/ofs.1992.763102).
- [64] B. Culshaw et al. “Evanescent wave methane detection using optical fibres”. In: *Electronics Letters* 28.24 (1992), pp. 2232–2234. DOI: [10.1049/el:19921434](https://doi.org/10.1049/el:19921434).
- [65] Y.L. Hoo, S.J. Liu, H.L. Ho, and W. Jin. “Fast response microstructured optical fiber methane sensor with multiple side-openings”. In: *IEEE Photonics Technology Letters* 22.5 (2010), pp. 296–298. DOI: [10.1109/LPT.2009.2039016](https://doi.org/10.1109/LPT.2009.2039016).
- [66] J.P. Carvalho et al. “Remote system for detection of low-levels of methane based on photonic crystal fibres and wavelength modulation spectroscopy”. In: *Journal of Sensors* 2009.2009 (2009). DOI: [10.1155/2009/398403](https://doi.org/10.1155/2009/398403).
- [67] R.M. Wynne, B. Barabadi, K.J. Creedon, and A. Ortega. “Sub-minute response time of a hollow-core photonic bandgap fiber gas sensor”. In: *Journal of Lightwave Technology* 27.11 (2009), pp. 1590–1596.
- [68] M.N. Petrovich, N.V. Heidt A.M. and Wheeler, N.K. Baddela, and D.J. Richardson. “High sensitivity methane and ethane detection using low-loss mid-IR hollow-core photonic bandgap fibers”. In: *In OFS2014 23rd International Conference on Optical Fiber Sensors, International Society for Optics and Photonics* (2014), 91573P–91573. DOI: [10.1117/12.2057842](https://doi.org/10.1117/12.2057842).
- [69] F. Yang, W. Jin, Y. Cao, H.L. Ho, and Y. Wang. “Towards high sensitivity gas detection with hollow-core photonic bandgap fibers”. In: *Optics Express* 22.20 (2014), pp. 24894–24907. DOI: [10.1364/OE.22.024894](https://doi.org/10.1364/OE.22.024894).
- [70] W. Jin, Y.C. Cao, F. Yang, and H.L. Ho. “Ultra-sensitive all-fibre photothermal spectroscopy with large dynamic range”. In: *Nature communications* 6.6767 (2015). DOI: [10.1038/ncomms7767](https://doi.org/10.1038/ncomms7767).
- [71] F. Yang, W. Jin, Y.C. Lin, et al. “Hollow-core microstructured optical fiber gas sensors”. In: *Journal of Lightwave Technology* 35.16 (2016), pp. 3413–3424. DOI: [10.1109/JLT.2016.2628092](https://doi.org/10.1109/JLT.2016.2628092).

- [72] Y.C. Lin, W. Jin, et al. “Pulsed photothermal interferometry for spectroscopic gas detection with hollow-core optical fibre”. In: *Scientific reports* 6.39410 (2016). DOI: [10.1038/srep39410](https://doi.org/10.1038/srep39410).
- [73] Y.C. Lin, W. Jin, F. Yang, Y.Z. Tan, and H.L. Ho. “Performance optimization of hollow-core fibre photothermal gas sensors”. to be published. 2017.
- [74] J.M. Fini. “Microstructure fibres for optical sensing in gases and liquids”. In: *Measurement Science and Technology*, 15.6 (2004), p. 1120. DOI: [10.1088/0957-0233/15/6/011](https://doi.org/10.1088/0957-0233/15/6/011).
- [75] M.N. Petrovich, F. Poletti, A. Van Brakel, and D.J. Richardson. “Robustly single mode hollow core photonic bandgap fiber”. In: *Optics Express* 16.6 (2008), pp. 4337–4346. DOI: [10.1364/OE.16.004337](https://doi.org/10.1364/OE.16.004337).
- [76] J.M. Fini, J.W. Nicholson, B. Mangan, L. Meng, R.S. Windeler, E.M. Monberg, A. DeSantolo, F.V. DiMarcello, and K. Mukasa. “Polarization maintaining single-mode low-loss hollow-core fibres”. In: *Nature communications*, 5, p.5085. 5 (2014), p. 5085. DOI: [10.1038/ncomms6085](https://doi.org/10.1038/ncomms6085).
- [77] C.C. Davis and S.J. Petuchowski. “Phase fluctuation optical heterodyne spectroscopy of gases”. In: *Applied optics* 20.14 (1981), pp. 2539–2554. DOI: [10.1364/AO.20.002539](https://doi.org/10.1364/AO.20.002539).
- [78] A. Rose, R. Vyas, and R. Gupta. “Pulsed photothermal deflection spectroscopy in a flowing medium: a quantitative investigation”. In: *Applied optics* 25.24 (1986), pp. 4626–4643. DOI: [10.1364/AO.25.004626](https://doi.org/10.1364/AO.25.004626).
- [79] S. Bialkowski. *Photothermal spectroscopy methods for chemical analysis*. Vol. 134. John Wiley & Sons, 1995. ISBN: 978-0-471-57467-5.
- [80] K. Krakenes and K. Blotekjaer. “Effect of laser phase noise in Sagnac interferometers”. In: *Journal of lightwave technology* 11.4 (1993), pp. 643–653. DOI: [10.1109/50.248130](https://doi.org/10.1109/50.248130).
- [81] S. Sumida, S. Okazaki, S. Asakura, H. Nakagawa, H. Murayama, and T. Hasegawa. “Distributed hydrogen determination with fiber-optic sensor”. In: *Sensors and Actuators B: Chemical* 108.1 (2005), pp. 508–514. DOI: [10.1016/j.snb.2004.11.068](https://doi.org/10.1016/j.snb.2004.11.068).
- [82] A. Garcia-Ruiz, J. Pastor-Graells, H.F. Martins, K.H. Tow, L. Thevenaz, S. Martin-Lopez, and M. Gonzalez-Herraez. “Distributed photothermal spectroscopy in microstructured optical fibers: towards high-resolution mapping of gas presence over long distances”. In: *Optics Express* 25.3 (2017), pp. 1789–1805. DOI: [10.1364/OE.25.001789](https://doi.org/10.1364/OE.25.001789).
- [83] R.M. Hanson R.K. and Spearrin and C.S. Goldenstein. *Spectroscopy and optical diagnostics for gases*. New York: Springer, 2016. ISBN: 978-3-319-23251-5.
- [84] H. Lefebvre-Brion and R.W. Field. *The Spectra and Dynamics of Diatomic Molecules: Revised and Enlarged Edition*. Academic Press, 2004.
- [85] HITRAN. “HITRAN database online”. In: *HITRAN* (). DOI: <http://hitran.org/>.
- [86] S. K. Dogra. *Physical Chemistry Through Problems*. Wiley, 1984. ISBN: 9780470274910.

- [87] L.S. Rothman et al. “The HITRAN 2008 molecular spectroscopic database”. In: *Journal of Quantitative Spectroscopy and Radiative Transfer* 110.9 (2008), pp. 533–572. DOI: [10.1016/j.jqsrt.2009.02.013](https://doi.org/10.1016/j.jqsrt.2009.02.013).
- [88] A. Miklos, P. Hess, and Z. Bozák. “Application of acoustic resonators in photoacoustic trace gas analysis and metrology”. In: *Review of scientific instruments* 72.4 (2001), pp. 1937–1955. DOI: [10.1063/1.1353198](https://doi.org/10.1063/1.1353198).
- [89] A.A. Kosterev, Y.A. Bakhirkin, R.F. Curl, and F.K. Tittel. “Quartz-enhanced photoacoustic spectroscopy”. In: *Optics Letters* 27.21 (2002), pp. 1902–1904. DOI: [10.1364/OL.27.001902](https://doi.org/10.1364/OL.27.001902).
- [90] R. Werle P.O. and Mücke and F Slemr. “The limits of signal averaging in atmospheric trace-gas monitoring by tunable diode-laser absorption spectroscopy (TDLAS)”. In: *Applied Physics B: Lasers and Optics* 57.2 (1993), pp. 131–139. DOI: [10.1007/BF00425997](https://doi.org/10.1007/BF00425997).
- [91] G.C. Bjorklund. “Frequency-modulation spectroscopy: a new method for measuring weak absorptions and dispersions”. In: *Optics Letters* 5.1 (1980), pp. 15–17. DOI: [10.1364/OL.5.000015](https://doi.org/10.1364/OL.5.000015).
- [92] M. Mazurenka, A.J. Orr-Ewing, R. Peverall, and G.A. Ritchie. “4 cavity ring-down and cavity enhanced spectroscopy using diode lasers”. In: *Annual Reports Section "C"(Physical Chemistry)* 101 (2005), pp. 100–142. DOI: [10.1039/B408909J](https://doi.org/10.1039/B408909J).
- [93] N.C. Wong et al. “Servo control of amplitude modulation in frequency modulation spectroscopy”. In: *JOSA B* 2.9 (1985), pp. 1527–1533. DOI: [10.1364/JOSAB.2.001527](https://doi.org/10.1364/JOSAB.2.001527).
- [94] J.A. Silver. “Frequency-modulation spectroscopy for trace species detection: theory and comparison among experimental methods”. In: *Applied Optics* 31.6 (1992), pp. 707–717. DOI: [10.1364/AO.31.000707](https://doi.org/10.1364/AO.31.000707).
- [95] J.M. Supplee, E.A. Whittaker, and W. Lenth. “Theoretical description of frequency modulation and wavelength modulation spectroscopy”. In: *Applied Optics* 33.27 (1994), pp. 6294–6302. DOI: [10.1364/AO.33.006294](https://doi.org/10.1364/AO.33.006294).
- [96] D.S. Bomse, A.C. Stanton, and J.A. Silver. “Frequency modulation and wavelength modulation spectroscopies: comparison of experimental methods using a lead-salt diode laser”. In: *Applied Optics* 31.6 (1992), pp. 718–731. DOI: [10.1364/AO.31.000718](https://doi.org/10.1364/AO.31.000718).
- [97] P. Kluczynski and O. Axner. “Theoretical description based on Fourier analysis of wavelength-modulation spectrometry in terms of analytical and background signals”. In: *Applied optics* 38.27 (1999), pp. 5803–5815. DOI: [10.1364/AO.38.005803](https://doi.org/10.1364/AO.38.005803).
- [98] S. Schilt, L. Thevenaz, and P. Robert. “Wavelength modulation spectroscopy: combined frequency and intensity laser modulation”. In: *Applied Optics* 42.33 (2003), pp. 6728–6738. DOI: [10.1364/AO.42.006728](https://doi.org/10.1364/AO.42.006728).
- [99] G.B. Rieker, J.B. Jeffries, and R.K. Hanson. “Calibration-free wavelength-modulation spectroscopy for measurements of gas temperature and concentration in harsh environments”. In: *Applied Optics* 48.29 (2009), pp. 5546–5560. DOI: [10.1364/AO.48.005546](https://doi.org/10.1364/AO.48.005546).

- [100] R. Arndt. “Analytical line shapes for Lorentzian signals broadened by modulation”. In: *Journal of Applied Physics* 36.8 (1965), pp. 2522–2524. DOI: [10.1063/1.1714523](https://doi.org/10.1063/1.1714523).
- [101] J. Reid and D. Labrie. “Second-harmonic detection with tunable diode lasers”. In: *Applied Physics B* 26.3 (1981), pp. 203–210. DOI: [10.1007/BF00692448](https://doi.org/10.1007/BF00692448).
- [102] S. Bialkowski. *Photothermal spectroscopy methods for chemical analysis*. John Wiley Sons, 1996.
- [103] S.E. Bialkowski and A. Chartier. “Diffraction effects in single and two laser photothermal lens spectroscopy”. In: *Applied Optics* 36.27 (1997), pp. 6711–6721. DOI: [10.1364/AO.36.006711](https://doi.org/10.1364/AO.36.006711).
- [104] W.B. Jackson, N.M. Amer, A.C. Boccara, and D. Fournier. “Photothermal deflection spectroscopy and detection”. In: *Applied optics* 20.8 (1981), pp. 1333–1344. DOI: [10.1364/AO.20.001333](https://doi.org/10.1364/AO.20.001333).
- [105] M.E. Long, R.L. Swofford, and A.C. Albrecht. “Thermal lens technique: a new method of absorption spectroscopy”. In: *Science* 191.4223 (1976), pp. 183–185. DOI: [10.1126/science.1246605](https://doi.org/10.1126/science.1246605).
- [106] N.J. Dovichi and S.E. Bialkowski. “Thermo-Optical Spectrophotometries in Analytical Chemistry”. In: *CRC Critical Reviews in Analytical Chemistry* 17.4 (1987), pp. 357–423. DOI: [10.1080/10408348708542799](https://doi.org/10.1080/10408348708542799).
- [107] A.J. Twarowski and D.S. Klinger. “Multiphoton absorption spectra using thermal blooming: I. Theory”. In: *Chemical Physics* 20.2 (1977), pp. 253–258. DOI: [10.1016/0301-0104\(77\)85029-5](https://doi.org/10.1016/0301-0104(77)85029-5).
- [108] F.R. Grabiner, D.R. Siebert, and G.W. Flynn. “Laser induced time-dependent thermal lensing studies of vibrational relaxation: translational cooling in  $CH_3F$ ”. In: *Chemical Physics Letters* 17.2 (1972), pp. 189–194. DOI: [10.1016/0009-2614\(72\)87051-9](https://doi.org/10.1016/0009-2614(72)87051-9).
- [109] J. Stone. “Measurements of the absorption of light in low-loss liquids”. In: *JOSA* 62.3 (1972), pp. 327–333. DOI: [10.1364/JOSA.62.000327](https://doi.org/10.1364/JOSA.62.000327).
- [110] A.D. Kersey, A. Dandridge, and A.B. Tveten. “Time division multiplexing of interferometric fiber sensors using passive phase generated carrier interrogation”. In: *Optics Letters* 12.10 (1987), pp. 775–777. DOI: [10.1364/OL.12.000775](https://doi.org/10.1364/OL.12.000775).
- [111] D.A. Jackson, A. Dandridge, and S.K. Sheem. “Measurement of small phase shifts using a single-mode optical-fiber interferometer”. In: *Optics Letters* 5.4 (1980), pp. 139–141. DOI: [10.1364/OL.5.000139](https://doi.org/10.1364/OL.5.000139).
- [112] M. Tateda, N. Shibata, and S. Seikai. “Interferometric method for chromatic dispersion measurement in a single-mode optical fiber”. In: *IEEE Journal of Quantum Electronics* 17.3 (1981), pp. 404–407. DOI: [10.1109/JQE.1981.1071115](https://doi.org/10.1109/JQE.1981.1071115).
- [113] S. Petuchowski, T. Giallorenzi, and S. Sheem. “A sensitive fiber-optic Fabry-Perot interferometer”. In: *IEEE Journal of Quantum Electronics* 17.11 (1981), pp. 2168–2170. DOI: [10.1109/JQE.1981.1070682](https://doi.org/10.1109/JQE.1981.1070682).
- [114] D.A. Jackson. “Monomode optical fibre interferometers for precision measurement”. In: *Journal of Physics E: Scientific Instruments* 18.12 (1985), p. 981. DOI: [10.1088/0022-3735/18/12/001](https://doi.org/10.1088/0022-3735/18/12/001).

- [115] A. Dandridge. “Fiber optic sensors based on the Mach-Zehnder and Michelson interferometers”. In: *Fiber Optic Sensors: An Introduction for Engineers and Scientists* (1991), pp. 271–323.
- [116] A. Yariv and P. Yeh. *Photonics: optical electronics in modern communications*. 6th ed. Oxford University Press, 2007.
- [117] A.D. Kersey, T.A. Berkoff, and W.W. Morey. “High-resolution fibre-grating based strain sensor with interferometric wavelength-shift detection”. In: *Electronics Letters* 28.3 (1992), pp. 236–238. DOI: [10.1049/el:19920146](https://doi.org/10.1049/el:19920146).
- [118] D.A. Jackson, R. Priest, A. Dandridge, and A.B. Tveten. “Elimination of drift in a single-mode optical fiber interferometer using a piezoelectrically stretched coiled fiber”. In: *Applied Optics* 19.17 (1980), pp. 2926–2929. DOI: [10.1364/AO.19.002926](https://doi.org/10.1364/AO.19.002926).
- [119] A.D. Kersey, D.A. Jackson, and M. Corke. “Passive compensation scheme suitable for use in the single-mode fibre interferometer”. In: *Electronics Letters* 18.9 (1982), pp. 392–393. DOI: [10.1049/el:19820268](https://doi.org/10.1049/el:19820268).
- [120] J. Frejlich, K.H. Garcia P.M. and Ringhofer, and E. Shamonina. “Phase modulation in two-wave mixing for dynamically recorded gratings in photo-refractive materials”. In: *JOSA B* 14.7 (1997), pp. 1741–1749. DOI: [10.1364/JOSAB.14.001741](https://doi.org/10.1364/JOSAB.14.001741).
- [121] H. Iwai, C. Fang-Yen, G. Popescu, A. Wax, K. Badizadegan, R.R. Dasari, and M.S. Feld. “Quantitative phase imaging using actively stabilized phase-shifting low-coherence interferometry”. In: *Optics Letters* 29.20 (2004), pp. 2399–2401. DOI: <https://doi.org/10.1364/OL.29.002399>.
- [122] A.A. Freschi and J. Frejlich. “Adjustable phase control in stabilized interferometry”. In: *Optics Letters* 20.6 (1995), pp. 635–637. DOI: [10.1364/OL.20.000635](https://doi.org/10.1364/OL.20.000635).
- [123] V.V. Krishnamachari, E.R. Andresen, S.R. Keiding, and E.O Potma. “An active interferometer-stabilization scheme with linear phase control”. In: *Optics Express* 14.12 (2006), pp. 5210–5215. DOI: [10.1364/OE.14.005210](https://doi.org/10.1364/OE.14.005210).
- [124] S.B. Cho and T.G. Noh. “Stabilization of a long-armed fiber-optic single-photon interferometer”. In: *Optics Express* 17.21 (2009), pp. 19027–19032. DOI: [10.1364/OE.17.019027](https://doi.org/10.1364/OE.17.019027).
- [125] A. Rosenthal, S. Kellnberger, G. Sergiadis, and V. Ntziachristos. “Wideband fiber-interferometer stabilization with variable phase”. In: *IEEE Photonics Technology Letters* 24.17 (2012), pp. 1499–1501. DOI: -.
- [126] S. Dorigi J.F. and Krishnaswamy and J.D Achenbach. “Stabilization of an embedded fiber optic Fabry-Perot sensor for ultrasound detection”. In: *IEEE transactions on ultrasonics, ferroelectrics, and frequency control* 42.5 (1995), pp. 820–824. DOI: [10.1109/58.464837](https://doi.org/10.1109/58.464837).
- [127] A. Dandridge, A. Tveten, and T. Giallorenzi. “Homodyne demodulation scheme for fiber optic sensors using phase generated carrier”. In: *IEEE Journal of Quantum Electronics* 18.10 (1982), pp. 1647–1653. DOI: [10.1109/JQE.1982.1071416](https://doi.org/10.1109/JQE.1982.1071416).
- [128] J.H. Cole, B.A. Danver, and J.A Bucaro. “Synthetic-heterodyne interferometric demodulation”. In: *IEEE Transactions on Microwave Theory and Techniques* 30.4 (1982), pp. 540–543. DOI: [10.1109/TMTT.1982.1131096](https://doi.org/10.1109/TMTT.1982.1131096).

- [129] Y.L. Lo and C.H. Chuang. “New synthetic-heterodyne demodulator for an optical fiber interferometer”. In: *IEEE journal of quantum electronics* 37.5 (2001), pp. 658–663. DOI: [10.1109/3.918578](https://doi.org/10.1109/3.918578).
- [130] J. Brooks, R. Wentworth, R. Youngquist, M. Tur, B.Y. Kim, and H.J. Shaw. “Coherence multiplexing of fiber-optic interferometric sensors”. In: *Journal of Lightwave Technology* 3.5 (1985), pp. 1062–1072. DOI: [10.1109/JLT.1985.1074308](https://doi.org/10.1109/JLT.1985.1074308).
- [131] S.K. Sheem. “Fiber-optic gyroscope with  $3 \times 3$  directional coupler”. In: *Applied Physics Letters* 37.10 (1980), pp. 869–871. DOI: [10.1063/1.91867](https://doi.org/10.1063/1.91867).
- [132] K. Kråkenes and K. Blotekjaer. “Sagnac interferometer for underwater sound detection: noise properties”. In: *Optics letters* 14.20 (1989), pp. 1152–1154. DOI: [10.1364/OL.14.001152](https://doi.org/10.1364/OL.14.001152).
- [133] S. Knudsen and K. Blotekjaer. “An ultrasonic fiber-optic hydrophone incorporating a push-pull transducer in a Sagnac interferometer”. In: *Journal of Lightwave Technology* 12.9 (1994), pp. 1696–1700. DOI: [10.1109/50.320954](https://doi.org/10.1109/50.320954).
- [134] B.J. Vakoc, M.J.F. Digonnet, and G.S. Kino. “A folded configuration of a fiber Sagnac-based sensor array”. In: *Optical Fiber Technology* 6.4 (2000), pp. 388–399. DOI: [10.1006/ofte.2000.0338](https://doi.org/10.1006/ofte.2000.0338).
- [135] J.C. Juarez and H.F. Taylor. “Polarization discrimination in a phase-sensitive optical time-domain reflectometer intrusion-sensor system”. In: *Optics Letters* 30.24 (2005), pp. 3284–3286. DOI: [10.1364/OL.30.003284](https://doi.org/10.1364/OL.30.003284).
- [136] P. Fomitchov, S. Stechenrider J.S. and Krishnaswamy, and J.D. Achenbach. “Frequency shifted low noise Sagnac sensor for ultrasonic measurements”. In: *Review of Progress in Quantitative Nondestructive Evaluation* (1997), pp. 2053–2060. DOI: [10.1007/978-1-4615-5947-4\\_268](https://doi.org/10.1007/978-1-4615-5947-4_268).
- [137] J. Ma, Y.Q. Yu, and W. Jin. “Demodulation of diaphragm based acoustic sensor using Sagnac interferometer with stable phase bias”. In: *Optics Express* 23.22 (2015), pp. 29268–29278. DOI: [10.1364/OE.23.029268](https://doi.org/10.1364/OE.23.029268).
- [138] K.H. Han, W. Jin, and B.Y. Kim. “Fiber-optic sensor array based on Sagnac interferometer with stable phase bias”. In: *IEEE Photonics Technology Letters* 13.2 (2001), pp. 148–150. DOI: [10.1109/68.910517](https://doi.org/10.1109/68.910517).
- [139] B.J. Vakoc, M.J. Digonnet, and G.S. Kino. “Demonstration of a folded Sagnac sensor array immune to polarization-induced signal fading”. In: *Applied Optics* 42.36 (2003), pp. 7132–7136. DOI: [10.1364/AO.42.007132](https://doi.org/10.1364/AO.42.007132).
- [140] G.L. Abbas, V.W.S. Chan, and T.K. Yee. “Local-oscillator excess-noise suppression for homodyne and heterodyne detection”. In: *Optics letters* 8.8 (1983), pp. 419–421. DOI: [10.1364/OL.8.000419](https://doi.org/10.1364/OL.8.000419).
- [141] R. Stierlin, R. Battig, P.D. Henchoz, and H.P. Weber. “Excess-noise suppression in a fibre-optic balanced heterodyne detection system”. In: *Optical and quantum electronics* 18.6 (1986), pp. 445–454. DOI: [10.1007/BF02041170](https://doi.org/10.1007/BF02041170).
- [142] É.I. Alekseev and E.N. Bazarov. “Theoretical basis of the method for reducing drift of the zero level of the output signal of a fiber-optic gyroscope with the aid of a Lyot depolarizer”. In: *Soviet journal of quantum electronics* 22.9 (1992), p. 834. DOI: [10.1070/QE1992v022n09ABEH003609](https://doi.org/10.1070/QE1992v022n09ABEH003609).

- [143] B. Szafraniec and G.A. Sanders. “Theory of polarization evolution in interferometric fiber-optic depolarized gyros”. In: *Journal of Lightwave Technology* 17.4 (1999), p. 579.
- [144] C.C. Davis. “Trace detection in gases using phase fluctuation optical heterodyne spectroscopy”. In: *Applied Physics Letters* 36.7 (1980), pp. 515–518. DOI: [10.1063/1.91590](https://doi.org/10.1063/1.91590).
- [145] H.S. Carslaw and J.C. Jaeger. *Heat in solids*. Clarendon Press, Oxford, 1959.
- [146] J.R. Whinnery. “Laser measurement of optical absorption in liquids”. In: *Accounts of Chemical Research* 7.7 (1974), pp. 225–231. DOI: [10.1021/ar50079a003](https://doi.org/10.1021/ar50079a003).
- [147] H.B. Lin and A.J. Campillo. “Photothermal aerosol absorption spectroscopy”. In: *Applied Optics* 24.3 (1985), pp. 422–433. DOI: [10.1364/AO.24.000422](https://doi.org/10.1364/AO.24.000422).
- [148] M.A. Owens, C.C. Davis, and R.R. Dickerson. “A photothermal interferometer for gas-phase ammonia detection”. In: *Analytical chemistry* 71.7 (1999), pp. 1391–1399. DOI: [10.1021/ac980810h](https://doi.org/10.1021/ac980810h).
- [149] N.D. Weston, P. Sakhivel, and P. Mukherjee. “Ultrasensitive spectral trace detection of individual molecular components in an atmospheric binary mixture”. In: *Applied Optics* 32.6 (1993), pp. 828–835. DOI: [10.1364/AO.32.000828](https://doi.org/10.1364/AO.32.000828).
- [150] A.J. Campillo, S.J. Petuchowski, C.C. Davis, and H.B. Lin. “Fabry–Perot photothermal trace detection”. In: *Applied Physics Letters* 41.4 (1982), pp. 327–329. DOI: [10.1063/1.93524](https://doi.org/10.1063/1.93524).
- [151] D.L. Mazzone and C.C. Davis. “Trace detection of hydrazines by optical homodyne interferometry”. In: *Applied Optics* 30.7 (1991), pp. 756–764. DOI: [10.1364/AO.30.000756](https://doi.org/10.1364/AO.30.000756).
- [152] A.J. Sedlacek III. “Real time detection of ambient aerosols using photothermal interferometry: folded Jamin interferometer”. In: *Review of scientific instruments* 77.6 (2006), p. 064903. DOI: [10.1063/1.2205623](https://doi.org/10.1063/1.2205623).
- [153] A. Cournoyer et al. “Photothermal measurements with a Jamin interferometer”. In: *Applied Optics* 36.21 (1997), pp. 5252–5261. DOI: [10.1364/AO.36.005252](https://doi.org/10.1364/AO.36.005252).
- [154] P.St J. Russell et al. “Hollow-core photonic crystal fibres for gas-based nonlinear optics”. In: *Nature Photonics* 8.4 (2014), pp. 278–286. DOI: [10.1038/nphoton.2013.312](https://doi.org/10.1038/nphoton.2013.312).
- [155] J.C. Wang and G.S. Springer. “Vibrational relaxation times in some hydrocarbons in the range 300–900 K”. In: *The Journal of Chemical Physics* 59.12 (1973), pp. 6556–6562. DOI: [10.1063/1.1680034](https://doi.org/10.1063/1.1680034).
- [156] R.W. Barber and D.R. Emerson. “The influence of Knudsen number on the hydrodynamic development length within parallel plate micro-channels”. In: *WIT Transactions on Engineering Sciences* 36 (2002).
- [157] D.C. Smith. “Thermal defocusing in CO<sub>2</sub> laser radiation in gases”. In: *Quantum Electronics* 5 (1969), pp. 600–607.
- [158] K.Z. Aghaie, M.J. Digonnet, and S. Fan. “Experimental assessment of the accuracy of an advanced photonic-bandgap-fiber model”. In: *Journal of Lightwave Technology* 31.7 (2013), pp. 1015–1022. DOI: [10.1109/JLT.2013.2238608](https://doi.org/10.1109/JLT.2013.2238608).

- [159] M.K. Davis, M.J.F. Digonnet, and R.H. Pantell. “Thermal effects in doped fibers”. In: *Journal of lightwave technology* 16.6 (1998), p. 1013.
- [160] A.W. Snyder and J. Love. *Optical waveguide theory*. Springer Science and Business Media, 2012.
- [161] B. Monson, R. Vyas, and R. Gupta. “Pulsed and cw photothermal phase shift spectroscopy in a fluid medium: theory”. In: *Applied optics* 28.13 (1989), pp. 2554–2561. DOI: [10.1364/AO.28.002554](https://doi.org/10.1364/AO.28.002554).
- [162] Y.C. Lin, W. Jin, F. Yang, and C. Wang. “Highly sensitive and stable all-fiber photothermal spectroscopic gas sensor”. In: *In CLEO: Science and Innovations (pp. STu4H-3)*. Optical Society of America (2016). DOI: [10.1364/CLEO\\_SI.2016.STu4H.3](https://doi.org/10.1364/CLEO_SI.2016.STu4H.3).
- [163] P. Werle et al. “Quantum-limited FM-spectroscopy with a lead-salt diode laser”. In: *Applied Physics B: Lasers and Optics* 49.2 (1989), pp. 99–108. DOI: [10.1007/BF00332268](https://doi.org/10.1007/BF00332268).
- [164] Y.C. Lin, W. Jin, et al. “Pulsed photothermal interferometry for spectroscopic gas detection with hollow-core optical fibre”. In: *Scientific reports* 6 (2016), p. 39410. DOI: [10.1038/srep39410](https://doi.org/10.1038/srep39410).
- [165] B. Moslehi. “Analysis of optical phase noise in fiber-optic systems employing a laser source with arbitrary coherence time”. In: *Journal of lightwave technology* 4.9 (1986), pp. 1334–1351. DOI: [10.1109/JLT.1986.1074894](https://doi.org/10.1109/JLT.1986.1074894).
- [166] S. Knudsen, A.B. Tveten, and A. Dandridge. “Measurements of fundamental thermal induced phase fluctuations in the fiber of a Sagnac interferometer”. In: *IEEE photonics technology letters* 7.1 (1995), pp. 90–92. DOI: [10.1109/68.363366](https://doi.org/10.1109/68.363366).
- [167] K.H. Wanser. “Fundamental phase noise limit in optical fibres due to temperature fluctuations”. In: *Electronics letters* 28.1 (1992), pp. 53–54. DOI: [10.1049/el:19920033](https://doi.org/10.1049/el:19920033).
- [168] D. Yan, J. Popp, M.W. Pletz, and T. Frosch. “Highly sensitive broadband Raman sensing of antibiotics in step-index hollow-core photonic crystal fibers”. In: *ACS Photonics* 4.1 (2017), pp. 138–145. DOI: [10.1021/acsp Photonics.6b00688](https://doi.org/10.1021/acsp Photonics.6b00688).
- [169] Y.C. Lin, W. Jin, F. Yang, and H.L. Ho. “Performance optimization of hollow-core fibre photothermal gas sensors”. being prepared for submit. 2017.
- [170] X. Bao and L. Chen. “Recent progress in distributed fiber optic sensors”. In: *Sensors* 12.7 (2012), pp. 8601–8639. DOI: [10.3390/s120708601](https://doi.org/10.3390/s120708601).
- [171] W. Eickhoff and R. Ulrich. “Optical frequency domain reflectometry in single-mode fiber”. In: *Applied Physics Letters* 39.9 (1981), pp. 693–695. DOI: [10.1063/1.92872](https://doi.org/10.1063/1.92872).
- [172] V. Dangui, M.J. Digonnet, and G.S. Kino. “Modeling of the propagation loss and backscattering in air core photonic bandgap fibers”. In: *Journal of Lightwave Technology* 27.17 (2009), pp. 3783–3789. DOI: [10.1109/JLT.2008.2010876](https://doi.org/10.1109/JLT.2008.2010876).
- [173] X. Fang. “Fiber-optic distributed sensing by a two-loop Sagnac interferometer”. In: *Optics Letters* 21.6 (1996), pp. 444–446. DOI: [10.1364/OL.21.000444](https://doi.org/10.1364/OL.21.000444).

- [174] Y. Lu, T. Zhu, L. Chen, and X. Bao. “Distributed vibration sensor based on coherent detection of phase-OTDR”. In: *Journal of Lightwave Technology* 28.22 (2010), pp. 3243–3249. DOI: [10.1109/JLT.2010.2078798](https://doi.org/10.1109/JLT.2010.2078798).
- [175] M.G. Herraiez, A. Garcia-Ruiz, et al. “Chirped-pulse Phase-sensitive Optical Time Domain Reflectometry”. In: *In Asia Communications and Photonics Conference. Optical Society of America* (2016).
- [176] A. Dandridge, A. Tveten, A. Kersey, and A. Yurek. “Multiplexing of interferometric sensors using phase carrier techniques”. In: *Journal of Lightwave Technology* 5.7 (1987), pp. 947–952. DOI: [10.1109/JLT.1987.1075587](https://doi.org/10.1109/JLT.1987.1075587).
- [177] K.P. Koo, A.B. Tveten, and A. Dandridge. “Passive stabilization scheme for fiber interferometers using  $3 \times 3$  fiber directional couplers”. In: *Applied Physics Letters* 41.7 (1982), p. 616. DOI: [10.1063/1.93626](https://doi.org/10.1063/1.93626).
- [178] X.G. He, S.R. Xie, F. Liu, and M. Zhang. “Multi-event waveform-retrieved distributed optical fiber acoustic sensor using dual pulse heterodyne phase sensitive OTDR”. In: *Optics Letters* 42.3 (2017), pp. 442–445. DOI: [10.1364/OL.42.000442](https://doi.org/10.1364/OL.42.000442).
- [179] F. Liu et al. “Efficient Common-Mode Noise Suppression for Fiber Optic Interferometric Sensor Using Heterodyne Demodulation”. In: *Journal of Lightwave Technology* 34.23 (2016), pp. 5453–5461. DOI: [10.1109/JLT.2016.2606758](https://doi.org/10.1109/JLT.2016.2606758).
- [180] K. Inoue. “Brillouin threshold in an optical fiber with bidirectional pump lights”. In: *Optics Communications* 120.1-2 (1995), pp. 34–38. DOI: [10.1016/0030-4018\(95\)00409-2](https://doi.org/10.1016/0030-4018(95)00409-2).
- [181] M. Nikles, L. Thevenaz, and P.A. Robert. “Brillouin gain spectrum characterization in single-mode optical fibers”. In: *Journal of Lightwave Technology* 15.10 (1997), pp. 1842–1851. DOI: [10.1109/50.633570](https://doi.org/10.1109/50.633570).
- [182] T. Horiguchi, K. Shimizu, T. Kurashima, M. Tateda, and Y. Koyamada. “Development of a distributed sensing technique using Brillouin scattering”. In: *Journal of Lightwave Technology* 13.7 (1995), pp. 1296–1302. DOI: [10.1109/50.400684](https://doi.org/10.1109/50.400684).
- [183] M.A. Soto, J.A. Ramirez, and L. Thevenaz. “Intensifying the response of distributed optical fibre sensors using 2D and 3D image restoration”. In: *Nature communications* 7 (2016). DOI: [10.1038/ncomms10870](https://doi.org/10.1038/ncomms10870).
- [184] L. Qin Z. and Chen and X. Bao. “Wavelet denoising method for improving detection performance of distributed vibration sensor”. In: *IEEE Photonics Technology Letters* 24.5 (2012), p. 542. DOI: [10.1109/LPT.2011.2182643](https://doi.org/10.1109/LPT.2011.2182643).
- [185] F. Liu et al. “A new measurement scheme for delay parameters in TDM fiber optic interferometric sensor network”. In: *Optical Fiber Sensors Conference (OFS)* (2017). DOI: [10.1117/12.2255876](https://doi.org/10.1117/12.2255876).
- [186] J.M. Masciotti, J.M. Lasker, and A.H. Hielscher. “Digital lock-in detection for discriminating multiple modulation frequencies with high accuracy and computational efficiency”. In: *IEEE Transactions on Instrumentation and Measurement* 57.1 (2008), pp. 182–189. DOI: [10.1109/TIM.2007.908604](https://doi.org/10.1109/TIM.2007.908604).
- [187] F.J. Harris. “On the use of windows for harmonic analysis with the discrete Fourier transform”. In: *Proceedings of the IEEE* 66.1 (1978), pp. 51–83. DOI: [10.1109/PROC.1978.10837](https://doi.org/10.1109/PROC.1978.10837).

- [188] G.P. Agrawal. *Nonlinear fiber optics*. Academic Press, 2007.
- [189] Y.Z. Tan et al. “Hollow-Core Fiber-Based High Finesse Resonating Cavity for High Sensitivity Gas Detection”. In: *Journal of Lightwave Technology* 35.14 (2017), pp. 2887–2893. DOI: [10.1109/JLT.2017.2705229](https://doi.org/10.1109/JLT.2017.2705229).
- [190] V. Dangui, M.J. Digonnet, and G.S. Kino. “Determination of the mode reflection coefficient in air core photonic bandgap fibers”. In: *Optics Express* 15.9 (2007), pp. 5342–5359. DOI: [10.1364/OE.15.005342](https://doi.org/10.1364/OE.15.005342).
- [191] F. Couny, F. Benabid, and P.S. Light. “Reduction of Fresnel back-reflection at splice interface between hollow core PCF and single mode fiber”. In: *IEEE Photonics Technology Letters* 19.13 (2007), pp. 1020–1022. DOI: [10.1109/LPT.2007.898770](https://doi.org/10.1109/LPT.2007.898770).
- [192] M. Nakazawa, M. Tokuda, and N Uchida. “Analyses of optical time-domain reflectometry for single-mode fibers and of polarization optical time-domain reflectometry for polarization-maintaining fibers”. In: *Optics Letters* 8.2 (1983), pp. 130–132. DOI: [10.1364/OL.8.000130](https://doi.org/10.1364/OL.8.000130).
- [193] L. Thevenaz. “Review and progress on distributed fibre sensing”. In: *In Optical Fiber Sensors (p. ThC1)*. Optical Society of America (2006). DOI: [10.1364/OFS.2006.ThC1](https://doi.org/10.1364/OFS.2006.ThC1).
- [194] F. Benabid and P.J. Roberts. “Linear and nonlinear optical properties of hollow core photonic crystal fiber”. In: *Journal of Modern Optics* 58.2 (2011), pp. 87–124. DOI: [10.1080/09500340.2010.543706](https://doi.org/10.1080/09500340.2010.543706).
- [195] H. Izumita, Y. Koyamada, S.I. Furukawa, and I. Sankawa. “The performance limit of coherent OTDR enhanced with optical fiber amplifiers due to optical nonlinear phenomena”. In: *Journal of lightwave technology* 12.7 (1994), pp. 1230–1238. DOI: [10.1109/50.301816](https://doi.org/10.1109/50.301816).
- [196] A. Rogers. “Distributed optical-fibre sensing”. In: *Measurement Science and Technology* 10.8 (1999), R75. DOI: [10.1088/0957-0233/10/8/201](https://doi.org/10.1088/0957-0233/10/8/201).
- [197] X. Bao and L. Chen. “Recent progress in Brillouin scattering based fiber sensors”. In: *Sensors* 11.4 (2011), pp. 4152–4187. DOI: [10.3390/s110404152](https://doi.org/10.3390/s110404152).
- [198] A.D. Pryamikov et al. “Demonstration of a waveguide regime for a silica hollow-core microstructured optical fiber with a negative curvature of the core boundary in the spectral region  $> 3.5 \mu\text{m}$ ”. In: *Optics Express* 19.2 (2011), pp. 1441–1448. DOI: [10.1364/OE.19.001441](https://doi.org/10.1364/OE.19.001441).
- [199] M. El-Amraoui et al. “Strong infrared spectral broadening in low-loss As-S chalcogenide suspended core microstructured optical fibers”. In: *Optics Express* 18.5 (2010), pp. 4547–4556. DOI: [10.1364/OE.18.004547](https://doi.org/10.1364/OE.18.004547).
- [200] A.S. Webb, F. Poletti, D.J. Richardson, and J.K. Sahu. “Suspended-core holey fiber for evanescent-field sensing”. In: *Optical Engineering* 46.1 (2007), p.010503. DOI: [10.1117/1.2430505](https://doi.org/10.1117/1.2430505).
- [201] L. Shiloh and A. Eyal. “Distributed acoustic and vibration sensing via optical fractional Fourier transform reflectometry”. In: *Optics Express* 23.4 (2015), pp. 4296–4306. DOI: [10.1364/OE.23.004296](https://doi.org/10.1364/OE.23.004296).
- [202] T. Parker, S. Shatalin, and M. Farhadiroushan. “Distributed Acoustic Sensing—a new tool for seismic applications”. In: *First Break* 32.2 (2014), pp. 61–69. DOI: [10.3997/1365-2397.2013034](https://doi.org/10.3997/1365-2397.2013034).

- 
- [203] P. Golacki, A. Masoudi, K. Holland, and T. Newson. “Distributed optical fibre acoustic sensors—future applications in audio and acoustics engineering”. In: *ACOUSTICS 2016, United Kingdom* (). DOI: <https://eprints.soton.ac.uk/403159/>.
- [204] H. Gabai and A. Eyal. “On the sensitivity of distributed acoustic sensing”. In: *Optics Letters* 41.24 (2017), pp. 5648–5651. DOI: [10.1364/OL.41.005648](https://doi.org/10.1364/OL.41.005648).

